R-09-21

Groundwater flow modelling of periods with periglacial and glacial climate conditions – Forsmark

Patrik Vidstrand, TerraSolve AB

Sven Follin, SF GeoLogic AB

Nada Zugec, Bergab

December 2010

Svensk Kärnbränslehantering AB
Swedish Nuclear Fuel
and Waste Management Co

Box 250, SE-101 24 Stockholm
Phone +46 8 459 84 00

SKB

ISSN 1402-3091
SKB R-09-21
ID: 1233544
Updated 2013-09

Groundwater flow modelling of periods with periglacial and glacial climate conditions – Forsmark

Patrik Vidstrand, TerraSolve AB

Sven Follin, SF GeoLogic AB

Nada Zugec, Bergab

December 2010

Keywords: Hydrogeology, Groundwater, Modelling, Permafrost, Ice sheet, Periglacial, Glacial, Forsmark, Safety assessment.

Update notice

The original report, dated December 2010, was found to contain both factual and editorial errors which have been corrected in this updated version. The corrected factual errors are presented below.

Updated 2013-09

Location	Original text	Corrected text
Page 41, Table 3-3, column 4, rows 1, 2 and 5	Wrong data in table	Table updated with correct data
Page 106, Table B-1, column 4, rows 1, 2 and 5	Wrong data in table	Table updated with correct data
Page 106, Table B-1, column 5	Wrong data in table	Table updated with correct data
Page 106, Table B-1, rows 12-15		New data in table
Page 106, Table B-4, column 5	Wrong data in table	Table updated with correct data
Page 107, Table B-7, column 5	Wrong data in table	Table updated with correct data
Page 191		*New appendix H*, DFN parameters for FFM02

The updated tables show the correct input values used in the modelling presented in the original version of this report; i.e. all results are identical between the original and the up-dated versions of the report.

Posterior to the completion of SR-Site, it was discovered that the orientation data used to model the discrete fracture network (DFN) of FFM02, see Table B-4, deviate from the data used for SDM-Site Forsmark, see Table C-2 in Follin (2008). A new appendix, Appendix H, has been inserted in this updated version. Appendix H explains the deviations and comments the implications for the groundwater flow modelling of periods with periglacial and glacial climate conditions.

Abstract

As a part of the license application for a final repository for spent nuclear fuel at Forsmark, the Swedish Nuclear Fuel and Waste Management Company (SKB) has undertaken a series of groundwater flow modelling studies. These represent time periods with different hydraulic conditions and the simulations carried out contribute to the overall evaluation of the repository design and long-term radiological safety.

The groundwater flow modelling study reported here comprises a coupled thermal-hydraulic-chemical (T-H-C) analysis of periods with periglacial and glacial climate conditions. Hydraulic-mechanical (H-M) issues are also handled but no coupled flow modelling is done. The objective of the report is to provide bounding hydrogeological estimates at different stages during glaciation and deglaciation of a glacial cycle for subsequent use in safety assessment applications within SKB's project SR-Site. Three cases with different climate conditions are analysed here: (i) Temperate case, (ii) Glacial case without permafrost, and (iii) Glacial case with permafrost. The glacial periods are transient and encompass approximately 19,000 years. The simulation results comprise residual fluid pressures, Darcy fluxes, and water salinities, as well as advective transport performance measures obtained by particle tracking such as flow path lengths, travel times and flow-related transport resistances. The modelling is accompanied by a sensitivity study that addresses the impact of the following matters: the direction of the ice sheet advance, the speed of the ice sheet margin, the bedrock hydraulic and transport properties, the temperature at the ice-subsurface interface close to the ice sheet margin, and the initial hydrochemical conditions.

Sammanfattning

I Svensk Kärnbränslehanterings (SKB) ansökan om ett slutförvar för använt kärnbränsle i Forsmark ingår olika grundvattenmodelleringsstudier. Studierna hanterar perioder med olika hydrauliska förhållanden och beräkningsresultaten från simuleringarna bidrar till bedömningsunderlaget inom design och långsiktig säkerhet.

Resultaten som redovisas i denna rapport kommer från en kopplad termisk-hydraulisk-kemisk (T-H-C) modell som simulerar grundvattenströmning under perioder med permafrost och inlandsis. Även hydro-mekaniska (H-M) frågor hanteras men simuleras inte kopplat. Arbetet har som mål att via flödessimuleringar gränssätta diverse hydrogeologiska parametrar under olika skeden av nedisning och avsmältning. Värdena används i SKB:s säkerhetsanlays (projket SR-Site). Simuleringarna omfattar tre fall med olika klimat: (i) tempererade förhållanden, (ii) glaciala förhållanden utan permafrost, och (iii) glaciala förhållanden med permafrost. De glaciala fallen är transienta och täcker en period av ca 19 000 år. Beräkningsresultaten omfattar residualtryck, darcyfluxer, grundvattnets salinitet, flödesvägar, advektiva transporttider och flödesrelaterat transportmotstånd. I arbetet ingår även en känslighetsstudie, som bland annat undersöker hur beräkningsresultaten påverkas av isen rörelsesriktning, isfrontens hastighet, bergets hydrauliska egenskaper, temperaturen i kontaktytan mellan is och berg närmast isfronten, samt förhållandena innan simuleringarna påbörjas.

Contents

1 Introduction

1.1 Background

The Swedish Nuclear Fuel and Waste Management Company (SKB) has conducted site investigations at two different locations, the Forsmark site and the Laxemar-Simpevarp site (Figure 1-1), with the objective of siting a final repository for spent nuclear fuel according to the KBS-3 concept. As a part of the application for a final repository for spent nuclear fuel at Forsmark[1], information from a series of groundwater flow modelling studies is evaluated to serve as a basis for an assessment of the repository design and long-term radiological safety premises. The present report is one of a series of three groundwater flow modelling studies that together handle different periods of the entire lifetime of a final repository at Forsmark. The three reports are:

- Groundwater flow modelling of the excavation and operation phases – Forsmark /Svensson and Follin 2010/.
- Groundwater flow modelling of periods with temperate climate conditions – Forsmark /Joyce et al. 2010/.
- Groundwater flow modelling of periods with periglacial and glacial climate conditions – Forsmark (this report).

A corresponding series of studies exists for the investigated area at Laxemar/Simpevarp. These support the site-selection report accompanying the application for Forsmark.

1.2 Scope and objectives

The main objective of the work reported here is to provide quantifications of, and uncertainty indicators for, the effects on the performance measures studied by SKB (see Section 1.3.4) as a function of the hydrogeological conditions associated with future periods with periglacial and glacial climate conditions at Forsmark. Furthermore, the study is undertaken to strengthen the link between SKB's climate modelling /SKB 2010/ and the safety assessment project SR-Site, which was considered necessary by the authorities in their review of the SR-Can project /SKB 2006/, see /Dverstorp and Strömberg 2008/[2].

To a large extent, the conclusions reached in this study are the results obtained, e.g. Darcy fluxes and fracture water salinities at repository level. This is because the work has been undertaken to provide inputs for use in subsequent safety assessment applications in SR-Site. Thus, this report presents and summarises the simulation results, but refrain from commenting on their safety implications. This is appropriate because such safety implications can only be evaluated when the results have been propagated through the safety assessment process.

[1] The decision to go forward with developing the safety case for the Forsmark site was presented to the public in June 2009.

[2] In July 1 2008, the Swedish Radiation Safety Authority (SSM) replaced the former Swedish authorities, SKI and SSI, that reviewed the SR-Can project.

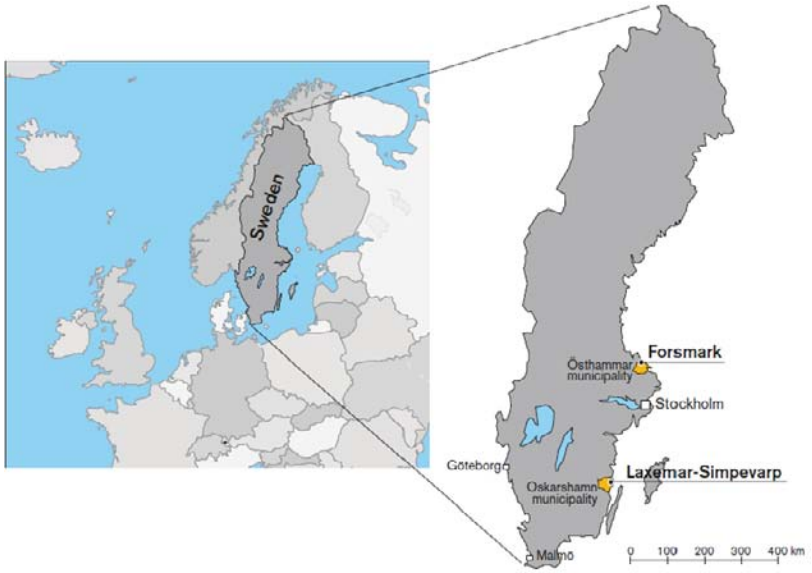

Figure 1-1. *Map of Sweden showing the location of the Forsmark and Laxemar-Simpevarp sites, located in the municipalities of Östhammar and Oskarshamn, respectively. (Source: Figure 1-1 in /SKB 2008a/.)*

1.3 Conceptual model

The literature review presented in Chapter 2 is undertaken with the objective of justifying hydraulic properties and boundary conditions of a groundwater flow model intended for a quantification of *bounding* hydraulic and chemical estimates during periglacial (permafrost) and glacial (ice sheet) conditions. This means that the objective of this report is different in several ways from the objectives of most periglacial and glacial studies reported in the literature, which generally are of a phenomenological character. The conceptual model behind the hydraulic properties and hydraulic top boundary condition applied here may be summarised as follows.

In front of an advancing ice sheet margin, the surface freezes because of low air temperatures. In the simulations that consider glacial conditions with permafrost, the freezing propagates into the subsurface and alters the flow and transport properties[3]. The freezing algorithm presented in Appendix A is used to modify the initial permeability values to water flow (hydraulic conductivity). The hydraulic properties derived during the site investigations at Forsmark are in this regard considered as representative of initial, temperate, conditions, see Chapter 3 for an overview.

An infinite source of meltwater with a hydraulic head at the base of the ice sheet equal to 92% of the ice sheet thickness is assumed at all times in all simulations. The notion of a tongue of permafrost beneath the ice sheet margin can be simulated by assigning a lower hydraulic head beneath the ice sheet close to its margin. The imposed boundary condition implies that subglacial meltwater infiltrates the subsurface and flows from areas with high hydraulic heads to areas with lower hydraulic heads, where it discharges. The simulated discharge locations vary in space depending on the setup of the particular simulation considered. Likely locations of so-called taliks[4] are estimated from the forecasted landscape development following the ongoing shoreline displacement /Brydsten and Strömgren 2010/.

Field measurements suggest that the hydraulic diffusivity of the connected open fractures in the sparsely fractured rock mass volumes between deformation zones may be fairly high /Follin 2008/.

[3] For fractured crystalline rock below a thin layer of glacial till, which is the dominating stratigraphy in the Fennoscandian Shield, the scarceness of field information in the literature is evident compared with the database reported for other geological conditions.

[4] Taliks are unfrozen “holes” in the permafrost layer that can connect the flow system at depth with that close to surface.

This implies a low mechanical loading efficiency, hence little or no delay in the pressure responses, and little or no changes in the storage of water in the flowing fracture system, as the top boundary conditions change during glaciation and deglaciation. Further, a low mechanical loading efficiency is also considered to be in line with the objective of the work as it enhances the hydraulic gradients imposed and thereby the Darcy fluxes and the chemical changes at repository depth. No mechanical coupling means that the classic hydraulic mass balance equation for transient groundwater flow is applied.

For the sake of clarity, the potential hydraulic impact of an uneven surface loading in proximity of the ice sheet margin (generally known as crustal flexure or the forebulge phenomenon) is addressed in the work reported here by incorporating results from the rock mechanics modelling conducted for SR-Site /Hökmark et al. 2010, Lönnqvist and Hökmark 2010/. Finally, in accordance with the climate modelling in /SKB 2010/, subglacial runoff through structures embedded in the ice sheet or occurring at the ice/rockhead interface, e.g. sub-glacial meltwater tunnels, are not considered here.

1.3.1 Studied cases

The reference evolution in /SKB 2010/ considers permafrost conditions in front of an advancing ice sheet margin. However, results for this case cannot be exported to the repository-scale and site-scale models of /Joyce et al. 2010/ as the hydraulic properties of the geosphere change continuously due to the presence of permafrost. Therefore, a Glacial case without permafrost in front of an advancing ice sheet margin constitutes a base case for all models (variant cases) treated in the work reported here including a Glacial case with permafrost in front of an advancing ice sheet margin, cf. cases (a) and (d) in Table 1-1. Another reason for the glacial case without permafrost as a base case is that this case produces the largest hydraulic gradients at the ice sheet margin, hence the greatest effects on the studied performance measures with regard to Darcy flux and fracture (advective) flow salinity at repository depth.

The groundwater flow modelling of the base case is divided into three stages, pre-LGM[5], LGM and post-LGM, see Figure 1-2. During the pre-LGM stage, both unfrozen and frozen (permafrost) conditions are considered. During the LGM stage (not shown in Figure 1-2), the model domain is completely covered by a thick ice sheet for thousands of years. During the post-LGM stage, submerged conditions are considered in the area in front of the retreating ice sheet margin.

The following flow simulations are carried out:

- **Pre-LGM stage.** Two different azimuth directions of ice sheet movement: 1. Advance from north-west, and 2. Advance from north; Three types of periglacial conditions: 1. No permafrost, 2. Permafrost in front of the ice sheet margin as well as 2 km beneath the tip of the ice sheet (permafrost tongue), and 3. Permafrost in front of the ice sheet margin only (no tongue); Three types of permeability conditions: 1. Undistorted conditions, i.e. present-day conditions, 2. Distorted conditions due to hydro-mechanical considerations, and 3. Distorted conditions due to freezing an thawing.
- **LGM stage.** The period of complete ice coverage lasts approximately 17,000 years. During this time period groundwater flow is mainly driven by buoyancy forces following the distorted salt water interface caused by the advancing ice sheet margin during the pre-LGM stage.
- **Post-LGM stage.** One azimuth direction of ice sheet movement (retreat from south-east); Submerged ground conditions in front of the ice sheet margin; Undistorted permeability conditions.

The different flow simulations are listed in Table 1-1. Figure 1-3 illustrates the difference between the main scenarios, without and with permafrost.

[5] LGM is a standard acronym used to denote the glacial maximum of the last glaciation (Weichsel), cf. /SKB 2010/.

1. SR-Site model domain (blue) vs SDM-Site model domain (red)

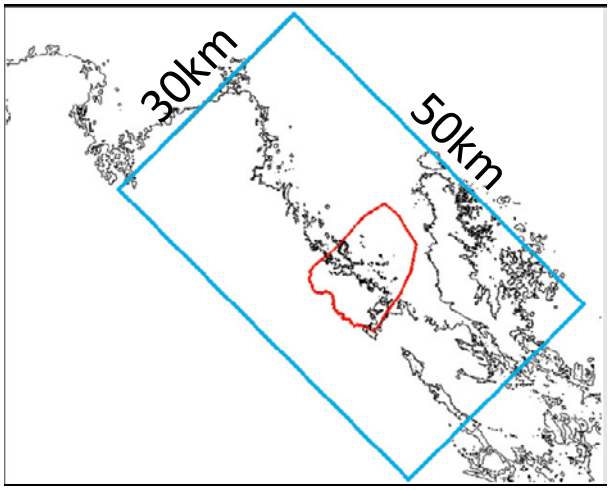

2. Hydraulic conditions for an advancing ice-sheet margin (pre-LGM)

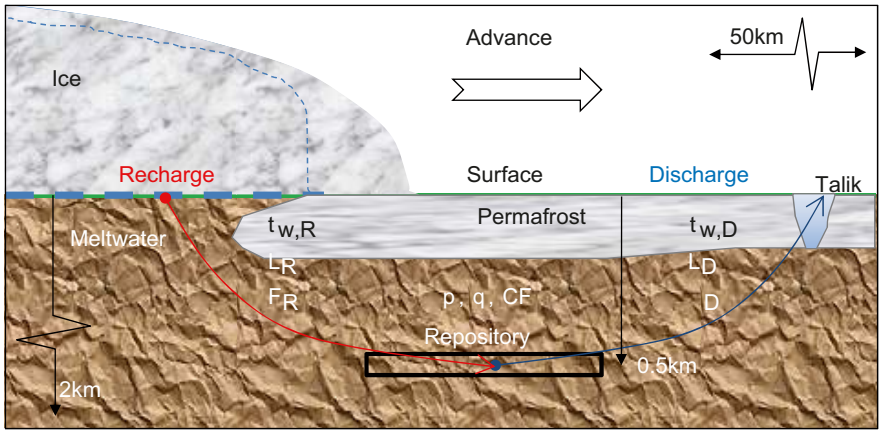

3. Hydraulic conditions for a retreating ice-sheet margin (post-LGM)

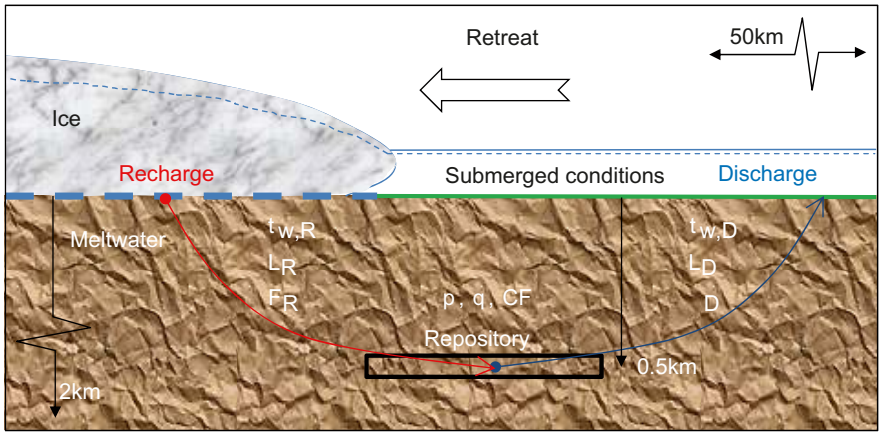

Figure 1-2. *Top: Map illustrating the size and location of the SR-Site model domain with regard to the model domain used in site-descriptive modelling (SDM-Site). Middle: Cartoon illustrating a repository beneath an advancing ice sheet margin with permafrost and taliks in the periglacial area in front of the margin. Bottom: Cartoon illustrating a repository beneath a retreating ice sheet margin with submerged ground conditions in front of the margin. The symbols shown denote the studied performance measures, see Section 1.3.4. LGM = the glacial maximum of the last glaciation.*

Table 1-1. Overview of flow simulations. The main scenarios, A and B, are divided into five cases (a)-(e). The bullets indicate the particular conditions modelled with each case considered. Case (a) constitutes the base case in the work reported here.

A. Glacial climate conditions without permafrost		
(a)	Pre-LGM stage	LGM stage
	Ice sheet movement from north-west.	Entire model domain is covered by an ice sheet
	No permafrost in front of the ice sheet margin.	Undistorted permeability conditions.
	Undistorted permeability conditions.	Post-LGM stages
		Submerged conditions in the ice free area.
		Undistorted permeability conditions.
Variants		
(b)	Pre-LGM stage	LGM and Post-LGM stages
(c)	As in (a), but ice sheet movement from north.	–
	As in (a), but distorted permeability conditions.	
B. Glacial climate conditions with permafrost		
(d)	Pre-LGM stage	LGM and Post-LGM stages
	Ice sheet movement from north-west.	–
	Permafrost in front of the ice sheet margin as well as 2 km below the tip (tongue) of the ice sheet margin.	
	Temperature-dependent permeability conditions.	
Variants		
(e)	Pre-LGM stage	LGM and Post-LGM stages
	As in (d), but no permafrost tongue.	–

1.3.2 Computational code

The groundwater flow modelling used version 3.2[6] of the DarcyTools computational code (see Chapter 4). This version of DarcyTools contains an algorithm that is used to simulate changes in the permeability due to freezing and thawing, see Appendix A. Changes of the groundwater salinity due to freezing and thawing are not considered. The heat flux from the repository to the surface is also omitted.

The flow model domain is approximately 50 km by 30 km by 2 km (depth), see Figure 1-2. The initial and top boundary conditions are based on the literature review reported in Chapter 2 and described in detail in Chapter 5. The parameter values used for the groundwater flow modelling with DarcyTools are presented in Appendix B. The values used are based on available hydraulic data from the site, see Chapter 3. In total, the model domain consists of 9.1 million cells.

1.3.3 Measurement localities (ML) and ice front locations (IFL)

The repository considered for hydrogeological modelling in SR-Site contains 6,916 deposition hole positions, see Figure 1-4. The thin lines in Figure 1-4 represent the deterministically modelled deformation zones. These are presented in greater detail in Chapter 3 (Figure 3-3). In Figure 1-4, the 6,916 deposition hole positions are coloured red or green depending on if the particular deposition hole had a position within a computational grid cell in DarcyTools that also contained one or several intercepts with the deterministically modelled deformation zones (red dot) or not (green dot) (cf. Section 5.6).

The labeled dots in Figure 1-4 represent five "measurement localities". These are denoted by ML 1-5 and are used to monitor changes in the hydrogeological quantities and performance measures specified in Section 1.3.4. The coordinates of ML 1-5 and their associated hydraulic properties in the model at repository depth are presented in Section 5.6. The simulated hydrogeological quantities and performance measures are reported for four different ice-front locations, denoted by IFL I-IV, see Figure 1-5.

[6] It is noted that the current documentation of DarcyTools relates to version 3.4 /Svensson et al. 2010/, but that the differences are insignificant for the applications reported here.

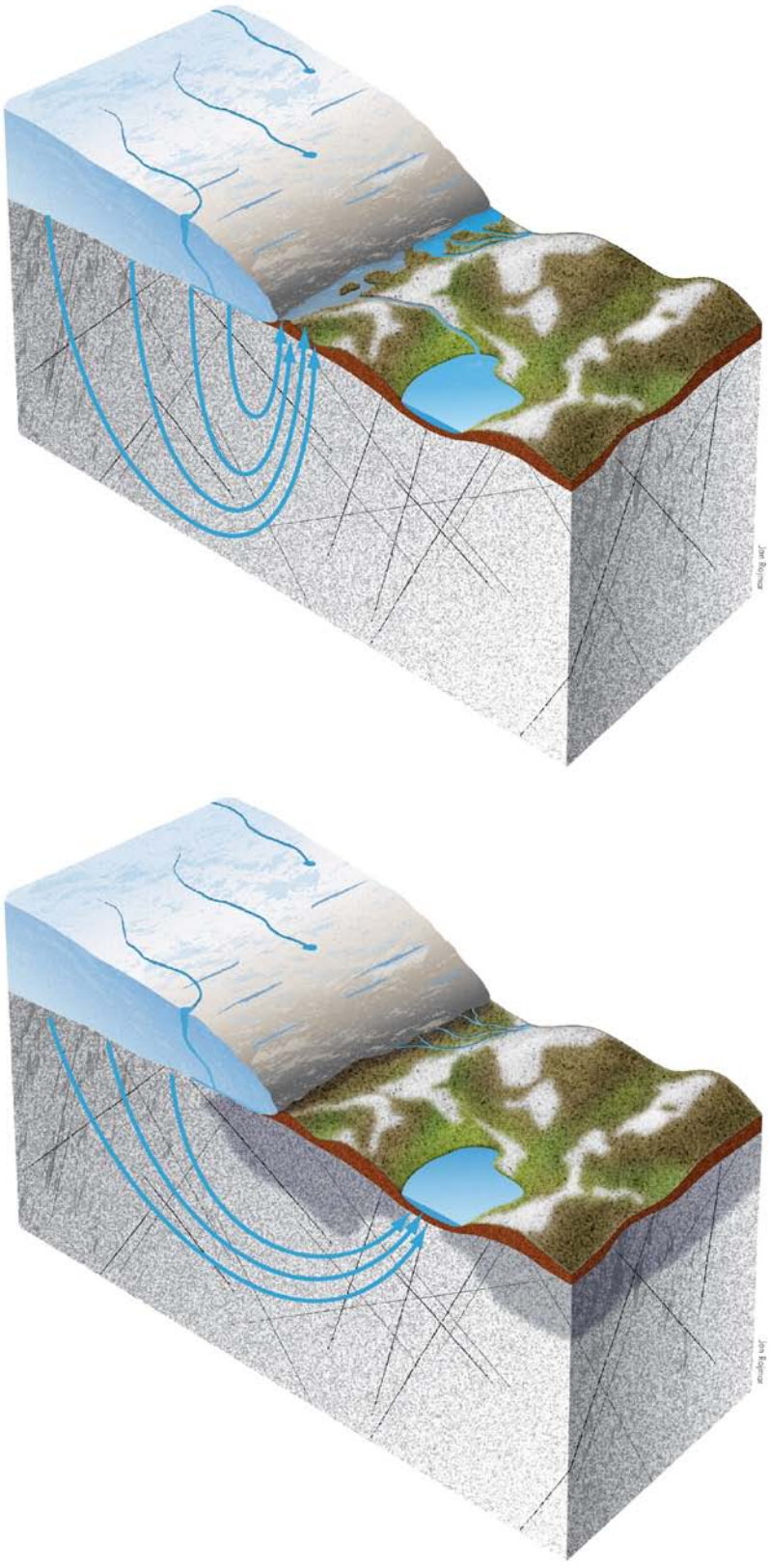

Figure 1-3. *Groundwater discharge for an advancing ice sheet margin occurs predominantly close to margin if there is no permafrost in the periglacial area (top) and in taliks if there is permafrost in the periglacial area (bottom).*

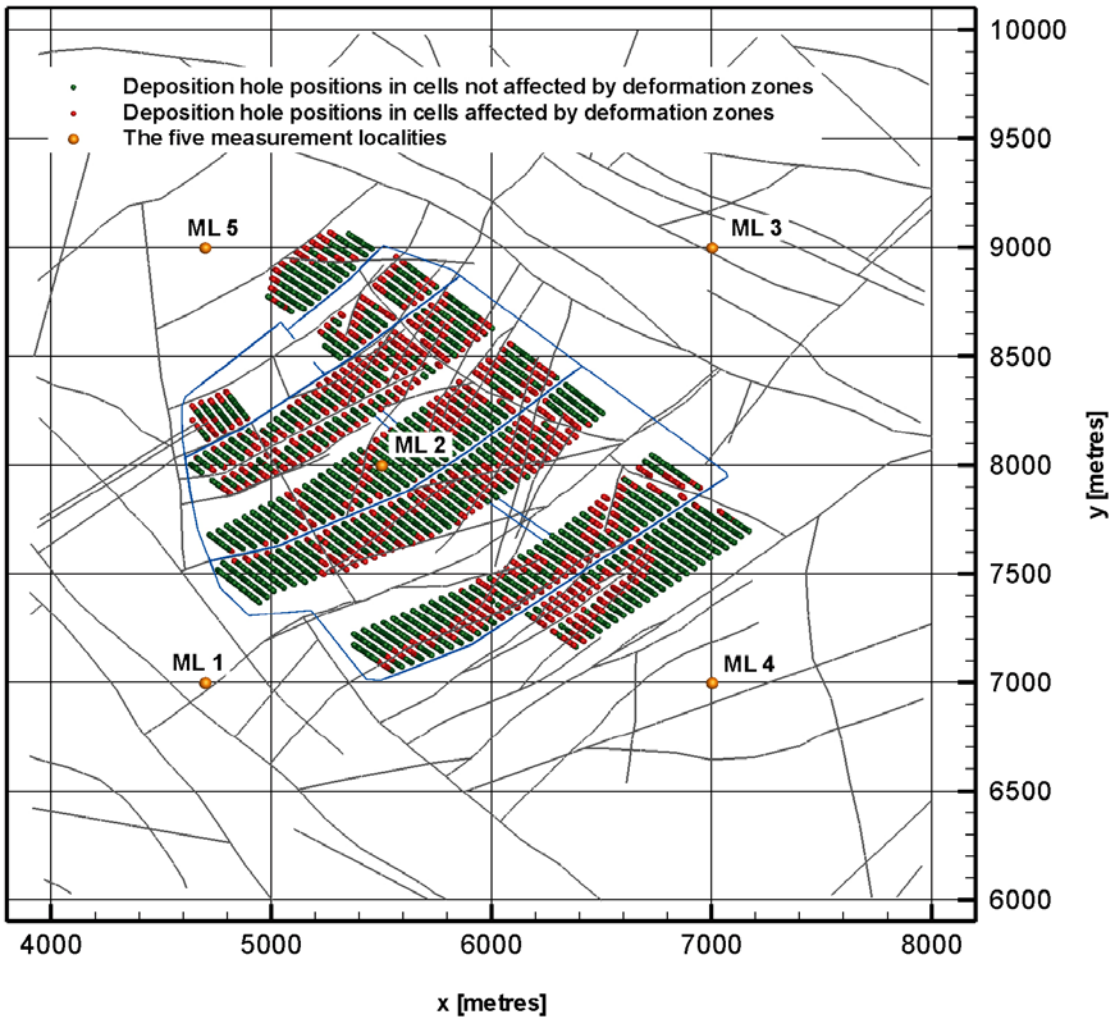

Figure 1-4. *Plane view of the studied repository layout at –465 m elevation. The thin lines represents deformation zones. It is noted that tunnels and deposition holes are not included in the model, but just shown in the figure for context. The five dots labelled ML 1-5 represent five measurement localities. The hydraulic properties in the model at these localities are presented in Section 5.7. The y-axis points towards north.*

Besides the four ice-front locations shown in Figure 1-5, two additional ice-front locations are discussed in the work reported here. These are denoted IFL 0 and IFL V and are located outside the model domain shown in Figure 1-5. IFL 0 is simply the start off position of the advancing ice sheet margin and IFL V is the start off position of the retreating ice sheet margin. In summary, the advancing ice sheet margin starts off at IFL 0 and passes IFL I-IV on its way to IFL V. At IFL V it stops and returns back to IFL 0. Conceptually, IFL 0 represents the temperate (initial) conditions at some time in the future (hence not 2000 AD), whereas IFL V coincides with the LGM.

It is emphasised that no repository is implemented in the work reported here. However, one particle is released at the coordinates of each deposition hole position and all particles are tracked backwards and forwards as a means to identify their recharge and discharge locations and performance measures specified in Section 1.3.4. It is noted that the Darcy fluxes are fixed in space and time during the particle tracking, which is a simplification since the boundary conditions at ground surface change with the movement of the advancing/retreating ice sheet margin.

The speed of the ice sheet margin varies a lot during a glacial cycle, although the general understanding is that the speed of the ice sheet margin during the pre-LGM stage is slower than the speed during the post-LGM stage, see /SKB 2010/. In the work reported here, a speed of 50 m/y is used during the pre-LGM stage, whereas a speed of 100 m/y is used during the post-LGM stage. (It is noted that the reference climate evolution in /SKB 2010/ considers an average retreat speed of 300 m/y. The implications of using an average retreat speed of 100 m/y instead of 300 m/y are

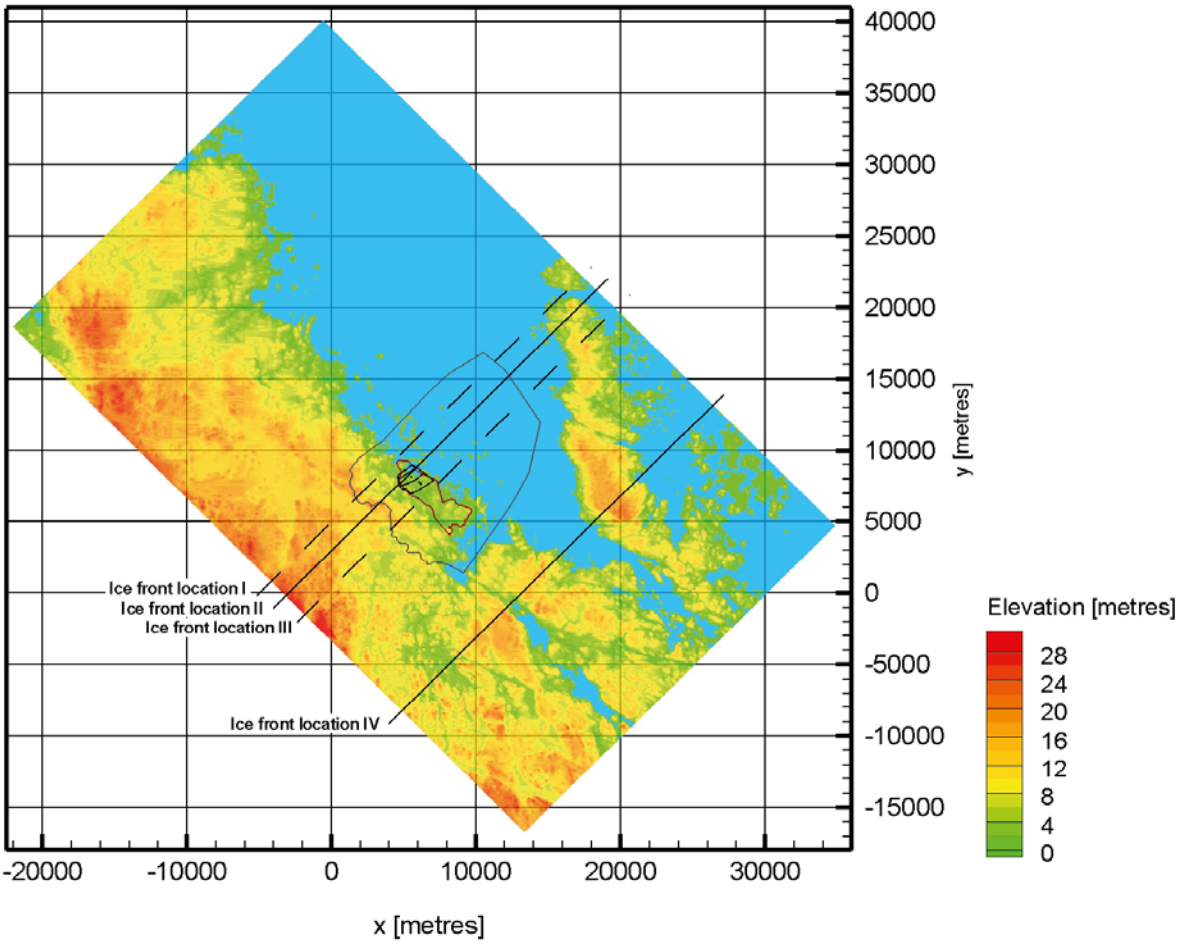

Figure 1-5. *Map showing the present-day topography at Forsmark and the positions of ice front locations IFL I-IV for a NW-SE orientation of the flow model domain. The large polygon in the centre shows the model domain used for groundwater flow modelling in SDM-Site. The small, polygon inside the large polygon shows the location of the investigated candidate area. The repository area is located in the north-western part of the small polygon. The y-axis points towards north.*

commented in Appendix D.) Each time step in the flow model represents a time period of six years, which means that the ice sheet margin advances and retreats with a spatial increment of 300 m and 600 m, respectively. The period of complete ice coverage lasts approximately 17,000 years. In total, the simulation between IFL 0 to IFL V and back to IFL 0 represents a period of approximately 19,000 years.

1.3.4 Hydrogeological quantities and performance measures

As shown in Figure 1-2, the following hydrogeological quantities are studied in each flow simulation:

- Fluid pressure P [$ML^{-1}T^{-2}$] (or [Pa])
- Darcy flux q [LT^{-1}] (or [m/s])
- Salinity C [MM^{-1}] (or [%])

A particle tracking algorithm is used to simulate advective transport of radionuclides. As shown in Figure 1-2, the following performance measures are studied for particles travelling from surface to repository depth (i.e. recharge, subscript R), and from repository depth back to surface (i.e. discharge, subscript D):

- Flow path lengths L [L] (or [m])
- Travel times t_w [T] (or [y])
- Flow-related transport resistances F [TL^{-1}] (or [y/m])

As briefly mentioned above, some of the results from the groundwater flow simulations reported here are used in other modelling studies for SR-Site.

- The residual pressure and salinity solutions are exported to the study by /Joyce et al. 2010/, since the repository layout and the excavated damage zone are not explicitly resolved within the model presented here. In the model of /Joyce et al. 2010/, performance measures are thus calculated also for glacial climate conditions. The results of /Joyce et al. 2010/ are used in the far-field radionuclide transport calculations and in the buffer erosion/canister corrosion analyses.
- Fracture water and matrix porewater salinities as well as advective flow path lengths, travel times, and flow-related transport resistances of particles travelling from surface to repository depth are exported to the hydrochemical modelling by /Salas et al. 2010/ and /Sidborn et al. 2010/.

1.4 Setting of the Forsmark site

The Forsmark area is located in northern Uppland within the municipality of Östhammar, about 120 km north of Stockholm (Figure 1-1 and Figure 1-6). The candidate area for site investigation is located along the shoreline of Öregrundsgrepen. It extends from the Forsmark nuclear power plant and the access road to SFR in the north-west (SFR is an existing repository for short-lived radioactive waste) to Kallrigafjärden in the south-east (Figure 1-6). It is approximately 6 km long and 2 km wide. The north-western part of the candidate area was selected as the target area for the complete site investigation work /SKB 2005b/ (Figure 1-7).

The Forsmark area consists of crystalline bedrock that belongs to the Fennoscandian Shield, one of the ancient continental nuclei of the Earth. The bedrock at Forsmark in the south-western part of this shield formed between 1.89 and 1.85 billion years ago during the Svecokarelian orogeny /SKB 2005a/. It has been affected by both ductile and brittle deformation. The ductile deformation has resulted in large-scale, ductile high-strain belts and more discrete high-strain zones. Tectonic lenses, in which the bedrock is less affected by ductile deformation, are enclosed between the ductile high strain belts. The candidate area is located in the north-west part of one of these tectonic lenses. This lens extends from north-west of the nuclear power plant to the area around Öregrund in the south-east (Figure 1-8). The brittle deformation has given rise to reactivation of the ductile zones in the colder, brittle regime and the formation of new brittle fracture zones of variable size.

The current ground surface in the Forsmark region forms a part of the sub-Cambrian peneplain in south-eastern Sweden. This peneplain comprises a relatively flat topographic surface with a gentle dip towards the east that formed more than 540 million years ago. The candidate area at Forsmark is characterised by small-scale topography at low altitude (Figure 1-9). The most elevated areas to the south-west of the candidate area are located at c. 25 m above the Swedish Ordnance Datum of 1970 (RHB 70). The whole area is located below the highest coastline associated with the last glaciation, and large parts of the candidate area emerged from the Baltic Sea only during the last 2,000 years. Both the flat topography and the still ongoing shore-level displacement of c. 6mm per year strongly influence the current landscape (Figure 1-9). Sea bottoms are continuously transformed into new terrestrial areas or freshwater lakes, and lakes and wetlands are successively infilled by peat.

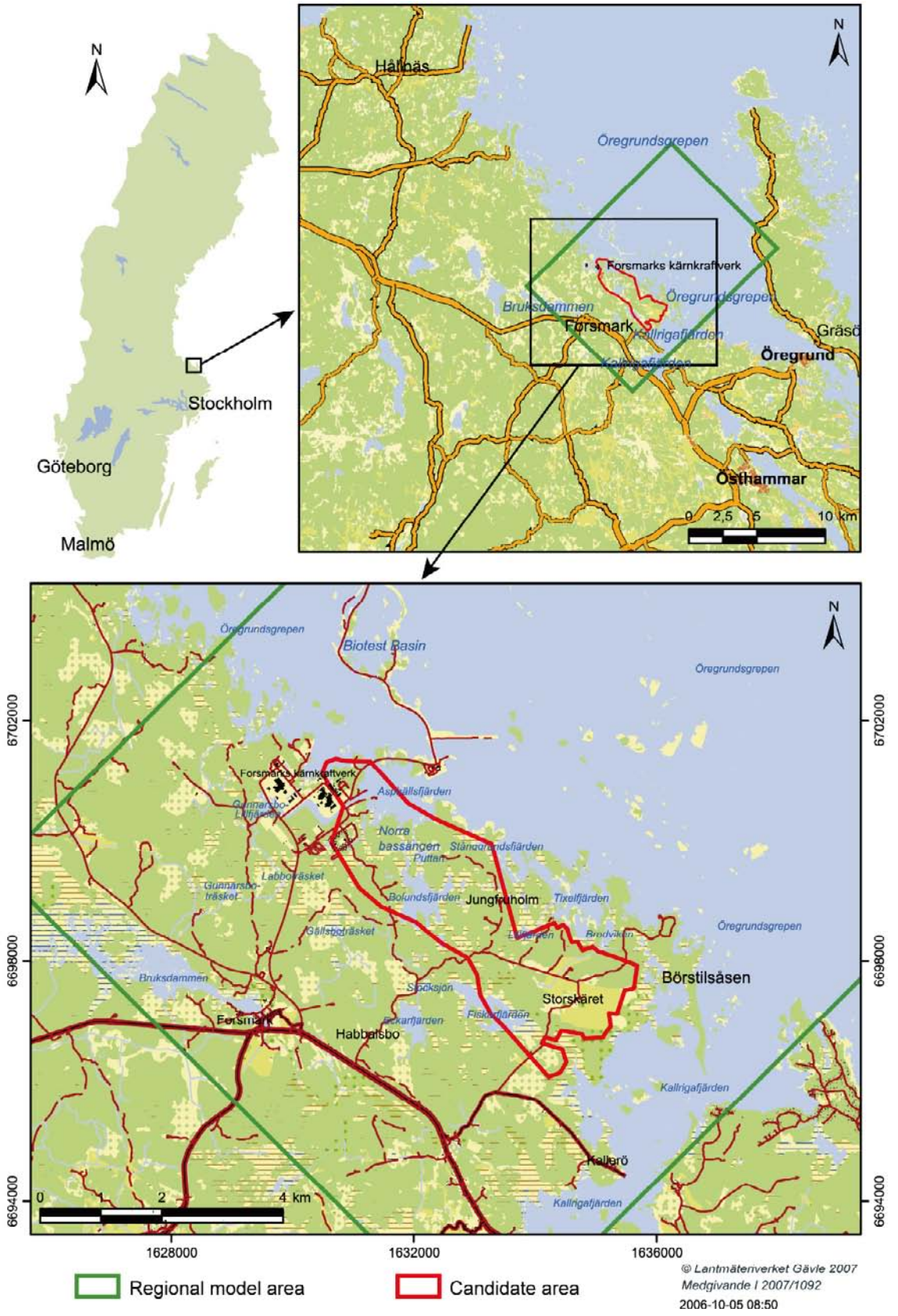

Figure 1-6. *The red polygon shows the size and location of the candidate area for site investigations at Forsmark. The green rectangle indicates the size and location of the regional model area for SDM-Site Forsmark. (Source: Figure 1-3 in /SKB 2008a/.)*

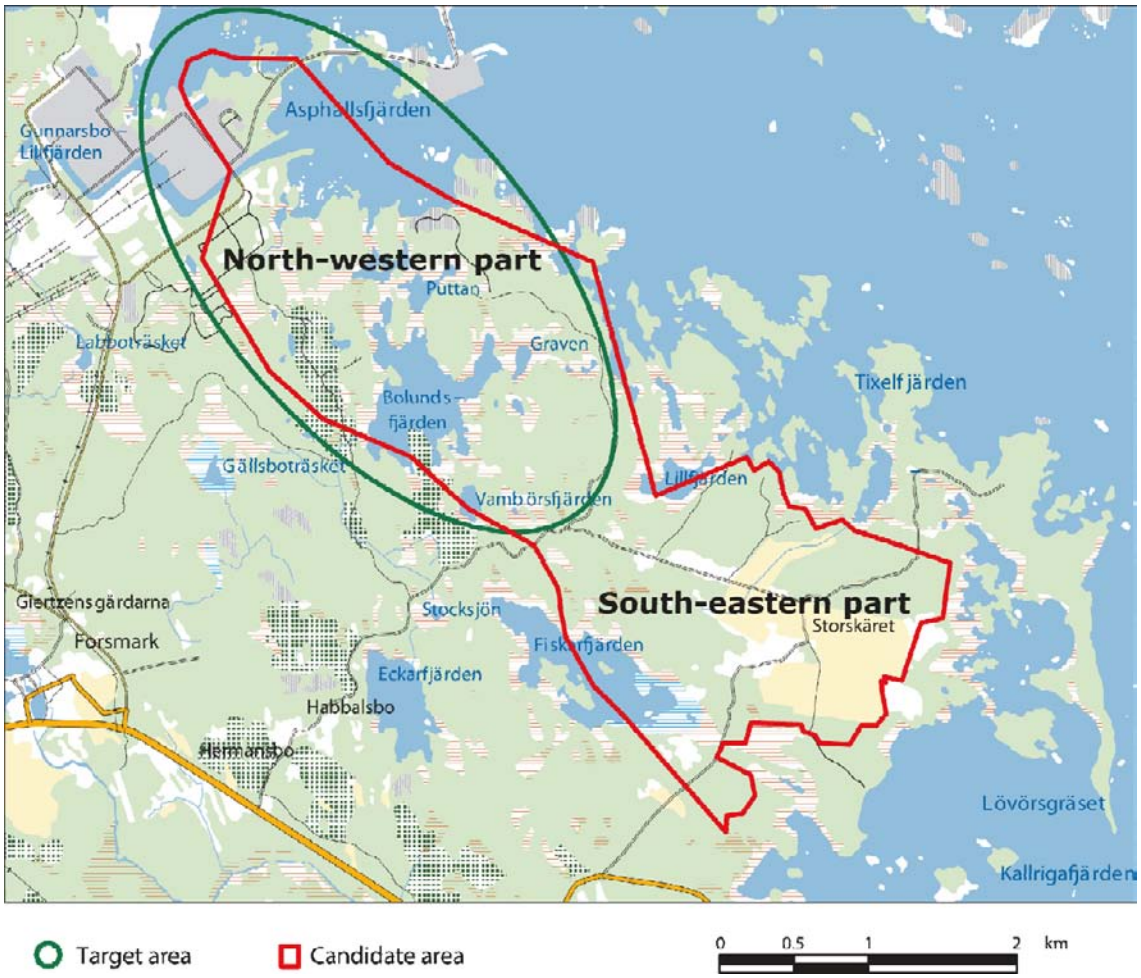

Figure 1-7. *The north-western part of the candidate area was selected as the target area for the complete site investigation work. (Modified after Figure 2-15 in /SKB 2005b/.)*

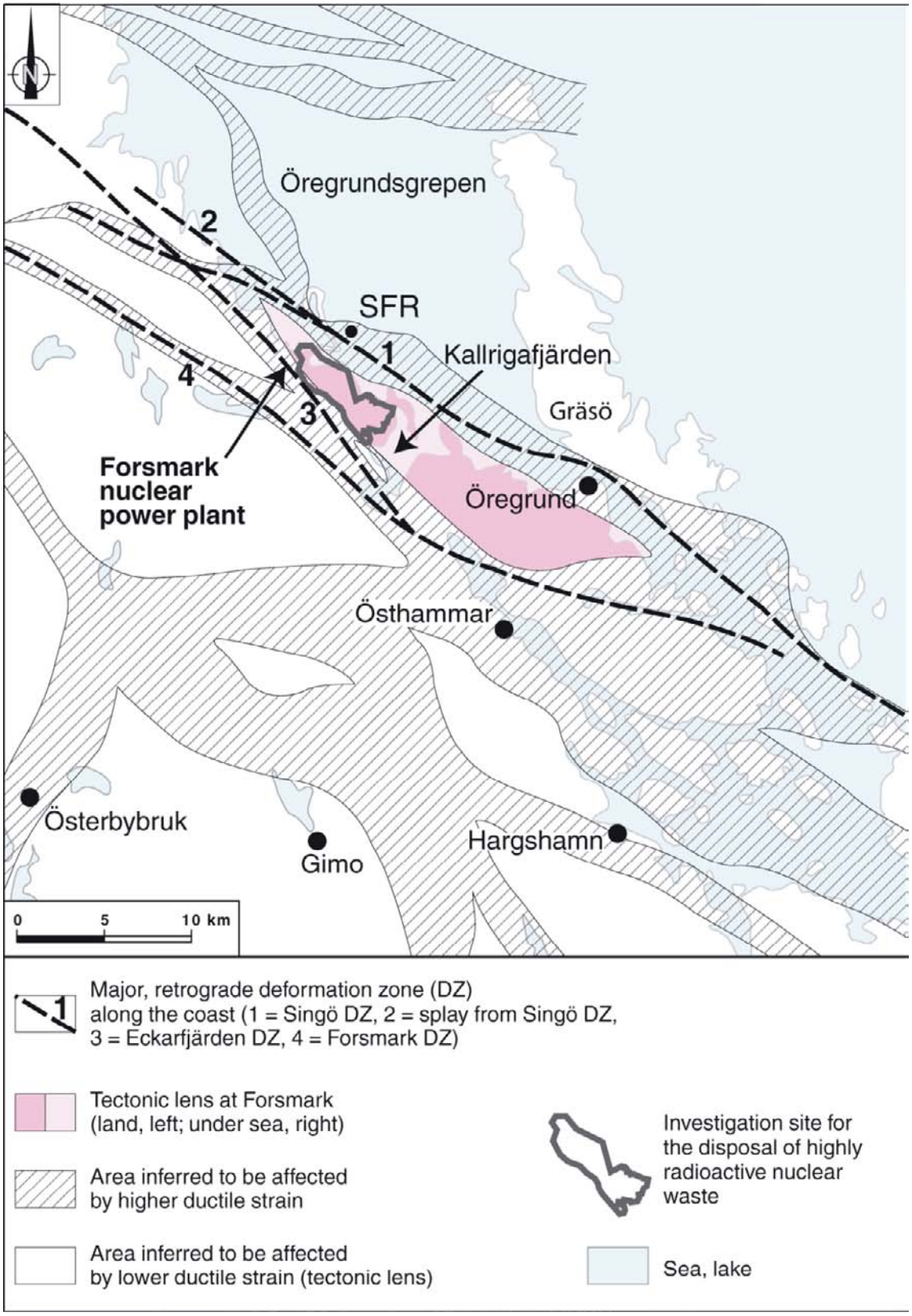

Figure 1-8. *Tectonic lens at Forsmark and areas affected by strong ductile deformation in the area close to Forsmark. (Source: Figure 4-1 in /Stephens et al. 2007/.)*

Figure 1-9. *Photographs from Forsmark showing the flat topography and the low-gradient shoreline with recently isolated bays due to land uplift. (Source: Figure 1-7 in /Follin 2008/.)*

1.5 This report

The following Chapters of the report are structured as follows.

Chapter 2 presents a review of previous studies on groundwater flow modelling of periods with periglacial (permafrost) and glacial conditions. It is written with the objective of providing appropriate understanding of the choice of top boundary conditions and hydraulic properties applied in the groundwater flow modelling.

Chapter 3 presents a summary of hydrogeological model derived in SDM-Site Forsmark /Follin 2008/.

Chapter 4 presents the primary concepts and methodology of the DarcyTools computational code /Svensson et al. 2010/.

Chapter 5 provides a description of the numerical setup, e.g. initial and boundary conditions of the cases studied (scenarios) and presents the format of the figures showing the calculated performance measures.

Chapter 6 summarises the key findings for SR-Site.

Chapter 7 summarises the scope of the work, the applied methodology, the key assumptions made and the conclusions drawn.

In addition, the report contains seven appendices, A to G.

A. This appendix presents the algorithm in DarcyTools version 3.2 that is used to change the permeability of the subsurface as a function of temperature.

B. This appendix presents the parameter values used in DarcyTools for the generation of hydrogeological discrete fracture network (Hydro-DFN) realisations.

C. This appendix lists the names and dates of all files that are used to parameterise the groundwater flow model.

D. This appendix discusses the support for the applied initial and boundary conditions during glaciation and deglaciation, in particular the data support for assuming a fixed (undisturbed) groundwater salinity at the bottom boundary of the model domain, and the interpretation of the simulated exchange of dissolved solids between the advective fracture water and the immobile matrix porewater.

E. This appendix presents detailed results from the simulations with temperate climate conditions in a tabular format

F. This appendix presents detailed results from the simulations of scenario A in Table 1-1 in a tabular format.

G. This appendix presents the results from the simulations of scenario B in Table 1-1 in a tabular format.

2 Hydraulic conditions during permafrost and glacial periods

2.1 Introduction

A literature review was made with the objective of defining and justifying hydraulic properties and top boundary conditions of a groundwater flow model intended for quantification of bounding permafrost and glacial (ice sheet) hydrogeological conditions for subsequent use within safety assessment applications. The literature review is summarised in Sections 2.2 and 2.3. Section 2.4 describes details of the key boundary condition for the work – the ice sheet profile.

2.2 Review of concepts used to model permafrost conditions

Permafrost is present if the ground temperature is at or below 0°C for at least two consecutive years (e.g. /French 1996, Lemieux et al. 2008b/). The greatest impact of permafrost on the subsurface hydrology is the phase change related to the freezing of groundwater, and permafrost is often imagined to create an almost impervious (small, but still nonzero permeability) layer near the surface, which decreases the potential groundwater recharge and discharge, highlighting the possibility of high groundwater pressures beneath the permafrost layer (e.g, /Burt and Williams 1976, Kleinberg and Griffin 2005, Bense and Person 2008, Lemieux et al. 2008a, b, c/ among others).

The above definition of permafrost does not imply that the surface is completely frozen, however. Due to capillary forces, water does not freeze completely and a thin film of liquid water covers the rock/soil grains even at low temperatures /Kane and Stein 1983, Gascoyne 2000, Vidstrand 2003/. The unfrozen water content under permafrost conditions is sufficient to maintain the groundwater table at or close to the surface /Person et al. 2007/. In this context, the occurrence of taliks[7] is considered to be an important top boundary condition (e.g. /McEwan and de Marsily 1991, Boulton et al. 1993, Haldorsen and Hein 1999/).

Physical permafrost models, which are based on the state equations for the phase change, suggest large variations in the unfrozen water content, and hence also in the hydraulic conductivity and transport properties, depending on the temperature and the geological material. /Burt and Williams 1976, Kleinberg and Griffin 2005/ provide some information about the field permeability of soils as a function of the unfrozen water content, but, on the whole, there are few field data reported in the literature. As a consequence, the choice of model parameters is often based on laboratory experiments (e.g. /Williams and Smith 1989/).

Two popular topics in the literature dealing with subsurface hydrology during permafrost conditions are the frozen, superficial layer, which can be hydraulically active during summer, and the hydrochemistry of the unfrozen groundwater below this layer. Different hypotheses have been suggested as a means to explain field observations. For instance, hydrochemical observations in areas subject to permafrost conditions have resulted in a hypothesis of increased salinity beneath the frozen, superficial layer. The elevated salinity is imagined to be caused by a salt-rejection process along with a continuous push downwards by the growth of the permafrost. /Starinsky and Katz 2003/, for example, hypothesised that this phenomenon is responsible for the formation of Shield brines, although the magnitude of the effect and its implications are uncertain.

The mathematical models used to represent permafrost conditions and their effects on the groundwater flow system vary highly in complexity as well as in realism. To exemplify the range of the simplifications invoked, four recent examples from the literature are given below.

[7] Taliks are unfrozen "holes" in the permafrost layer that can connect the flow system at depth with that close to surface. Taliks have been observed below large surface water bodies, even where the permafrost is quite deep in the surrounding regions /Lemieux et al. 2008b/.

- The 3-D HMC[8] mathematical model reported by /Lemieux et al. 2008a, b, c/ is used to simulate the impact of glaciations on continental groundwater flow systems. Rather than simulating permafrost development as such, the groundwater flow model is linked to the GSM[9] climate model as a means of obtaining information about permafrost development (laterally and vertically) over time. Further, rather than specifying a permeability water relationship, the hydraulic conductivity is simply allowed to switch between its frozen and unfrozen states. For the frozen state, a low hydraulic conductivity is specified, i.e. a six order of magnitude reduction relative to the corresponding Holocene hydraulic conductivity values.
- The 2-D THC mathematical model reported by /Hartikainen et al. 2010/ is used to simulate permafrost growth in a vertical cross-section at Forsmark by means of a coupled energy transport and variable-density flow model. The state of the phase change between groundwater and ice is defined by the criterion that the Gibbs free energies of water and ice are in equilibrium. Figure 2-1 shows the unfrozen groundwater content as a function of temperature in different geomaterials for the case of zero salinity and reference water pressure, and for the case with a constant salinity concentration of 2% by weight and a water pressure of 5 MPa. It can be seen that, due to effects of pressure and salinity concentration, a temperature of –1.4°C is required to begin the freezing. In the model, the minimum value of the hydraulic conductivity due to freezing is specified as $1 \cdot 10^{-13}$ m/s. The maximum penetration depth of the simulated permafrost during a glacial cycle is about 250 m, see Figure 2-2.
- The 3-D HM mathematical model reported by /Walsh and Avis 2010/ is used to study the effects of glaciation on groundwater flow and radionuclide transport for a hypothetical repository in the Canadian Shield. The authors did not address variable-density flow (i.e. no T and no C processes, only H and M process) when representing studying the effect of permafrost. All Holocene hydraulic conductivity values (except below taliks) are deterministically modified above a given elevation to $1 \cdot 10^{-13}$ m/s. The permafrost depth is deterministically varied between 100 m and 250 m, depending on the permafrost period considered.
- The 3-D HCM mathematical model reported by /Cohen et al. 2010/ is used to simulate the origin and extent of fresh palaeowaters on the Atlantic Continental Shelf. The authors did not model permafrost growth as a transient process but changed the Holocene hydraulic conductivity values abruptly by three orders of magnitude where the atmospheric temperature on the top boundary is below –2°C to represent near-surface freezing. The permafrost algorithm used did not allow for the development of a thick (>100 m) permafrost zone.

Although there is a consensus on that the hydraulic conductivity of soils and rocks is greatly reduced by the freezing during permafrost conditions, there is, as it appears, neither a consensus on the magnitude of the reduction nor how it should be modelled. /Boulton and de Marsily 1997/ commented on the state of the art and concluded that the paucity of data to constrain the assumptions in glacial and permafrost modelling is evident.

In addition to a wide range of ways of modelling permafrost and its potential effects on the hydraulic conductivity, it is noted that the effects on other flow transport parameters, e.g. the kinematic porosity, are poorly discussed in the literature. As it appears from the literature review, other flow and transport properties are often assumed to remain unchanged, i.e. unaffected by the permafrost process. This simplification is probably due to lack of data as well as to prohibiting computational constraints. Hence, it is no surprise that the physically more elaborated and complex coupled model by /Hartikainen et al. 2010/ is constrained to handle only 2-D groundwater flow. For the same reason, /Hartikainen et al. 2010/ is the only study among the four examples given here that considered the potential effects of salt exclusion on salinity due to freezing. However, it is noted that /Vidstrand et al. 2006/ studied the importance of this process for groundwater flow through highly hydraulically heterogeneous media such as fractured crystalline rocks. Based on flow simulations, /Vidstrand et al. 2006/ suggested that even a small perturbation in the hydraulic conductivity field will initiate a substantial density-driven mixing along the transmissive fractures/deformation zones; i.e. a saline water layer below the permafrost due to salt rejection is not stable.

[8] T, H, M, and C denote thermal, hydraulic, mechanical and chemical processes, respectively.

[9] The Memorial University of Newfoundland/University of Toronto Glacial Systems Model (GSM).

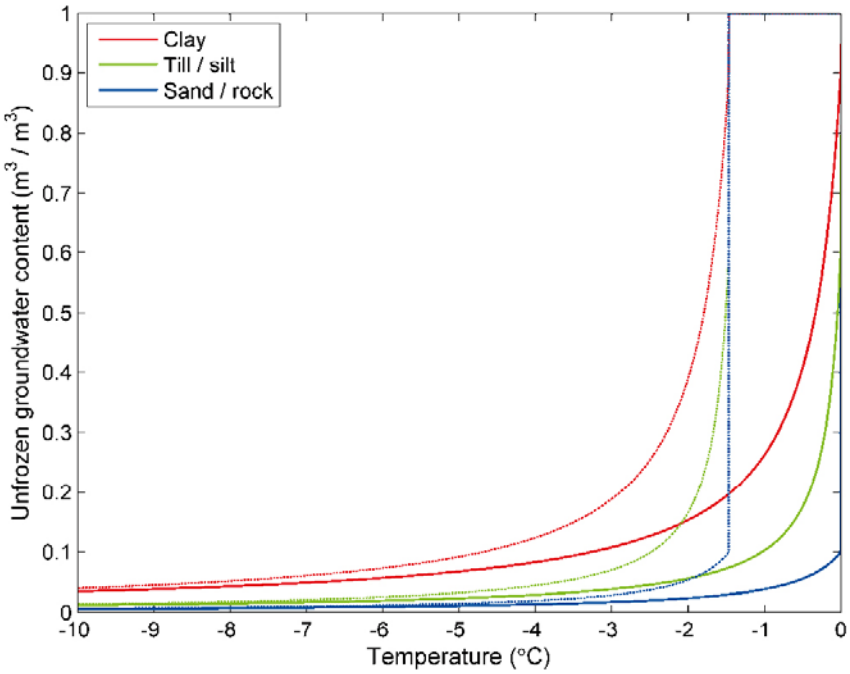

Figure 2-1. *Unfrozen volumetric groundwater content versus temperature in different geological materials for a constant salinity concentration of 2% by weight and a water pressure of 5 MPa (the three graphs peaking at –1.5°C), and for zero salinity and reference water pressure (the three graphs peaking at 0°C). (Source: Figure 3-1 in /Hartikainen et al. 2010/.)*

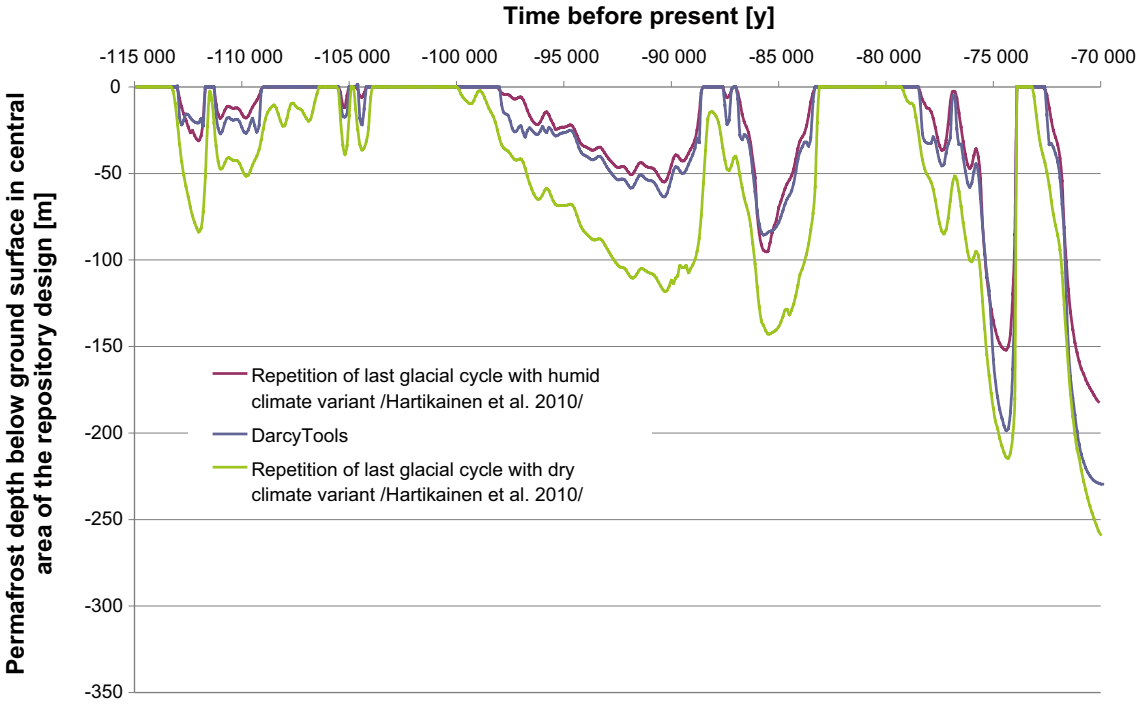

Figure 2-2. *Permafrost depth simulated with DarcyTools in comparison with the two main cases in /Hartikainen et al. 2010/.*

2.3 Review of concepts used to model glacial conditions

A continental ice sheet cycle implies that a huge region is covered by a thick ice sheet. The foremost part of a continental ice sheet (the tip) is generally conceived to be more or less underlain by permafrost, whereas the thicker parts in the rear are imagined to by underlain by unfrozen ground due to, e.g. the frictional heat generated at the base of the ice sheet, the geothermal heat flux through the ground below and the temperature isolation due to the substantial thickness of the ice sheet (e.g. /Hughes 1998, Boulton et al. 1996, Boulton and de Marsily 1997, King-Clayton et al. 1995, Lemieux et al. 2008a/). During summer, surface meltwater can gather in ponds or lakes from which it may reach the basal meltwater through crevasses and/or moulins, at least in the ablation area of the ice sheet, i.e. close to the ice sheet margin /Jay Zwally et al. 2002, van der Veen 2007/. Subglacial meltwater generated because of ice sheet isolation, ice sheet subglacial friction and the Earth's geothermal gradient will either flow towards the ice sheet margin through a transmissive "subglacial layer" (e.g. /Flowers and Clarke 2002, Breemer et al. 2002/ among others) or recharge into the subsurface (e.g. /Boulton et al. 1995, Piotrowski 1997a, b/ among others).

Although widely recognised and commonly accepted nowadays, the concept of a transmissive subglacial layer has been interpreted in very different ways in the past. Examples of studies that have considered different types of models under turbulent flow conditions are, e.g. /Röthlisberger 1972/ and /Nye 1976/. There are also examples of studies that have considered different types of models of "conduits" or "channels" under laminar flow conditions (e.g. /Weertman 1972, Kamb 1987, Walder and Fowler 1994/).

The abundance of eskers in the Fennoscandian Shield demonstrates the frequency of major meltwater tunnels during the retreat of the Weichselian ice sheet. The eskers occur at the ground surface on top of the crystalline bedrock, which reveals that it was here that the bulk of the meltwater runoff took place. The high potential for discharging large amounts of meltwater and glaciofluvial material would have resulted in noticeable drawdown of the hydraulic head at the ice-subsurface interface /Jansson et al. 2007, Boulton et al. 2007a/.

The role of meltwater tunnels for groundwater flow has been interpreted in different ways. /Boulton et al. 1995/ modelled groundwater flow in an approximately 1,500 km long transect running from Norway to the Netherlands. A limited recharge of meltwater into the subsurface was assumed, implying that the bulk of the meltwater runoff at the ice-subsurface interface is not assumed to be a part of the groundwater flow on this scale. The limited recharge of meltwater at the ice-subsurface interface is constrained by a criterion that the generated subglacial head at the ice-subsurface interface must be kept below the ice sheet elevation. /Svensson 1999/ and /Jaquet and Siegel 2003/ also used a prescribed recharge rate at the ice-subsurface interface. However, in contrast to /Boulton et al. 1995/, these authors used a 3-D model domain with hydrogeological conditions typical of the Fennoscandian Shield. In particular, they included two extensive meltwater tunnels of constant hydraulic conductivity and size in the flow model. The hydraulic conductivity of the tunnles is calibrated such that the prescribed recharge did not generate a subglacial head above the ice sheet elevation. The two tunnels are placed perpendicular to the ice sheet margin along the boundaries the 250 km long model domain. This model is elaborated by /Jaquet and Sigel 2006/, who included a stochastic component representing heterogeneous hydraulic properties in the bedrock and the Quaternary deposits (sub-glacial layer) between the two deterministically modelled meltwater tunnels located at the edges of the model domain.

/Boulton et al. 2007b/ used a groundwater flow model that applied a theory that meltwater tunnels, with dynamic (self-organising) geometrical and hydraulic properties, form at the ice-subsurface interface, where groundwater recharge alone is not able to discharge the meltwater flow rates without the generation of excess subglacial heads. The meltwater tunnels are formed at locations near the ice sheet margin where the subglacial heads can increase to balance the weight of ice. This condition is likely to vary between seasons and, in consequence, the spacing between long-term stable meltwater tunnels is found to be determined by winter meltwater flow rates.

Groundwater flow beneath a continental ice sheet is mainly due to two processes (e.g. /Boulton et al. 1999, Clark et al. 2000, Douglas et al. 2000, Grasby et al. 2000, Ferguson et al. 2007, Person et al. 2007/): (i) transient recharge and discharge conditions at the ice-subsurface interface, and (ii) consolidation of the bedrock, which causes an expulsion of existing storage of groundwater water in the fracture system.

The meltwater is under ice sheet pressure and, where the hydraulic conductivity is sufficient, the meltwater is driven into the subsurface. The hydraulic head required to keep a thick ice sheet floating on top of the subglacial meltwater is typically 92% of the ice sheet thickness /Paterson 1994/. For periglacial conditions, an assumption that the groundwater table elevation equals the topographic surface is often made. During its retreat, the height of the ice sheet profile is lower than during its advance /SKB 2010/. In addition, huge amounts of meltwater will cover the periglacial area.

/Lemieux et al. 2008a/ modelled the dynamics of groundwater recharge and seepage over the Canadian Shield during the Wisconsinian glaciation (~ –120ka to present). The authors concluded that, in the model, much of the infiltration of subglacial meltwater occurred during ice sheet progression, whereas during ice sheet regression, groundwater mainly exfiltrated at the surface, in both the subglacial and periglacial areas. /Lemieux et al. 2008a/ estimated that 15-70% of the meltwater infiltrated into the subsurface as recharge, with an average of 43%. The simulated average infiltration/exfiltration fluxes ranged between 0 and 12 mm/y.

The deformation of the crust by the weight of the ice sheet is such that the Earth's surface elevation will be depressed underneath the ice sheet and raised beyond its margins, see Figure 2-3. The full isostatic compensation of ice sheet loading is according to /Marshall and Clark 2002, Tarasov and Peltier 2004, 2007/ 28%, which implies that an ice sheet of a few kilometres thickness has a weight sufficient to depress the Earth's crust by about 1 km. Hence, it is likely that the surface loading by glacial ice produces a mechanical deformation that increases subsurface pore pressure. By the same token, the increased load beneath a continental ice sheet is likely to reduce the hydraulic conductivity through compression of pores and closure of fractures /Walsh and Avis 2010/. /Wang 2000/ and /Neuzil 2003/ asserted that the assumption of purely vertical strain below an ice sheet is a reasonable assumption in 2-D and 3-D flow regimes provided that only homogeneous and laterally extensive overburden changes occur. However, this assumption is not valid where vertical loads vary significantly within the model domain, as would occur at the margin of an advancing or retreating ice sheet margin, see Figure 2-3. Consequently, the HM coupling suggested by /Wang 2000/ and /Neuzil 2003/ can only be viewed as an approximate solution, providing an estimate of how mechanical pressurisation of the subsurface under transient glacial loading might impact the flow field and the resulting transport solution.

The assertion of /Wang 2000/ and /Neuzil 2003/ is invoked in the 3-D studies by /Lemieux et al. 2008a, b, c, Walsh and Avis 2010, Cohen et al. 2010/ to describe transient groundwater flow during the advance and retreat of a continental ice sheet. The assumption allows a great simplification of the hydro-mechanical analysis, allowing transient flow due to hydro-mechanical coupling to be fully represented by the fluid flow equation alone. The effect on the flow field of a pressure increase caused by mechanical loading is incorporated in an additional storage term, see Equation 2-1, which describes the coupled mass balance equation to handle hydro-mechanical deformation along with the effect of variable-density groundwater flow /Lemieux et al. 2008b/:

$$\frac{\partial}{\partial x_i}\left(K_{ij}\frac{\mu_0}{\mu}\left(\frac{\partial h^*}{\partial x_j}+\rho_r\frac{\partial z}{\partial x_j}\right)\right)=S_s\left(\frac{\partial h^*}{\partial t}\right)-S_s\left(\zeta\frac{1}{\rho g}\frac{\partial \sigma_{zz}}{\partial t}\right),\quad i,j=1,2,3 \qquad (2\text{-}1)$$

where K_{ij} is the hydraulic conductivity tensor [LT^{-1}], h^* is the equivalent freshwater head [L], r_r is the relative density [dimensionless], S_s is the specific storage [L^{-1}], z is the one-dimensional loading efficiency [dimensionless], and s_{zz} is the excess vertical stress [$MT^{-2}L^{-1}$] caused by the ice weight.

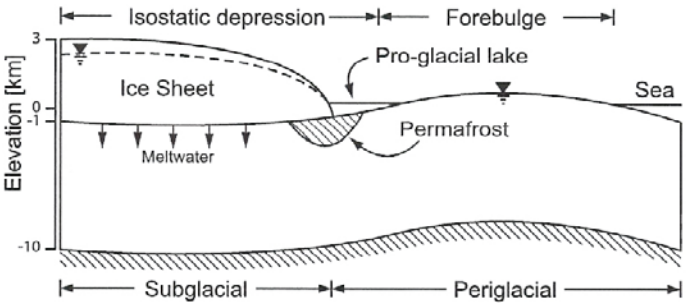

Figure 2-3. *Cross-section along an ice flow line showing hydraulic conditions during a glacial cycle. (Source: Figure 1 in /Lemieux et al. 2008a/.)*

m_0 is the reference viscosity [$ML^{-1}T^{-1}$], $m(\theta,C)$ is water viscosity [$ML^{-1}T^{-1}$], $r(\theta,C)$ is water density [ML^{-3}], and g is gravitational acceleration [LT^{-2}]. h^*, r_r , S_s, and z are defined as /Lemieux et al. 2008b/:

$$h^* = \frac{p}{\rho_0 g} z \tag{2-2}$$

$$\rho_r = \frac{\rho}{\rho_0} - 1 \tag{2-3}$$

$$S_s = \rho_0 g(\beta_{pm} - \phi\beta_f) \tag{2-4}$$

$$\zeta = \left(\frac{\beta_{pm}}{\beta_{pm} - \phi\beta_f} \right) \tag{2-5}$$

where p is fluid pressure [$MT^{-2}L^{-1}$], f is the kinematic porosity [dimensionless], and b_{pm} and b_f are, respectively, the porous medium and water compressibility [$LT^{-2}M^{-1}$].

The one-dimensional loading efficiency, z, specifies how much of the surface loading is transferred to the subsurface fluid. The loading efficiency can be computed from the elastic properties of the bedrock (cf. /Walsh and Avis 2010/), but the paucity of data introduces considerable uncertainty /Lemieux et al. 2008a/.

By definition, the loading efficiency varies between 0 and 1. If z is large, the ice weight is transferred to the fluid because of a highly compressible solid medium. For z = 1, the entire ice load is transferred to the subsurface fluid, thus rapidly increasing pore pressures at all depths, which in turn greatly reduces the vertical hydraulic gradient and inhibits groundwater recharge. Conversely, if z is small, the ice load is supported by the matrices of the media and pore pressure does not increase in the subsurface because of ice loading. Consequently, z = 0 implies that there is a strong vertical hydraulic gradient and groundwater recharge is high where the hydraulic conductivity is sufficient. Physically, z = 0 equates Equation 2-1 and the classic hydraulic mass balance equation for transient density and viscosity-dependent groundwater flow:

$$\frac{\partial}{\partial x_i}\left(K_{ij} \frac{\mu_0}{\mu} \left(\frac{\partial h^*}{\partial x_j} + \rho_r \frac{\partial z}{\partial x_j} \right) \right) = S_s \left(\frac{\partial h^*}{\partial t} \right), \quad i, j = 1,2,3 \tag{2-6}$$

In conclusion, the role of the chosen value of the specific storage, S_s, is important in different ways in Equation 2-1 and Equation 2-6. However, in both equations, a high value of the specific storage causes a delay in the reaction of the system to changes in boundary conditions during glacial advances. Conversely, when the ice retreats, the glacially induced pore pressures in the subsurface persist for some time.

/Lemieux et al. 2008a/ tested different values of z (including 0 and 1) centred around a base case value of z = 0.2, whereas /Walsh and Avis 2010/ used a fixed value of z = 0.33 and /Cohen et al. 2010/ used a fixed value of z = 1. Thus, the stiffness of the medium varied between the three glacial groundwater flow models. The flow model analysed by /Lemieux et al. 2008a/ is the stiffest and the flow model analysed by /Cohen et al. 2010/ is the most compressible.

The implications for groundwater flow and transport of incorporating a 1-D loading efficiency are not readily concluded because the simulation results are dependent on the chosen combination of thermal, hydraulic, chemical, and mechanical boundary conditions and properties. Some parameter combinations are more realistic than others, though. For instance, for a warm-based glacial advance it is not reasonable to have an extensive permafrost layer under the entire ice sheet. By the same token, for a cold based glacial advance, it is less probable to assume an abundance of meltwater such that the hydraulic head at the surface reaches 92% of the ice sheet thickness, since this value implies that ice sheet is floating despite the cold conditions at the base. As illustrated in the cartoon shown in Figure 1-2, the foremost tip of an advancing warm-based ice sheet may be underlain by permafrost. This situation can arise if the thawing of a thick permafrost layer does not take place at the same rate as the speed of an advancing warm-based ice sheet /SKB 2010/. Finally, it is recalled that Equation 2-1 is based on the assumption of purely vertical strain below an ice sheet where only homogeneous and laterally extensive overburden changes occur. This assumption is not valid where vertical loads vary significantly over short distances, e.g. close to the ice sheet terminus.

The hydro-mechanical coupling described above is closely linked to the following issues:

- isostatic compensation,
- the forebulge phenomenon, and
- structural geology and hydraulic properties.

Isostatic compensation – The groundwater flow model adopted by /Lemiuex et al. 2008a, b, c/ is asynchronously linked to the GSM climate model as a way of obtaining information about the development of ice sheet thickness in space and time. The depression of the bedrock is accounted for in the groundwater flow model by adjusting the elevations of the mesh nodes in each vertical grid column uniformly as the ice sheet margin advanced or retreated in the GSM climate model. /Walsh and Avis 2010/ and /Cohen et al. 2010/ use polynomial expressions for the ice sheet thickness provided by /Oerlemans 2005/ and /van der Veen 1998/, respectively. The expressions are conditioned (scaled) against available field information, e.g. the Greenland Ice Core Project (GRIP) sea-level data. Further, the depression of the bedrock is accounted for in an implicit fashion in the groundwater flow model by changing the shapes of the two polynomial expressions for the ice thickness function by c. 10%, see Figure 2-4 for an example. /Cohen et al. 2010/ conclude that the implicit approach resulted in a reduction of the hydraulic heads assigned to the nodes beneath the ice sheet by as much as 100 m and diminished the vertical hydraulic gradients beneath the ice sheet.

/Lemieux 2008a, b, c/ assert that the temporally and geographically changing elevation component of the hydraulic head has a significant transient impact on the simulated groundwater flow pattern; since the elevation component of the hydraulic heads in the ice-free periglacial regions remain unchanged. In conclusion, there may be a difference in effects between a geometrical adjustment of the mesh elevations and a hydraulic adjustment of the top boundary condition.

For the sake of clarity, it is noted that /Lemieux et al. 2008a/ assume a mixed top boundary condition, whereas both /Walsh and Avis 2010/ and /Cohen et al. 2010/ assume a specified hydraulic head. That is, both /Walsh and Avis 2010/ and /Cohen et al. 2010/ assumed *a priori* that the groundwater recharge fluxes are not in excess of local melt rates even for cold base ice sheet periods.

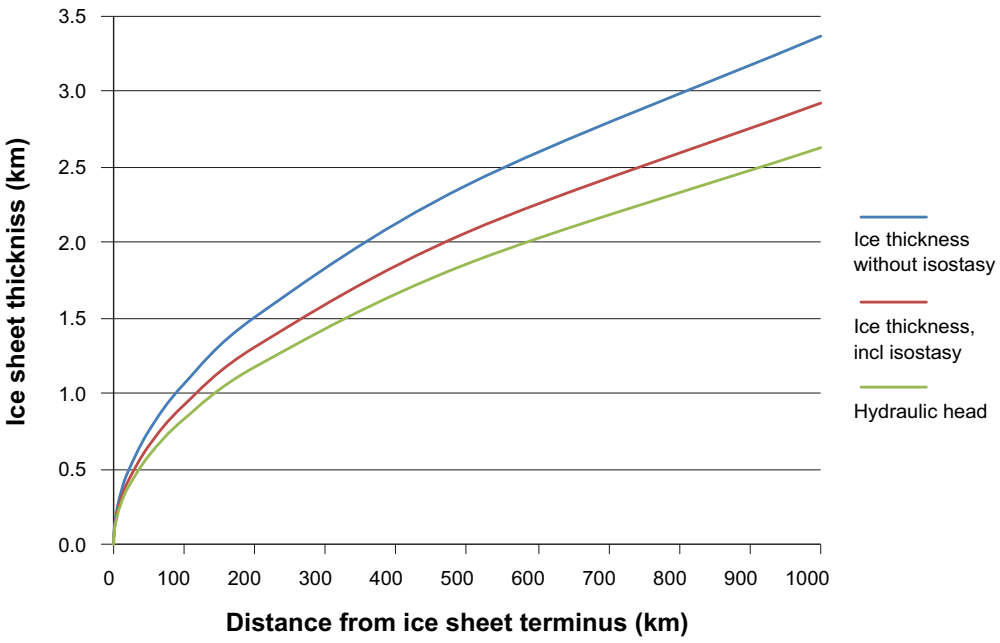

Figure 2-4. *Visualisation of the analytical expression from /Oerlemans 2005/ used by /Walsh and Avis 2010/ to obtain information about the ice thickness as a function of the distance from the ice sheet terminus (blue). The effect of isostasy is accounted for by reducing the thickness by c. 13% (red). The equivalent freshwater hydraulic head on the top boundary is calculated by multiplying the decreased ice sheet thickness by ice sheet density (assumed to be 900 kg/m³).*

Forebulge phenomenon – /Walsh and Avis 2010/ note that the uneven surface loading at the ice sheet terminus, see Figure 2-3, could lead to a wide-spread opening of vertical faults. Most groundwater flow models, however, do not consider how high surface loading and hydraulic pressure changes might lead to transient alterations of the hydraulic properties of the rock mass.

Structural geology and hydraulic properties – /Walsh and Avis 2010/ draw the conclusion that the highly connected and relatively conductive deformation zone system considered in their model is critical in allowing meltwater to penetrate beyond the upper more permeable layers, allowing a small fraction to eventually reach repository depth. A different distribution of material parameters could change the water flow rates and flow directions during different stages of the glacial cycle.

2.4 Ice sheet profile

It is readily concluded that the key boundary condition during a glacial cycle is the thickness and the properties of the ice sheet (warm or cold based). The thickness and the properties affect all processes involved regardless of whether they are thermal (T), hydraulic (H), mechanical (M) or chemical (C). The literature review describes how this has been represented in previous studies. Below follows a short description of how the ice sheet profile is defined in the modelling work reported here.

Beneath the ice sheet, the pressure is specified using theoretical/empirical ice sheet thickness relationships /Paterson 1994/. This approach has been used in various earlier numerical groundwater flow simulations and is, in general, believed to overestimate the impact of an ice sheet, e.g. /Chan et al. 2005/.

/Paterson 1994/ reported two possible equations for expressing the ice sheet thickness. If the ice is assumed to be a perfectly plastic material the ice thickness adjusts to the shear stress at the base. For such conditions, the ice thickness can be expressed as:

$$h^2 = \frac{2 \cdot \tau_0}{\rho g} \cdot (L - x) \qquad (2\text{-}7)$$

where h [L] is the ice thickness at location x [L]; L [L] is the size of the ice sheet between the front and its centre (origin of x). Hence, (L-x) is the distance backward from the ice sheet margin. τ_0 [$MT^{-2}L^{-1}$] is the shear stress at the base. Values on the shear stress are reported between 0 and 100kPa with a mean at about 50 kPa /Paterson 1994/. Adopting 50kPa yields:

$$h = 3.4 \cdot \sqrt{L - x} \qquad (2\text{-}8)$$

Equation 2-8 has previously been assessed in hydrogeological studies by SKB either as a specified head boundary condition e.g. /Vidstrand et al. 2007/ or as a criterion for assigning a head dependent flux, e.g. /Jaquet and Siegel 2006/.

If the assumption of perfect plasticity is dropped another equation for ice thickness is obtained:

$$h = H \cdot \left(1 - \left(\frac{x}{L} \right)^{\frac{4}{3}} \right)^{\frac{3}{8}} \qquad (2\text{-}9)$$

where H [L] is the ice sheet thickness at the centre and L [L] is the maximum ice sheet horizontal extension.

Equation 2-9 is applied in the SR-Site project in the rock mechanics modelling conducted by /Lönnqvist and Hökmark 2010/, who set H to 3 km and L to 400 km. For the sake of comparison, Equation 2-9 yields an ice sheet thickness approximately twice the thickness of Equation 2-7.

Figure 2-5 shows the three ice sheet profiles discussed in this study.

- The red graph is the so-called “theoretical maximum profile” presented in /SKB 2010/. This profile is considered valid for the pre-LGM stage (an advancing ice sheet margin) and is readily modelled by Equation 2-9. The dotted red line represents the specified pressure head curve assigned on the top boundary in the majority of the groundwater flow simulations reported here. The pressure head is set to 92% of the ice sheet thickness.

- The blue graph represents the shape of the "theoretical maximum profile" when the ice sheet margin has reach the last glacial maximum (LGM) south of the Baltic Sea. The solid black line represents the tangent to the blue graph at a location corresponding to the Forsmark site. During the period of complete ice sheet coverage at Forsmark, the slope of the tangent (1.2m/km) is used to model the ice sheet profile in the work reported here.
- The green graph mimics the "simulated reference climate evolution profile" presented in /SKB 2010/. This profile is considered valid for the post-LGM stage (a retreating ice sheet margin) and applicable for describing ice thickness in terrestrial areas, i.e. areas that are unaffected by the increase in the sea level caused by the abundance of meltwater.

In the work reported here, the "theoretical maximum profile" is used for both the pre-LGM and post-LGM stages.

2.5 Limitations

It is noted that the review presented in this Chapter is restricted to a limited number of recent studies rather than being a comprehensive review of the literature. Thus, it is emphasised that not all approaches to THCM modelling of permafrost and ice sheets are discussed in the work reported here.

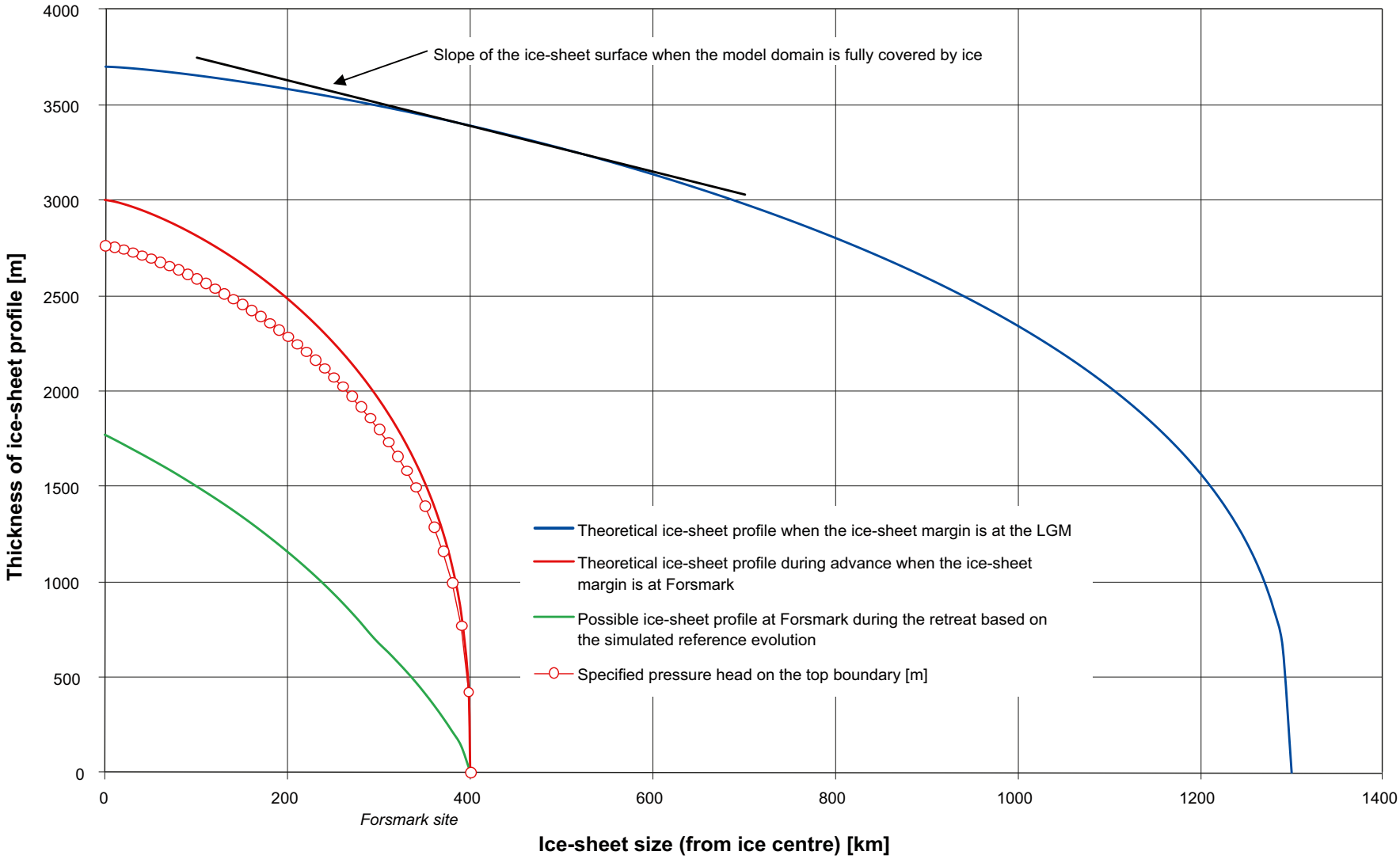

Figure 2-5. *Illustration of ice sheet profiles.*

3 Hydrogeological model of the Forsmark site

3.1 Supporting documents

Three versions of a site descriptive model were completed for Forsmark prior to the final site descriptive model, SDM-Site /SKB 2008a/. Version 0 established the state of knowledge prior to the start of the site investigation programme. Version 1.1 was essentially a training exercise and was completed during 2004. Version 1.2 was a preliminary site description and concluded the initial site investigation work (ISI) in June 2005. The site descriptive modelling resulting in the final site description, SDM-Site, has involved three modelling stages, 2.1-2.3. The first modelling stage, referred to as stage 2.1, included an updated geological model for Forsmark and aimed to provide a feedback from the modelling working group to the site investigation team to enable completion of the site investigation work. The two background reports reported in stage 2.2 are key to repository engineering, one documenting the hydraulic properties of deformation zones and fracture domains /Follin et al. 2007a/ and one the development of a conceptual flow model and the results of numerical implementation and calibration of the flow model /Follin et al. 2007b/. Since the flow model with its calibrated hydraulic properties is also an essential input to the radiological safety assessment, the main findings of the flow modelling in stage 2.2 were revisited in stage 2.3. /Follin et al. 2008/ addressed the impact of parameter heterogeneity on the flow modelling results as well as the impact of the new field data acquired in data freeze 2.3 on the conceptual model development. Table 3-1 shows the cumulative number of boreholes providing hydraulic information about the bedrock at Forsmark. (The table shown in /Follin 2008/ provides the reference numbers of the background reports on bedrock hydrogeology in relation to the three model versions and the three modelling stages carried out in preparation of the SDM-Site report /SKB 2008a/.)

3.2 Systems approach in SDM-Site

Figure 3-1 illustrates schematically the division of the groundwater system into hydraulic domains as used by SKB in the SDM for both Forsmark and Laxemar/Simpevarp. The hydrogeological model consists of three hydraulic domains, HCD, HRD and HSD, where:

- HCD (Hydraulic Conductor Domain) represents deformation zones,
- HRD (Hydraulic Rock mass Domain) represents the less fractured bedrock in between the deformation zones, and
- HSD (Hydraulic Soil Domain) represents the regolith (Quaternary deposits).

The division into hydraulic domains constituted the basis for the conceptual modelling, the planning of the site investigations and the groundwater flow modelling carried out in the SDM studies. Besides the three hydraulic domains, the systems approach also encompasses the following three model components:

- a dual-porosity model for the modelling of salt transport in the fracture system (advection and dispersion) and in the rock matrix (diffusion),
- initial conditions for groundwater flow and hydrochemistry, and
- boundary conditions for groundwater flow and hydrochemistry.

Table 3-1. The cumulative number of cored boreholes (KFM) providing geometrical and hydraulic information about the bedrock at Forsmark at the end of each of the three model versions and three model stages carried out for SDM-Site. (Modified after Table 1-2 in /Follin 2008/.)

	Initial site investigation (ISI)		Complete site investigation (CSI)		
Desk top exercise	**Training exercise**	**Preliminary SDM**	**Feedback and strategy**	**Hydrogeological model**	**Model verification and uncertainty assessment**
Version 0	**Version 1.1**	**Version 1.2**	**Stage 2.1**	**Stage 2.2**	**Stage 2.3**
0 KFM (0%) ∑ length: 0 km	1 KFM (4%) ∑ length: 1 km	5 KFM (21%) ∑ length: 5 km	9 KFM (38%) ∑ length: 7 km	20 KFM (83%) ∑ length: 15.9 km	25 KFM (100%) ∑ length: 19.4 km

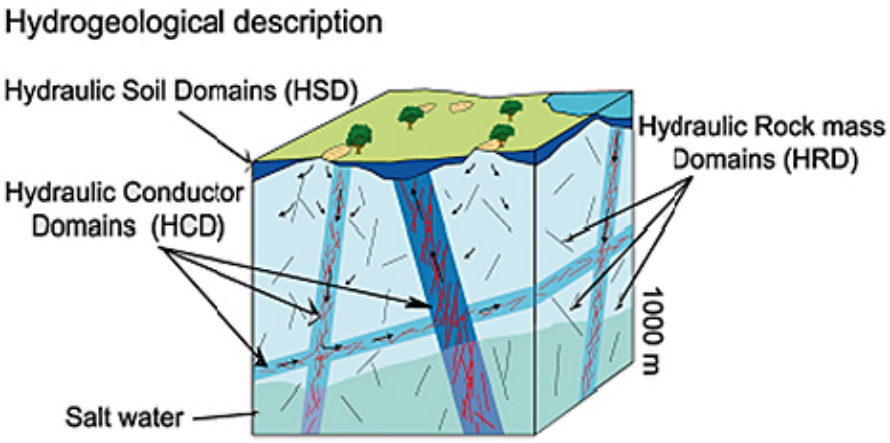

Figure 3-1. *Cartoon showing the division of the crystalline bedrock and the regolith (Quaternary deposits) into three hydraulic domains, HCD, HRD and HSD. (Source: Figure 3-2 in /Rhén et al. 2003/.)*

3.3 Summary of the bedrock hydrogeological model

3.3.1 General

The bedrock in the Forsmark area has been thoroughly characterised with both single-hole and cross-hole (interference) tests. Constant-head injection tests and difference flow logging pumping tests have been used in parallel to characterise the fracture properties close to the boreholes, and interference tests have been used for larger-scale studies. The overall experience from these investigations is that spatial variability in the structural geology significantly affects the bedrock hydrogeology and associated hydraulic properties at all depths. There is a substantial depth trend in deformation zone transmissivity and in the conductive fracture frequency in the bedrock between the deformation zones; the uppermost part of the bedrock is found to be significantly more conductive than the deeper parts. In conclusion, the strong contrasts in the structural-hydraulic properties with depth encountered inside the target volume suggest a hydraulic phenomenon that causes shallow penetration depths of the near-surface groundwater flow system. This probably contributes to the observed slow transient evolution of fracture water and porewater hydrochemistry at repository depth, although the slow evolution is mainly due to the low permeability at these depths.

The left picture in Figure 3-2 illustrates the high water yield of boreholes drilled in the uppermost part of the bedrock close to ground surface. The right picture shows a man carrying two unbroken 3m long drill cores acquired from repository depth. Hundreds of such unbroken drill cores were obtained within the target volume, information that conforms to the low water yields encountered at repository depth. The spatial extent of these two observations, a permeable “shallow bedrock aquifer” on top of a sparsely fractured bedrock of low permeability, was hypothesised in modelling stage 2.2. The hypothesis was not falsified by data from the drilling of boreholes, single-hole hydraulic tests and interference tests conducted in modelling stage 2.3. The frequency and the transmissivity of conductive fractures are plotted versus depth in Figure 3-12.

Figure 3-2. *Two key features of the bedrock in the target area at Forsmark. Left: High water yields are often observed in the uppermost c. 150 m of the bedrock. Right: The large number of unbroken drill cores gathered at depth support the observation of few flowing test sections in the deeper bedrock. (Figure 10-1 in /Follin 2008/.)*

3.3.2 Hydraulic characteristics of hydraulic conductor domains (HCD)

The hydrogeological model suggested for the deterministically modelled deformation zones (Figure 3-3) has four main characteristics.

- The division of the deformation zones into major sets and subsets is useful from a hydrogeological point of view. Most of these structural entities are steeply dipping and strike WNW-NW, NNW and NNE-NE-ENE; one is gently dipping (G).
- All deformation zones, regardless of orientation (strike and dip), display a substantial decrease in transmissivity with depth. The data suggest a contrast of c. 20,000 times in the uppermost one kilometre of the bedrock, i.e. more than four orders of magnitude. Hydraulic data below this depth are lacking (Figure 3-4).
- The lateral heterogeneity in transmissivity is also substantial (a few orders of magnitude) but more irregular.
- The highest transmissivities within the candidate area, regardless of depth, have been observed among the gently dipping deformation zones. The steeply dipping deformation zones that strike WNW and NW have, relatively speaking, higher mean transmissivities than steeply dipping deformation zones in other directions.

An exponential model for the depth dependency of the in-plane deformation zone transmissivity was simulated in /Follin et al. 2007b/ based on the data shown in Figure 3-4. The depth trend model used may be written as:

$$T(z) = T(0)\ 10^{z/k} \qquad (3\text{-}1)$$

where $T(z)$ [L^2T^{-1}] is the deformation zone transmissivity, z [L] is elevation relative the Swedish Ordnance Datum (see Section 1.4), $T(0)$ is the expected value of the transmissivity of the deformation zone at zero elevation, and k [L] is the depth interval that gives an order of magnitude decrease of the transmissivity. The value of k at Forsmark is 232.5 m. The value of $T(0)$ can be estimated by inserting a measured value [z', $T(z')$] in Equation 3-1, i.e.:

$$T(0) = T(z')\ 10^{-z'/k} \qquad (3\text{-}2)$$

In the case of several measurements at different locations in the same zone, the geometric mean of the calculated values of $T(0)$ is used as an effective value, $T_{eff}(0)$ in Equation 3-1. With this approach, the effect of conditioning to a measurement was to extrapolate the conditioned value over the entire

extent of the deformation zone laterally, but not more than 100 m vertically, see Figure 3-5. Lateral heterogeneity was simulated in /Follin et al. 2008/ by adding a log-normal random deviate to the exponent in Equation 3-1, i.e.:

$$T(z) = T(0)\ 10^{z/k + N(0,\sigma_{log(T)})} \qquad (3\text{-}3)$$

where $s_{log(T)} = 0.632$. This value implies a 95% confidence interval in the lateral spread in $\log(T)$ of about 2.5 orders of magnitude. Furthermore, the transmissivity model assumed a nugget covariance model for the lateral spatial variability, which was conditioned on measured transmissivity data. Since the heterogeneity away from the measurement boreholes is undetermined, this required a stochastic approach using several model realisations, see Figure 3-5 for an example. The calibrated deterministic base model realisation derived in /Follin et al. 2007b/ corresponds to case where $s_{log(T)}$ was set to zero.

The kinematic porosity of the deformation zones was not investigated. In the groundwater flow modelling, values of the kinematic porosity were calculated from the ratio between the transport aperture and the geological thickness. The transport apertures were calculated from the transmissivities of the deformation zones (see Equation 2-1 in /Follin 2008/ and Equation 4-18 in Section 4.2.2) and the values of the geologic thicknesses were provided by /Stephens et al. 2007/.

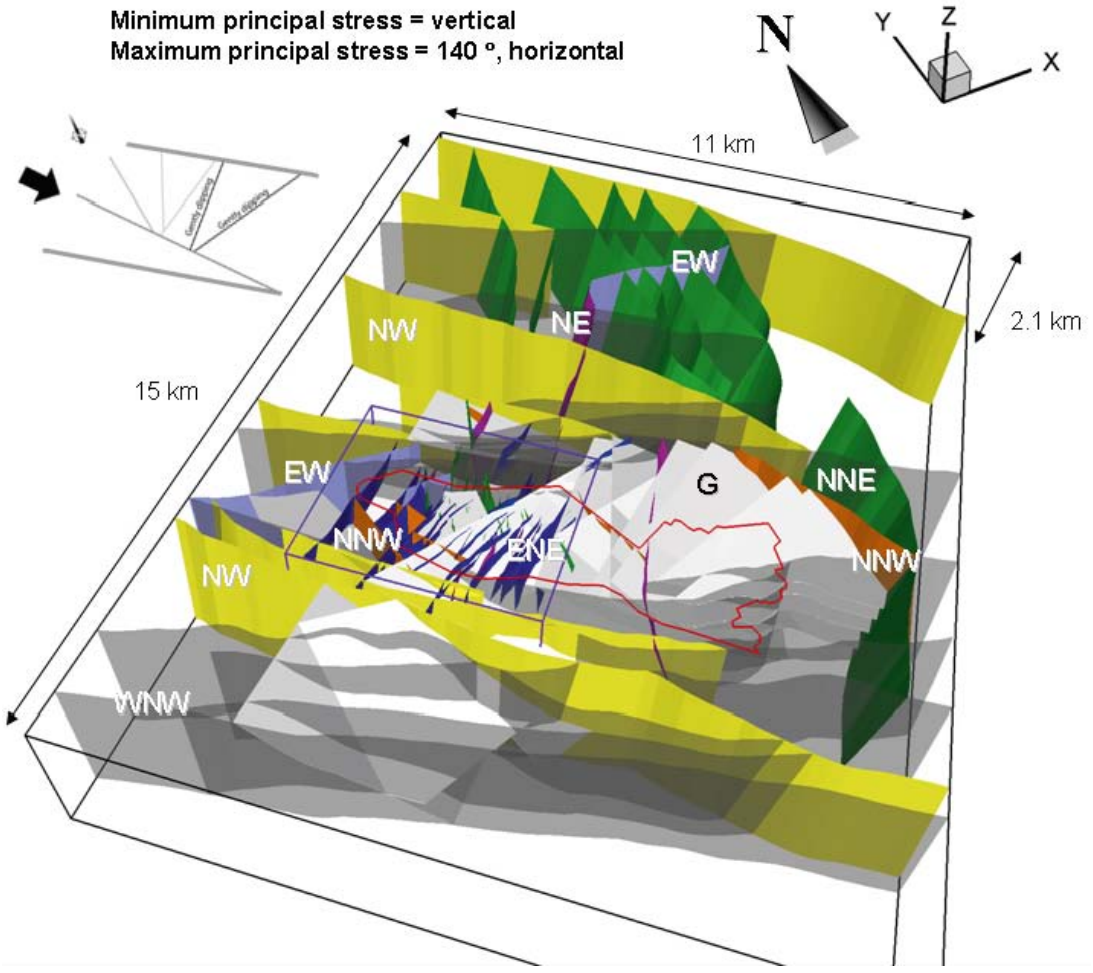

Figure 3-3. *3-D visualisation of the regional model domain and the 131 deformation zones modelled deterministically for Forsmark stage 2.2. The steeply dipping deformation zones (107) are shaded in different colours and labelled with their principal direction of strike. The gently dipping zones (24) are shaded in pale grey and denoted by a G. The border of the candidate area is shown in red and regional and local model domains in black and purple, respectively. The inset in the upper left corner of the figure shows the direction of the main principal stress. (Source: Figure 3-4 in /Follin 2008/.)*

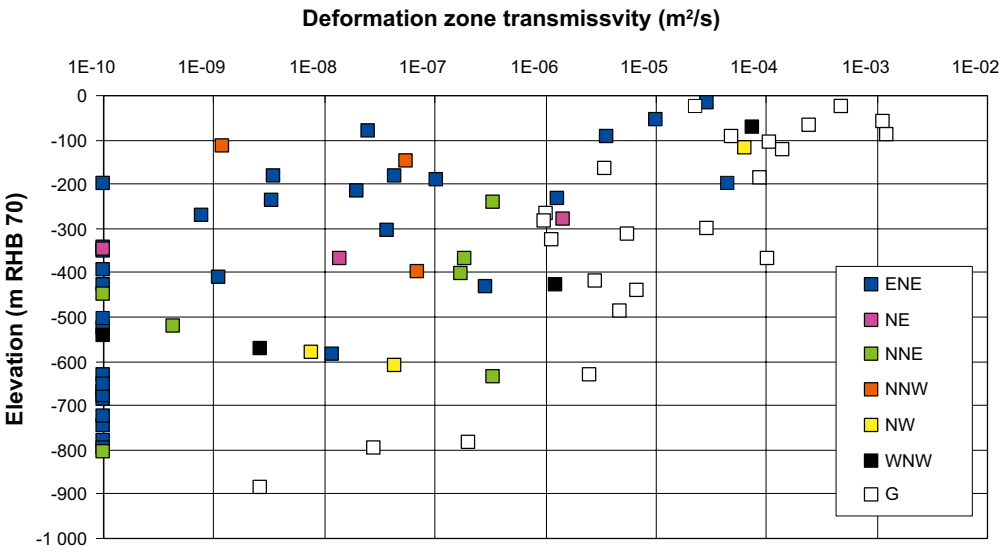

Figure 3-4. *Transmissivity data versus depth for the deterministically modelled deformation zones. The transmissivities are coloured with reference to the orientations of the deformation zones, where G means gently dipping. The deformation zones with no measurable flow are assigned an arbitrary low transmissivity value of 1 · 10^{-10} m^2/s in order to make them visible on the log scale. (Source: Figure 5-1 in /Follin 2008/.)*

3.3.3 Hydraulic characteristics of the hydraulic rock domains (HRD)

The hydrogeological model of the fracture domains, i.e. the fractured bedrock between the deterministically modelled deformation zones (Figure 3-6, Figure 3-7, and Figure 3-8) has four main characteristics:

- The division of the bedrock between the deterministically modelled deformation zones in the candidate area into six fracture domains, FFM01-06, and five fracture sets, NS, NE, NW, EW and HZ, is useful from a hydrogeological point of view.
- The conductive fracture frequency shows very strong variations with depth, and a discrete network model for conductive fractures within the target volume is adopted that is split into three layers; above 200 m depth, between 200–400 m depth, and below 400 m depth.
- The hydraulic character of the fracture domains is dominated by the gently dipping HZ fracture set, and with only a small contribution from the steeply dipping NS and possibly NE fracture sets. However, the depth trend in fracture transmissivity for the fracture domains is not as conclusive as for the deformation zones.
- The sparse number of steeply dipping flowing features at depth within the target volume suggests that fractures associated with the gently dipping HZ fracture set may be fairly long (large) in order to form a sufficiently connected network.

For the bedrock outside the candidate area, due to lack of data the discrete fracture network (DFN) approach associated with the fracture domain concept was replaced by a continuous porous medium (CPM) approach in the hydrogeological modelling for the SDM. Approximate values for this rock were taken from hydraulic single-hole tests in deep boreholes at Finnsjön /Andersson et al. 1991/ using the results given for the geometric mean of 3 m double-packer injection tests in the bedrock between deformation zones, see Table 3-2. A depth dependency is suggested by the data, which was simplified in the SDM to a step-wise model consistent with the depth zonations used in FFM01 in SDM-Site, see Section 3.3.4.

Table 3-2. Homogeneous and isotropic hydraulic properties used for the HRDs outside the candidate area. (Source: Table 3-6 in /Follin et al. 2007a/.)

Elevation *z* [m]	Hydraulic conductivity *K* [m/s]	Kinematic porosity ϕ [-]
> –200	$1 \cdot 10^{-7}$	$1 \cdot 10^{-5}$
–200 to –400	$1 \cdot 10^{-8}$	$1 \cdot 10^{-5}$
< –400	$3 \cdot 10^{-9}$	$1 \cdot 10^{-5}$

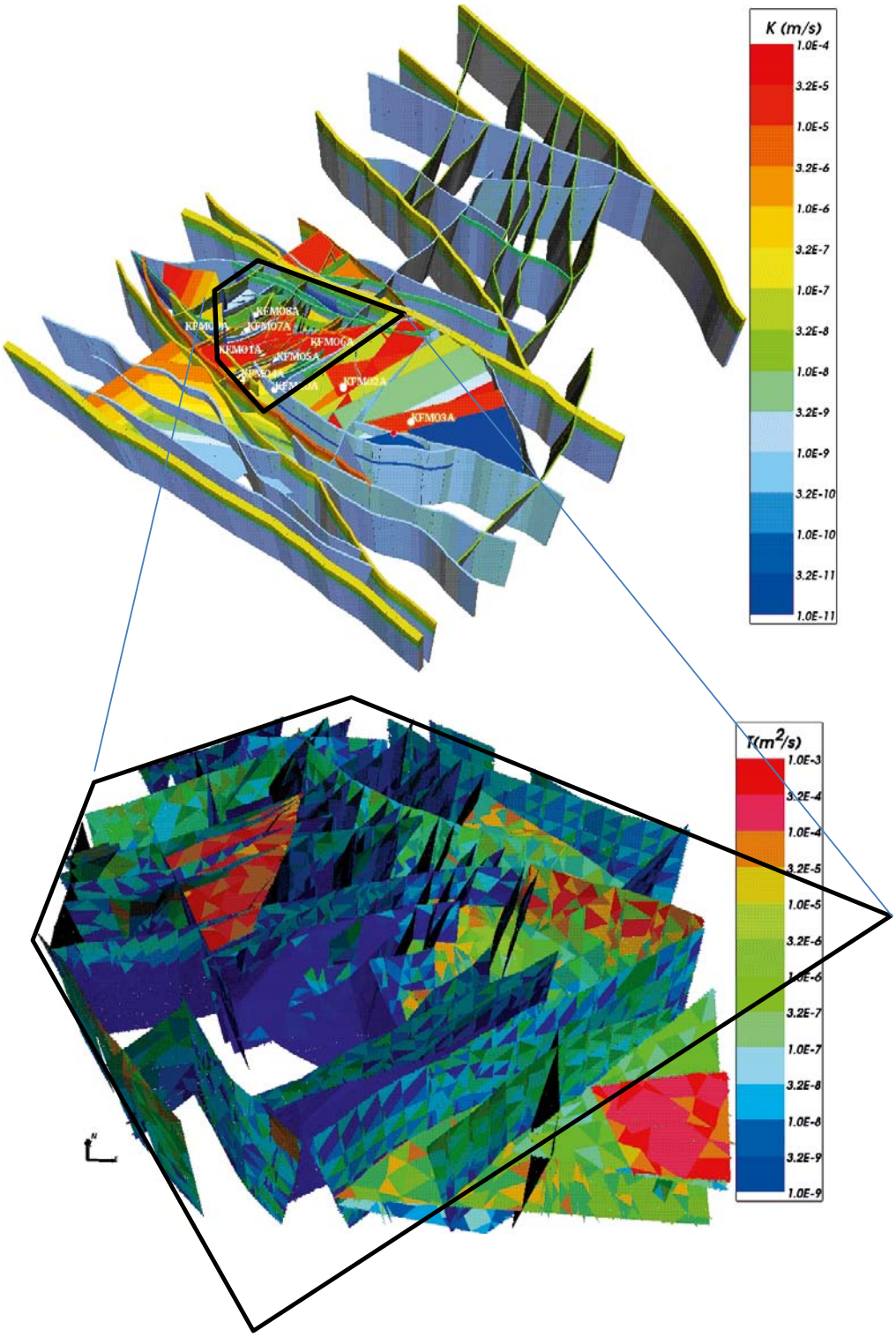

Figure 3-5. *Top: The resulting homogeneous (deterministic) property model of the HCDs using Equation 3-1. Here, the regional scale deformation zones are coloured to indicate the hydraulic conductivity within the zones and drawn as volumes to show their assigned hydraulic width. Bottom: Example visualisation of a stochastic realisation of the deformation zones that occur inside the local model domain using Equation 2-3 to define heterogeneous hydraulic properties. (Modified after Figure 6-1 and Figure 6-2 in /Follin 2008/.)*

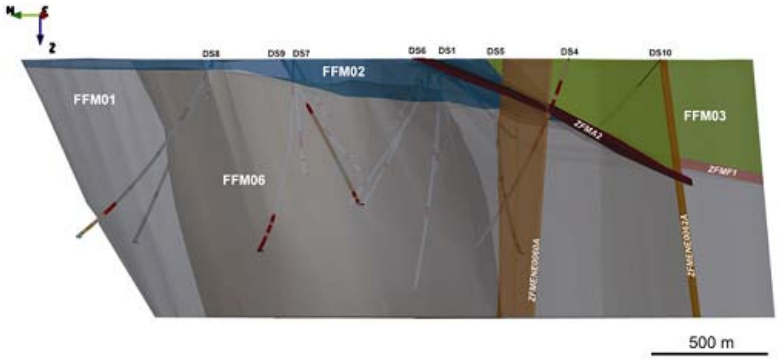

Figure 3-6. *Three-dimensional view of the fracture domain model, viewed towards ENE. Fracture domains FFM01, FFM02, FFM03 and FFM06 are coloured grey, dark grey, blue and green, respectively. The gently dipping and sub-horizontal zones A2 and F1 as well as the steeply dipping deformation zones ENE0060A and ENE0062A are also shown. (Source: Figure 3-10 in /Follin 2008/.)*

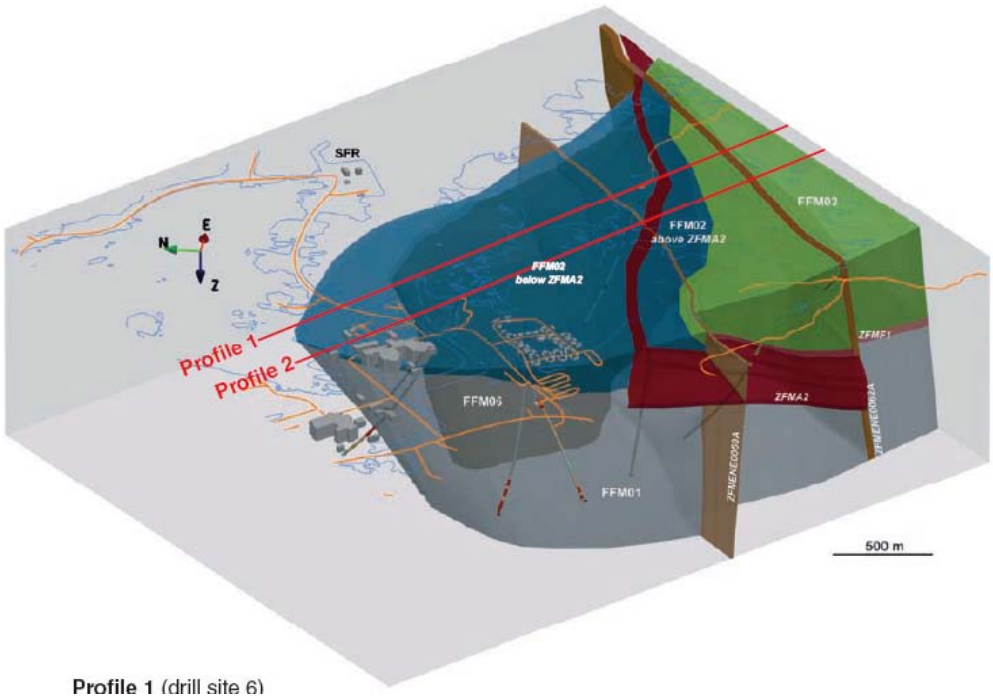

Figure 3-7. *Three-dimensional view towards ENE showing the relationship between deformation zone A2 (red) and fracture domain FFM02 (blue). Profile 1 and 2 are shown as cross-sections in Figure 3-8. (Source: Figure 3-11 in /Follin 2008/.)*

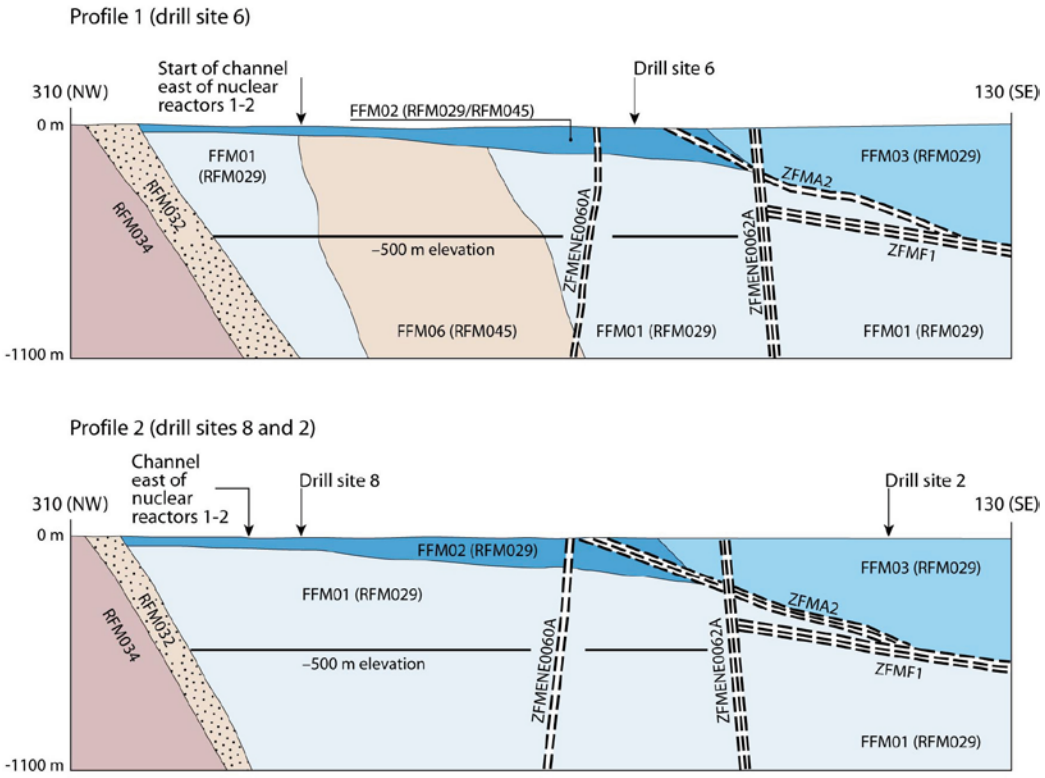

Figure 3-8. *Simplified profiles in a NW-SE direction that pass through the target volume. The locations of the profiles are shown in Figure 3-7. The key fracture domains, FFM01, -02 and -06, for a final repository at Forsmark occur in the footwall of zones A2 (gently dipping) and F1 (sub-horizontal). The major steeply dipping zones ENE0060A and ENE0062A are also included in the profiles. (Source: Figure 5-4 in /Olofsson et al. 2007/.)*

3.3.4 Hydrogeological characteristics of the target volume

The cross-section cartoon in Figure 3-9 summarises the key components of the conceptual model of the bedrock hydrogeology in the target volume at Forsmark.

- The flow at repository depth in fracture domains FFM01 and FFM06 is probably channelised in the sparse network of connected fractures, **D**, which is dominated by two fracture sets, HZ and NE. The HZ fracture set is interpreted to be longer and probably more transmissive than the NE set.
- **D** connects to **A** and **C**, where **A** represents the steeply dipping NNE-ENE deformation zones, which are abundant but hydraulically heterogeneous, and **C** represents the intensely fractured fracture domain FFM02, which lies on top of **D**.
- The groundwater flow in **C** is dominated by the HZ fracture set, which occurs with a high frequency. More importantly, **C** is intersected by several extensive, horizontal fractures/sheet joints, **B** (Figure 3-10), which can be very transmissive (Figure 3-2).
- **B** and **C** and the outcropping parts of **A** probably form a shallow network of flowing fractures. The network is interpreted to be highly anisotropic, structurally and hydraulically. Together with **D**, which is close to the percolation threshold, the network creates a hydrogeological situation that is referred to as a shallow bedrock aquifer on top of a thicker bedrock segment with aquitard-type properties (Figure 3-11).

Figure 3-12 summarises the findings of the investigations with PFL-f method[10] in fracture domains FFM01-03 and -06. As an example, the hydrogeological DFN parameters deduced for FFM01 and FFM06 are tabulated in Table 3-3. The semi-correlated transmissivity-fracture size model referenced in the table may be written as:

$$\log(T_f) = \log(a\, r^b) + \sigma_{\log(Tf)}\, N[0,1] \qquad (3\text{-}4)$$

where T is the fracture transmissivity, r is the fracture radius, a and b are constants and $N[0,1]$ denotes a normally distributed random deviate with a mean equal to zero and a standard deviation of 1. In Table 3-3, r_0 [L] and k_r [-] are the location parameter and the shape parameter, respectively, of a power-law size distribution:

$$f(r) = \frac{k_r r_0^{k_r}}{r^{k_r+1}} \qquad (3\text{-}5)$$

where $r_0 > 0$ and $k_r > 0$.

The kinematic porosity of individual fractures, ϕ_f [-], was not investigated during the site investigations. In the groundwater flow modelling conducted in SDM-Site, values of the grid cell kinematic porosity of an equivalent continuous porous medium (ECPM) model, ϕ_c [-], were calculated from the fracture transport apertures, $(e_t)_f$ [L]. These were, in turn, calculated from the fracture transmissivities, T_f [L^2T^{-1}]:

$$(e_t)_f = a\,(T_f)^b \qquad (3\text{-}6)$$

The values of the parameters a and b used in SDM-Site are defined in /Dershowitz et al. 2003/, where $a = 0.46$ and $b = 0.5$.

Further, $P_{32,o}$ [L^{-1}] in Table 3-3 represents the 3-D intensity of open fractures. In SDM-Site, it is assumed that:

$$P_{32,o} = P_{10,o,\mathrm{corr}} \qquad (3\text{-}7)$$

where $P_{10,o,corr}$ is the borehole fracture frequency corrected for borehole orientation bias.

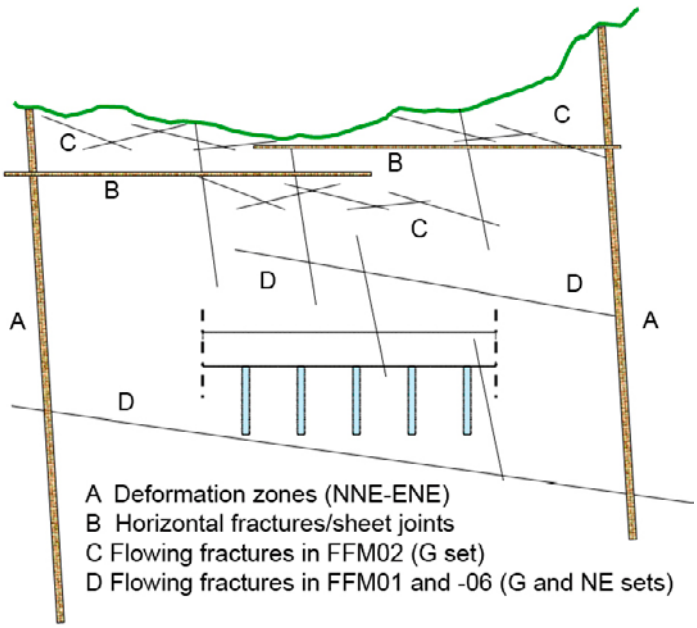

Figure 3-9. *A 2-D cartoon looking NE that summarises the hydrogeological conceptual model of the bedrock within the target volume at Forsmark. (Source: Figure 10-3 in /Follin 2008/.)*

[10] The PFL tool is a logging device developed by Posiva Oy to detect continuously flowing fractures in sparsely fractured crystalline rock. The physical limitations of the PFL tool and the principles for its operation are explained in detail in SKB's P-report series, e.g. /Rouhiainen and Sokolnicki 2005/, The PFL-f method implies a particular measurement procedure, where the specific capacity is determined fracture-wise with a spatial resolution of 0.1m. In Sicada, the specific capacity is called fracture transmissivity.

Figure 3-10. *Picture from the construction of the 13 m deep and more than one kilometre long canal between the Baltic Sea and the nuclear power reactors in Forsmark. Horizontal fractures/sheet joints are encountered along the entire excavation. The sheet joints follow the undulations of the bedrock surface implying that many of them do not outcrop, but stay below the bedrock surface as this dips under the Baltic Sea. There are several "horizons" of extensive sheet joints on top of each other as determined by the hydraulic interference tests. (Source: Figure 5-14 in /Follin 2008/.)*

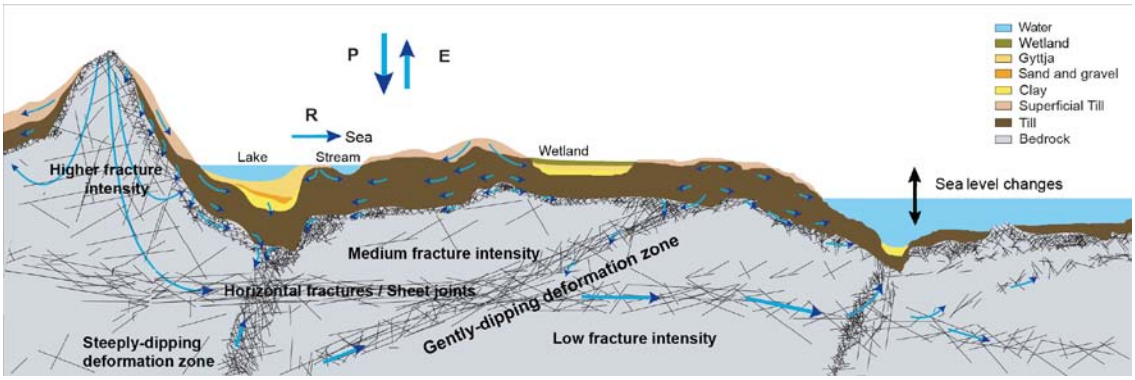

Figure 3-11. *Cross-section cartoon visualising the notion of a shallow bedrock aquifer and its impact on the groundwater flow system in the uppermost part of the bedrock within the target area. The shallow bedrock aquifer is hydraulically heterogeneous but at many places it is limiting the penetration of the recharge from above. The shallow bedrock aquifer is also conceived to constitute an important discharge horizon for the groundwater flow in outcropping deformation zones. P=precipitation, E= evapotranspiration, R=runoff. (Source: Figure 5-16 in /Follin 2008/.)*

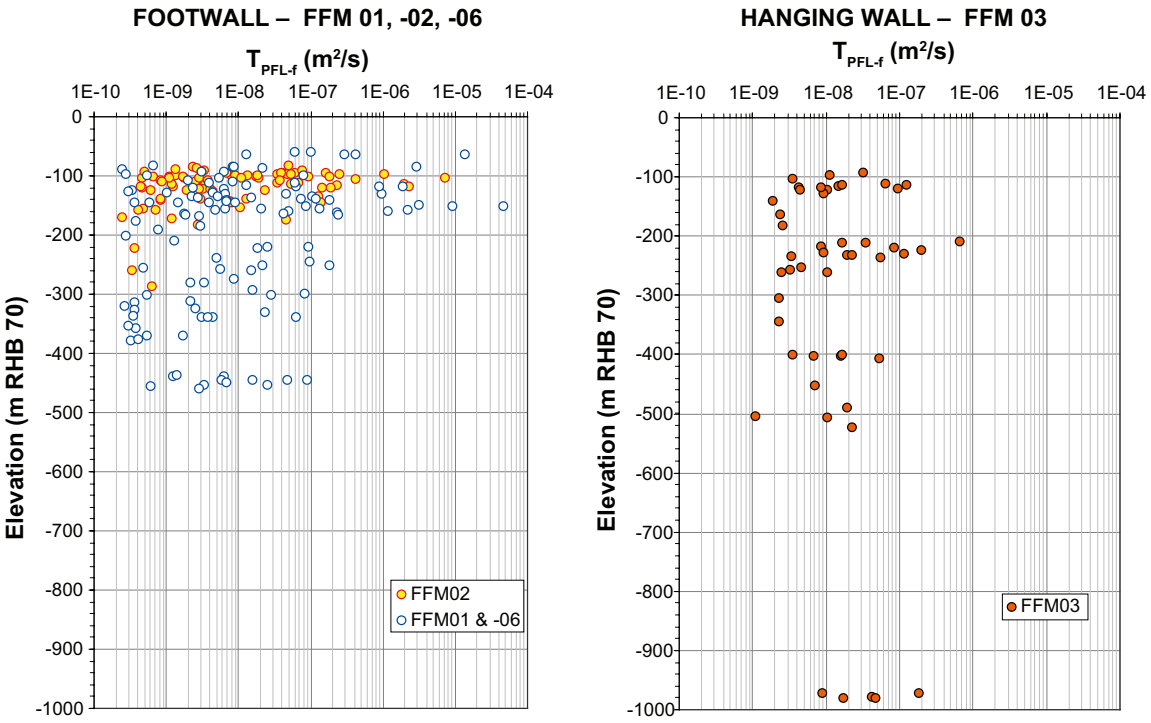

Figure 3-12. *Inferred transmissivities of connected open fractures detected with the PFL-f method in fracture domains FFM01, -02 and -06 (left) and in FFM03 (right). In the legend, "footwall" and "hanging wall" refer to the gently dipping deformation zone ZFMA2. (Source: Figure 5-12 in /Follin 2008/.)*

Table 3-3. Hydrogeological DFN parameters for the semi-correlated transmissivity model of FFM01 and FFM06 with depth dependency: above –200 m, –200 m to –400 m and below –400 m. (Source: Appendix C in /Follin 2008/.)

Fracture domain [m RHB 70]	Fracture set name	Orientation set pole: (trend, plunge), conc. [°,°, -]	Power-law size distribution (r_0, k_r) [m, -]	Intensity ($P_{32,open}$) valid size interval: (r_0, 564 m) [m²/m³]	Transmissivity model constants Equation (3-4)
FFM01 & -06 > –200	NS	(292, 1) 17.8	(0.038, 2.50)	0.073	$(a,b,\sigma) = (6.3 \cdot 10^{-9}, 1.3, 1.0)$
	NE	(326, 2) 14.3	(0.038, 2.70)	0.319	
	NW	(60, 6) 12.9	(0.038, 3.10)	0.107	
	EW	(15, 2) 14.0	(0.038, 3.10)	0.088	
	HZ	(5, 86) 15.2	(0.038, 2.38)	0.543	
FFM01 & -06 –200 to –400	NS	As above	As above	0.142	$(a,b,\sigma) = (1.3 \cdot 10^{-9}, 0.5, 1.0)$
	NE	As above	As above	0.345	
	NW	As above	As above	0.133	
	EW	As above	As above	0.081	
	HZ	As above	As above	0.316	
FFM01 & -06 < –400	NS	As above	As above	0.094	$(a,b,\sigma) = (5.3 \cdot 10^{-11}, 0.5, 1.0)$
	NE	As above	As above	0.163	
	NW	As above	As above	0.098	
	EW	As above	As above	0.039	
	HZ	As above	As above	0.141	

3.4 Summary of the regolith hydrogeological model (HSD)

All known deposits at Forsmark were deposited during the Quaternary period, and thus are generally referred to as Quaternary deposits. In addition, most of the Quaternary deposits at Forsmark were probably deposited during or after the latest deglaciation (Weichsel). Figure 3-13 shows the conceptual model of the stratigraphy. The model consists of nine layers (L1-L3, Z1-Z6). Not all layers exist everywhere, and the thickness of individual layers varies significantly. The overall thickness of the Quaternary deposits varies from less than a decimetre to a maximum of 42 m /Hedenström et al. 2008/. The definition of the nine layers is shown in Figure 3-14.

The conceptual model was developed for the area shown in Figure 3-14, which covers most of the site descriptive regional model area. The model was truncated in the south slightly more than in the regional-scale hydrogeological model. The interpreted thicknesses of the Quaternary deposits are also shown in Figure 3-14. The compilation of different kinds of data obtained from several types of investigations has produced this model, the accuracy of the map varies, therefore. The most detailed information was obtained from the central part of the model area and in the near-shore coastal area. The profile in Figure 3-14 shows the stratification of the Quaternary deposits beneath Lake Bolundsfjärden as an example.

Table 3-4. Names and definitions of Quaternary deposits (Modified after Table 2-4 in /Hedenström et al. 2008/.)

Layer	Description and comments
L1	Layer consisting of different kinds of gyttja/mud/clay or peat. Interpolated from input data, thickness will therefore vary.
L2	Layer consisting of sand and gravel. Interpolated from input data, thickness will therefore vary.
L3	Layer consisting of different clays (glacial and postglacial). Interpolated from input data, thickness will therefore vary.
Z1	Surface affected layer present all over the model, except where peat is found and under lakes with lenses. Thickness is 0.10 m on bedrock outcrops, 0.60 m elsewhere. If total regolith thickness is less than 0.60 m, Z1 will have the same thickness as the total, i.e. in those areas only Z1 will exist.
Z2	Surface layer consisting of peat. Zero thickness in the sea. Always overlies Z3.
Z3	Middle layer of sediments. Only found where surface layers are other than till, clay or peat.
Z4a	Middle layer consisting of postglacial clay. Always overlies Z4b.
Z4b	Middle layer of glacial clay.
Z5	Corresponds to a layer of till. The bottom of layer Z5 corresponds to the bedrock surface.
Z6	Upper part of the bedrock. Fractured rock. Constant thickness of 0.5 m. Calculated as an offset from Z5.

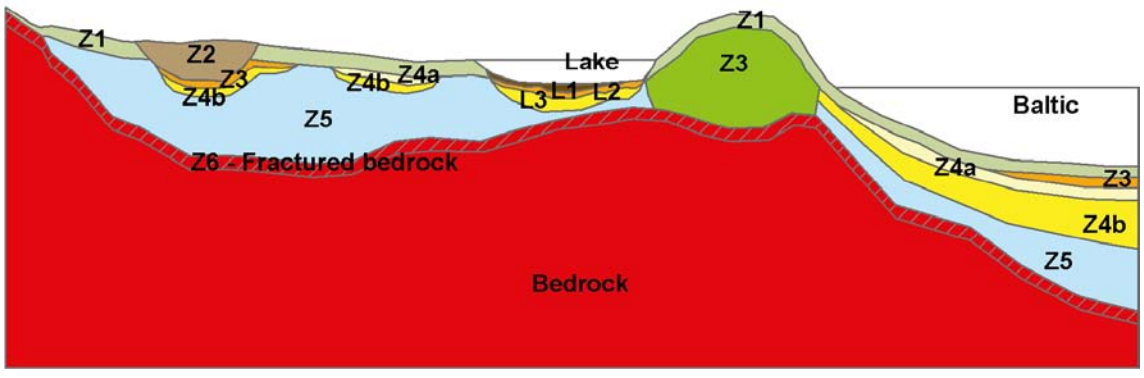

Figure 3-13. *Conceptual model for the layering of Quaternary deposits at Forsmark. The different layers are explained in Table 3-4 (Source: Figure 3-1 in /Hedenström et al. 2008/.)*

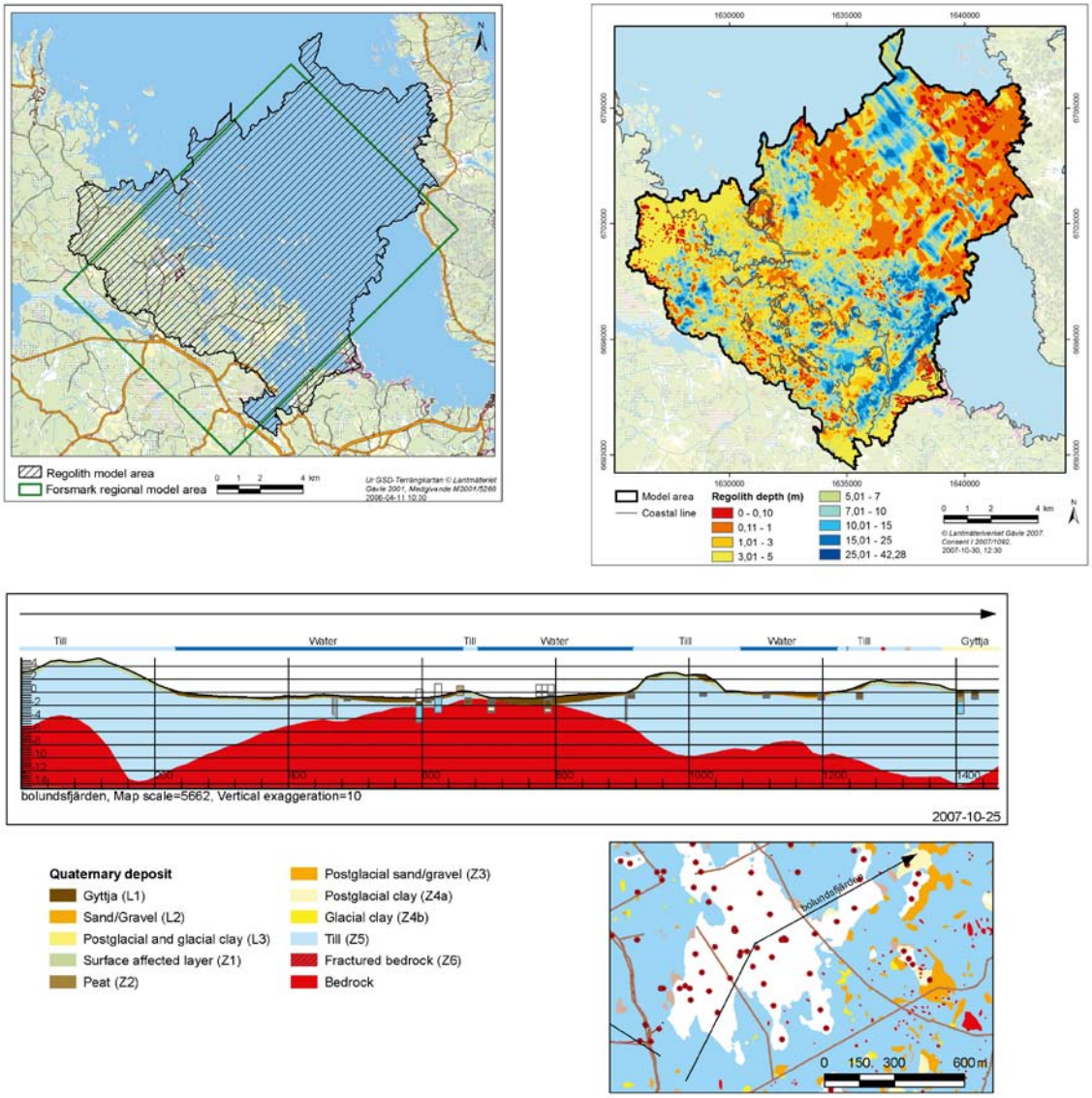

Figure 3-14. *Top left: Extent of the model of the Quaternary deposits in stage 2.2. Top right: Interpreted total thickness of the Quaternary deposits. Bottom: Example cross-section showing the interpreted stratification and thicknesses of the Quaternary deposits beneath Lake Bolundsfjärden. (Based on figures from Appendix 2 of /Hedenström et al. 2008/.)*

Table 3-5 and Table 3-6 show the parameter values provided for groundwater flow modelling by the surface system group /Bosson et al. 2008/. Most of the values represent so-called 'best estimates' based on site-specific data supported by generic data when site-specific data are scarce, cf. /Johansson 2008/.

Table 3-5. Values of the total porosity and the specific yield of the Quaternary deposits suggested for groundwater flow modelling in SDM stage 2.2. (Modified after Table 2-4 in /Bosson et al. 2008/.)

Layer	Total porosity [–] and specific yield [–] of layers with several types of Quaternary deposits					
	Fine till	Coarse till	Gyttja	Clay	Sand	Peat
L1	–	–	0.50 / 0.03	–	–	0.60 / 0.20
Z1	0.35 / 0.15	0.35 / 0.15	–	0.55 / 0.05	0.35 / 0.20	0.40 / 0.05
Z5	0.25 / 0.03	0.25 / 0.05	–	–	–	–
	Total porosity [–] and specific yield [–] of layers with one type of Quaternary deposits					
L2	0.35 / 0.20					
L3	0.55 / 0.05					
Z2	0.40 / 0.05					
Z3	0.35 / 0.20					
Z4	0.45 / 0.03					

Table 3-6. Values of the saturated hydraulic conductivity of the Quaternary deposits suggested for groundwater flow modelling in SDM stage 2.2. (Modified after Table 2-4 in /Bosson et al. 2008/.)

Layer	*K* [m/s] of layers with several types of Quaternary deposits					
	Fine till	Coarse till	Gyttja	Clay	Sand	Peat
L1	–	–	$3 \cdot 10^{-7}$	–	–	$1 \cdot 10^{-6}$ less than 0.6m depth
Z1	$3 \cdot 10^{-5}$	$3 \cdot 10^{-5}$	–	$1 \cdot 10^{-6}$	$1.5 \cdot 10^{-4}$	$3 \cdot 10^{-7}$ greater than 0.6m depth
Z5	$1 \cdot 10^{-7}$	$1.5 \cdot 10^{-6}$	–	–	–	–
	K [m/s] of layers with one type of Quaternary deposits					
L2	$3 \cdot 10^{-4}$					
L3	$1 \cdot 10^{-6}$ less than 0.6 m depth and $1.5 \cdot 10^{-8}$ greater than 0.6 m depth					
Z2	$3 \cdot 10^{-7}$					
Z3	$1.5 \cdot 10^{-4}$					
Z4	$1.5 \cdot 10^{-8}$					

This complex stratigraphy was handled in different ways in the SDM studies depending on the objectives of the flow modelling and the software used, see /Follin et al. 2007b/ and /Bosson et al. 2008/. In /Follin et al. 2007b/, the Quaternary deposits were substituted by four element layers each of constant 1m thickness. The same equivalent hydraulic conductivity tensor was specified for each vertical stack of four grid elements, but was varied horizontally from element-to-element, and was anisotropic between horizontal and vertical components. The horizontal component of the tensor was based on the arithmetic mean of the hydraulic properties of the original stratigraphy, whereas the vertical component was based on its harmonic mean. The resulting hydraulic conductivity distribution is illustrated in Figure 3-15.

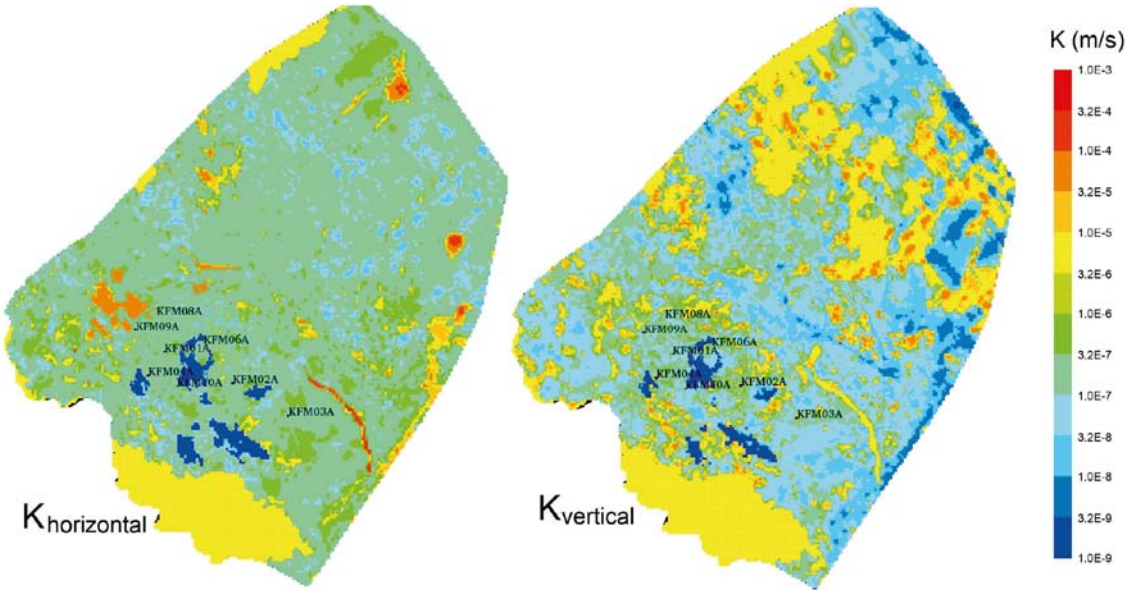

Figure 3-15. *Resulting effective hydraulic conductivity for HSD top layer based on Quaternary deposits layer thicknesses and hydraulic properties. Left: E-W horizontal component. Right: vertical component. (Source: Figure 6-10 in /Follin 2008/.)*

3.5 Groundwater flow modelling and confirmatory testing

The main objectives of the groundwater flow modelling carried out for the SDM were to investigate the behaviour of a numerical implementation of the conceptual hydrogeological model and test its performance against three sets of confirmatory data:

- transient, large-scale cross-hole (interference) test responses,
- steady-state, natural (undisturbed) groundwater levels in the uppermost 150 m, and
- hydrochemical observations in deep boreholes.

In general, the behaviour of the numerical flow model was found to be sound and the matching against the confirmatory data sets reasonable. However, it was noted that the performance of the groundwater flow model, which was based on equivalent continuous porous media (ECPM) properties, was slightly improved if the anisotropy of the horizontal to vertical hydraulic conductivity ratios of the upscaled values for both the Quaternary deposits (HSD) and the fracture domains (HRD) were increased compared with the upscaled values derived from the initial structural-hydraulic settings described above. The objective of the multiple simulations carried out in /Follin et al. 2008/ was to address the sensitivity of the resulting calibrated deterministic base model simulation developed in /Follin et al. 2007b/ to parameter uncertainty, e.g. heterogeneity.

4 Concepts and methodology

4.1 Governing equations

Coupled groundwater flow and salt transport in fractured rocks that give rise to variations in salinity and hence fluid density are modelled in DarcyTools according to the following formulation of the mass conservation equation:

$$\frac{\partial \rho \phi}{\partial t} + \frac{\partial}{\partial x}(\rho u) + \frac{\partial}{\partial y}(\rho v) + \frac{\partial}{\partial z}(\rho w) = Q \tag{4-1}$$

where ρ is fluid density [ML^{-3}], ϕ is the kinematic porosity [–], t is time [T], (u, v, w) are the directional components of the volumetric (Darcy) flux **q** [LT^{-1}] at the location (x, y, z) [L,L,L] in a Cartesian coordinate system, and Q is a source/sink term per unit volume of fluid mass [$ML^{-3}T^{-1}$]. The mass conservation equation is turned into a pressure equation by invoking the assumptions behind Darcy's law:

$$\begin{aligned} \rho u &= -\frac{K_x}{g}\frac{\partial P}{\partial x} \\ \rho v &= -\frac{K_y}{g}\frac{\partial P}{\partial y} \\ \rho w &= -\frac{K_z}{g}\frac{\partial P}{\partial z} - K_z(\rho - \rho_0) \end{aligned} \tag{4-2}$$

where K_x, K_y and K_z are the orthogonal components of the hydraulic conductivity tensor parallel to the Cartesian coordinate system [LT^{-1}], g is the acceleration due to gravity [LT^{-2}], ρ_0 is a reference fluid density [ML^{-3}], and P is the residual (dynamic) fluid pressure [$ML^{-1}T^{-2}$] at the location (x, y, z):

$$P = p + \rho_0 g\, z \tag{4-3}$$

where p is the gauge pressure [$ML^{-1}T^{-2}$] and $\rho_0 g\, z$ is the hydrostatic pressure, P_0.

The hydraulic conductivity K is related to the permeability k [L^2] through the relation:

$$K = \frac{\rho g}{\mu} k \tag{4-4}$$

where μ is the fluid dynamic viscosity [$ML^{-1}T^{-1}$]. For variable-density flow at isothermal conditions, ρ and μ are given by the following state laws:

$$\rho = \rho_0 [1 + \alpha C] \tag{4-5}$$

$$\mu = \mu_0 \tag{4-6}$$

where α and μ_0 are constants and C represents the salinity (mass fraction) [–]:

$$C = TDS / \rho \tag{4-7}$$

The migration of salt is modelled in DarcyTools in terms of advection and dispersion processes in the mobile (fracture) pore system and as a diffusion process in the immobile (rock matrix) pore system. The advection-dispersion equation for the mobile pore system is modelled in DarcyTools according to the following equation:

$$\begin{aligned} \rho\phi\frac{\partial C}{\partial t} &+ \frac{\partial}{\partial x}\left(\rho u C - \rho\gamma D_x \frac{\partial C}{\partial x}\right) \\ &+ \frac{\partial}{\partial y}\left(\rho v C - \rho\gamma D_y \frac{\partial C}{\partial y}\right) \\ &+ \frac{\partial}{\partial z}\left(\rho w C - \rho\gamma D_z \frac{\partial C}{\partial z}\right) = QC + Q_C \end{aligned} \tag{4-8}$$

where D_x, D_y and D_z are the orthogonal components of the diffusion tensor parallel to the Cartesian coordinate system [L^2T^{-1}], QC and Q_C are source/sink terms per unit volume of fluid mass [$ML^{-3}T^{-1}$], where Q_C represents the diffusive exchange of salt per unit volume of fluid mass between the mobile and immobile pore volumes [$ML^{-3}T^{-1}$], and γ is a dimensionless coefficient that describes the dependency of the kinematic porosity ϕ [-] of the mobile pore system on the dynamic pressure:

$$\phi = \phi_0 \gamma \tag{4-9}$$

$$\gamma = 1 + \frac{S_s}{\phi_0}\frac{\left(P - P_0\right)}{\rho g} \tag{4-10}$$

where S_s is the specific storage of the conductive pore system [L^{-1}].

It is noted that the concept of longitudinal and transverse hydrodynamic dispersion (dispersivity) is not considered in DarcyTools, see Equation 4-8.

The heat conservation equation may be written as:

$$\begin{aligned}\rho\phi\frac{\partial c\theta}{\partial t} + \rho_r\frac{\partial(1-\phi)c_r\theta}{\partial t} + \frac{\partial}{\partial x}\left(\rho u c\theta - \lambda_x\frac{\partial\theta}{\partial x}\right) \\ + \frac{\partial}{\partial y}\left(\rho v c\theta - \lambda_y\frac{\partial\theta}{\partial y}\right) \\ + \frac{\partial}{\partial z}\left(\rho w c\theta - \lambda_z\frac{\partial\theta}{\partial z}\right) = \left(\frac{\partial\rho u}{\partial x} + \frac{\partial\rho v}{\partial y} + \frac{\partial\rho w}{\partial z}\right)c\theta + Q_T\end{aligned} \tag{4-11}$$

where θ is the temperature [K], c is the specific heat capacity of the fluid [$L^2T^{-2}K^{-1}$] (or [J/(kg K)]), c_r is the specific heat capacity of the rock [$L^2T^{-2}K^{-1}$] (or [J/(kg K)]), ρ_r is the rock density [ML^{-3}] and λ_x, λ_y and λ_z are the orthogonal components of the equivalent (i.e. rock with fluid) thermal conductivity tensor [$MLT^{-3}K^{-1}$] (or [W/(m K)]). Q_T represents a sink/source term [$ML^{-1}T^{-3}$] ([or W/m^3]).

4.2 Methodology

4.2.1 Finite volume method

DarcyTools uses a staggered computational grid, which means that scalar quantities such as pressure, flow porosity and salinity use a cell-centred mesh, whereas directional quantities such as hydraulic conductivity, hydrodynamic diffusivity, mass flux, and Darcy flux use a mesh centred at the cell walls. This grid arrangement was first introduced by /Harlow and Welch 1965/ and is described in textbooks, e.g. /Patankar 1980/. Each variable is assumed to be representative for a certain control volume, which is the volume for which the equations are formulated. DarcyTools uses the finite volume method to transform the differential equations into algebraic equations of the type:

$$a_P\Phi_P = a_W\Phi_W + a_E\Phi_E + a_S\Phi_S + a_N\Phi_N + a_B\Phi_B + a_T\Phi_T + S_\Phi \tag{4-12}$$

where Φ denotes the variable in question, a_i are direction coefficients (West, East, South, North, Bottom, and Top) and S_Φ represents source/sink terms. The equations are solved by the MIGAL multi-grid equation solver.

4.2.2 Continuum representation of hydraulic properties of discrete fractures

Principle

The principle used to represent hydraulic properties of discrete fractures as equivalent grid cell hydraulic properties in DarcyTools works as follows:

A fracture variable (P_f) contributes to the grid cell variable (P_c) by an amount which is equal to the intersecting volume of the fracture (V_f) times the value of the fracture variable. Contributions from all fractures (N) that intersect the grid cell control volume are added and the sum is divided by the volume of the cell (V_c), i.e.:

$$P_c = \sum_{i=1}^{N} \left(V_f \, P_f \right)_i / V_c \tag{4-13}$$

The intersecting volume of the fracture *f* may be written as:

$$V_f = L_f \, W_f \, b_f \tag{4-14}$$

where L_f, W_f and b_f denote the physical dimensions (length, width and thickness) of the intersecting fracture in three orthogonal directions. For the sake of simplicity, it is assumed in the equations below that the fracture thickness b_f is much thinner than the geometrical resolution of the computational grid (the grid size).

Grid-cell hydraulic conductivity

DarcyTools assumes that fracture transmissivity (T_f) is a scalar quantity and that fracture hydraulic conductivity (K_f) may be written as:

$$K_f = T_f / b_f \tag{4-15}$$

Thus, the contribution from an intersecting fracture to the hydraulic conductivity of the intersected grid cell may be written as:

$$(K_c)_f = (L_f \, W_f \, T_f) / V_c \tag{4-16}$$

As DarcyTools uses a staggered computational grid, $(K_c)_f$ is a directional quantity.

Grid-cell kinematic porosity and fracture aperture

The contribution from an intersecting fracture, deterministic or stochastic, to the kinematic porosity of the intersected grid cell can approximately be written as:

$$(\phi_c)_f = (L_f \, W_f \, (e_t)_f / V_c \tag{4-17}$$

where $(e_t)_f$ is the fracture transport aperture. In SDM-Site, a power-law function between the fracture aperture and the fracture transmissivity was assumed:

$$(e_t)_f = a \, (T_f)^b \tag{4-18}$$

with $a = 0.46$ and $b = 0.5$ /Dershowitz et al. 2003/.

In the work reported here, the transport apertures of the deterministically modelled deformation zones are based on Equation 4-18, whereas all stochastically modelled zones and fractures are given a constant transport aperture of $1 \cdot 10^{-4}$ m, see Appendix B for details.

Fracture transmissivity

The equations given above reveal that fracture transmissivity is the key hydraulic quantity in DarcyTools, i.e. fracture transmissivity is used to define both grid cell hydraulic conductivity and grid cell kinematic porosity.

DarcyTools assumes that a power-law function prevails between fracture transmissivity and fracture size (L_f). The power-law function may be written as /Svensson et al. 2010/:

$$\log(T_f) = \log\left[a_T \left(\frac{L_f}{100} \right)^{b_T} \right] + d_T \, U\,[-0.5,0.5] \tag{4-19}$$

where a_T is the transmissivity value of a fracture with L_f = 100 m and b_T is the exponent of the power-law function. d_T is a factor that scales a uniformly distributed[11] random deviate U and is used when uncertainty in the power-law function is addressed.

For the sake of clarity it is noted that the relationship between the power-law parameters used in DarcyTools (a_T,b_T) and the corresponding power-law parameters (a,b) derived in SDM-Site and recommended for use in SR-Site Forsmark /Selroos and Follin 2010/ can be written as:

$$b_T = b \tag{4-20}$$

$$a_T = a\left(100/\sqrt{\pi}\right)^{b_T} \tag{4-21}$$

4.2.3 Particle tracking performance assessment measures

A particle tracking algorithm is used to represent advective transport of radionuclides. In DarcyTools, particles are tracked in a deterministic way by moving along a discretised path within the local finite-element velocity-field. The particle tracking routine in DarcyTools, PARTRACK, has two modes of operation; the first is the classic way of moving the particle along the local velocity vector, whereas the second method uses the so called "flux-weighting" approach, and works as follows.

- A particle entering a scalar cell will, if no dispersion effects are activated, stay in the cell for a time that is equal to the free volume of the cell divided by the flow rate through the cell.
- When the particle is ready to leave the cell, it will leave through one of the cell walls that has an outgoing flow direction. The choice between cell walls with an outgoing flow is made with a likelihood that is proportional to the outflows. If several particles are traced, the cloud will thus split up in proportion to the flow rates. Complete mixing in a cell is assumed.

In the work reported here, we use the classic way of moving the particle along the local velocity vector. Three performance measures are calculated, see Figure 1-2:

- Flow path length L [L]
- Advective travel time t_w [T]
- Flow-related transport resistance F [TL^{-1}]

Flow path length

The flow path length L [L] is calculated as:

$$L = \sum_l \delta l \tag{4-22}$$

where δl [L] is a step length along a flow path of l steps.

Travel time

In principle, the travel time t_w [T] is calculated as:

$$t_w = \sum_l \frac{\phi\, \delta l}{q} \tag{4-23}$$

where ϕ [-] is the kinematic porosity along a flow path of l steps, δl [L] is a step length along the flow path, and q [LT^{-1}] is the Darcy flux along the flow path. Inserting Equation 4-15 and Equation 4-17 into Equation 4-23, the travel time spent in a grid cell intersected by a single fracture may be written as:

$$(t_w)_f = \frac{(\phi_c)_f\, L_f}{(K_c)_f\, J_f} = \frac{(e_t)_f\, L_f}{T_f\, J_f} \tag{4-24}$$

where J_f is the hydraulic gradient [LL^{-1}]. That is, the travel time depends largely on the relationship between the fracture aperture and the fracture transmissivity.

[11] In SDM-Site Forsmark, the values of the random deviate were generated by means of a truncated normal distribution. This difference, normal vs. uniform, is considered insignificant in the work reported here.

Flow-related transport resistance

The flow-related transport resistance F [TL^{-1}] is a measure of the potential for retention and retardation of radionuclides along a flow path through the fractured bedrock. In a continuous porous media code such as DarcyTools, the flow-related transport resistance is defined as:

$$F = \sum_{l} \frac{a_r \delta l}{q} \tag{4-25}$$

where a_r [L^{-1}] is the flow wetted fracture surface area per unit volume of rock along a flow path of l steps, δl [L] is a step length along the flow path, and q [LT^{-1}] is the Darcy flux along the flow path. The values of a_r used in the work reported here are specified in Appendix B.

4.2.4 Exchange of dissolved solids

In DarcyTools, the exchange of dissolved solids between the fracture water and the matrix porewater is modelled with a one-dimensional multi-rate diffusion model /Haggerty and Gorelick 1995/. The diffusion process is represented by a series of discrete exchange rate coefficients, α_{min}-α_{max} [T^{-1}], where the time scale of the remotest diffusive exchange is $1/\alpha_{min}$. Another parameter governing the diffusion process in the model of /Haggerty and Gorelick 1995/ is the ratio between the diffusive and advective pore spaces, β [-]. In fractured crystalline rock, the matrix porosity is approximately 10-100 times greater than the kinematic porosity /Follin et al. 2005/.

The chosen range of values of the exchange rate coefficients not only affects the time scales but also the penetration depths of the multi-rate diffusion process. In the work reported here, ten exchangerate coefficients are used. The value of α_{min} is set to $4 \cdot 10^{-12}$ s^{-1}, which implies a time scale of approximately 8,000 years for the remotest diffusive exchange, and the value of β is set to 10, i.e. ten times more pore space in the matrix than in the fractures. Both settings are regarded as provisional. A somewhat more elaborated discussion is provided in Appendix D.

5 Model specifications

5.1 Studied cases

In addition to the five glacial cases (a)-(e) listed in Table 1-1, a temperate case without ice and permafrost is also studied. This allows for relative comparisons of the defined hydrogeological quantities and performance measures. In this work, the differences in Darcy flux (q) and water salinity (C) are looked at by computing the ratios q/q_{temp} and C/C_{temp} obtained from the flow solutions. The differences in advective travel time (t_w) and flow-related transport resistance (F) are looked at by comparing the cumulative distribution (probability) plots obtained from the particle tracking.

The essence of Table 1-1 is repeated in Table 5-1 and visualised in Figure 5-1, Figure 5-2 and Figure 5-3. The key "climate events" looked at in SR-Site are highlighted in *italics* in Figure 5-1, Figure 5-2 and Figure 5-3. These are:

- Temperate (used to produce scaled (normalised) entities for SR-Site),
- Glacial case without permafrost,
- Glacial maximum,
- Submerged,
- Permafrost,
- Glacial case with permafrost and a 2 km long tongue, and
- Glacial case with permafrost but no tongue.

5.2 Simulation methodology

5.2.1 Temperate climate conditions

Flow and salt transport

The governing equations for flow and salt transport are solved using fixed boundary conditions and initial conditions as applied in SDM-Site Forsmark /Follin 2008/. The initial and boundary conditions for the temperate case are shown in Table 5-2 and Table 5-3, respectively.

Transport (particle tracking)

The flow and salt transport solutions are fixed in time and particle tracking is performed. Particles are released at the 6,916 deposition hole positions.

Table 5-1. Overview of two scenarios, A and B, and the five studied cases (a)–(e). The cases are visualised in Figure 5-1 through Figure 5-3.

Case	Explanation
	A. Glacial climate conditions without Permafrost
(a)	NW-SE ice sheet movement
(b)	N-S ice sheet movement
(c)	Distorted permeability conditions based on rock mechanical information (THM)
	B. Glacial climate conditions with Permafrost
(d)	A 2 km long tongue of permafrost below the tip of the ice sheet
(e)	No tongue of permafrost below the tip of the ice sheet

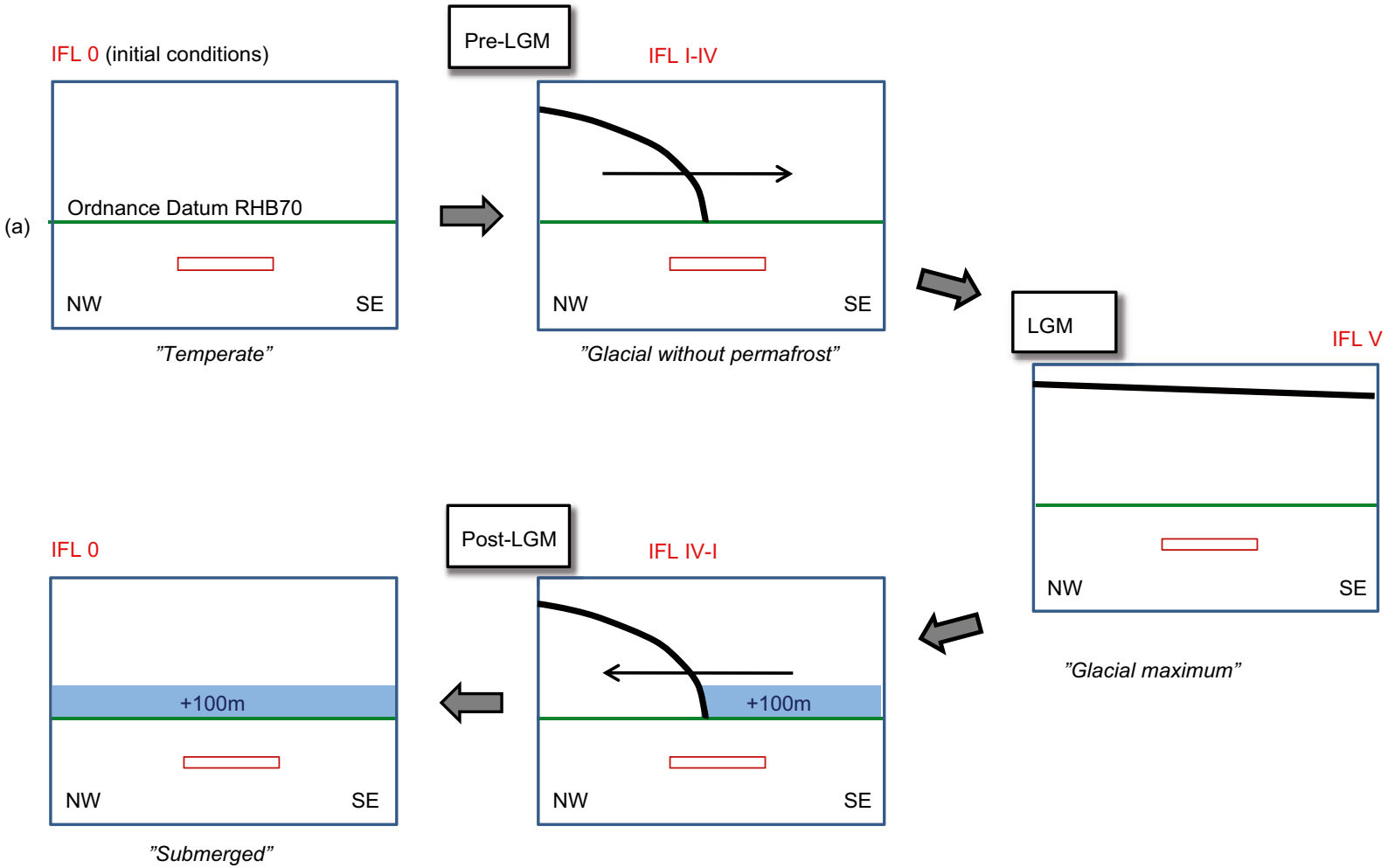

Figure 5-1. *Cartoons visualising the modelling associated with case (a), see Table 5-1. The deep repository is shown as a rectangle.*

A. GLACIAL CASES WITHOUT PERMAFROST (continued)

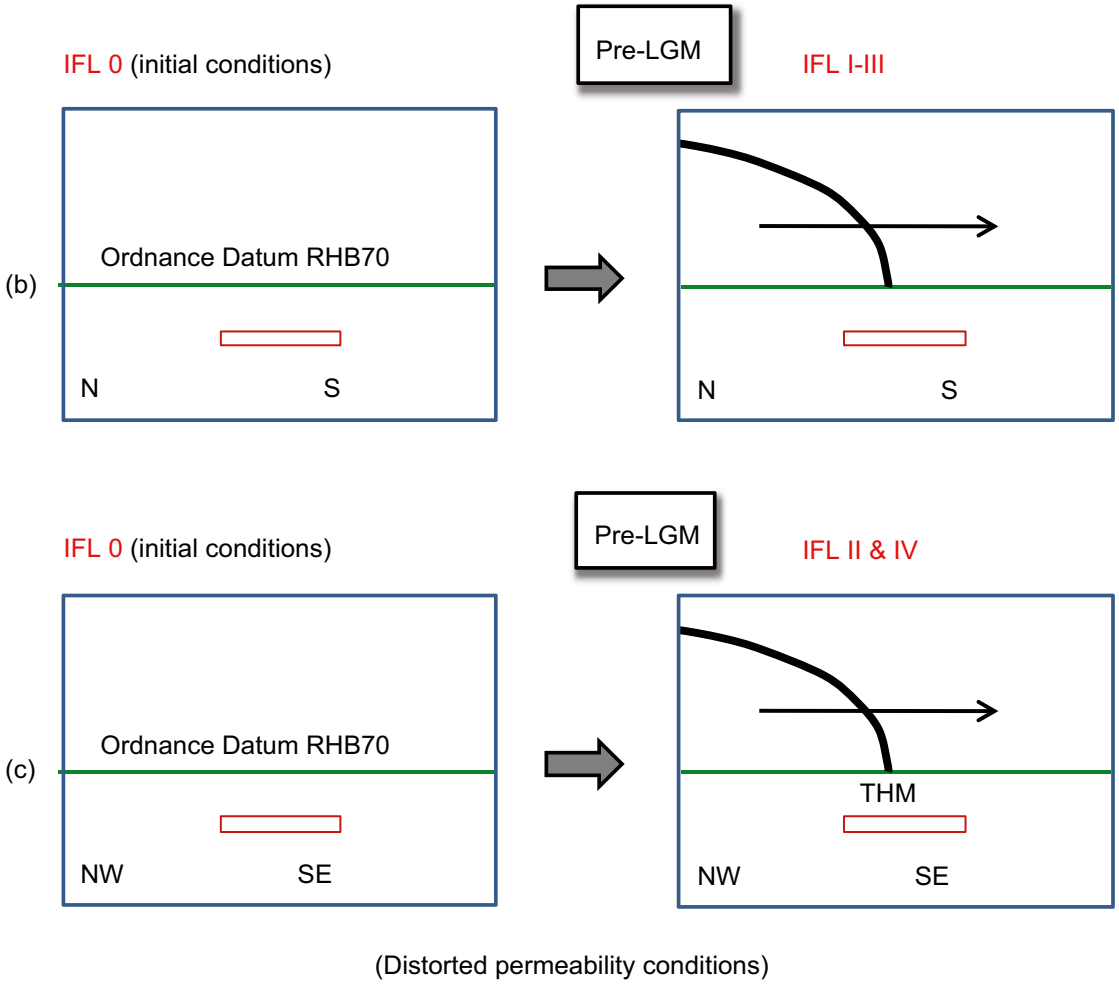

Figure 5-2. *Cartoons visualising the modelling associated with case (b) and case (c), see Table 5-1. The deep repository is shown as a rectangle.*

B. GLACIAL CASES WITH PERMAFROST

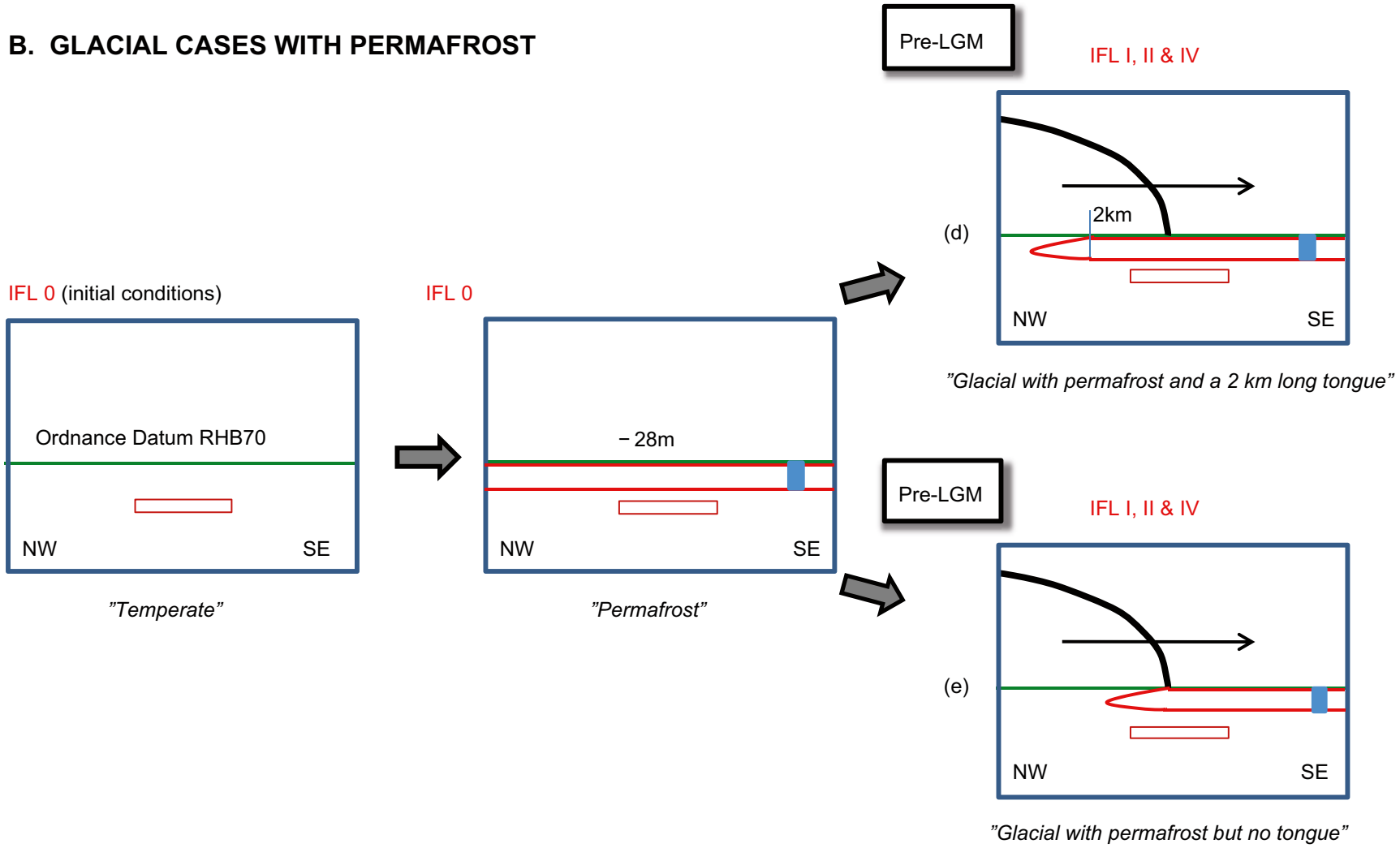

Figure 5-3. *Cartoons visualising the modelling associated with case (d) and case (e), see Table 5-1. The deep repository is shown as a rectangle.*

Output

Pressure (P), Darcy flux (q), salinity (C) at the five specified measurement localities (ML 1-5) surrounding the repository. Flow path length (L), travel time (t_w), and flow-related transport resistance (F) for each particle.

5.2.2 Glacial climate conditions without permafrost

Flow and salt transport

The flow and salt transport solutions derived for the temperate case are used as initial conditions together with the transient top boundary conditions shown in Figure 5-1, Figure 5-2 and Table 5-4. The solutions to the governing equations for flow and salt transport are saved for each ice-front location. During the LGM stage, the ice sheet profile addressed in case (a) was changed over approximately 17,000 years, see Section 1.3.1. During the retreat of the ice sheet margin, the sea level was raised from the present-day elevation to +100 m above the Swedish Ordnance Datum FRHB 70 causing submerged ground conditions in front of the margin, see Figure 5-1.

Transport (particle tracking)

See the corresponding paragraph in Section 5.2.1.

Output

See the corresponding paragraph in Section 5.2.1.

5.2.3 Glacial climate conditions with permafrost

Flow and salt transport

First, the flow and salt transport solutions derived for the temperate case are used as initial conditions to a simulation where the sea level elevation is displaced from the present-day elevation to –28 m below the Swedish Ordnance Datum, see Figure 5-3. Second, the flow and salt transport solutions to the shoreline displacement simulation are used as initial conditions to a simulation where a constant temperature at the ground surface of –4.5°C prevails over a period of 2,000 years. This boundary condition is applied across the entire model domain except where there are water bodies (taliks), where the temperature is set to +4°C. The topography is used to make informed judgements as to where taliks might occur. Table 5-5 and Table 5-6 show the initial and boundary conditions applied for the generation of permafrost. Third, the flow and transport solutions to the permafrost development simulation are used as initial conditions to a simulation where an ice sheet margin moves across the model domain, see Figure 5-3. The difference between case (d) and case (e) is accomplished by applying different boundary conditions beneath the tip of the ice sheet, cf. the description in Section 1.3. The transient boundary conditions for the glacial cases with permafrost are specified in Table 5-7.

Transport (particle tracking)

See the corresponding paragraph in Section 5.2.1.

Output

See the corresponding paragraph in Section 5.2.1.

Table 5-2. Initial conditions of the fracture water and matrix porewater salinities. (Modified after Figure 2-11 in /Follin 2008/.)

Region	Depth interval	Initial salinity
Target volume (Fracure domains FFM01, FFM0202 and FFM06)	Ground surface to –350 m	0%
	–350 m to –1,500 m	Linearly increasing to 7.2%
	Below –1,500 m	7.2%
Elsewhere	Ground surface to –500 m	0%
	–500 m to –2,300 m	Linearly increasing to 7.2%
	Below –2,300 m	7.2%

Table 5-3. Boundary conditions for the temperate case.

Boundary	Boundary conditions
Shoreline elevation	0 m RHB 70
Top boundary, land above sea	P=0 at ground surface; C=0
Top boundary, land below sea	P=g ρ_0 (sea depth); C=0%
Lateral (vertical) boundaries	∂P/∂x=∂P/∂y=0 and ∂C/∂x=∂C/∂y=0
Bottom boundary at –1,984 m	∂P/∂z=0; C=5.94% by weight outside target volume an 7.2% inside target volume

Table 5-4. Boundary conditions for the glacial cases without permafrost.

Boundary	Boundary conditions
Shoreline elevation	0 m RHB 70
Top boundary, land without ice	P=0 at ground surface; C=0
Top boundary, land below sea	Hydrostatic pressure: P=g ρ_0 (sea depth); C=0%
Top boundary, land below ice	P according to Equation 2-9; C=0%
Lateral (vertical) boundaries	∂P/∂x=∂P/∂y=0 and ∂C/∂x=∂C/∂y=0
Bottom boundary at –1,984 m	∂P/∂z=0; C=5.94% by weight outside target volume an 7.2% inside target volume

Table 5-5. Initial temperature conditions prior to the permafrost simulations.

Location	Temperature
At sea	0.1°C
On land	1.0°C
Depth gradient	0.015°C/m

Table 5-6. Boundary conditions for the generation of permafrost.

Boundary	Boundary condition
Shoreline elevation	–28 m RHB 70
Top boundary, land without ice	T=–4.5°C
Top boundary, taliks	T=+4°C
Top boundary, land below sea	T=+4°C
Lateral (vertical) boundaries	∂T/∂x=0; ∂T/∂y=0
Bottom boundary at –1, 984 m	q_{heat} = 0.0555 W/m^2

Table 5-7. Boundary conditions for the glacial cases with permafrost.

Boundary	Boundary conditions
Shoreline elevation	–28 m RHB 70
Top boundary, permafrost areas	P=0 at ground surface; C=0; T=–4.5°C
Top boundary, taliks	P=0 at talik water level; C=0; T=+4°C
Top boundary, unfrozen land Below sea: Below ice:	 P=g ρ_0 (sea depth); C=0 ; T=+4°C P according to Equation 2-9/; C=0 ; T=+0.01°C
Lateral (vertical) boundaries	∂P/∂x=0 , ∂C/∂x=0 , ∂T/∂x=0 ; ∂P/∂y=0 , ∂C/∂y=0 , ∂T/∂y=0
Bottom boundary at –1,984 m	∂P/∂z=0; q_{heat} = 0.0555 W/m^2 and C=5.94% by weight outside target volume and 7.2% inside target volume

5.3 Model domain, measurement localities and ice-front locations

A NW-SE orientation of the model domain is conceived to be the most appropriate orientation to study for an advancing ice sheet margin. Figure 5-4 shows the location of the NW-SE model domain studied in cases (a) and (c)-(e) and Figure 5-5 shows the location of the N-S model domain studied in case (b).

The NW-SE model domain is approximately 50 km long, 30 km wide and 2 km deep. The corresponding data for the N-S domain are approximately 40 km, 25 km and 2 km, respectively. Hence, a super-regional modelling approach is used. Examples of previous studies for SKB focusing on hydrogeological issues on a super-regional scale are, among others, /Follin and Svensson 2003, Holmén et al. 2003, Holmén 2008, Ericsson et al. 2006, Ericsson and Holmén 2010/.

The coordinates of the cell centre of each corner cell are shown in Table 5-8. The coordinates of the five measurement locations (ML 1-5) shown in Figure 1-4 are shown in Table 5-9.

The Roman numerals shown in Figure 5-4 indicate the positions of the studied ice-front locations (IFL I-IV) for the NW-SE model domain, see Table 5-10 for coordinates. Ice-front location II (IFL II) is positioned right above the repository. The corresponding information for the N-S model domain is shown in Figure 5-5 and Table 5-11.

Table 5-8. Cell centre coordinates of the model domain corner cells.

	NW-SE model domain (Figure 5-4)		N-S model domain (Figure 5-5)	
Corner	Coordinate (x,y) (DarcyTools)	Coordinate (x,y) (RT90)	Coordinate (x,y) (DarcyTools)	Coordinate (x,y) (RT90)
NW	(–21992, 18704)	(1604008, 6710704)	(-5000, 30000)	(1621000, 6722000)
NE	(–584, 40112)	(1625416, 6732112)	(19992, 30000)	(1645992, 6722000)
SW	(13336, –16656)	(1639336, 6675344)	(-5000, –10000)	(1621000, 6682000)
SE	(34776, 4784)	(1660776, 6696784)	(19992, –10000)	(1645992, 6682000)

Table 5-9. Coordinates of the measurement localities ML 1-5.

Measurement locality	Coordinate (x,y,z) (DarcyTools local)	Coordinate (x,y,z) (RT 90, RHB 70)
1	(4700, 7000, –465)	(1630700, 6699000,–465)
2	(5500, 8000, –465)	(1631500, 6700000,–465)
3	(7000, 9000, –465)	(1633000, 6701000,–465)
4	(7000, 7000, –465)	(1633000, 6699000,–465)
5	(4700, 9000, –465)	(1630700, 6701000,–465)

Table 5-10. Coordinates of ice-front locations I-IV for the NW-SE model domain. The ice front is oriented at 45 degrees trending NE-SW.

Ice-front location	Coordinate (x,y) (DarcyTools local)	Coordinate (x,y) (RT 90)
I	(-5300,0)	(1620700, 6692000)
II	(-2900, 0)	(1623100, 6692000)
III	(-500, 0)	(1625500, 6692000)
IV	(13000, 0)	(1639000, 6692000)

Table 5-11. Coordinates of ice-front locations I-III for the N-S model domain.

Ice-front location	Coordinate (x,y) (DarcyTools local)	Coordinate (x,y) (RT 90)
I	(-, 17150)	(-, 6709150)
II	(-, 8150)	(-, 6700150)
III	(-, 3950)	(-, 6695950)

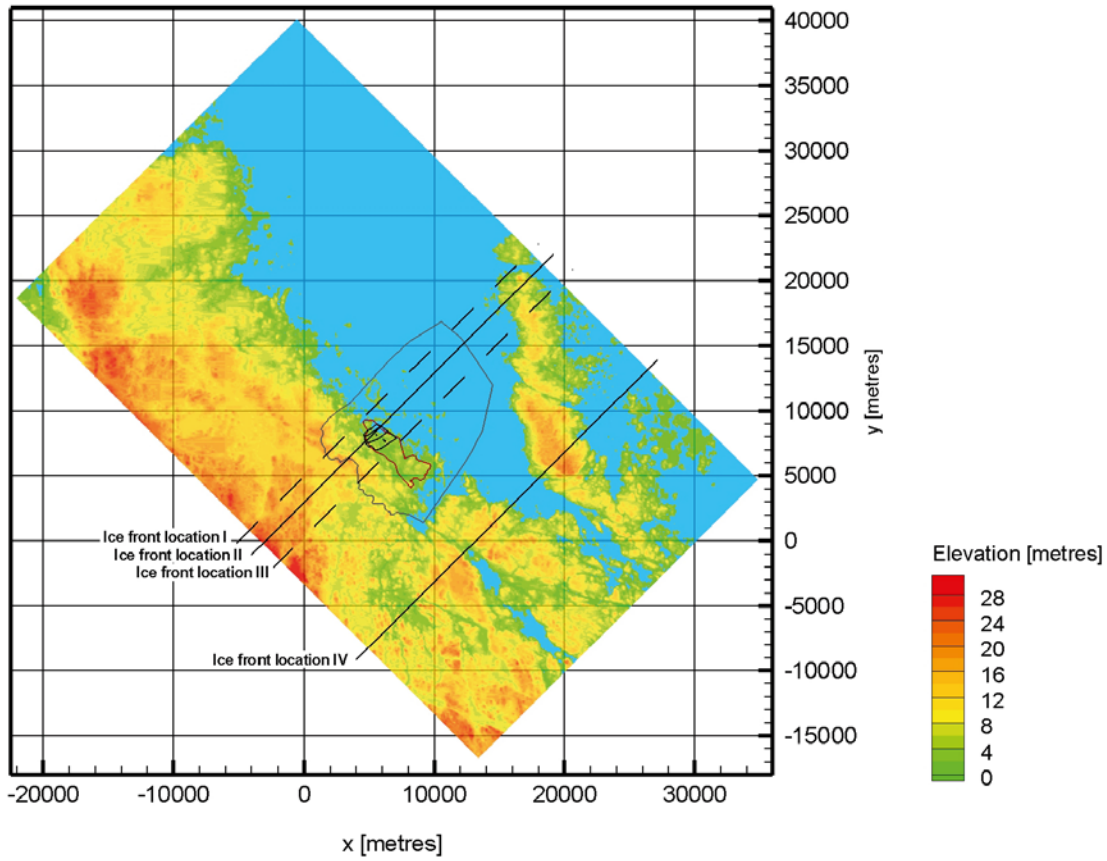

Figure 5-4. *Location of the model domain in cases (a), (c), (d) and (e). The map shows the present-day topography at Forsmark and the positions of the studied ice-front locations (IFL I-IV). The large polygon in the centre is the regional flow domain used in the groundwater flow modelling for SDM-Site Forsmark /Follin 2008/. The locations of the investigated candidate area (small elongated polygon) and the suggested final repository for spent nuclear fuel inside the candidate area are also shown. The y-axis points towards north.*

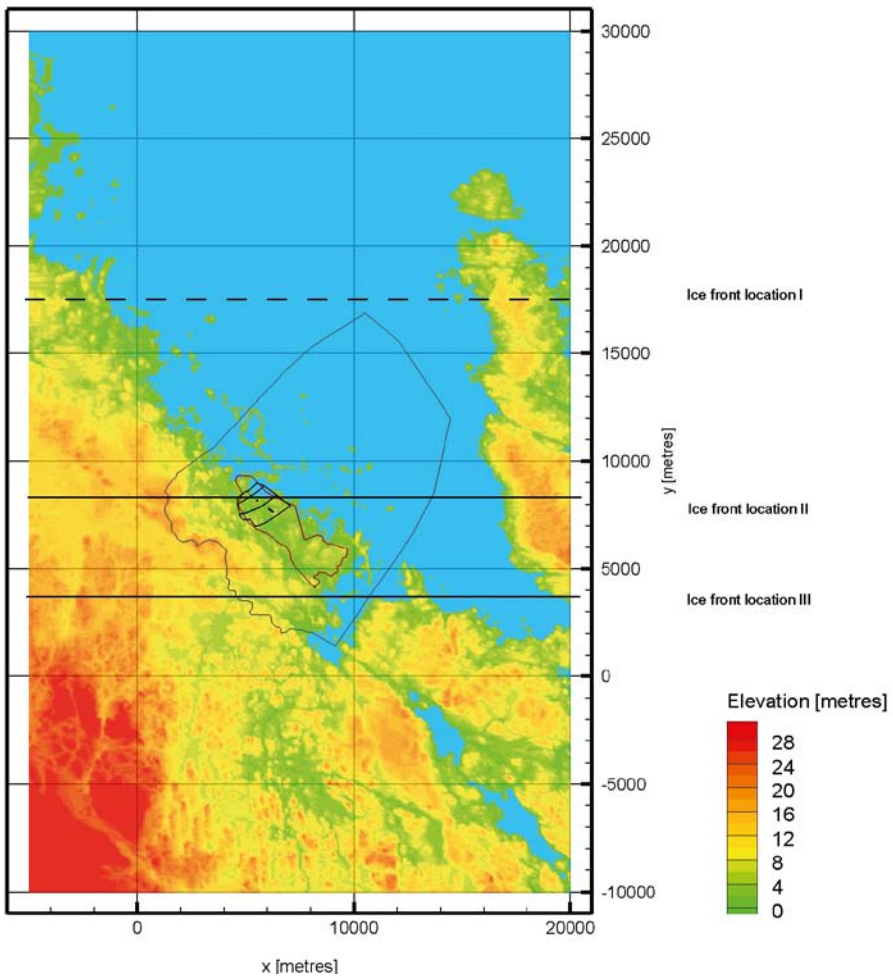

Figure 5-5. *Location of the model domain used in case (b). The map shows the present-day topography at Forsmark and the positions of the studied ice-front locations (IFL I-III). The polygons shown in the centre are explained The y-axis points towards north.*

5.4 Hydraulic properties

The geometry and hydraulic properties of discrete geological features in the bedrock such as deformation zones and sheet joints are the same as in SDM-Site. The data used here are imported from /Joyce et al. 2010/ and visualised in Figure 5-6, Figure 5-7 and Figure 5-8.

Concerning the stochastic hydrogeological properties of the fracture domains within the candidate area, the statistical distributions used here are identical to those used by /Joyce et al. 2010/ and /Svensson and Follin 2010/. However, a single realisation is studied in the work reported here, whereas /Joyce et al. 2010/ study several realisations and /Svensson and Follin 2010/ study two realisations.

The parameters and the parameter values used to generate a hydrogeological realisation of the fracture domains within the candidate area are listed in Appendix B, which also presents the hydraulic properties used for the bedrock outside the fracture domains and the deformation zones modelled deterministically in SDM-Site.

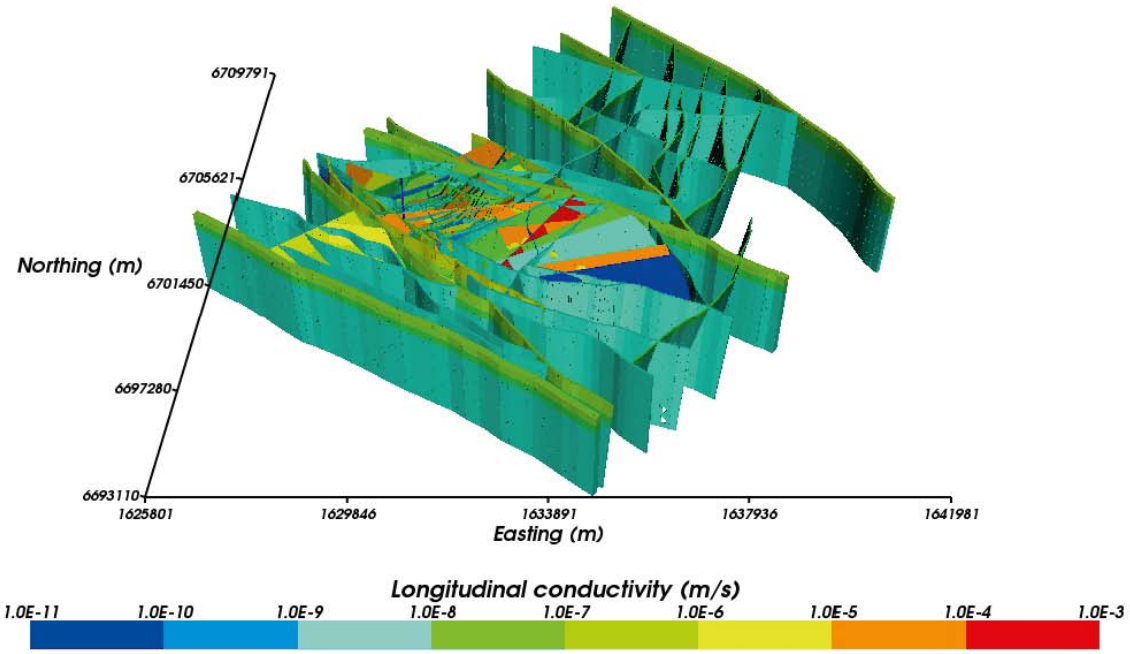

Figure 5-6. *Visualisation of regional and local scale deformation zones (HCD). Each zone is coloured by its hydraulic conductivity and drawn according to its inferred geological thickness (cf. the top image of Figure 3-5). The y-axis points towards north. (Source: Figure 4-1 in /Joyce et al. 2010/.)*

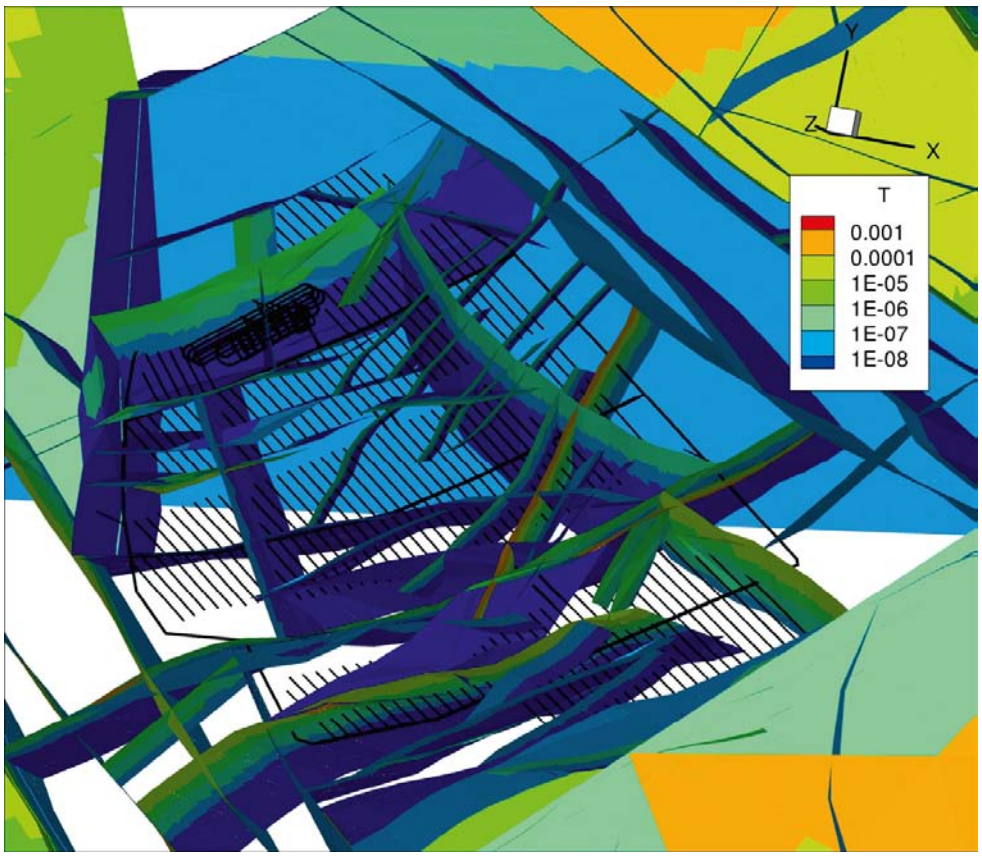

Figure 5-7. *Example view of the suggested repository layout at –465 m elevation and the deterministically modelled deformation zones nearby. (The sheet joints and some of the deformation zones are excluded for the sake of visibility.) The deformation zones were assigned homogeneous hydraulic properties with a depth dependency according to Equation 3-1. The y-axis points towards north. (Source: Figure 4-4 in /Svensson and Follin 2010/.)*

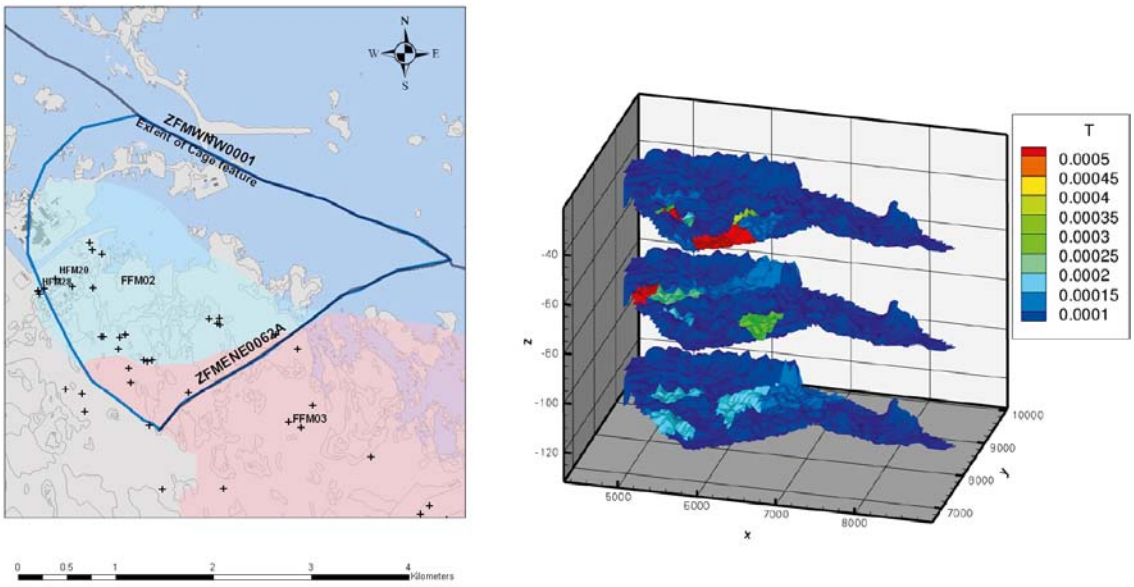

Figure 5-8. *The hypothesised lateral extent, elevations, and transmissivities of the discrete features modelled deterministically to represent the sheet joints observed in the shallow bedrock aquifer in the SDM work (cf. Figure 3-10 and Figure 3-11). The crosses in the left image mark the positions of percussion- and core-drilled boreholes for which transmissivity measurements were available. The bluish/greenish area in the left hand image represents fracture domain FFM02 and the pinkish area represents fracture domain FFM03. (Source: Figure 5-17 in /Follin 2008/.)*

The grid cell hydraulic properties of the uppermost 20 m of the model domain and the minimum values of the hydraulic properties below 20 m depth are shown in Table 5-12 and Figure 5-9.

Table 5-12. Grid cell hydraulic properties applied in this work in the uppermost 20 m of the model domain and the minimum values allowed below this depth. (Modified after Table 4-1 in /Svensson and Follin 2010/.)

Grid cell property	Depth interval	Value
Hydraulic conductivity K_c [m/s]	< 20 m depth	$K_{c,h} = \max \begin{cases} 1 \cdot 10^{-7} \\ 5 \cdot 10^{-3}\, 10^{-Depth/3} \end{cases}$ $K_{c,v} = 1 \cdot 10^{-6}$
	≥ 20 m depth	$K_{c,h} \geq 3 \cdot 10^{-11}$ $K_{c,v} \geq 3 \cdot 10^{-11}$
Kinematic porosity ϕ_c [-]	< 20 m depth	$\phi_c = \max \begin{cases} 1 \cdot 10^{-3} \\ 5 \cdot 10^{-2}\, 10^{-Depth/20} \end{cases}$
	≥ 20 m depth	$\phi_c \geq 1 \cdot 10^{-5}$
Specific storage $S_{s,c}$ [m^{-1}]	≥ 0 m depth	$S_{s,c} = 1 \cdot 10^{-9}$

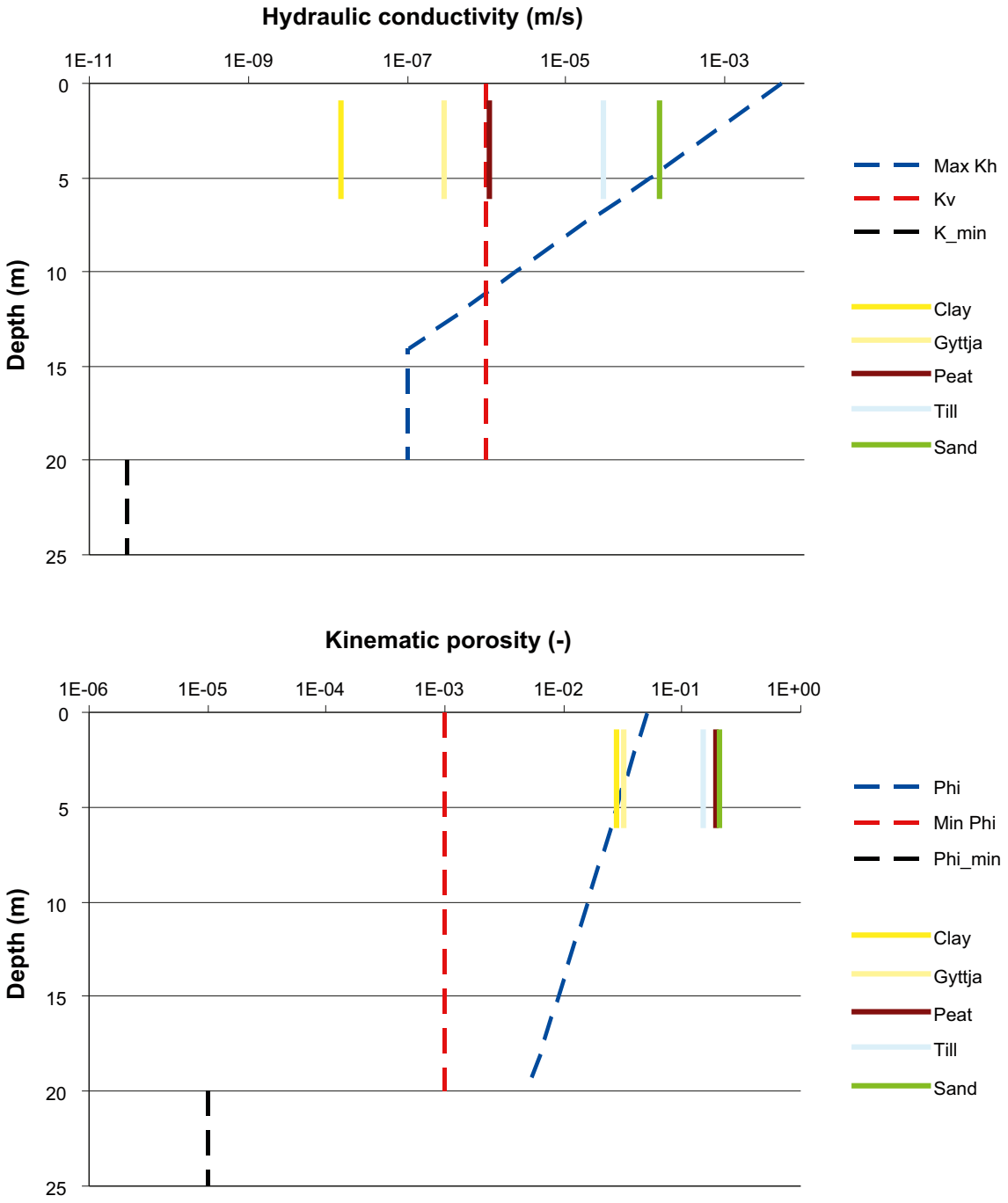

Figure 5-9. *The blue and red dashed lines show the values used in this work to simulate the hydraulic properties of the Quaternary deposits and the uppermost bedrock, i.e. above 20 m depth. The black dashed lines represent the minimum values of hydraulic properties of the non-fractured parts of the bedrock below this depth (cf. Table 5-12). The solid lines represent the values shown in Table 3-5 and Table 3-6.*

Figure 5-10 shows an example of the effect of freezing on the permeability using the algorithm described in Appendix A. This range of reduction is similar to the reduction simulated by /Hartikainen et al. 2010/.

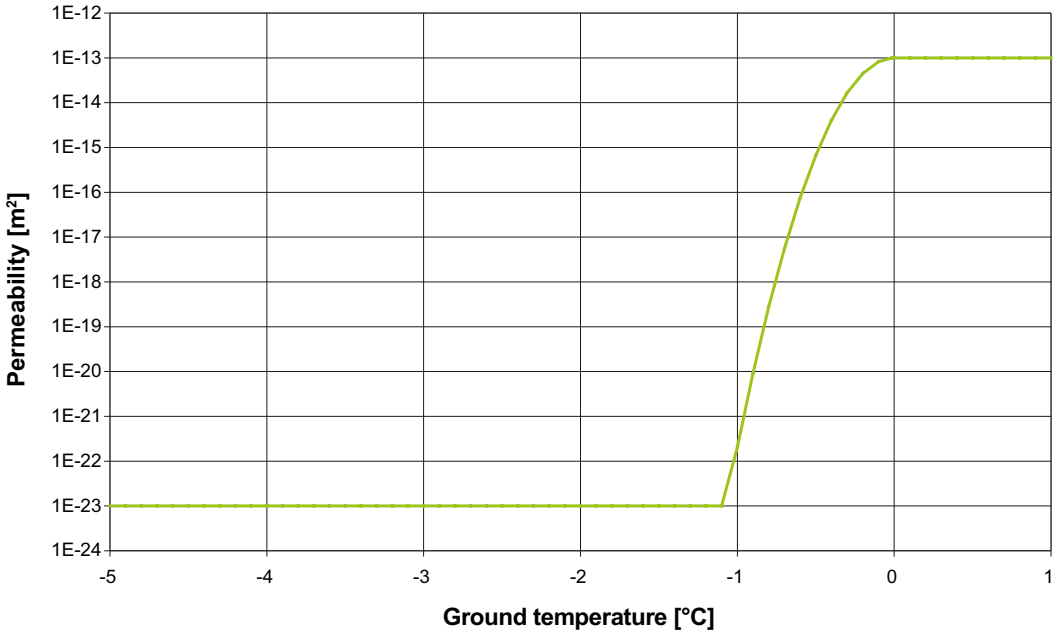

Figure 5-10. *An example of how the permeability depends on the temperature in the work reported here.*

5.5 Thermal properties

The values used in the flow simulations are shown in Table 5-13. The properties assigned are based on estimated mean values taken from /Hartikainen et al. 2010/ and /Sundberg et al. 2009/.

5.6 Computational grid

The model domain is discretised by an unstructured grid. Close to ground surface, the 50 m digital elevation model[12] is refined to fit a cell size of 32 m in the horizontal directions. The resolution of the topographic variations in the vertical direction is set to 2 m. The bottom of the model domain is located at an elevation of –2,048 m. The thickness of the bottom cell layer is constant throughout the model domain and set to 128 m. (The elevation of the pressure node in bottom cell layer is located at –1,984m [=–2,048 m+(128 m/2)].)

Within the area specified in Table 5-14, the cell size is $(32\ m)^3$ (cf. the area shown in Figure 1-4). Far away from this area, the largest cell size is $(512\ m)^3$. In between, a varying cell size is used. In total, the model domain consisted of 9.1 million cells.

Table 5-13. Thermal properties.

Property	Value
Thermal conductivity [W/mK]	3.45
Heat capacity [J/m³K]	$2.07 \cdot 10^6$

Table 5-14. Corner coordinates of the area shown in Figure 1-4.

Corner	Coordinate (x,y) (DarcyTools local)	Coordinate (x,y) (RT90)
NW	(4000, 10000)	(1630000, 6702000)
NE	(8000, 10000)	(1634000, 6702000)
SW	(4000, 6000)	(1630000, 6698000)
SE	(8000, 6000)	(1634000, 6698000)

[12] Brydsten L, 2009. Data set delivery 50 m DEM of regional extent (see Appendix C).

5.7 Permeability at the five measurement localities

Measurement localities ML 1-5 are located nearby the repository in regions with different hydraulic properties. Figure 5-11 shows a close-up view around measurement locality ML 2. The hydraulic properties of the grid cells containing red dots are affected by the hydraulic properties of the deformation zones nearby as a result of the chosen discretisation.

Figure 5-12 shows the positions of the five measurement localities (ML 1-5) and the permeability field at repository depth. Figure 5-13 shows a close-up view around each locality.

- ML 1 is placed close to a NW-SE trending and steeply dipping deformation zone (NW0003). The maximum permeability of the grid cell hosting ML 1 is $6 \cdot 10^{-16}$ m^2.
- ML 2 is placed in the centre of the target volume and is not affected by any deformation zone. The maximum permeability of the grid cell hosting ML 2 is $6 \cdot 10^{-18}$ m^2.
- ML 3 is placed not far from the regional Singö deformation zone /Follin 2008/. The maximum permeability of the grid cell hosting ML 3 is $2 \cdot 10^{-16}$ m^2.
- ML 4 is placed within a SW-NE trending and gently dipping deformation zone (A2). The maximum permeability of the grid cell hosting ML 4 is $2 \cdot 10^{-14}$ m^2.
- ML 5 is placed at the north-west periphery of the target volume. The maximum permeability of the grid cell hosting ML 5 is $6 \cdot 10^{-16}$ m^2.

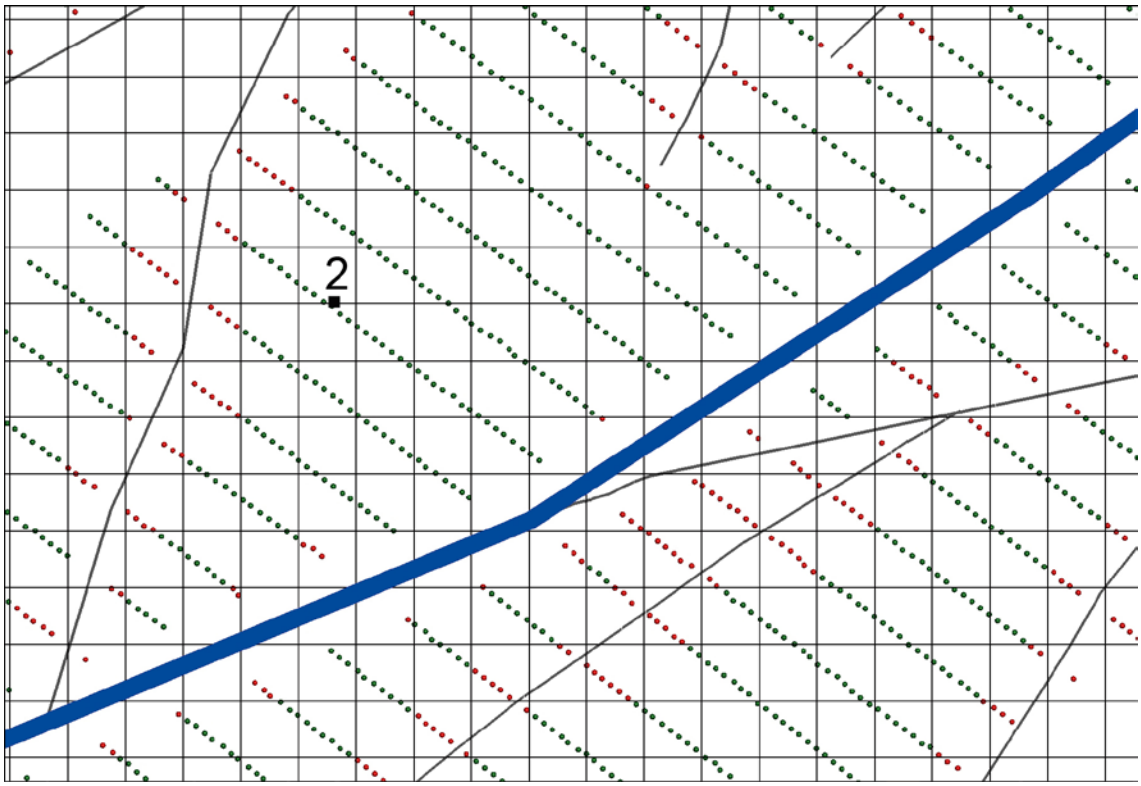

Figure 5-11. *Horizontal view of the computational grid around measurement locality number 2. The resolution of the computational grid adjacent to the repository is 32 m. The transportation tunnels are shown as blue lines and the deposition hole positions as dots. The dots are coloured red or green depending on if they are positioned within grid cells that also contain one or several intercepts with the deterministically modelled deformation zones (red dot) or not (green dot). That is, the hydraulic properties of the cells with red dots are affected by the hydraulic properties of the deformation zones as a result of the chosen discretisation. The deformation zones are here visualised as trace lines (scan lines without geological thickness).*

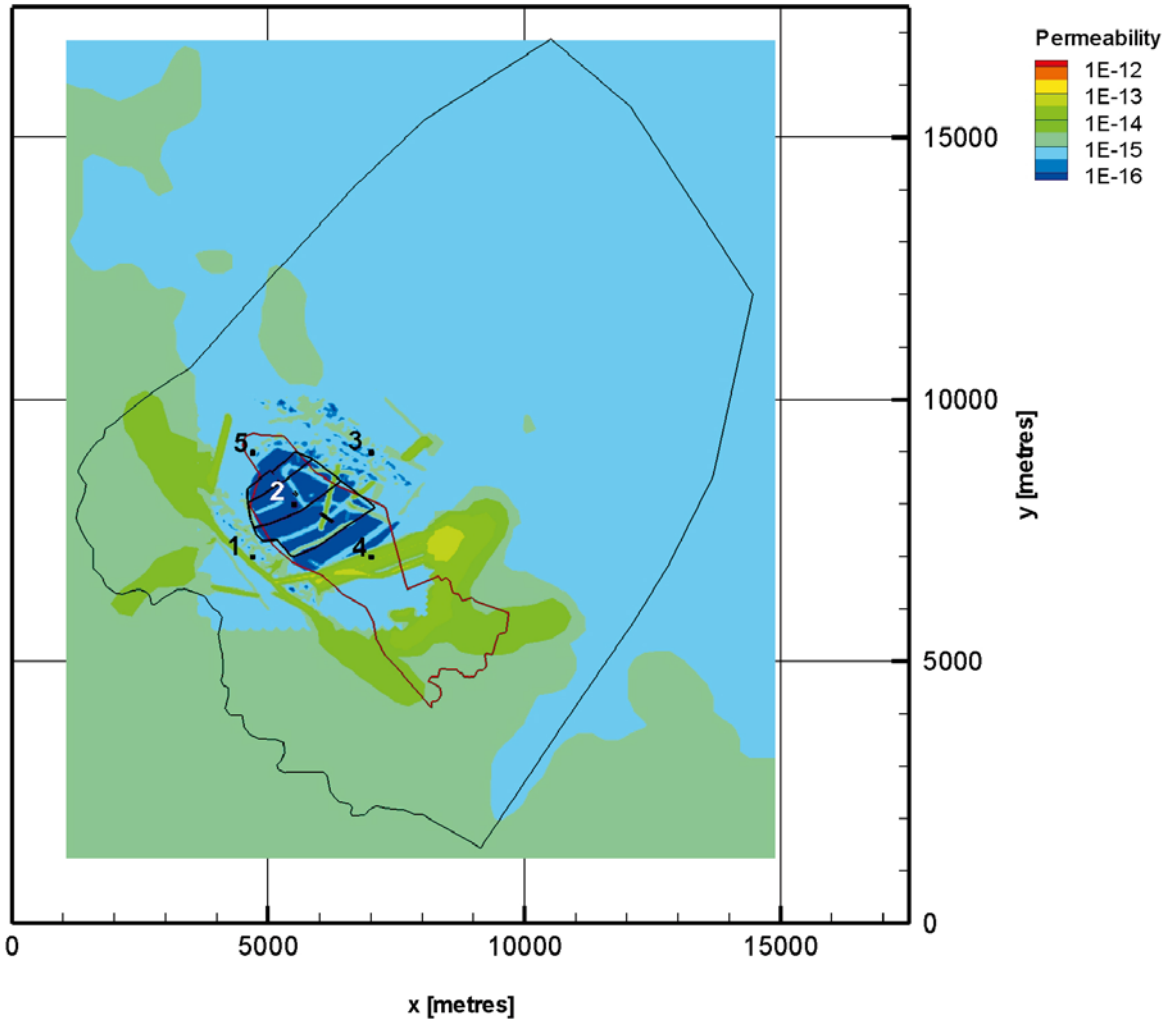

Figure 5-12. *Horizontal view showing the five measurement localities (ML 1-5) and the permeability field at repository depth (elevation –465 m). The large polygon shows the regional flow domain used in SDM-Site /Follin 2008/. The elongated polygon inside the large polygon is the candidate area. The deep repository is located in the north-western part of the candidate area. The y-axis points towards north.*

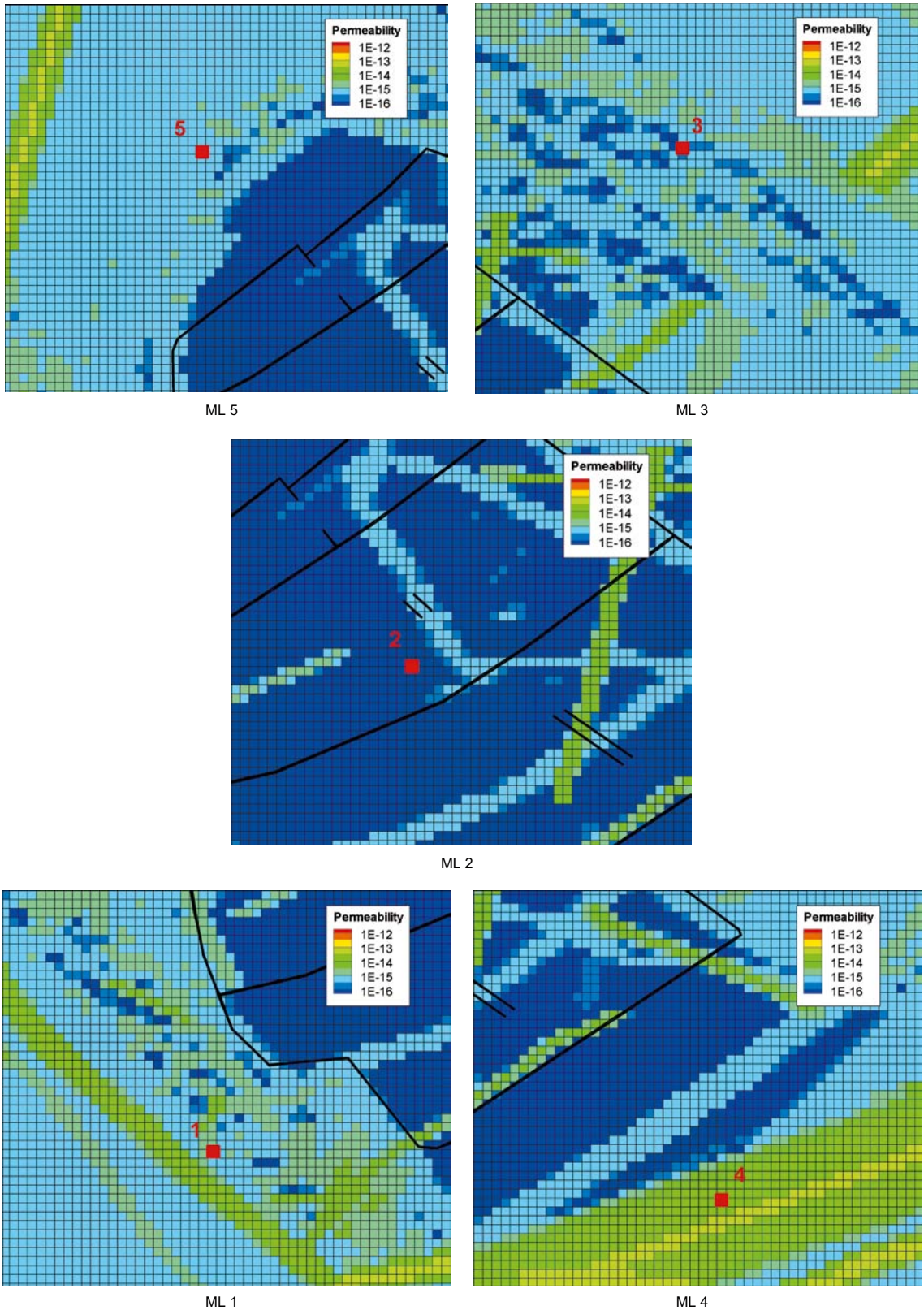

Figure 5-13. *Horizontal views of the permeability field around the five measurement localities (ML 1-5). Maximum grid cell permeability values are shown.*

6 Results for SR-Site

6.1 Introduction

Appendices E-G present detailed information from the groundwater flow simulations of the temperate case, the glacial case without permafrost and the glacial case with permafrost in a tabular format. Below, key findings for SR-Site are summarised.

6.2 Temperate climate conditions

The results from the temperate case simulation reported in Appendix E are not intended for use in SR-Site as such but are aimed at (i) providing initial conditions for the glacial simulations, and (ii) producing scaled (normalised) entities of the modelling results obtained from the glacial simulations. Further, as the results from glacial simulations are exported to other model applications within SR-Site, e.g. /Joyce el al. 2010, Sidborn et al. 2010, Salas et al. 2010/, a judgment of the confidence that could be placed in the underpinning temperate case simulation is needed.

Figure 6-1 shows a comparison of the simulated Darcy fluxes at the 6,916 deposition hole positions during temperate climate conditions using two types of flow concepts, Discrete Fracture Network (DFN) and Equivalent Continuous Porous Medium (ECPM). The red curve shows the results obtained from the simulations conducted with DarcyTools (ECPM) on a super-regional scale, and the blue curve shows the results from the simulations conducted with ConnectFlow (DFN) on a repository scale. The results are in a reasonable agreement given the differences in flow concept and model scale.

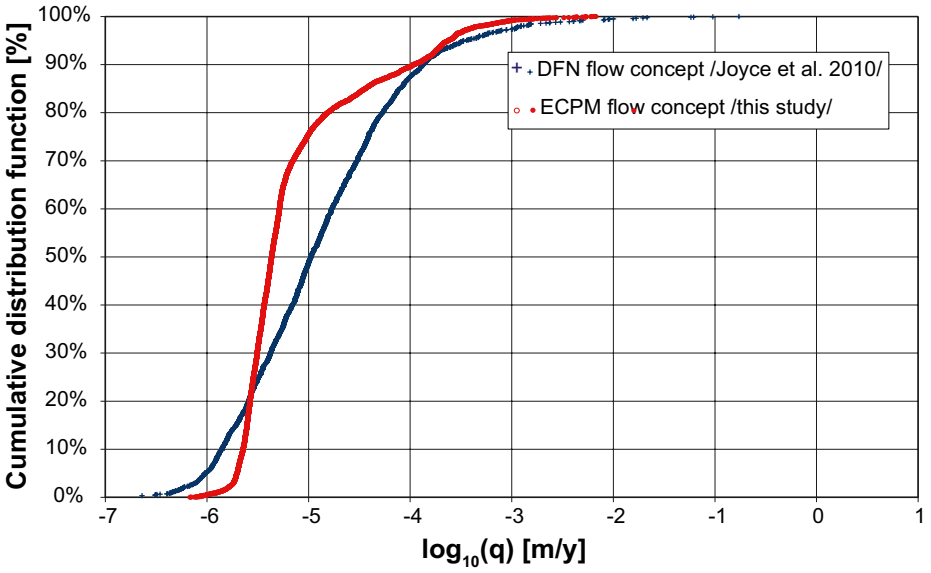

Figure 6-1. *Cumulative distribution function plot of the Darcy fluxes at 6,916 deposition hole positions during temperate climate condition for two different flow modelling concepts, Discrete Fracture Network (DFN) and Equivalent Continuous Porous Medium (ECPM). The result from /Joyce et al. 2010/ only includes those deposition hole positions that have particles successfully reaching the model top boundary.*

6.3 Glacial climate conditions

The key analyses with relevance for SR-Site performed are:

- **Hydrogeological evolution.** The changes in Darcy flux (q) and advective (fracture) water salinity (C) at repository depth relative to temperate climate conditions (q_{temp} and C_{temp}) are simulated on a super-regional scale. To a lesser extent, the exchange of salt between the advective (fracture water) salinity and diffusive (matrix porewater) salinity is also looked at. It is noted that groundwater chemistry is here represented by salinity alone.
- **Recharge and discharge locations in the biosphere.** The recharge and discharge locations are identified using forward and backward particle tracking from positions representing the deposition hole locations within the repository footprint. The particle tracking is performed for steady-state velocity fields representing different ice front locations relative to the location of the repository.
- **Performance measures.** The hydrogeological performance measures of interest in SR-Site are the Darcy flux (q) at each deposition hole location, and the flow-related transport properties along flow paths from the deposition hole locations, i.e. the advective travel time (t_w) and the flow-related transport resistance (F). In principle, these are directly obtained from the super-regional model for all ice front locations. However, the repository structures are not explicitly included in the super-regional model, and hence results for the different release paths from a repository considered in SR-Site are not obtained from the work reported here. By transferring boundary conditions from the super-regional scale model to the combined repository-scale and site-scale models of /Joyce et al. 2010/, where the repository is included, all performance measures during glacial conditions needed for subsequent radionuclide transport calculations in SR-Site are obtained. For the sake of future comparisons in SR-Site, the cumulative density function plots of the Darcy flux and flow-related transport resistance obtained from the super-regional model are shown here for the glacial case without permafrost.
- **Site related variants.** Some properties of the site, with specific relevance to glacial conditions, as well as the glacial conditions related to the glacial climate are uncertain. The impacts of alternative parameterisations related to these issues are assessed in order to judge their importance.

Hydrogeological evolution

Permafrost is a key process to consider as it reduces the permeability of subsurface materials to water flux. Permafrost does not develop instantaneously, but its development is a transient process. The performance of the freezing algorithm used to modify Holocene hydraulic conductivity values as a function of temperature is illustrated in Figure 6-2. The input to the permafrost model is obtained from the ground surface temperature time series described in /SKB 2010/.

A discontinuous permafrost layer is considered in the work reported here, which implies that the permafrost layer contains more or less unfrozen sections depending on the local boundary conditions and material properties. Probable locations for taliks are estimated from the forecasted landscape development carried out in the SR-Site project based on the shoreline displacement at Forsmark.

As the speed of the ice sheet margin during glaciation (50 m/y) is greater than the rate of the thawing of the permafrost layer, a tongue of trapped permafrost is created close to the ice sheet margin, cf. Figure 5-3. Figure 6-3 suggests insignificant differences in Darcy flux between the two cases of permafrost conditions studied at the ice sheet margin, i.e. cased (d) and (e). It is noted that the oscillations near the peak in Figure 6-3 reflect transient effects at the top boundary due to the transient hydraulic properties of the permafrost.

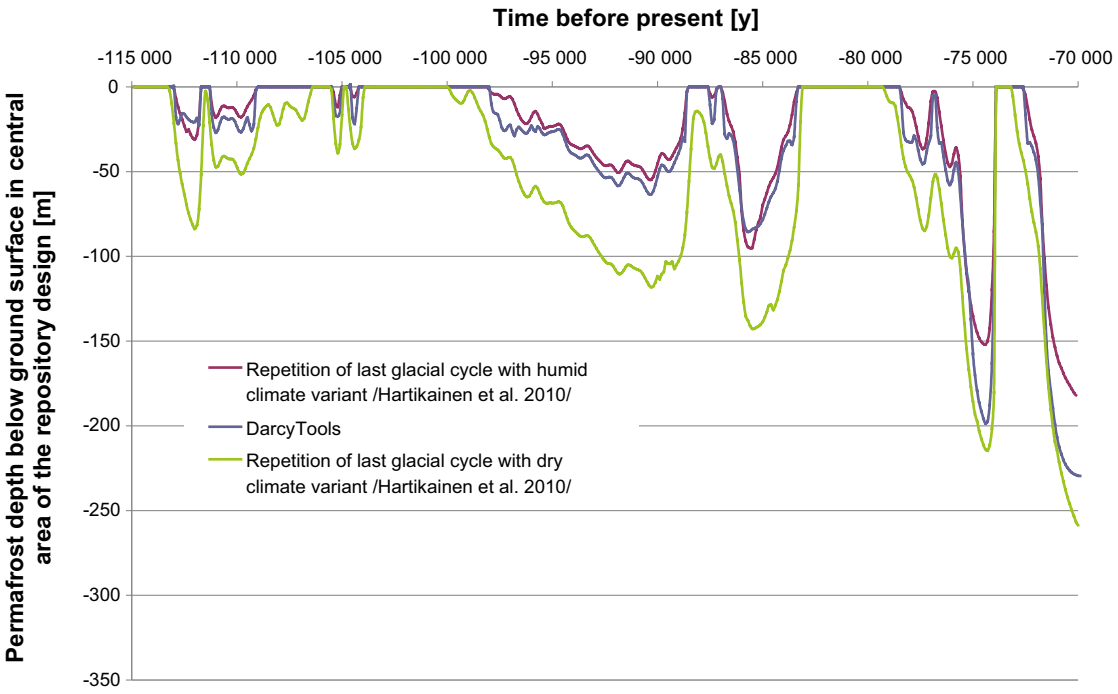

Figure 6-2. *Permafrost depth simulated with DarcyTools in comparison with the two main cases in /Hartikainen et al. 2010/.*

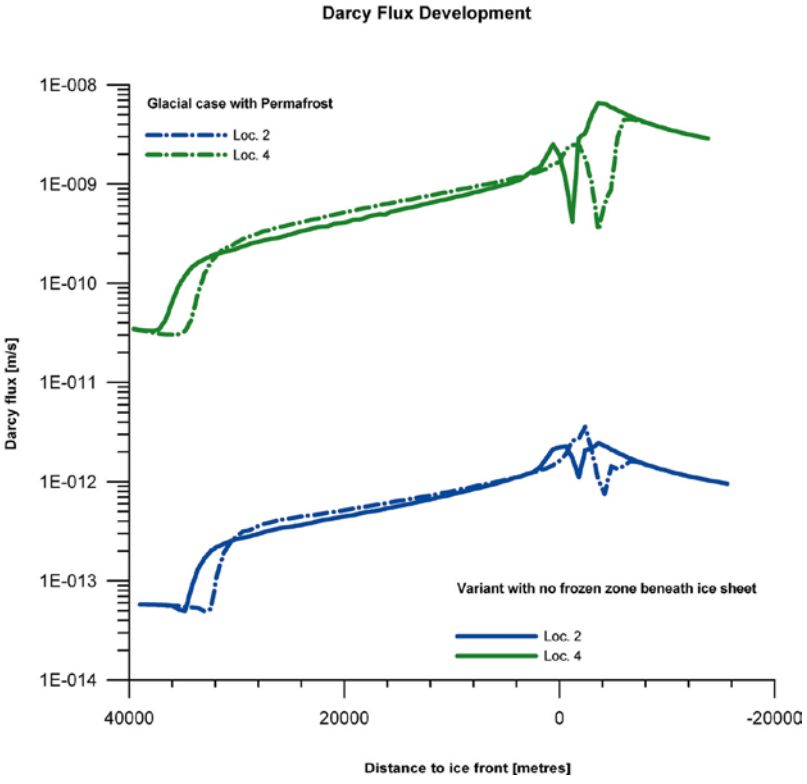

Figure 6-3. *Comparison of the Darcy flux at ML 2 and ML 4 for two the permafrost models studied; case (d) Glacial case with permafrost and a 2 km long tongue of permafrost behind the ice sheet margin (dashed lines), and case (e) Glacial case with permafrost but no tongue of permafrost (Solid lines). Positive distance values mean that the ice sheet margin has not yet arrived to the measurement locations.*

Figure 6-4 shows Darcy fluxes for a NW-SE vertical cross-section through the potential repository area. Three cases are shown. The upper most cross-section represents temperate conditions (IFL 0). The cross-section in the middle represents an advancing ice sheet margin at IFL II without permafrost in the periglacial area. The bottom most cross-section represents an advancing ice sheet margin at IFL II with permafrost conditions in the periglacial area.

Figure 6-5 shows the salinity field for a NW-SE vertical cross-section through the potential repository area. Three cases are shown. The upper most cross-section represents temperate conditions (IFL 0). The cross-section in the middle represents an advancing ice sheet margin at IFL II without permafrost in the periglacial area. The bottom most cross-section represents an advancing ice sheet margin at IFL II with permafrost conditions in the periglacial area. Figure 6-6 shows the same salinity fields but on a horizontal plane placed at –465 m through the target volume.

In summary, Figure 6-4 and Figure 6-5 show that the hydraulic pressures at the bottom of the ice sheet distort the temperate conditions and causes glacial meltwater to recharge and flush the advective system. In effect, the more saline water in the fractures is pushed forwards and upwards (upconing).The reason for the, in general, higher salinity near the ground surface for the glacial case with permafrost is that the permafrost hinders discharge at the top boundary (cf. the bottom most image in Figure 6-4), except where taliks (unfrozen ground) occur.

The changes in Darcy flux and fracture water salinity during the simulated period (IFL 0 → IFL V → IFL 0) are monitored at the five measurement localities ML 1-5 and expressed as ratios relative to the corresponding initial, temperate values, see Figure 6-7 and Figure 6-9. It is recalled that the term temperate is not to be understood as 2000 AD, but rather as a time slot in the future when the ice sheet margin is close to, but still outside, the flow model domain, i.e. IFL 0.

In Figure 6-7, it is seen that the Darcy flux increases dramatically during the two ice front passages. The immediate shift to low and constant values at the start of the period of complete ice coverage is an artifact of the instantaneous shift in ice sheet gradient at the same moment. In reality, a more smooth transition is expected. For the glacial case with permafrost, slightly different shapes of the curves are obtained during glacial advance, see Figure 6-8. However, for the remaining parts of the cycle, the curves are identical to those shown in Figure 6-7 as there is no permafrost during these periods.

The normalised change in the salinity development is shown in Figure 6-9. The glacial passage during advance (pre-LGM) is characterised by an initial upconing followed by an out flushing resulting in lower salinities than during the initial temperate conditions. However, during the subsequent stage, i.e. when the site is completely covered by the ice sheet (LGM), a gradual increase in fracture water salinity at repository depth occurs. This gain of the "salt water interface" is due to an accommodation of the buoyancy forces to the very weak top boundary condition of an almost uniform ice sheet thickness, and to the slow, but continuous advective transport of salt from below. (It is recalled that the fracture water salinity at great depth is assumed to be undisturbed (fixed) at all times in the flow model. The support for this assumption is presented in Appendix D.

The glacial passage during retreat (post-LGM) is also characterised by an upconing and flushing event, but the effects are considerable smaller than during the advance. The reason for this is twofold; (i) the speed of the retreating ice sheet margin is twice as fast as the speed of the advancing ice sheet margin (100 m/y versus 50 m/y), and (ii) the area in front of the retreating ice sheet margin is submerged. These conditions reduce the duration and the magnitude of the hydraulic gradient across the ice sheet margin significantly.

Figure 6-10 shows the simulated difference in flushing as a function of the average speed of the retreating ice sheet margin. A retreat speed of 300 m/y yields less flushing than a retreat speed of 100 m/y. It is noted that the average speed of the retreating ice sheet margin considered for the reference climate evolution in /SKB 2010/ is 300 m/y; i.e. three times the speed considered in the work reported here. Second, the retreating ice sheet profile considered is significantly thicker and more steep at the ice sheet margin than the ice sheet profile considered for the reference climate evolution in /SKB 2010/, see Figure 2-5 in Section 2.4. Thus, the conditions considered here exaggerate the impact of the ice sheet; still the results indicate that the fracture water salinities are more or less restored during the simulated period (IFL 0 → IFL V → IFL 0). In conclusion, low fracture water salinities, i.e. dilute conditions, are mainly found in conjunction with the ice front passages. The results presented in Figure 6-9 indicate that fracture water salinities reach values below ten per cent of the values at temperate conditions for a limited period of time only.

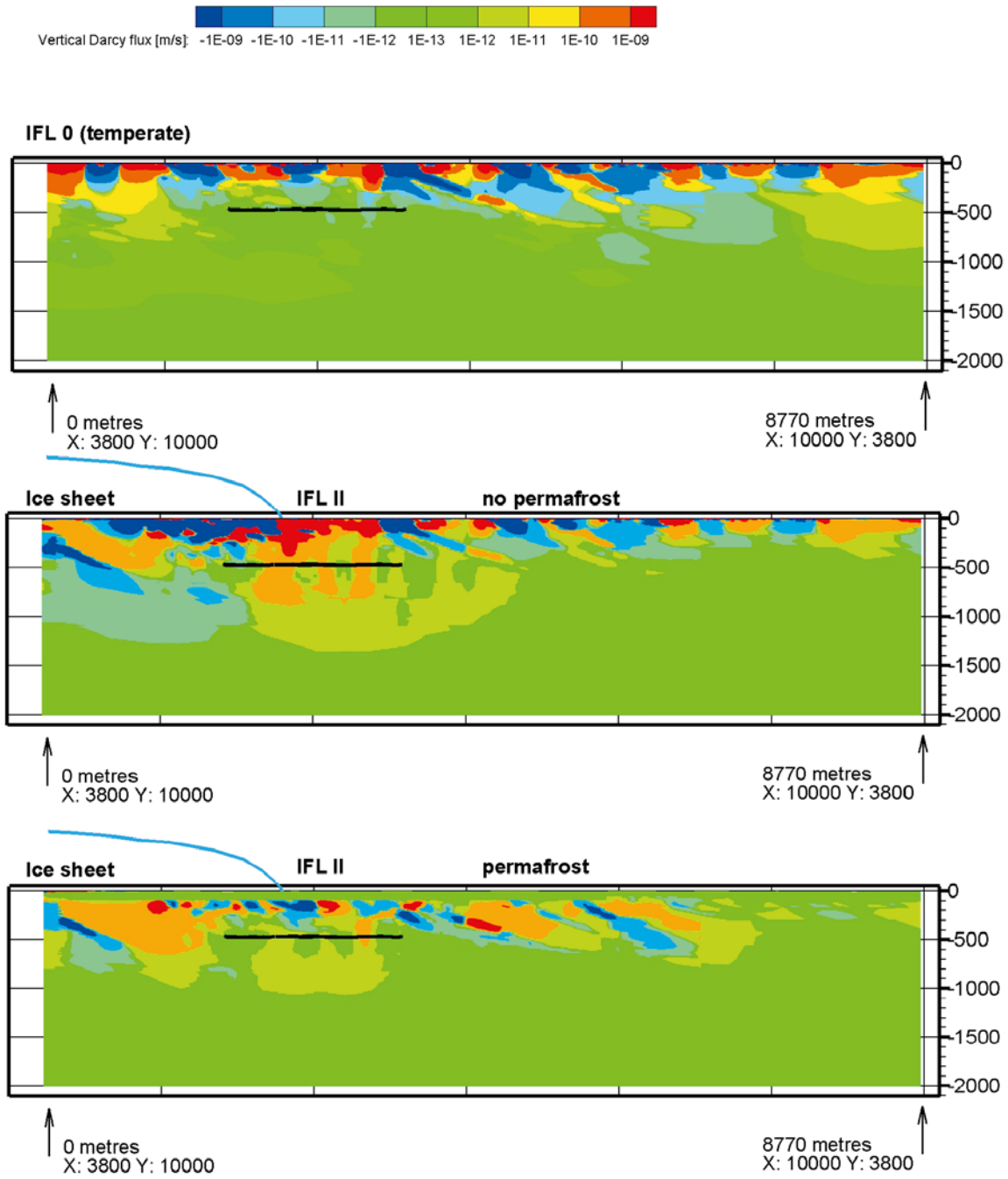

Figure 6-4. *Top: Darcy flux during temperate conditions mapped on a cross-section parallel with direction of the ice sheet movement during glaciation. The images in the middle and at the bottom show the Darcy fluxes when the ice sheet margin is at IFL II for the glacial case without permafrost (middle) and for the glacial case with permafrost (bottom). Negative values represent downward directed fluxes. The position of the ice sheet profile is illustrated with a blue curve.*

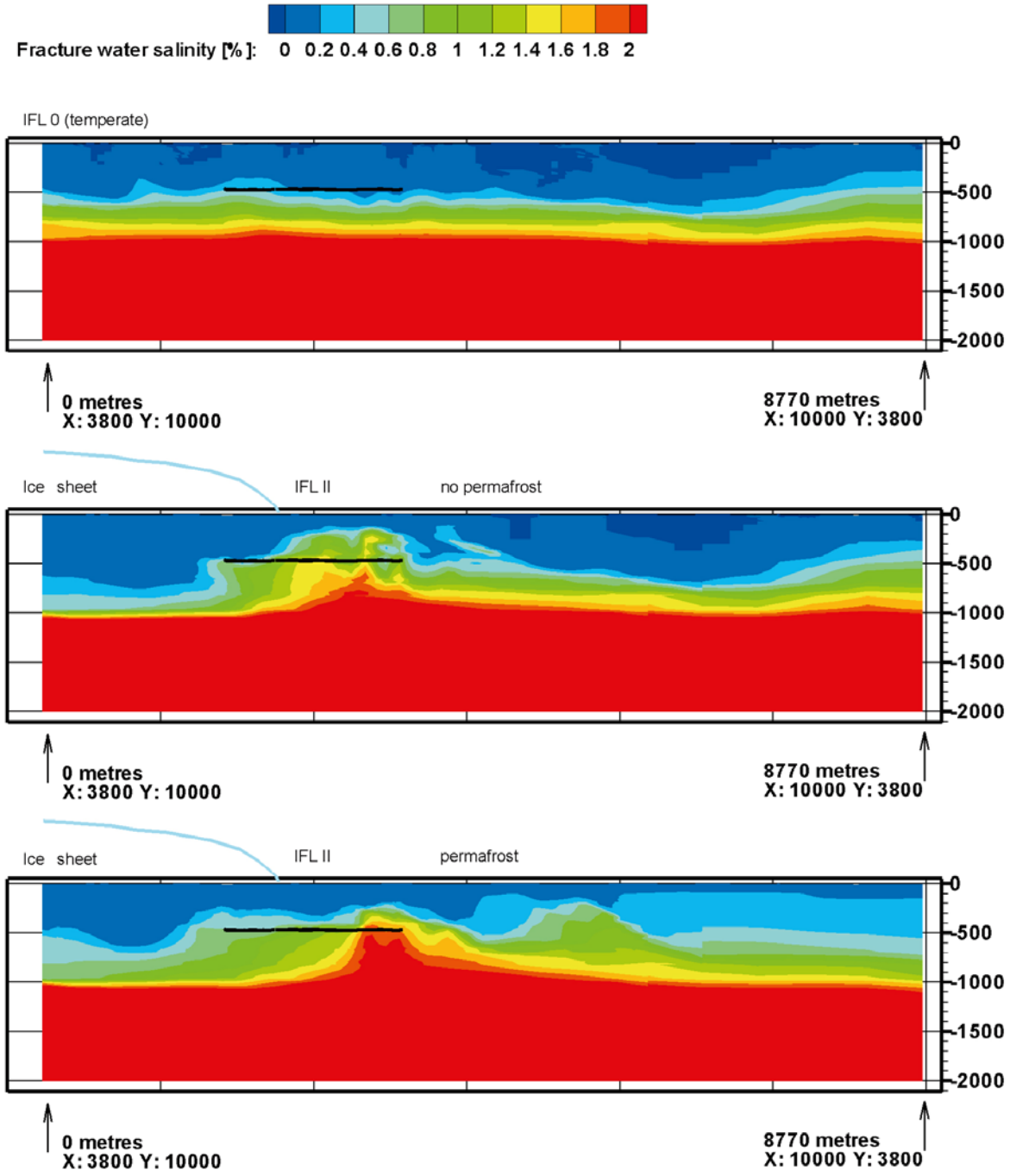

Figure 6-5. *Top: Fracture (advective) water salinity during temperate conditions mapped on a cross-section parallel with direction of the ice sheet movement during glaciation. The images in the middle and at the bottom show the fracture water salinity when the ice sheet margin is at IFL II for the glacial case without permafrost (middle) and for the glacial case with permafrost (bottom). The position of the ice sheet profile is illustrated with a blue curve.*

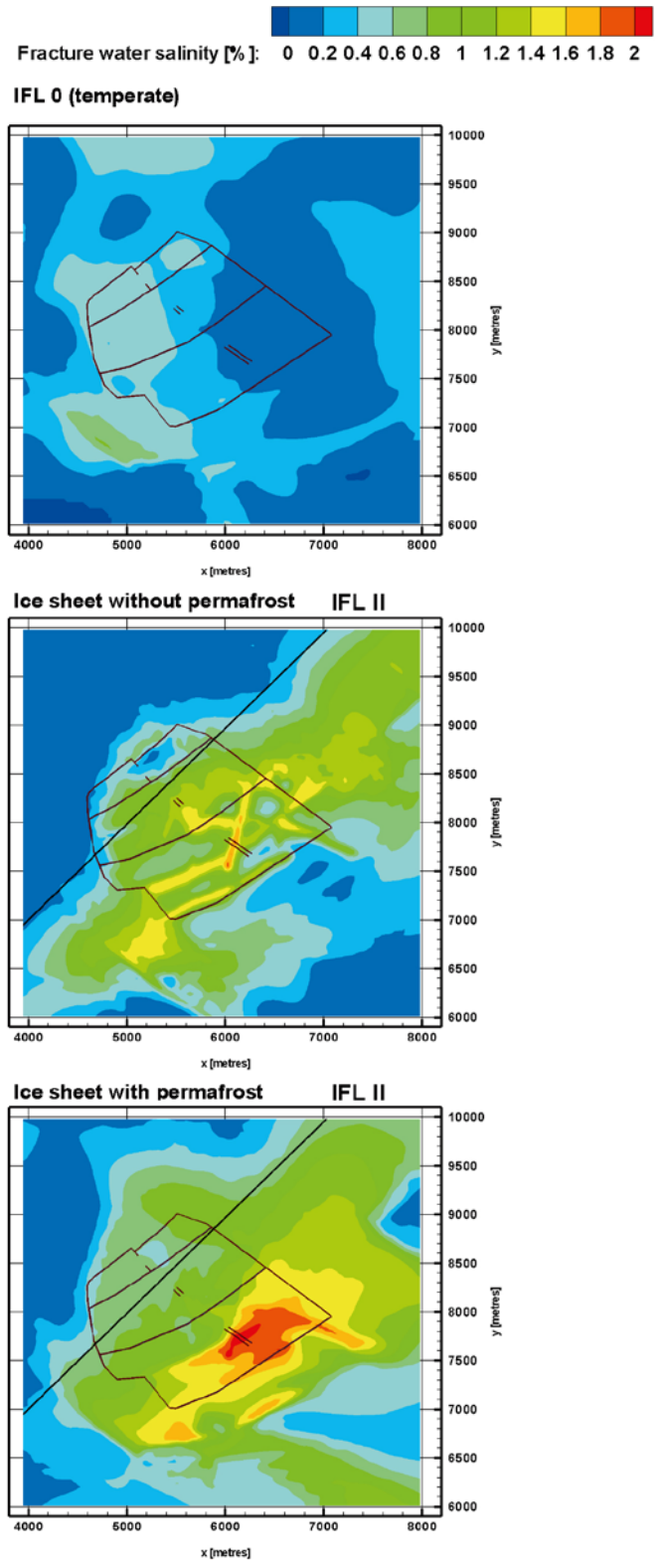

Figure 6-6. *Top: Fracture (advective) water salinity during temperate conditions mapped on a horizontal plane located at –465 m. The images in the middle and at the bottom show the fracture water salinity when the ice sheet margin is at IFL II for the glacial case without permafrost (middle) and for the glacial case with permafrost (bottom). The black thin lines represent main repository tunnels.*

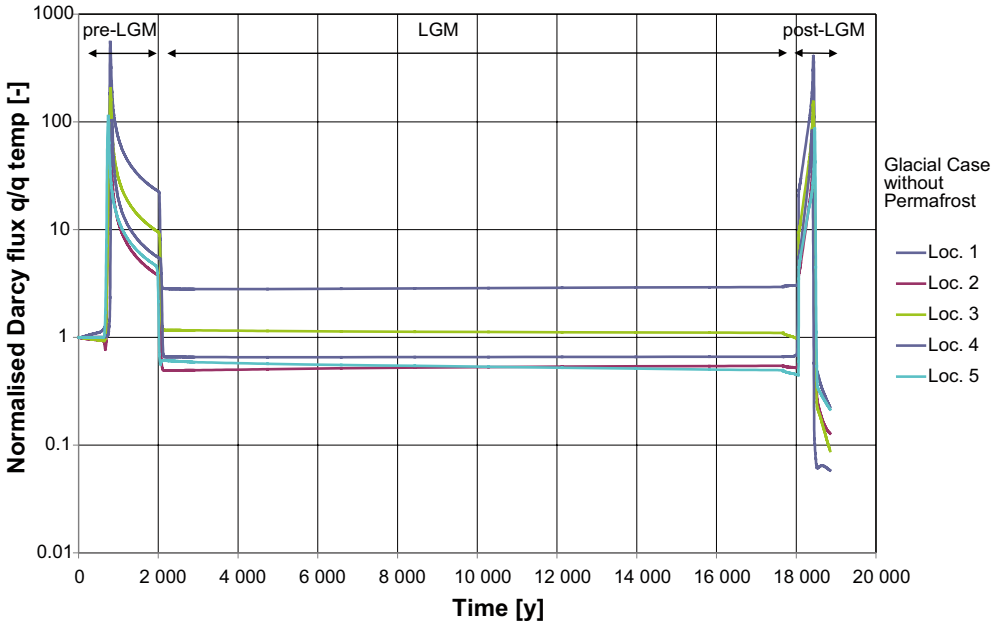

Figure 6-7. *Plot showing the normalised change in Darcy flux, (q/q_{temp}), at ML 1-5 during approximately 19,000 years for the glacial case without permafrost. ML 1 is located close to a steeply dipping deformation zone).*

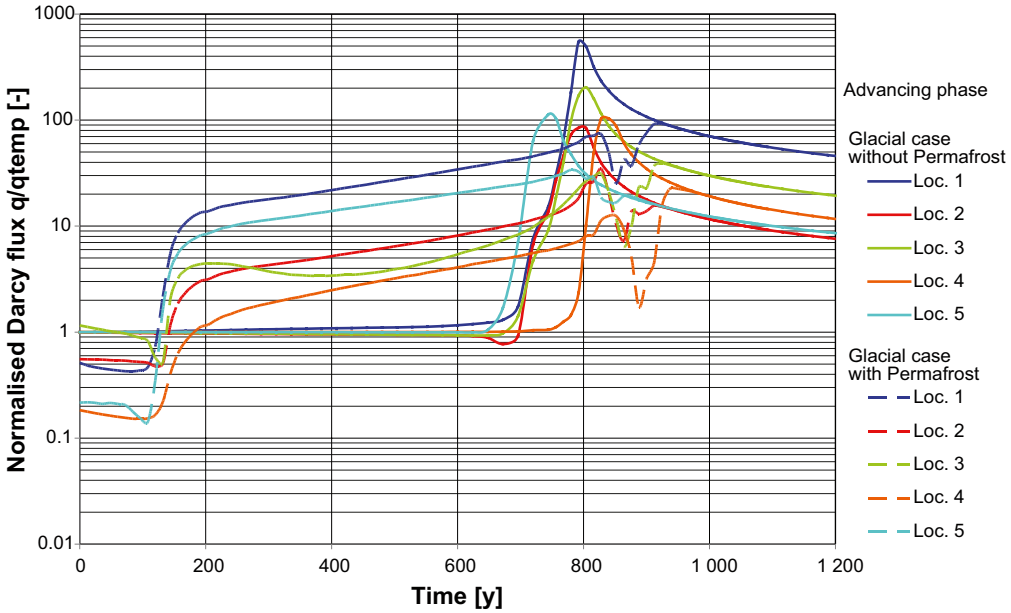

Figure 6-8. *Close-up of the plot in Figure 6-7 showing the normalised change in Darcy flux, (q/q_{temp}), at ML 1-5 during glaciation (pre-LGM). Besides the glacial case with permafrost (solid lines), the evolution of the glacial case without permafrost (dashed lines). After approximately 1,000 years, the two scenarios are identical.*

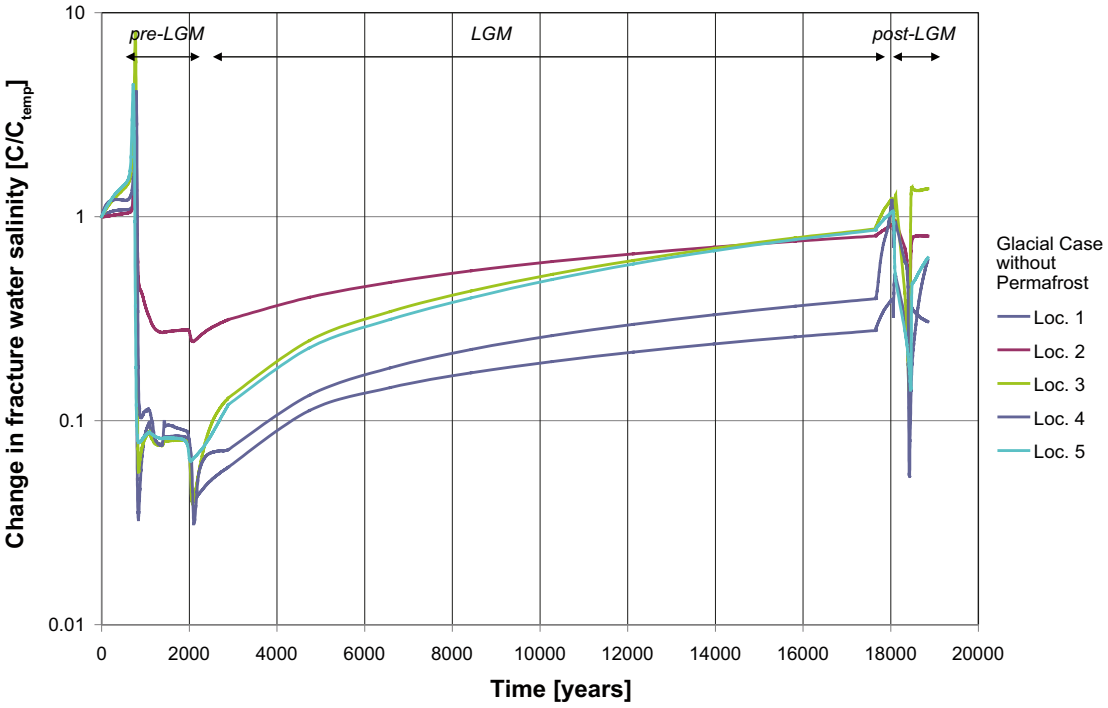

Figure 6-9. *Plot showing the normalised change in concentration, (C/C_{temp}), at ML 1-5 during approximately 19,000 years for the glacial case without permafrost.*

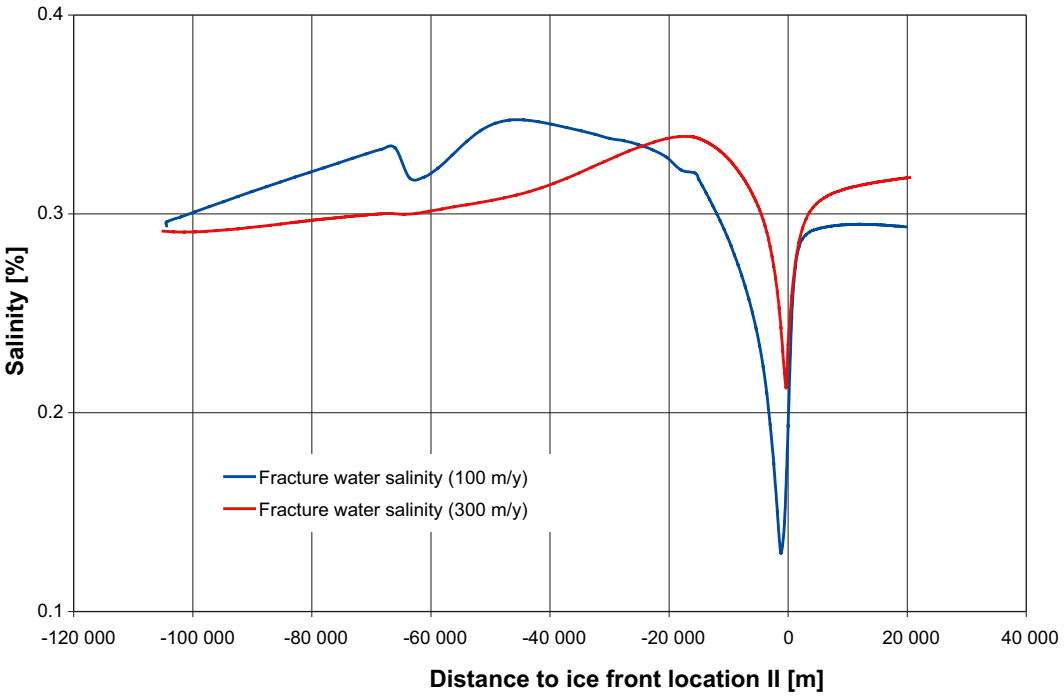

Figure 6-10. *Plot showing the difference in flushing as a function of the average speed of the retreating ice sheet margin at ML 2. A retreat speed of 300 m/y yields lesser flushing. (Ice sheet margin moves from left to right in this plot.)*

Regarding the simulated exchange of salt between the fracture water and the matrix porewater, the exchange appears to be from the matrix porewater to the fracture water for a limited period of time only coinciding with the passages of the ice sheet margin. During the long period of complete ice coverage the conditions are the opposite, see Figure 6-11, although it is noted that a quasi-equilibrium between fracture and matrix waters exists. The reason for not a full equilibrium developing is that there is a continuous advective transport of salt from the bottom boundary of the model. Furthermore, the results indicate that it takes roughly 3,000 years to establish this quasi-equilibrium after flushing has occurred. This also implies that it is the matrix close to the fracture surface that is included in the model rather than the matrix further away. The support for assuming a fixed fracture water salinity on the bottom boundary of the model domain and the interpretation of a limited penetration depth of the simulated matrix diffusion are discussed in Appendix D.

Recharge and discharge location in the biosphere

The top image in Figure 6-12 shows the recharge and discharge locations when the ice sheet margin reaches ice-front location II for the glacial case without permafrost, and the bottom image in Figure 6-12 shows the corresponding results for the glacial case with permafrost. For the glacial case without permafrost a few particles recharge at the upstream boundary of the model domain. For the glacial case with permafrost all particles recharge at the upstream boundary. This suggests that the model domain is too small to give a fully undisturbed view of all recharge locations for a fixed Darcy flux field. Nevertheless, it may be concluded that the present-day topographic water divides, which play an important role for the recharge and discharge during temperate conditions, are significantly diminished during glacial conditions.

In contrast, the discharge locations are predominantly found well within the physical boundaries of the model domain and often very close to the margin of the ice sheet. The differences seen in the discharge pattern between the two glacial cases are largely caused by the varying hydraulic properties and boundary conditions. For the glacial case with permafrost there are two centres of discharge:

- The deformation zone model that exists within the regional model domain for SDM-Site Forsmark. In this simulation approximately two percent of the released particles exit along deformation zones.
- The taliks positioned at the topographic lows in front of the ice sheet margin to the east (outside the regional model domain). In this simulation, the taliks catch approximately 98% of the released particles.

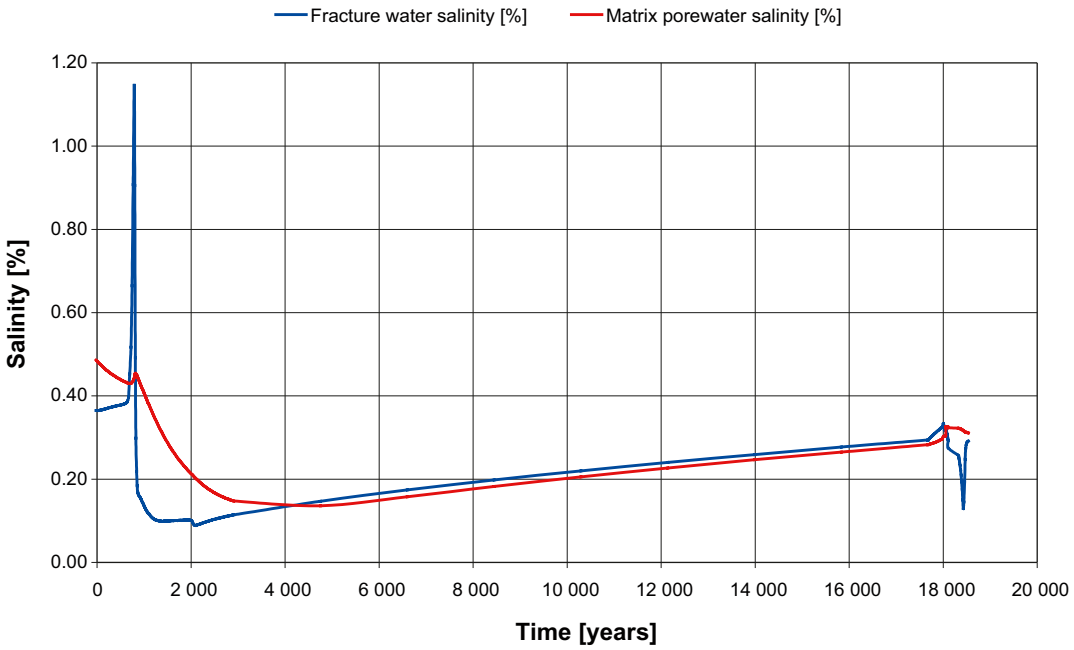

Figure 6-11. *Plot showing the fracture water and matrix porewater salinities at ML 2 during approximately 19,000 years for the glacial case without permafrost.*

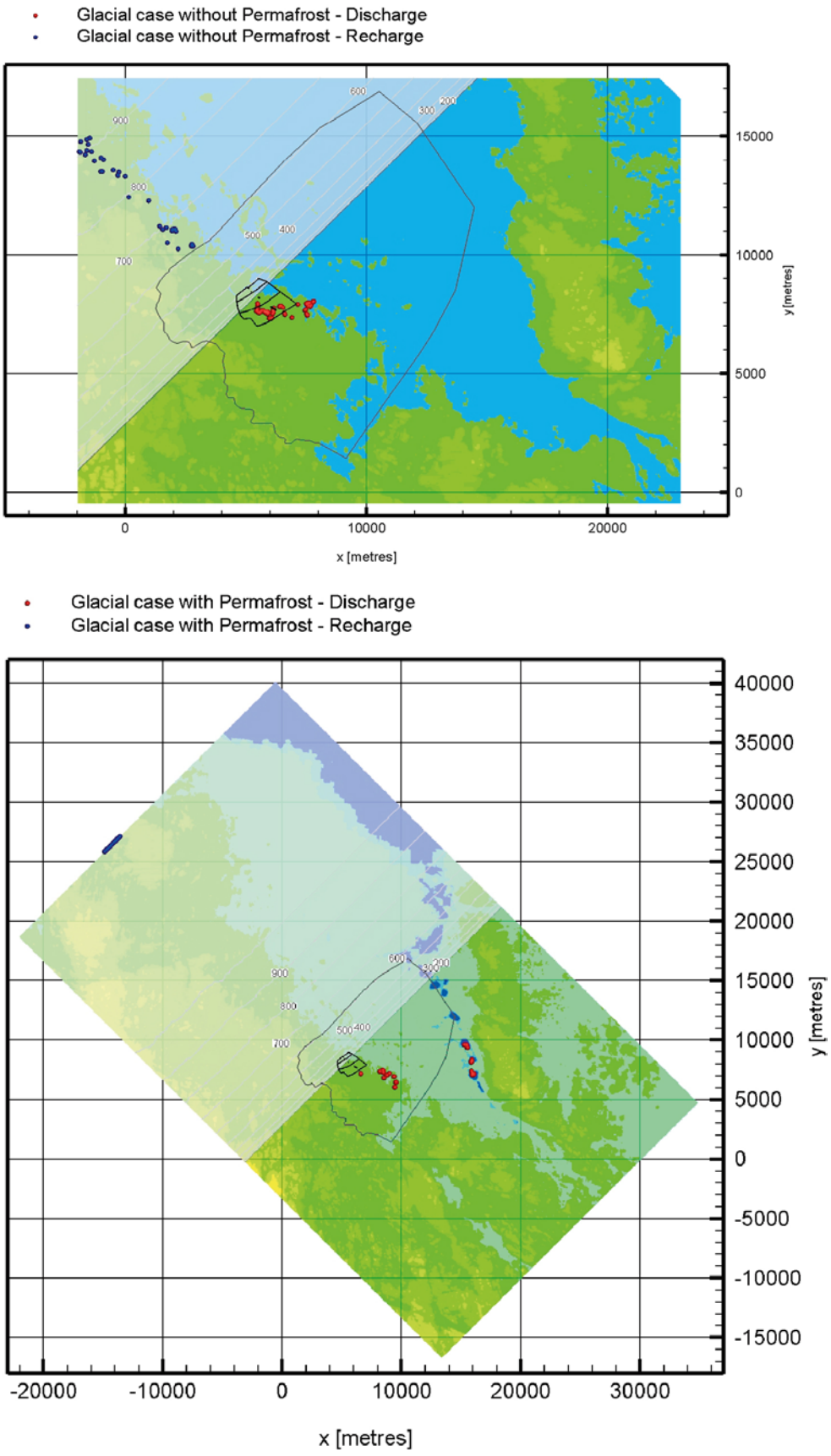

Figure 6-12. *Recharge (blue) and discharge (red) locations of the 6,916 particles released at repository depth when the advancing ice sheet margin is at ice-front location II. Top: Ice sheet without permafrost. Bottom: Ice sheet with permafrost and taliks. The taliks are positioned in the topographic lows in front of the ice sheet margin to the east (outside the polygon that indicates the SDM-Site model domain).*

Performance measures

For the sake of future comparisons in SR-Site, the Darcy flux and flow-related transport resistance are shown in Figure 6-13 and Figure 6-14, respectively, for the glacial case without permafrost when the ice sheet margin is at IFL II and IFL IV. It is observed in Figure 6-13 that the median Darcy flux of the temperate case is increased by approximately 1.5-2 order of magnitude when the ice sheet margin is at IFL II. A corresponding decrease of the flow-related transport resistance is observed in Figure 6-14. Also, Figure 6-13 indicates that the Darcy fluxes are more or less uniformly influenced by the glacial boundary conditions. Thus, it appears that regions with low fluxes are equally affected by the high gradients induced by the ice sheet as regions with high fluxes. However, this results may be due to the fact that the super-regional model reported here treats the crystalline bedrock as a continuous porous medium. Indeed, the sparsely fractured rock characterising the Forsmark site at depth is better represented by a discrete representation implying that all deposition holes may not be connected to a flowing fracture /Follin 2008/.

Site related variants

N-S ice advance direction

Based on the historic and modelled data described in /SKB 2010/, a NW-SE orientation of the model domain is conceived to be the most appropriate orientation to study for an advancing ice sheet margin. (The most appropriate retreat direction is probably somewhat more parallel to S-N.) The simulations carried out includes a variant sensitivity test where a N-S ice advance direction is used. In conclusion, the simulation results suggest minor differences of probably insignificant importance. For example, Figure 6-15 displays the Darcy fluxes at measurement localities 2 and 4 for the two different ice advance directions. The evolutions and magnitudes are quite similar.

THM properties

Isostasy is not accounted for in the work reported here but the potential impact on groundwater flow of an uneven surface loading at the ice sheet terminus (the forebulge phenomenon) is addressed here by changing the transmissivity of all deformation zones and fractures that strike towards northwest based on the results from the rock mechanics modelling conducted for SR-Site /Hökmark et al. 2010, Lönnqvist and Hökmark 2010/, see Table B-13 in Appendix B. Still, the simulation results suggest insignificant differences in the peak values of the Darcy flux also for these exaggerated values. As an example, Figure 6-16 displays the Darcy fluxes at measurement localities 1 to 5.

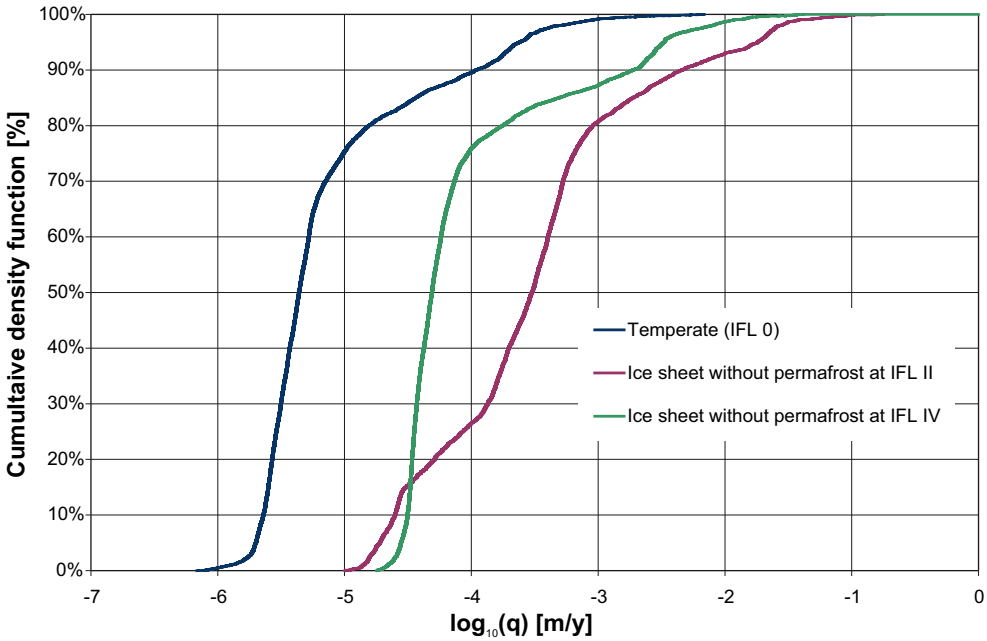

Figure 6-13. *Cumulative distribution function plot of Darcy fluxes for the temperate case (IFL 0) and the glacial case without permafrost when the ice sheet margin is at IFL II and IFL IV, respectively.*

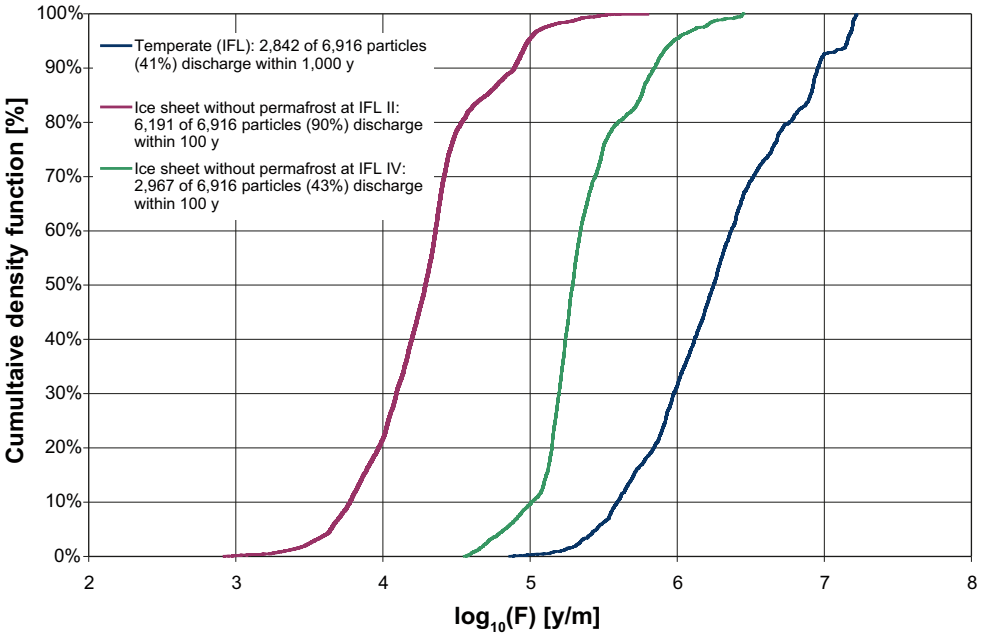

Figure 6-14. *Cumulative distribution function plot of flow-related transport resistances for the temperate case (IFL 0) and the glacial case without permafrost when the ice sheet margin is at IFL II and and IFL IV, respectively.*

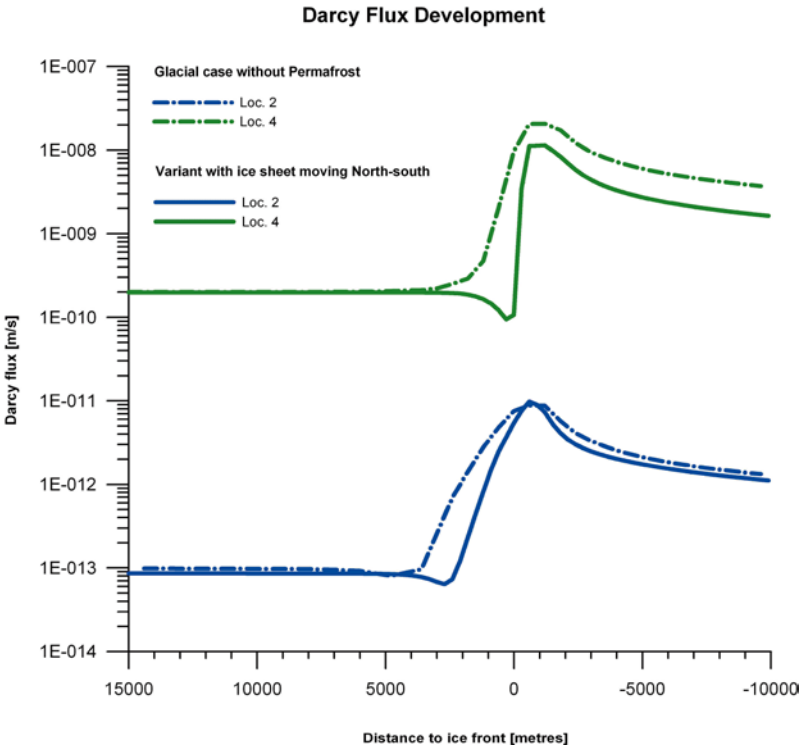

Figure 6-15. *Comparison between the Darcy flux at ML 2 and ML 4 during glaciation for the two ice sheet movement directions considered; Dashed line = NW-SE, Solid lines = N-S. Positive distance values mean that the ice sheet margin has not yet arrived to the measurement locations.*

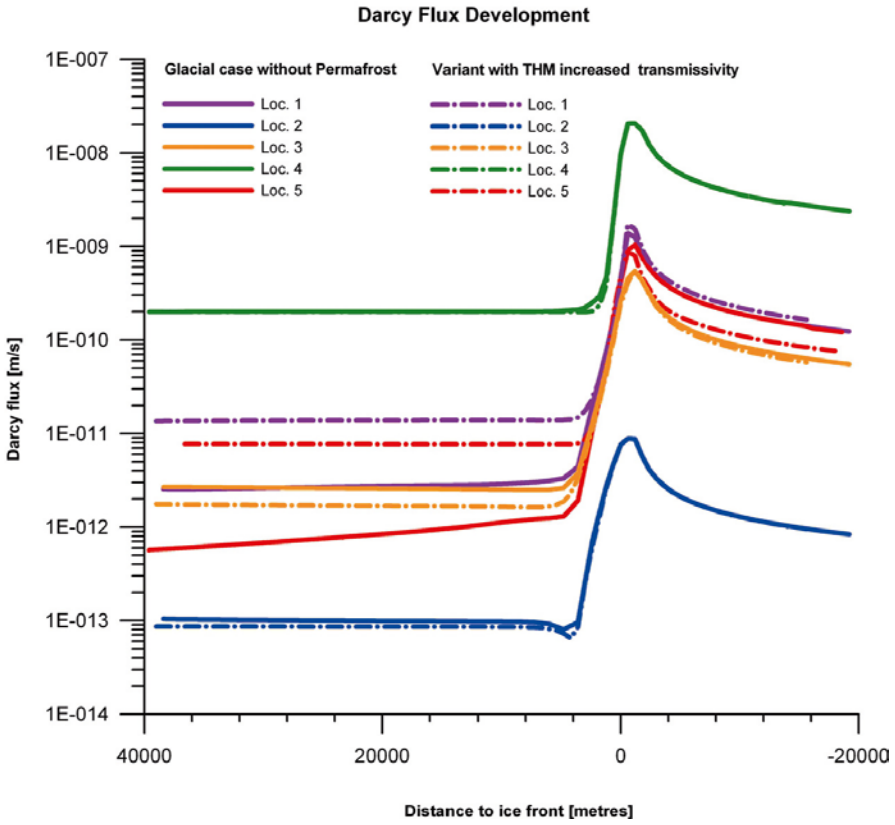

Figure 6-16. *Comparison between the Darcy flux at ML 1-5 during glaciation for the two permeability conditions considered; Dashed lines = Disturbed permeability, Solid lines = undisturbed permeability. Positive distance values mean that the ice sheet margin has not yet arrived to the measurement locations.*

6.4 Overview of performance measures

6.4.1 Temperate climate conditions

The recharge locations of the particle traces that pass through the 6,916 deposition hole positions coincide with topographic highs inside or along the upstream boundary of the regional model domain for groundwater flow as depicted in SDM-Site /Follin 2008/.

The Darcy fluxes at the investigated 6,916 deposition hole positions vary between $2 \cdot 10^{-14}$ and $2 \cdot 10^{-10}$ m/s with a median value around $1 \cdot 10^{-13}$ m/s. The mobile fracture water salinity varies between 0.5 and 1%.

Table 6-1 presents median values on some of the considered performance measures (flow path length, travel time, and flow-related transport resistance) for the five measurement localities, ML 1-5.

Table 6-1. Performance measures for the temperate case: Median flow path lengths, travel times, and flow-related transport resistances at measurement localities ML 1-5.

	Discharge			Recharge		
ML	Flow path length [m]	Travel time [y]	Flow-related transport resistance [y/m]	Flow path length [m]	Travel time [y]	Flow-related transport resistance [y/m]
1	602	11	$3.4 \cdot 10^{5}$	3,104	60	$1.8 \cdot 10^{6}$
2	3,403	875	$8.4 \cdot 10^{6}$	4,570	330	$3.9 \cdot 10^{6}$
3	1,918	380	$8.9 \cdot 10^{6}$	2,221	63	$1.0 \cdot 10^{6}$
4	1,635	4	$4.4 \cdot 10^{4}$	2,338	38	$9.2 \cdot 10^{5}$
5	1,198	361	$7.6 \cdot 10^{5}$	2,467	50	$1.4 \cdot 10^{6}$

6.4.2 Glacial climate conditions without permafrost

The recharge flow paths for the glacial case without permafrost are significantly longer than the discharge flow paths. Indeed, most of the discharge locations are found in front of the ice sheet margin or in close proximity to nearby deformation zones.

The Darcy fluxes at repository depth generally increase by two orders of magnitude during glaciation (pre-LGM) when the ice sheet margin is located right above the repository (ice-front location II). Typical Darcy fluxes are between $7 \cdot 10^{-14}$ and $2 \cdot 10^{-8}$ m/s with a median value around $6 \cdot 10^{-12}$ m/s. The salinity at repository depth varies significantly during the passage of the ice sheet margin. The salinities first increases to about 2% and then decreases to about 0.5%. However, during the subsequent stage, i.e. when the site is completely covered by the ice sheet (LGM), the Darcy fluxes are low and a gradual increase in fracture water salinity to about 1% at repository depth occurs. This recovery of the "saltwater interface" is due to an accommodation of the buoyancy forces to the new, gentle, top boundary condition, and to the slow, advective transport of salt from below. In the model, the fracture water salinity at great depth is assumed to be undisturbed (fixed) at all times. The data support for this assumption is presented in SDM-Site.

The glacial passage during retreat (post-LGM) is also characterised by an upconing and flushing event, but then salinities attain almost the original values of the temperate conditions. Thus, the results indicate that salinities in fact are more or less restored during the simulated period:

Table 6-2 presents median values on some of the considered performance measures (flow path length, travel time, flow-related transport resistance) for the five measurement localities, ML 1-5 when the ice sheet margin is at ice-front location II.

6.4.3 Glacial climate conditions with permafrost

The recharge flow paths for the glacial case with permafrost are significantly longer than the discharge flow paths though discharge flow paths may be of significant length in a permafrost region depending on the location of taliks.

The Darcy fluxes at repository depth generally increase by two orders of magnitude during glaciation (pre-LGM) when the ice sheet margin is located right above the repository (ice-front location II). Typical Darcy fluxes are between $2 \cdot 10^{-14}$ and $2 \cdot 10^{-9}$ m/s with a median value around $2 \cdot 10^{-12}$ m/s. The salinity variations during glaciation, complete ice coverage and deglaciation resembles the variations obtained from the simulation of the glacial case without permafrost. However, as the permafrost prevents discharge of the upconing saline water near the ice sheet margin, the upconing saline water is pushed forward beneath the permafrost towards more distant discharge locations, i.e. taliks.

Table 6-3 presents median values on some of the considered performance measures (flow path length, travel time, flow-related transport resistance) for the five measurement localities, ML 1-5 when the ice sheet margin is at ice-front location II.

Table 6-2. Performance measures for the glacial case without permafrost: Median flow path lengths, travel times, and flow-related transport resistances at measurement localities ML 1-5 when the ice sheet margin is at ice front location IFL II.

	Discharge			Recharge		
ML	Flow path length [m]	Travel time [y]	Flow-related transport resistance [y/m]	Flow path length [m]	Travel time [y]	Flow-related transport resistance [y/m]
1	815	0.1	$2.8 \cdot 10^{3}$	24,896	159.5	$1.1 \cdot 10^{5}$
2	997	3.1	$2.4 \cdot 10^{4}$	14,737	137.4	$7.7 \cdot 10^{4}$
3	764	1.3	$1.0 \cdot 10^{4}$	28,414	9.9	$3.2 \cdot 10^{5}$
4	1,505	2.9	$2.2 \cdot 10^{4}$	31,004	32.0	$9.3 \cdot 10^{5}$
5	2,038	0.8	$1.2 \cdot 10^{4}$	25,831	40.5	$1.6 \cdot 10^{5}$

Table 6-3. Performance measures for the glacial case with permafrost: Median flow path lengths, travel times, and flow-related transport resistances at measurement localities ML 1-5 when the ice sheet margin is at ice front location IFL II.

ML	Discharge			Recharge		
	Flow path length [m]	Travel time [y]	Flow-related transport resistance [y/m]	Flow path length [m]	Travel time [y]	Flow-related transport resistance [y/m]
1	13,032	24	$7.0 \cdot 10^5$	27,876	40	$1.2 \cdot 10^6$
2	12,155	36	$5.5 \cdot 10^5$	28,162	168	$2.9 \cdot 10^6$
3	9,537	7	$1.7 \cdot 10^5$	29,859	287	$8.5 \cdot 10^6$
4	10,580	25	$7.3 \cdot 10^5$	30,989	8	$2.6 \cdot 10^5$
5	6,650	3	$4.3 \cdot 10^4$	25,410	31	$1.7 \cdot 10^5$

6.4.4 Comparison of the Darcy flux at different time slots

Figure 6-17 shows the minimum, median and maximum values of the Darcy flux at all deposition hole positions during the main "climate events" during the simulated period (IFL 0 → IFL V → IFL 0) of periglacial and glacial climate conditions.

- Temperate (used to produce normalised quantities for SR-Site, see Figure 6-18) (IFL 0)
- Glacial case without permafrost (IFL II),
- Glacial maximum (IFL V),
- Submerged (IFL 0),
- Permafrost (IFL 0),
- Glacial case with permafrost and a 2 km long tongue (IFL II), and
- Glacial case with permafrost but no tongue (IFL II).

The climate condition Glacial case without permafrost provides the highest maximum as well as highest median value of all simulated climate events. Relative to the median temperate period value, the median Glacial without Permafrost value is almost two orders of magnitude higher. The maximum Glacial without Permaforst value is also almost two orders of magnitude higher than the maximum Temperate period value. Conditions of complete ice coverage, or when only permafrost prevail or when the domain is completely submerged provide the smallest Darcy fluxes of all climate situations. The values for these three cases are below the temperate period value.

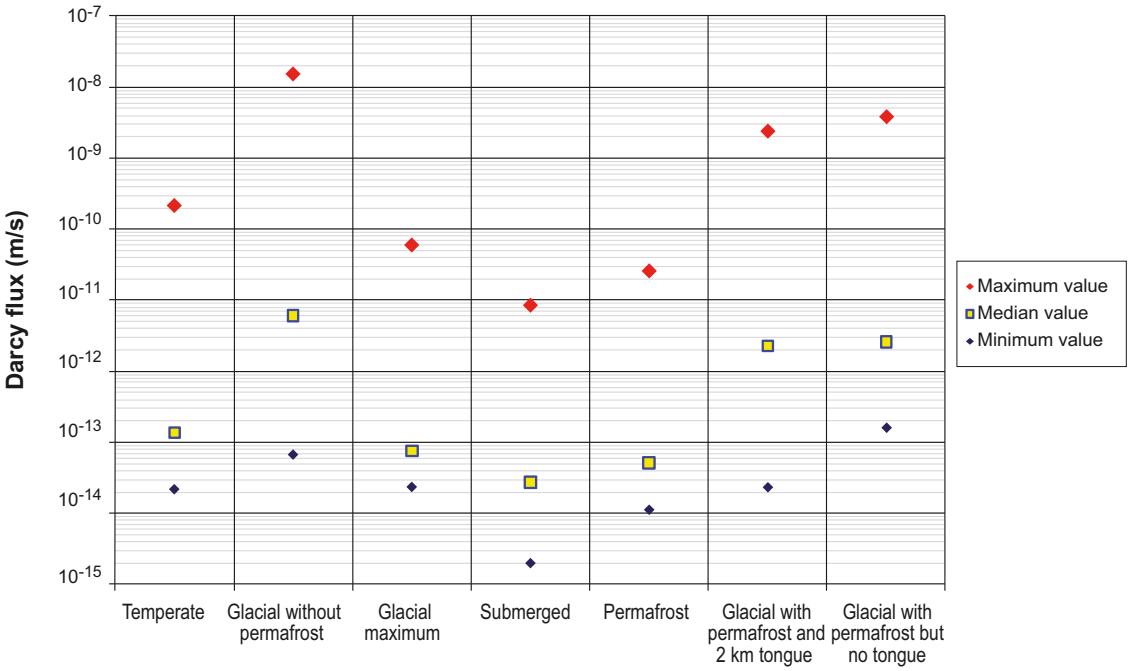

Figure 6-17. *Darcy flux at repository depth for the main climate events considered during the simulated period of periglacial and glacial climate conditions.*

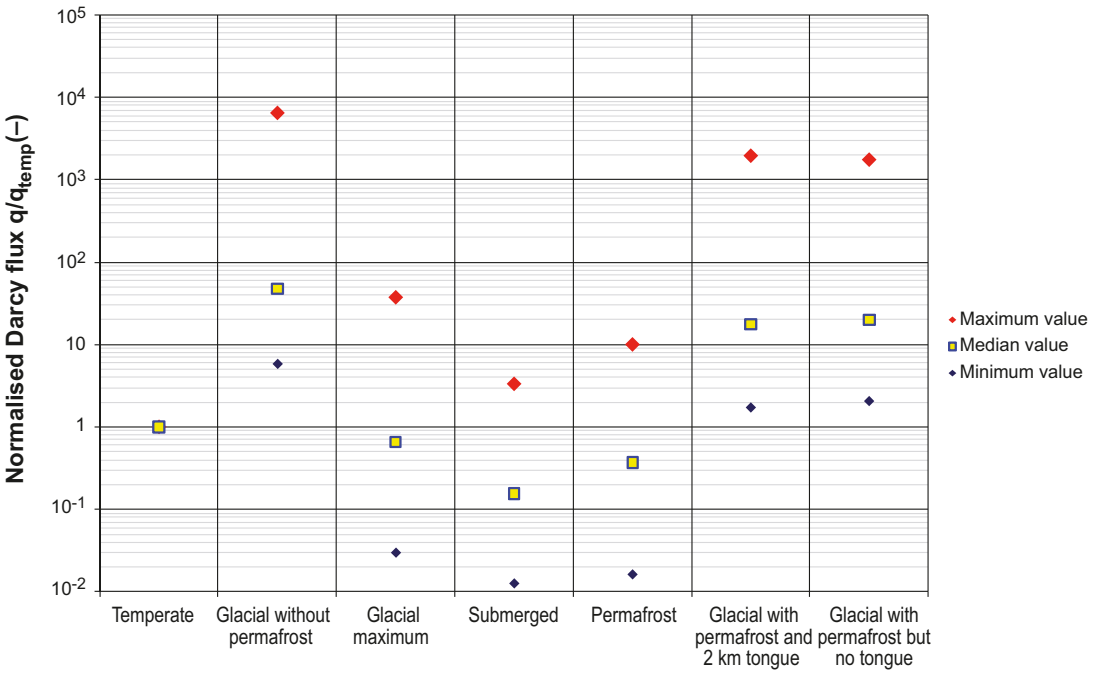

Figure 6-18. *Normalised Darcy flux at repository depth for the main climate events considered during the simulated period of periglacial and glacial climate conditions.*

7 Summary and conclusions

7.1 Scope of work

The primary driving force for groundwater flow at repository depth during periods of periglacial (permafrost) and glacial climate conditions is the difference in residual hydraulic pressure below the ice sheet and in front of the ice sheet margin. The expected effects of this gradient with relevance for long-term safety are related to the groundwater chemistry, the performance measures of groundwater flow at repository depth, and the flow-related transport parameters. In order to assess the magnitude of these impacts, groundwater flow simulations, based on the hydrogeological models developed as part of SDM-Site, have been performed. The overall objective of these simulations has been to assess the effects of periglacial and glacial climate conditions on site hydrogeochemical and hydrogeological conditions in the presence of a backfilled repository.

The study aims at providing bounding hydrogeological estimates for the Forsmark site during periglacial and glacial climate conditions for subsequent safety assessment applications within the SR-Site project. The study is coordinated with the present-day conditions at Forsmark as defined in SDM-Site as well the future conditions considered for the reference climate evolution in /SKB 2010/.

7.2 Methodology

The groundwater flow modelling conducted during temperate climate conditions by /Joyce et al. 2010/ considers the evolution between 8000 BC and 12,000 AD. To a large extent the setup of the temperate flow modelling of /Joyce et al. 2010/ follows the specifications of the groundwater flow modelling considered in SDM-Site, which dealt with the evolution between 8000 BC and 2000 AD, a time period known as the Holocene.

In comparison, the groundwater flow modelling during periglacial and glacial climate conditions reported here is less specific with regard to time although the flow modelling as such encompasses periglacial and glacial climate conditions during a time period of approximately 19,000 years. That is, there is no particular start time associated with the flow simulations conducted during periglacial and glacial climate conditions. Furthermore, it is noted that the work reported here focus on studying the effects of a number of bounding hydraulic assumptions rather than striving for realism in every detail. Although some of the studied assumptions create overly pessimistic premises for the flow simulations, as compared to the reference climate evolution presented in /SKB 2010/, they are useful for safety assessment applications as they provide bounds on the uncertainties involved.

Based on the reference climate evolution described in /SKB 2010/, the flow modelling is divided into three stages referred to as pre-LGM[13], LGM, and post-LGM. During the pre-LGM stage, the ice sheet grows and the ice sheet margin moves across the site in a forward (advancing) direction. During the LGM stage, the model domain is completely covered by ice for thousands of years. During the post-LGM stage, the ice sheet melts and its margin moves across the site in a backward (retreating) direction. The three stages implies transient top boundary conditions.

The groundwater flow modelling uses a coupled thermal-hydraulic-chemical analysis of the different periods of a glacial cycle. The simulations are based on version 3.2 of the DarcyTools code. This version of DarcyTools contains an algorithm that can account for changes in permeability as a function of temperature, which is considered necessary in order to simulate transient and spatially varying hydrological and hydraulic conditions during the evolution of permafrost and ice sheets. The flow modelling did not consider changes in groundwater salinity due to freezing and thawing. Nor did it consider any heat flux from the repository to the surface. Hydraulic-mechanical issues are discussed in the report but no coupled hydro-mechanical modelling is done.

[13] LGM is a standard acronym used to denote the glacial maximum of the last glaciation (Weichsel), cf. /SKB 2010/.

The flow simulation results comprise residual fluid pressures (P), Darcy fluxes (q), and water salinities (C), as well as advective transport performance measures obtained by particle tracking such as flow path lengths (L), travel times (t_w), and flow-related transport resistances (F). The Darcy fluxes, the water salinities and the flow-related transport resistances constitute the primary output quantities. Residual pressures, travel times and flow path lengths constitute second-order performance measures.

Residual fluid pressures, Darcy fluxes, and water salinity values are captured in increments of six years at five measurement locations for an advancing and retreating ice sheet margin. Advective flow path lengths, travel times, and flow-related transport resistances are calculated for all (6,916) deposition hole positions at four specified ice-front locations. The modelling is accompanied by a sensitivity study, which among other matters, investigated the impact of different ice sheet flow directions, different hydraulic properties, and different temperatures at the ice-subsurface interface close to the ice sheet margin.

It is noted that a repository is not included in the work reported here. However, the influence of the hydraulic characteristics of the backfilled tunnels on the performance measures during periods with periglacial and glacial climate conditions is accounted for by exporting the simulation results to be used as input (boundary conditions) in the groundwater flow modelling conducted by /Joyce et al. 2010/. The results from the conducted simulations are presented by /Joyce et al. 2010/.

In summary, the following stages are considered in the work reported here:

- **Pre-LGM stage.** Two different azimuth directions of ice sheet movement: 1. Advance from north-west, and 2. Advance from north; Three types of periglacial conditions: 1. No permafrost, 2. Permafrost in front of the ice sheet margin as well as 2 km beneath the tip of the ice sheet (permafrost tongue), and 3. Permafrost in front of the ice sheet margin only (no tongue); Three types of permeability conditions: 1. Undistorted conditions, i.e. present-day conditions, 2. Distorted conditions due to hydro-mechanical considerations, and 3. Distorted conditions due to freezing an thawing.
- **LGM stage.** The model domain is completely covered by a thick ice sheet during approximately 17,000 years.
- **Post-LGM stage.** One azimuth direction of ice sheet movement (retreat from south-east); submerged ground conditions in front of the ice sheet margin; undistorted permeability conditions.

The flow simulations are listed in Table 1-1. There are two main scenarios, without permafrost and with permafrost, and five cases, see Figure 5-1 to Figure 5-3.

7.3 Assumptions

The study is based on several assumptions and simplifications. The most important ones are listed below.

1. The size of the model domain used in the work reported here is much larger than the model domain used for SDM-Site. Hence, simplifying assumptions are made regarding the hydraulic properties away from the target area. Although the size of the chosen model domain is sufficiently large to address many issues of relevance for the SR-Site project, the model domain is still not large enough to encompass recharge areas under permafrost conditions.
2. Permafrost is a key process to consider as it reduces the permeability of subsurface materials (hydraulic conductivity). Permafrost does not develop instantaneously, but is a transient process. A freezing algorithm is used to modify reported Holocene hydraulic conductivity values in a transient fashion. The thermal input to the permafrost model comes from the temperature time series described in /SKB 2010/.
3. Permafrost reduces mainly the permeability of subsurface materials to water flow (hydraulic conductivity) . Other flow and transport parameters were assumed to be unaffected in the work reported here due to the paucity of data, e.g. the kinematic porosity.

4. A discontinuous permafrost layer is modelled, where probable locations of taliks are estimated from the forecasted landscape development and the projected shoreline displacement. However, while likely positions of taliks can be identified before the first glaciation, it seems likely that ice sheet related changes in the topography during deglaciation will be sufficient to make it difficult to identify likely talik locations for cold periods subsequent to the first glaciation.
5. The ice sheet margin is set to advance with an average speed of 50 m/y and retreat with an average speed of 100 m/y. During the retreat, the height of the ice sheet profile is the same as during the advance. In addition, the sea level is raised to +100 m above the Ordnance Datum causing submerged ground conditions in front of the ice sheet margin.
6. An infinite source of meltwater with a hydraulic head at the base of the ice sheet equal to 92% of the ice sheet thickness is assumed at all times in all simulations. This value is assigned to all parts below the ice sheet that are not affected by permafrost. Elsewhere, the hydraulic head is assumed to follow the topography in all terrestrial parts. In effect, subglacial meltwater that infiltrates into the subsurface will flow from areas with high hydraulic heads to areas with lower hydraulic heads.
7. The classic hydraulic mass balance equation for transient density and viscosity-dependent groundwater flow is favoured over the hydro-mechanical mass balance equation considered in the literature. That is, a one-dimensional loading efficiency of zero is taken to be more relevant for the objectives of this report as it enhances the gradients and thereby the fluxes at repository depth. In addition, field measurements suggest a low value of the specific storage in the sparsely fractured crystalline rock at Forsmark, which implies that there is little or no delay in the pressure responses of the groundwater system to changes in the boundary conditions during the advance and retreat of the ice sheet margin.
8. Isostasy is not accounted for, but the potential impact on groundwater flow of uneven surface loading at the ice sheet margin (the forebulge phenomenon) is addressed by incorporating a change in fracture transmissivity data suggested by the THM modelling within the SR-Site project, see /Hökmark et al. 2010, Lönnqvist and Hökmark 2009/.
9. The abundance of eskers in the Fennoscandian Shield demonstrates the frequency of major meltwater tunnels during the retreat of the Weichselian ice sheet. The eskers occur on top of crystalline bedrock, which reveals that it was here that the bulk of the meltwater runoff took place during the deglaciation. The role of meltwater tunnels for groundwater flow during deglaciation has been interpreted in different ways in the literature. In the work reported here, the transient boundary conditions on the top boundary of the model domain are coordinated with those considered in /SKB 2010/, i.e. meltwater tunnels are not taken into account during glaciation and their impact on the groundwater flow at repository depth during deglaciation is considered insignificant.
10. The structural-hydraulic properties of the sparsely fractured bedrock between the deterministically modelled deformation zones are modelled stochastically. However, the variability between realisations is not addressed.

7.4 Temperate climate conditions

The temperate case is represented by a flow and salt transport solution using the SDM-Site hydrogeological model as input information /Follin 2008/.

The groundwater flow is primary controlled by the regional gradient being from southwest towards north-east. However, local differences due to variations in geological conditions are encountered with flow directions dependent on the transmissivity values of major conductive deformation zones.

The recharge locations of the particle traces that pass through the 6,916 deposition hole positions coincide with topographic highs inside or along the upstream boundary of the regional model domain for groundwater flow as depicted in SDM-Site /Follin 2008/.

7.5 Glacial climate conditions without permafrost

The recharge flow paths are significantly longer than the discharge flow paths for the glacial cases without permafrost. Indeed, most of the discharge locations are found in front of the ice sheet margin or in close proximity to nearby deformation zones.

The Darcy fluxes at repository depth generally increase by two orders of magnitude during glaciation (pre-LGM) when the ice sheet margin is located right above the repository (ice-front location II). The salinity at repository depth varies significantly during the passage of the ice sheet margin. The salinity first increases and then decreases. During the period of complete ice coverage (LGM), the Darcy fluxes are low and a gradual increase in fracture water salinity occurs. This gain of the "salt water interface" is due to an accommodation of the buoyancy forces to the new, gentle, top boundary condition, and to the slow, advective transport of salt from below. In the model, the fracture water salinity at great depth is assumed to be undisturbed (fixed) at all times. The data support for this assumption is presented in Appendix D.

The glacial passage during retreat (post-LGM) is also characterised by an upconing and flushing event, but then salinities attain almost the original values of the temperate conditions. The simulations indicate that salinities are more or less restored during the simulated period.

7.6 Glacial climate conditions with permafrost

The recharge flow paths for the glacial cases with permafrost are significantly longer than the discharge flow paths, though discharge flow paths may be of significant length in a permafrost region depending on the location of taliks.

The Darcy fluxes at repository depth generally increase by two orders of magnitude during glaciation (pre-LGM) when the ice sheet margin is located right above the repository (ice-front location II). The salinity variations during glaciation, complete ice coverage and deglaciation resembles the variations obtained from the simulation of the glacial case without permafrost. However, as the permafrost prevents discharge of the upconing saline water near the ice sheet margin, the upconing saline water is pushed forward beneath the permafrost towards more distant discharge locations, i.e. taliks.

7.7 Conclusions

The results reached in this study are the Darcy fluxes and fracture water salinities at repository level. These and other quantities are reported in Appendices E-G. Chapter 6 summarises the key simulation results for SR-Site as the work has been undertaken to provide inputs for use in subsequent safety assessment applications. The report refrains from commenting on their safety implications, however. Such safety implications can only be evaluated when the results have been propagated through the safety assessment process.

In respect of the assumptions listed in Section 7.3, the following observations are made in the groundwater flow simulations reported here:

- The primary hydraulic driving force for groundwater flow during periods of periglacial and glacial conditions is the difference in hydraulic pressure below the ice sheet and the hydraulic pressure in front of the ice sheet margin, i.e. in the periglacial area. The present-day topographic water divides are significantly diminished during periglacial and glacial climate conditions.
- It is during the passages of the ice sheet margin, the hydraulic gradients and the Darcy fluxes reach their maximum values during a glacial cycle. It is also then the interface between fresh water and saline water is distorted the most.
- The hydraulic and hydrochemical disturbances during the advance stage (pre-LGM) are probably greater than the disturbances during the retreat phase (post-LGM). The reason for this notion is threefold; during the retreat phase, the ice profile at the ice sheet margin is probably thinner and less steep, the average speed of the ice sheet margin is probably higher, and the periglacial area in front of the ice sheet margin is probably submerged.

- During the period of complete ice coverage (LGM), the hydraulic gradients are probably smaller and more uniform than during temperate conditions. A gradual increase in fracture water salinity at repository depth is observed in the simulations. This gain of the "saltwater interface" is due to an accommodation of the buoyancy forces to the very weak top boundary condition caused by an almost uniform ice sheet thickness, and to the slow, but continuous advective transport of salt from the bottom boundary of the model.
- Regarding the simulated exchange of salt between the fracture water and the matrix porewater, the exchange appears to be from the matrix porewater to the fracture water for a limited period of time only coinciding with the passages of the ice sheet margin. During the long period of complete ice coverage the conditions are the opposite, although it is noted that a quasi-equilibrium between fracture and matrix waters exists. The reason for not a full equilibrium developing is the continuous advective transport of salt from the bottom boundary of the model. Furthermore, the results indicate that it takes roughly 3,000 years to establish this quasi-equilibrium after flushing has occurred. This also implies that it is the matrix close to the fracture surface that is included in the model rather than the matrix further away (cf. Section D3 in Appendix D).
- In this work, the model that simulates permafrost decreases the permeability values of the major deformation zones to around 10^{-22} m^2. Still, the particle tracking performed suggests that the permafrost layer is not impervious, and hence allows a few particles to discharge where the hydraulic gradient is high. If this is an imperfection of the particle algorithm used, or a physical phenomenon to be expected, e.g. due to high hydraulic gradients, is unclear.
- The discharge locations of released particles are predominantly found well within the physical boundaries of the model domain and often very close to the ice sheet margin. The differences seen between the two glacial cases studied depend on the handling of permafrost. If permafrost is included, the majority of the discharge occurs in taliks located in the periglacial area.

8 References

SKB's (Svensk Kärnbränslehantering AB) publications can be found at www.skb.se/publications.

Andersson J-E, Nordqvist R, Nyberg G, Smellie J, Tirén S, 1991. Hydrogeological conditions in the Finnsjön area. Compilation of data and conceptual model. SKB TR 91-24, Svensk Kärnbränslehantering AB.

Bath A, Lalieux P, 1999. Technical summary of the SEDE Workshop on the use of hydrogeochemical information in testing groundwater flow models. In: Use of hydrogeochemical information in testing groundwater flow models: technical summary and proceedings of a workshop organised by the NEA Co-ordinating Group on Site Evaluation and Design of Experiments for Radioactive Waste Disposal (SEDE) and hosted by the Swedish Nuclear Fuel and Waste Management Company (SKB), Borgholm, Sweden, 1–3 September 1997. Paris: OECD, pp 13–30.

Bense V F, Person M A, 2008. Transient hydrodynamics within intercratonic sedimentary basins during glacial cycles. Journal of Geophysical Research, 113, pp 1–17.

Bosson E, Gustafsson L-G, Sassner M, 2008. Numerical modelling of surface hydrology and near-surface hydrogeology at Forsmark. Site descriptive modelling, SDM-Site Forsmark. SKB R-08-09, Svensk Kärnbränslehantering AB.

Boulton G S, de Marsily G, 1997. Hydrogeological aspects of glaciation. In: King-

Clayton L, Chapman N, Ericsson L O, Kautsky F (eds). Glaciation and hydrogeology. Proceedings of the workshop on the impact of climate change and glaciations on rock stresses, groundwater flow and hydrochemistry – past, present and future. Hässelby, Sweden, 17–19 April 1996. SKI Report 97:13, Statens kärnkraftinspektion (Swedish Nuclear Power Inspectorate).

Boulton G S, Slot T, Blessing K, Glasbergen P, Leijnse T, van Gijssel K, 1993. Deep circulation of groundwater in overpressured subglacial aquifers and it's geological consequences. Quaternary Science Reviews, 12, pp 739–745.

Boulton G S, Caban P E, Van Gijssel K, 1995. Groundwater flow beneath ice sheets: part I – large scale patterns. Quaternary Science Reviews, 14, pp 545–562.

Boulton G S, Caban P E, van Gijssel K, Leijnse A, Punkari M, van Weert F H A, 1996. The impact of glaciations on the groundwater regime of Northwest Europe. Global and Planetary Change, 12, pp 397–413.

Boulton G S, Lunn R J, Vidstrand P, Zatsepin S, 2007a. Subglacial drainage by groundwater-channel coupling, and the origin of esker systems: part I – glaciological observations. Quaternary Science Reviews, 26, pp 1067–1090.

Boulton G S, Lunn R J, Vidstrand P, Zatsepin S, 2007b. Subglacial drainage by groundwater-channel coupling, and the origin of esker systems: part II – theory and simulation of a modern system. Quaternary Science Reviews 26, pp 1091–1105.

Bremeer C W, Clark P U, Haggerty R, 2002. Modeling the subglacial hydrology of the late Pleistocene Lake Michigan Lobe, Laurentide Ice Sheet. GSA Bulletin, 114, pp 665–674.

Brydsten L, Strömgren M, 2010. A coupled regolith-lake development model applied to the Forsmark site. SKB TR-10-56, Svensk Kärnbränslehantering AB.

Burt T P, Williams J, 1976. Hydraulic conductivity in frozen soils. Earth Surface Processes, 1, pp 349–360.

Chan T, Christiansson R, Boulton G S, Ericsson L O, Hartikainen J, Jensen R M, Mas Ivars D, Stanchell W F, Vidstrand P, Wallroth T, 2005. DECOVALEX III BMT3/BENCHPAR WP4: The thermo-hydro-mechanical responses to a glacial cycle and their potensial implication for deep geological disposal of nuclear fuel waste in a fractured crystalline rock mass. International Journal of Rock Mechanics and Mining Science, 42, pp 805–827.

Clark I D, Douglas M, Raven K, Bottomley D, 2000. Recharge and preservation of Laurentide glacial melt water in the Canadian Shield, Ground Water, 38, pp 735–742.

Cohen D, Person M, Wang P, Gable W C, Hutchinson D, Marksamer A, Dugan B, Kooi H, Groen K, Lizarralde D, Evans R L, Day-Lewis F D, Lane J W, 2010. Origin and extent of fresh paleowaters on the Atlantic continental shelf, USA. Ground Water, 48, pp 143–158.

Dershowitz W, Winberg A, Hermanson J, Byegård J, Tullborg E-L, Andersson P, Mazurek M, 2003. Äspö Task Force on modelling of groundwater flow and transport of solutes. Task 6c. A semi synthetic model of block scale conductive structures at the Äspö HRL. Äspö Hard Rock Laboratory, International Progress Report IPR-03-13, Svensk Kärnbränslehantering AB.

Douglas M, Clark I D, M, Raven K, Bottomley D, 2000. Groundwater mixing dynamics at a Canadian Shield mine. Journal of Hydrology, 235, pp 88–103.

Dverstorp B, Strömberg B, 2008. SKI's and SSI's review of SKB's safety report SR-Can. SKI Report 2008:23, Statens kärnkraftinspektion (Swedish Nuclear Power Inspectorate), SSI Report 2008:04 E, Statens strålskyddsinstitut (Swedish Radiation Protection Authority).

Ericsson L O, Holmén J, 2010. Storregional grundvattenmodellering – en känslighetsstudie av några utvalda konceptuella förenklingar. SKB R-10-43, Svensk Kärnbränslehantering AB (in Swedish).

Ericsson L O, Holmén J, Rhén I, Blomqvist N, 2006. Storregional grundvattenmodellering – fördjupad analys av flödesförhållanden i östra Småland. Jämförelse av olika konceptuella beskrivningar. SKB R-06-64, Svensk Kärnbränslehantering AB.

Ferguson G A. G, Betcher R. N, Grasby S E, 2007. Hydrogeology of the Winnipeg formation in Manitoba, Canada. Hydrogeology Journal, 15, pp 573–587.

Flowers G E, Clarke G K C, 2002. A multicomponent coupled model of glacier hydrology. 1. Theory and synthetic examples. Journal of Geophysical Research, 107, 2287, doi:10.1029/2001JB001122.

Follin S, 2008. Bedrock hydrogeology Forsmark. Site descriptive modelling, SDM-Site Forsmark. SKB R-08-95, Svensk Kärnbränslehantering AB.

Follin S, Svensson U, 2003. On the role of mesh discretisation and salinity for the occurrence of local flow cells. Results from a regional-scale groundwater flow model of Östra Götaland. SKB R-03-23, Svensk Kärnbränslehantering AB.

Follin S, Stigsson M, Svensson U, 2005. Regional hydrogeological simulations for Forsmark – numerical modelling using DarcyTools. Preliminary site description. Forsmark area – version 1.2. SKB R-05-60, Svensk Kärnbränslehantering AB.

Follin S, Levén J, Hartley L, Jackson P, Joyce S, Roberts D, Swift B, 2007a. Hydrogeological characterisation and modelling of deformation zones and fracture domains, Forsmark modelling stage 2.2. SKB R-07-48, Svensk Kärnbränslehantering AB.

Follin S, Johansson P-O, Hartley L, Jackson P, Roberts D, Marsic N, 2007b. Hydrogeological conceptual model development and numerical modelling using CONNECTFLOW, Forsmark modelling stage 2.2. SKB R-07-49, Svensk Kärnbränslehantering AB.

Follin S, Hartley L, Jackson P, Roberts D, Marsic N, 2008. Hydrogeological conceptual model development and numerical modelling using CONNECTFLOW, Forsmark modelling stage 2.3. SKB R-08-23, Svensk Kärnbränslehantering AB.

French H M, 1996. The periglacial environment. 2nd ed. Harlow: Longman.

Gascoyne M, 2000. A review of published literature on the effects of permafrost on the hydrogeochemistry of bedrock. Posiva 2000-09, Posiva Oy, Finland.

Grasby S E, Osadetz K, Betcher R, Render F, 2000. Reversal of the regional-scale flow system of the Williston basin in response to Pleistocene glaciation. Geology, 28, pp 635–638.

Haggerty R, Gorelick S M, 1995. Multiple-rate mass transfer for modelling diffusion and surface reactions in media with pore-scale heterogeneity. Water Resources Research, 31, pp 2383–2400.

Haldorsen S, Heim M, 1999. An arctic groundwater system and its dependence upon climatic change: an example from Svalberg. Permafrost and Periglacial Processes, 10, pp 137–149.

Harlow F H, Welsch J E, 1965. Numerical calculations of time-dependent viscous incompressible flow of fluid with free surface. Physics of Fluids, 8, pp 2182–2189.

Hartikainen J, Kouhia R, Wallroth T, 2010. Permafrost simulations at Forsmark using a numerical 2D thermo-hydro-chemical model. SKB TR-09-17, Svensk Kärnbränslehantering AB.

Hedenström A, Sohlenius G, Strömgren M, Brydsten L, Nyman H, 2008. Depth and stratigraphy of regolith at Forsmark. Site desprictive modelling, SDM-Site Forsmark. SKB R-08-07, Svensk Kärnbränslehantering AB.

Holmén J G, 2008. Premodelling of the importance of the location of the upstream hydraulic boundary of a regional flow model of the Laxemar-Simpevarp area. Site descriptive modelling, SDM-Site Laxemar. SKB R-08-60, Svensk Kärnbränslehantering AB.

Holmén J G, Stigsson M, Marsic N, Gylling B, 2003. Modelling of groundwater flow and flow paths for a large regional domain in northeast Uppland. A three-dimensional, mathematical modelling of groundwater flows and flow paths on a super-regional scale, for different complexity levels of the flow domain. SKB R-03-24, Svensk Kärnbränslehantering AB.

Hughes T J, 1998. Ice sheets. New York: Oxford University Press.

Hökmark H, Lönnqvist M, Fälth B, 2010. THM-issues in repository rock. Thermal, mechanical, thermo-mechanical and hydro-mechanical evolution of the rock at the Forsmark and Laxemar sites. SKB TR-10-23, Svensk Kärnbränslehantering AB.

Jansson P, Näslund J-O, Rodhe L, 2007. Ice sheet hydrology – a review. SKB TR-06-34, Svensk Kärnbränslehantering AB.

Jaquet O, Siegel P, 2003. Groundwater flow and transport modelling during a glaciation period. SKB R-03-04, Svensk Kärnbränslehantering AB.

Jaquet O, Siegel P, 2006. Regional groundwater flow model for a glaciation scenario. Simpevarp subarea – version 1.2. SKB R-06-100, Svensk Kärnbränslehantering AB.

Jay Zwally H, Abdalati T, Herring T, Larson K, Saba J, Steffen K, 2002. Surface melt-induced acceleration of Greenland ice sheet flow. Science, 297, pp 218–222.

Johansson P-O, 2008. Description of surface hydrology and near-surface hydrogeology at Forsmark. Site descriptive modelling, SDM-Site Forsmark. SKB R-08-08, Svensk Kärnbränslehantering AB.

Joyce S, Simpson T, Hartley L, Applegate D, Hoek J, Jackson P, Swan D, Marsic N, Follin S, 2010. Groundwater flow modelling of the temperate period – Forsmark. SKB R-09-20, Svensk Kärnbränslehantering AB.

Kamb B, 1987. Glacier surge mechanism based on linked cavity configuration of the basal water conduit system. Journal of Geophysical Research, 92, pp 9083–9100.

King-Clayton L M, Chapman N A, Kautsky F, Svensson N-O, de Marsily G, Ledoux E, 1995. The central scenario for SITE-94: a climate change scenario. SKI Report 95:42, Statens kärnkraftinspektion (Swedish Nuclear Power Inspectorate).

Kleinberg R L, Griffin D D, 2005. NMR measurements of permafrost: unfrozen water assay, pore-scale distribution of ice, and hydraulic permeability of sediments. Cold Regions Science and Technology, 42, pp 63–77.

Lemieux J-M, Sudicky E A, Peltier W R, Tarasov L, 2008a. Simulating the impact of glaciations on continental groundwater flow systems: 1. Relevant processes and model formulation. Journal of Geophysical Research, 113, F03017, doi:10.1029/2007JF000928.

Lemieux J-M, Sudicky E A, Peltier W R, Tarasov L, 2008b. Simulating the impact of glaciations on continental groundwater flow systems: 2. Model application to the Wisconsinian glaciation over the Canadian landscape. Journal of Geophysical Research, 113, F03018, doi:10.1029/2007JF000929.

Lemieux J-M, Sudicky E A, Peltier W R, Tarasov L, 2008c. Dynamics of groundwater recharge and seepage over the Canadian landscape during the Wisconsinian glaciation. Journal of Geophysical Research, 113, F01011, doi:10.1029/2007JF000838.

Lindborg T (ed), 2010. Landscape Forsmark – Indata, methodology and results for SR-Site. SKB TR-10-05, Svensk Kärnbränslehantering AB.

Lönnqvist M, Hökmark H, 2010. Assessment of potential for glacially induced hydraulic jacking at different depths. SKB R-09-35, Svensk Kärnbränslehantering AB.

Marshall S J, Clark P U, 2002. Basal temperature evolution of North American ice sheets and implications for the 100-kyr cycle. Geophysical Research Letters, 29, 2214, doi:10.1029/2002GL015192.

McEwan T, de Marsily G, 1991. The potential significance of permafrost to the behaviour off a deep radioactive waste repository. SKI TR 91:8, Statens kärnkraftinspektion (Swedish Nuclear Power Inspectorate).

NEA-OECD, 1993. Paleohydrogeological methods and their application: proceedings of a

NEA workshop, Paris, 9–10 November 1992. Paris : Nuclear Energy Agency, Organisation for Economic Co-operation and Development.

Neuzil C E, 2003. Hydromechanical coupling in geological processes. Hydrogeology Journal, 11, pp 41–83.

Nye J F, 1973. Water at the bed of a glacier. In: Proceedings of the Symposium on the hydrology of glaciers, Cambridge, 7–13 September 1969. Wallingford: IAHS. (IAHS publication 95), pp 189–194.

Oerlemans J, 2005. Extracting a climate signal from 169 glacier records. Science, 308, pp 675–677.

Olofsson I, Simeonov A, Stephens M, Follin S, Nilsson A-C, Röshoff K, Lindberg U, Lanaro F, Fredriksson A, Persson L, 2007. Site descriptive modelling Forsmark, stage 2.2. A fracture domain concept as a basis for the statistical modelling of fractures and minor deformation zones, and inter-disciplinary coordination. SKB R-07-15, Svensk Kärnbränslehantering AB.

Patankar S V, 1980. Numerical heat transfer and fluid flow. New York: Hemisphere.

Paterson W S B, 1994. The physics of glaciers. 3rd ed. Oxford: Pergamon.

Person M, McIntosh J, Bense V, Remenda V H, 2007. Pleistocene hydrology of North America: the role of ice sheets in reorganising groundwater flow systems. Reviews of Geophysics, 45, RG3007, doi:10.1029/2006RG000206.

Piotrowski J A, 1997a. Subglacial groundwater flow during the last glaciation in north-western Germany. Sedimentary Geology, 111, pp 217–224.

Piotrowski J A, 1997b. Subglacial hydrology in north-western Germany during the last glaciation: groundwater flow, tunnel valleys and hydrological cycles. Quaternary Science Reviews, 16, pp 169–185.

Påsse T, 1997. A mathematical model of past, present and future shore level displacement in Fennoscandia. SKB TR 97-28, Svensk Kärnbränslehantering AB.

Rhén I, Forsmark T, Hartley L, Joyce S, Roberts D, Gylling B, Marsic N, 2009. Bedrock hydrogeology. Model testing and synthesis. Site descriptive modelling, SDM-Site Laxemar. SKB R-08-91, Svensk Kärnbränslehantering AB.

Rhén I, Follin S, Hermanson J, 2003. Hydrological site descriptive model – a strategy for its development during site investigations. SKB R-03-08, Svensk Kärnbränslehantering AB.

Rouhiainen P, Sokolnicki M, 2005. Difference flow logging in borehole KFM06A. Forsmark site investigation. SKB P-05-15, Svensk Kärnbränslehantering AB.

Röthlisberger H, 1972. Water pressure in intra- and subglacial channels. Journal of Glaciology, 11, pp 177–203.

Salas J, Gimeno M J, Auqué L F, Molinero J, Gómez J, Juárez I, 2010. SR-Site. Hydrogeochemical evolution of the Forsmark site. SKB TR-10-58, Svensk Kärnbränslehantering AB.

Selroos J-O, Follin S, 2010. Groundwater flow modelling methodology, setup and results – SR-Site Forsmark. SKB R-09-22, Svensk Kärnbränslehantering AB.

Sidborn M, Sandström B, Tullborg E-L, Delos A, Molinero J, Hallbeck L, Pedersen K, 2010. SR-Site: Oxygen ingress in the rock at Forsmark during a glacial. SKB TR-10-57, Svensk Kärnbränslehantering AB.

SKB, 2005a. Preliminary site description. Forsmark area – version 1.2. SKB R-05-18, Svensk Kärnbränslehantering AB.

SKB, 2005b. Programme for further investigations of geosphere and biosphere. Forsmark site investigation. SKB R-05-14, Svensk Kärnbränslehantering AB.

SKB, 2006. Climate and climate-related issues for the safety assessment SR-Can. SKB TR-06-23, Svensk Kärnbränslehantering AB.

SKB, 2008a. Site decription of Forsmark at completion of the site investigation phase. SDM-Site Forsmark. SKB TR-08-05, Svensk Kärnbränslehantering AB.

SKB, 2008b. Underground design Forsmark. Layout D. SKB R-08-116, Svensk Kärnbränslehantering AB

SKB, 2010. Climate and climate related issues for the safety assessment SR-Site. SKB TR-10-49, Svensk Kärnbränslehantering AB.

Starinsky A, Katz A, 2003. The formation of natural cryogenic brines. Geochimica et Cosmochimica Acta, 67, pp 1475–1484.

Stephens M B, Fox A, La Pointe P, Simeonov A, Isaksson H, Hermanson J, Öhman J, 2007. Geology Forsmark. Site descriptive modelling Forsmark stage 2.2. SKB R-07-45, Svensk Kärnbränslehantering AB.

Sundberg J, Back P-E, Ländell M, Sundberg A, 2009. Modelling of temperature in deep boreholes and evaluation of geothermal heat flow at Forsmark and Laxemar. SKB TR-09-14, Svensk Kärnbränslehantering AB.

Svensson U, 1999. Subglacial groundwater flow at Äspö as governed by basal melting and ice tunnels. SKB R-99-38, Svensk Kärnbränslehantering AB.

Svensson U, Follin S, 2010. Groundwater flow modelling of the excavation and operation phases – SR-Site Forsmark. SKB R-09-19, Svensk Kärnbränslehantering AB.

Svensson U, Ferry M, Kuylenstierna H-O, 2010. DarcyTools, Version 3.4. Concepts, methods, and equations. SKB R-07-38, Svensk Kärnbränslehantering AB.

Tarasov L, Peltier W R, 2004. A geophysically constrained large ensemble analysis of the deglacial history of the North American ice sheet complex. Quaternary Science Reviews, 23, pp 359–388.

Tarasov L, Peltier W R, 2007. Co-evolution of continental ice cover and permafrost extent over the last glacial-interglacial cycle in North America. Journal of Geophysical Research, 112, F02S08, doi:10.1029/2006JF000661.

van der Veen C J, 1998. Fundamentals of glacier dynamics. Rotterdam: Balkema.

van der Veen C J, 2007. Fracture propagation as means of rapidly transferring surface meltwater to the base of glaciers. Geophysical Research Letters, 34, L01501, doi:10.1029/2006GL028385.

Vidstrand P, 2003. Surface and subsurface conditions in permafrost areas – a literature review. SKB TR-03-06, Svensk Kärnbränslehantering AB.

Vidstrand P, Svensson U, Follin S, 2006. Simulation of hydrodynamic effects of salt rejection due to permafrost. Hydrogeological numerical model of density-driven mixing, at a regional scale, due to a high salinity pulse. SKB R-06-101, Svensk Kärnbränslehantering AB.

Vidstrand P, Näslund J-O, Hartikainen J, Svensson U, 2007. Hydrogeological flux scenarios at Forsmark. Generic numerical flow simulations and compilation of climatic information for use in the safety analysis SFR1 SAR-08. SKB R-07-63, Svensk Kärnbränslehantering AB.

Vilks P, 2007. Rock matrix permeability measurements on core samples from borehole KFM01D. Forsmark site investigation. SKB P-07-162, Svensk Kärnbränslehantering AB.

Walder J S, Fowler A, 1994. Channelized subglacial drainage over a deformable bed. Journal of Glaciology, 40, pp 3–15.

Walsh R, Avis J, 2010. Glacial scenario: groundwater and radionuclide transport studies. NWMO TR-2010-09, Nuclear Waste Management Organization, Canada.

Wang H F, 2000. Theory of linear poroelasticity: with applications to geomechanics and hydrogeology. Princeton, N.J.: Princeton University Press.

Weertman J, 1972. General theory of water flow at the base of a glacier or ice sheet. Review of Geophysics and Space Physics, 10, pp 287–333.

Williams P J, Smith M W, 1989. The frozen earth: fundamentals of geocryology. Cambridge: Cambridge University Press.

Appendix A

Permafrost modelling

A.1 Introduction

The ice module in DarcyTools is used to simulate the effect of permafrost (frozen ground conditions) on the permeability for groundwater flow. The module is driven by the specified boundary conditions, i.e. the temperature at the ground surface and the geothermal heat flux. The creation of taliks (unfrozen locations) depends on the specified conditions.

The ice module presently works with one set of thermal properties and does not capture all physical and chemical aspects of permafrost. For example, salt rejection is ignored, which means that water freezes without accounting for its original salinity, and hence the salinity of the remaining unfrozen water is unaffected. Further, the module does not change the transport porosity for particle tracking.

A.2 Objectives

This appendix describes the main features of the ice module in DarcyTools and how these affect the permeability within the model domain. Further, it includes a brief description of the permafrost modelling by /Hartikainen et al. 2010/ and results from a simulation conducted with DarcyTools are compared with results provided by /Hartikainen et al. 2010/.

A.3 Essentials of the permafrost module in DarcyTools

In order to account for the phase change of water when the temperature is below the melting-point (freezing) material properties need to be changed. The kinematic porosity is retained, changed by a content of ice.

$$\phi_i = ic\ \phi$$
$$\phi_f = (1-ic)\ \phi \qquad \text{(A-1)}$$

where ϕ [-] is the kinematic porosity, the indices i and f stand for ice and fluid, respectively, and ic [-] is an ice content function:

$$ic = ic_{\max}\left(1-\exp(-\beta)\right)$$
$$\beta = \left(\frac{\min\{T, T_L\} - T_L}{w}\right)^2 \qquad \text{(A-2)}$$

where ic_{max} is the fraction of the total kinematic porosity available for ice, typically 1, T [K] is the prevailing temperature, T_L is the freezing-point temperature, typically 0°C, and w [-] is a freezing parameter that depends on the *in situ* conditions.

Figure A-1 illustrates how the setting of the w parameter influences the relative ice content simulated in DarcyTools. The shape may be matched to fit empirical curves reported in literature. It should be observed that no information is found for till or fractured crystalline rock.

In the permafrost modelling by /Hartikainen et al. 2010/, till is assumed to be equivalent to silt and fractured crystalline rock is assumed to be equivalent to sand. Figure A-2 presents the curves for clay, silt/till, and sand/rock used by /Hartikainen et al. 2010/. The three curves shown to the right in Figure A-2 represent atmospheric pressure conditions and should be used in a comparison with Figure A-1. (In Figure A-2, an unfrozen water content of 0 means an ice content of 1.)

The change in permeability k [L^2] due to freezing is modelled as:

$$k = \alpha\ k_{ref} \qquad \text{(A-3)}$$

$$\alpha = \max[\alpha_{\min}, (1-ic)^a] \qquad \text{(A-4)}$$

where α [-] is a reduction factor, k_{ref} [L^2] is the initial (unfrozen) permeability, α_{min} [-] is the maximum allowed reduction factor, and a [-] is a material dependant constant. Figure A-3 shows how the

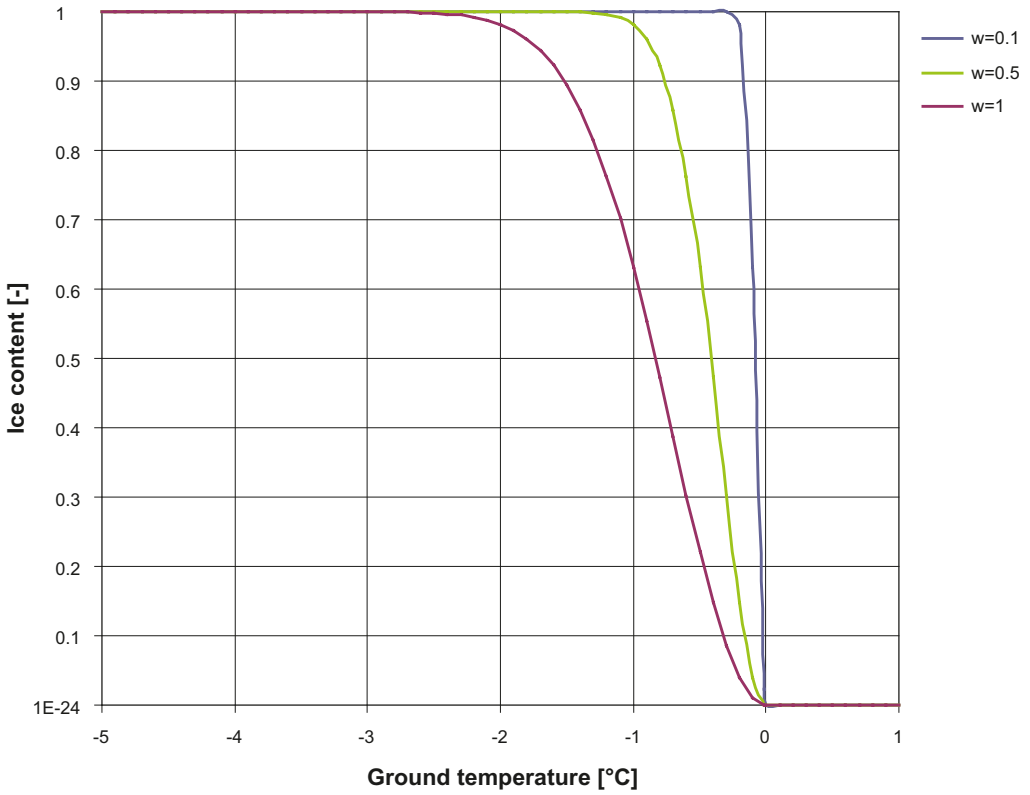

Figure A-1. *Ice content as a function of the freezing interval parameter w [-].*

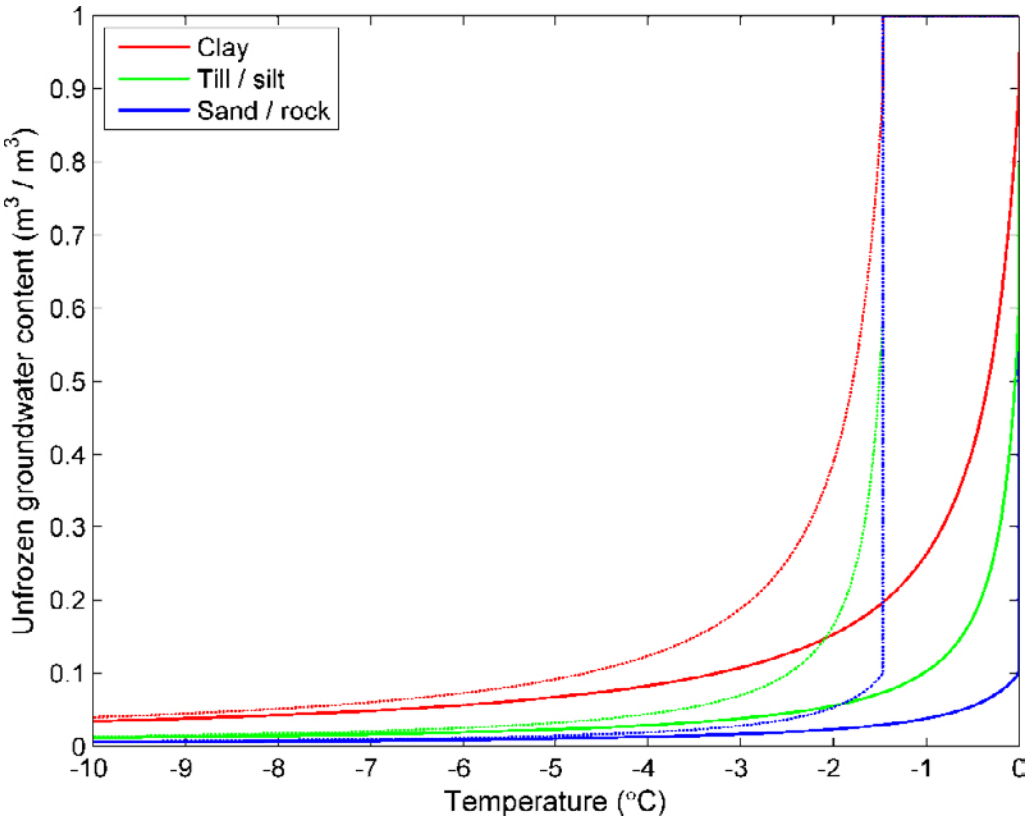

Figure A-2. *Unfrozen volumetric groundwater content versus temperature in different geological materials for a constant salinity concentration of 2% by weight and a water pressure of 5 MPa (the three graphs peaking at –1.5°C), and for zero salinity and reference water pressure (the three graphs peaking at 0°C). (Source: Figure 3-1 in /Hartikainen et al. 2010/.)*

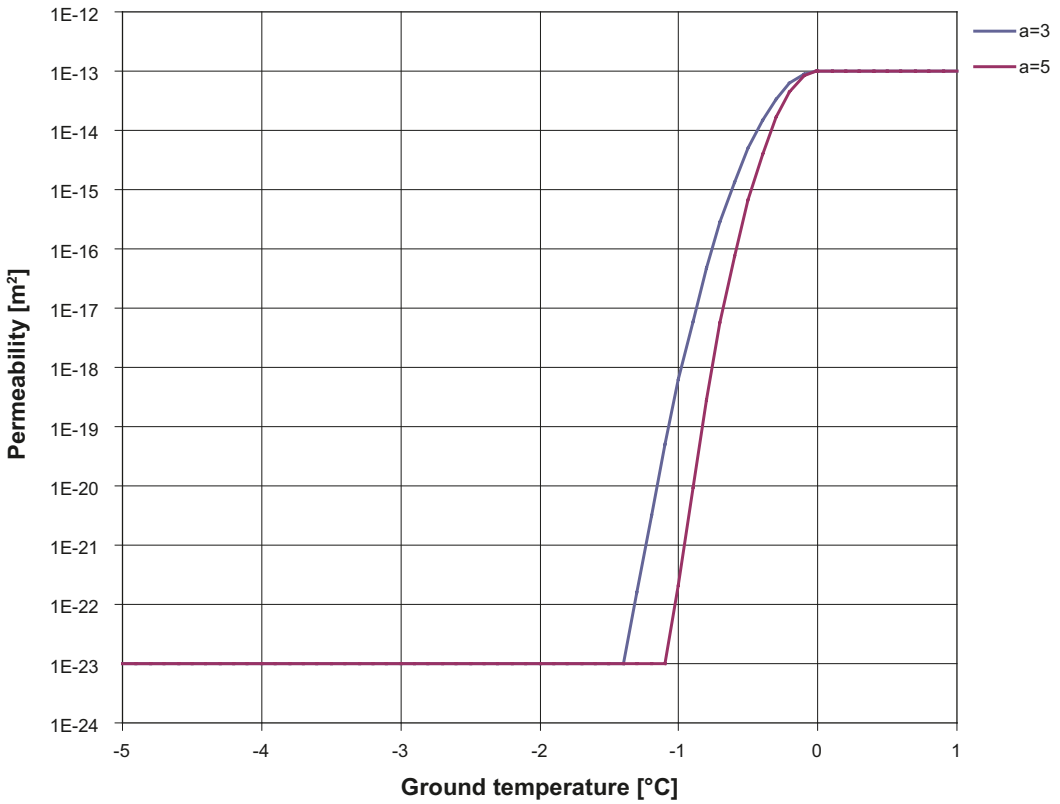

Figure A-3. *Permeability of frozen ground for different values of* a*. In these graphs, the maximum allowed reduction is set to ten orders of magnitude and w is set to 0.5.*

frozen ground permeability depends on the value of *a*. Different combinations of *w* and *a* makes it possible to match most empirical curves reported. Again, it should be observed that no information on *a* typical for till and fractured crystalline has been found in the literature.

A.4 Work by /Hartikainen et al. 2010/

The study of /Hartikainen et al. 2010/ is a direct continuation of the one-dimensional modelling work done in SR-Can /SKB 2006, Section 3.4 and 4.4.1/. It provides a numerical estimation of the development of permafrost and frozen ground in a 2-D vertical cross-section for site-specific subsurface conditions and surface conditions at the Forsmark site.

The permafrost simulations are carried out for 15 km long and 10 km deep vertical cross-sections using site-specific data from Forsmark (see Figure A-4). The same climate characteristics as used for the last glacial cycle in the SR-Can permafrost simulations are simulated again, this time for the period 115–70 ka BP, i.e. for the ice-free period up to the first phase of ice sheet coverage in the safety assessment reconstruction of the last glacial cycle, see /SKB 2006, 2010/.

The model by /Hartikainen et al. 2010/ handles all physical aspects of the phase change and is also able to work with a multitude of different material property units for thermal properties as well as for hydrogeological properties. Figure A-5 illustrates the detailed thermal diffusivity used by /Hartikainen et al. 2010/.

A.5 Numerical simulation with DarcyTools

Figure A-6 shows the results of a DarcyTools simulation in comparison with the results of two main cases studied by /Hartikainen et al. 2010/. The DarcyTools results fall in between the two bounding curves from /Hartikainen et al. 2010/ with a closer match to the humid case. The thermal properties used for the permafrost simulation with DarcyTools are based on estimated mean values taken from /Hartikainen et al. 2010/. The ground surface temperature sequence in DarcyTools is the same as in /Hartikainen et al. 2010/ and is reported in /SKB 2010/**.**

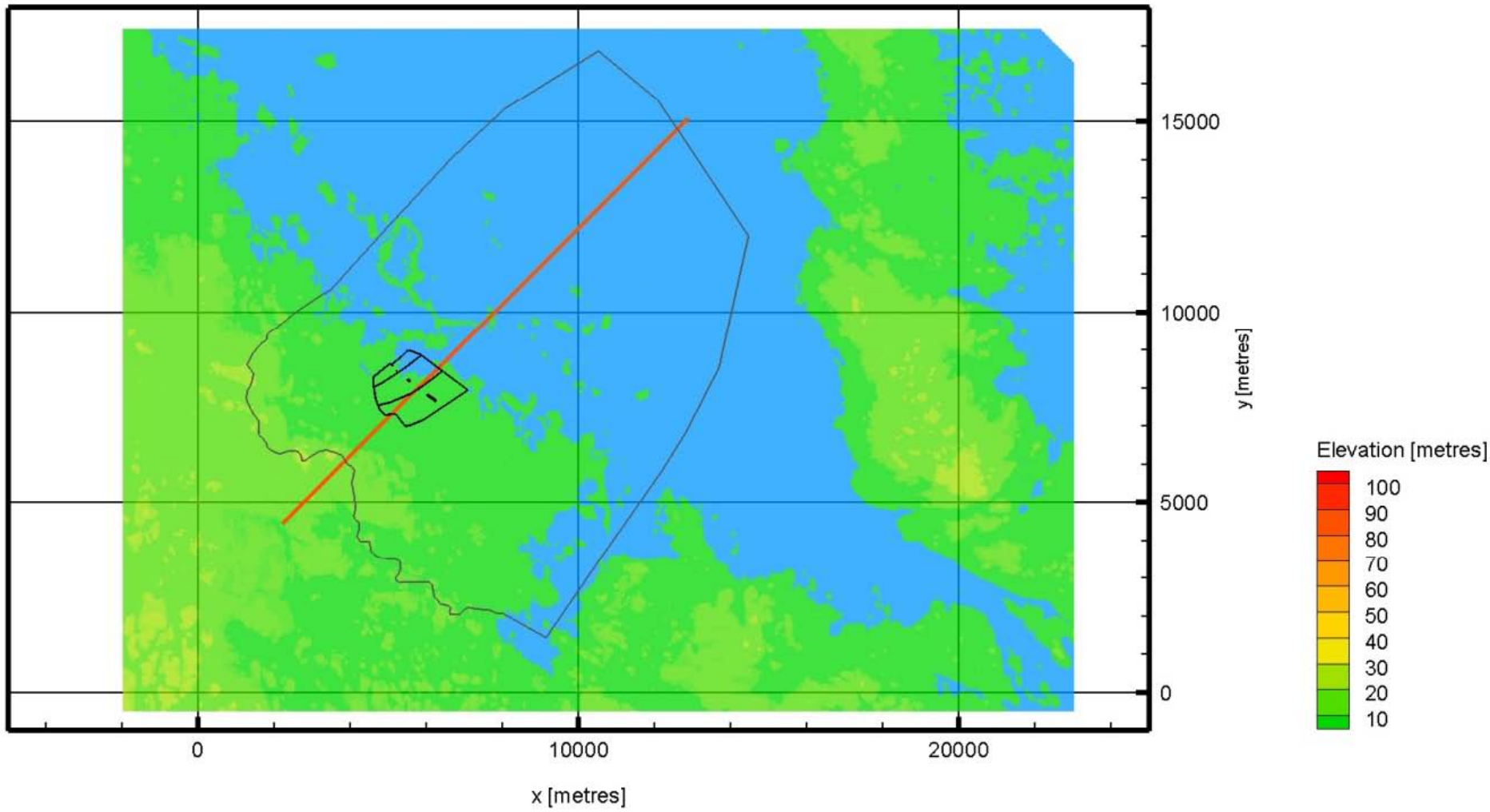

Figure A-4. *The location of the 2-D section used in /Hartikainen et al. 2010/ within a sub-volume of the domain used in this work.*

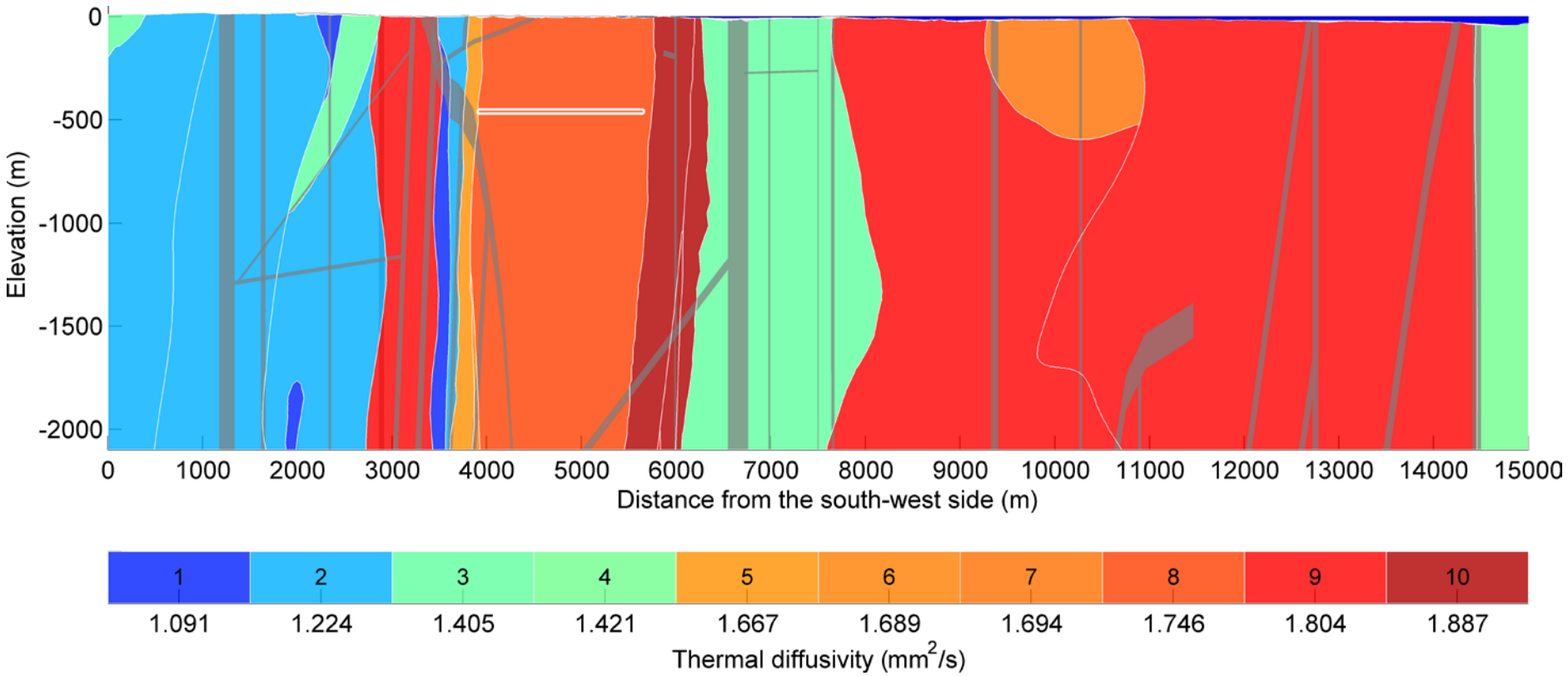

Figure A-5. *Illustration of the detailed information used by /Hartikainen et al. 2010/ on different thermal property units. Taken from /Hartikainen et al. 2010/.*

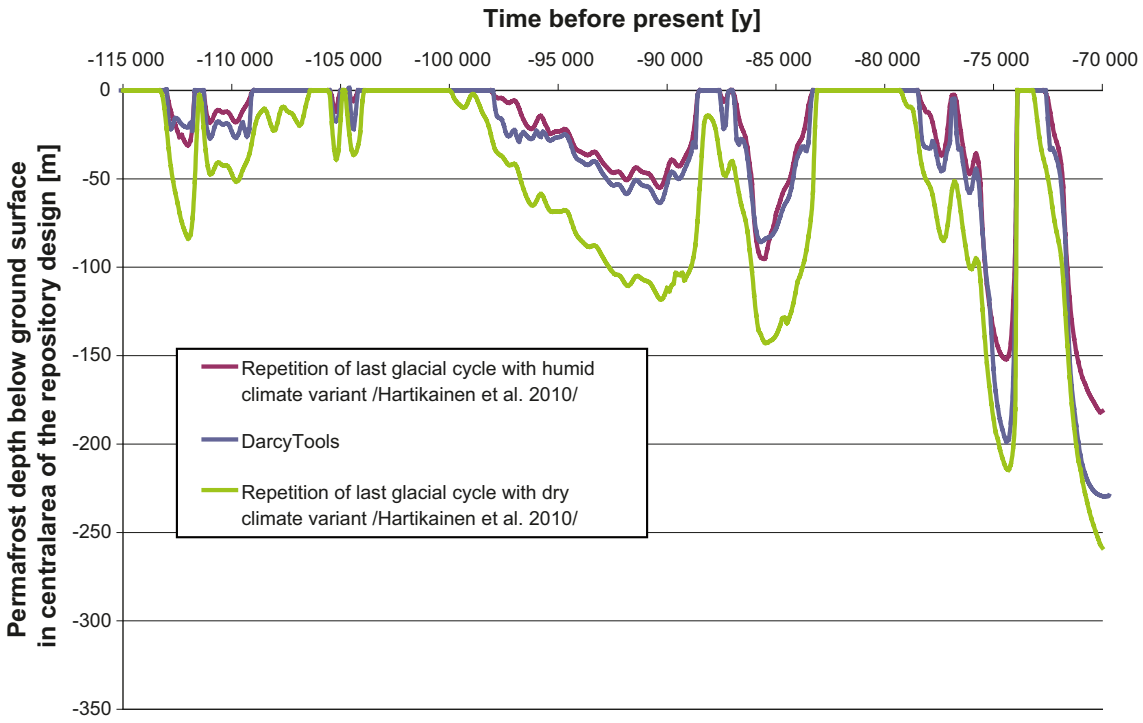

Figure A-6. *Permafrost depth from DarcyTools in comparison with the two main cases in /Hartikainen et al. 2010/.*

A.6 Summary and conclusions

A comparative simulation has been conducted in DarcyTools in order to compare the overall behavior of the permafrost module in DarcyTools with a physically more complete code used in SR-Site and reported in /Hartikainen et al. 2010/. The simulation with DarcyTools is found to produce results of permafrost depth within the recognised uncertainty bounds estimated in different simulation cases by /Hartikainen et al. 2010/.

Appendix B

Parameters for HRD modelling

B.1 Introduction

This appendix presents the model parameters used in DarcyTools for generating stochastic hydrogeological discrete fracture network (DFN) properties of the fracture domains within the candidate area. The up-scaling of these properties to equivalent continuous porous medium (ECPM) properties is performed inside the code DarcyTools, see /Svensson et al. 2010/ for details. This appendix specifies also the hydraulic continuous porous media (CPM) properties used for the fracture domain located outside the candidate area.

B.2 Fracture size-intensity relationship

In DarcyTools, the number of fractures (n) in the size range [L, $L+dL$] may be calculated as:

$$n = I\left[\left(\frac{L+dL}{L_{ref}}\right)^{D} - \left(\frac{L}{L_{ref}}\right)^{D}\right] / D \qquad \text{(B-1)}$$

where I is the number of fractures of size L_{ref} per unit volume and D is the exponent (shape factor) of a power law size distribution. The relationships between the notation used in DarcyTools and that reported for SDM-Site Forsmark may be written as:

$$L_0 = r_0 \cdot \sqrt{\pi} \qquad \text{(B-2)}$$

$$I = P_{32}[r_0, \infty] \cdot L_0^{(k_r-2)} \cdot (k_r - 2) / L_{ref}^{k_r} \qquad \text{(B-3)}$$

$$D = -k_r \qquad \text{(B-4)}$$

$$\lambda_1 = \cos(90-tr) \cdot \cos(pl) \cdot \kappa \qquad \text{(B-5)}$$

$$\lambda_2 = \sin(90-tr) \cdot \cos(pl) \cdot \kappa \qquad \text{(B-6)}$$

$$\lambda_3 = -\sin(pl) \cdot \kappa \qquad \text{(B-7)}$$

where L_0 [m] equals the side length of the smallest fracture generated (represented as a square), r_0 [m] is its equivalent radius and $P_{32}[r_0,\infty]$ [L^2/L^3] is the fracture surface area per unit volume for all fractures in the size range [r_0,∞]. Each fracture set is assumed to obey a Fisher distribution of its own, which is characterised by a Fisher concentration κ, a mean trend tr and a mean plunge pl. Moreover, the sizes of the generated fractures are assumed to be power-law distributed, with one shape factor k_r per fracture set. The orientations of the generated fractures are fully described by λ_1–λ_3, which are the normal vectors.

The relationship between the incremental fracture intensity, $P_{32}[r_1, r_2]$, and the total intensity, $P_{32}[r_0,\infty]$, may be written as:

$$P_{32}[r_1, r_2] = P_{32}[r_0, \infty]\left(\frac{(r_1)^{(2-k_r)} - (r_2)^{(2-k_r)}}{(r_0)^{(2-k_r)}}\right) \qquad \text{(B-8)}$$

B.3 Fracture input statistics

Table B-1. Parameter values used in the present report for fracture domains FFM01 and FFM06 (Appendix C in /Follin 2008/).

Elevation [m RHB 70]	Fracture set name	Orientation set pole: (trend, plunge), conc. κ [°,°, -]	Size model, power-law (r_0, k_r) [m, -]	Intensity ($P_{32,open}$) [m^2/m^3]	Transmissivity model constants Equation (3-4)
> –200	NS	(292, 1) 17.8	(0.038, 2.50)	0.073	$(a,b,\sigma_{logT}) = (6.3 \cdot 10^{-9}, 1.3, 1.0)$
	NE	(326, 2) 14.3	(0.038, 2.70)	0.319	
	NW	(60, 6) 12.9	(0.038, 3.10)	0.107	
	EW	(15, 2) 14.0	(0.038, 3.10)	0.088	
	HZ	(5, 86) 15.2	(0.038, 2.38)	0.543	
–200 to –400	NS	As above	As above	0.142	$(a,b,\sigma_{logT}) = (1.3 \cdot 10^{-9}, 0.5, 1.0)$
	NE	As above	As above	0.345	
	NW	As above	As above	0.133	
	EW	As above	As above	0.081	
	HZ	As above	As above	0.316	
< –400	NS	As above	As above	0.094	$(a,b,\sigma_{logT}) = (5.3 \cdot 10^{-11}, 0.5, 1.0)$
	NE	As above	As above	0.163	
	NW	As above	As above	0.098	
	EW	As above	As above	0.039	
	HZ	As above	As above	0.141	

Table B-2. DFN parameter values used in the present report for fracture domains FFM01 and FFM06.

Set	λ_1 [-]	λ_2 [-]	λ_3 [-]	D [-]	L_{ref} [m]	I: > –200 [m^{-3}]	I: –200 to –400 [m^{-3}]	I: < –400 [m^{-3}]
NS	–16.50136	6.66698	–0.31065	–2.50	1	0.00955	0.018579	0.012299
NE	–7.99159	11.84802	–0.49906	–2.70	1	0.03383	0.036584	0.017285
NW	11.11053	6.41467	–1.34842	–3.10	1	0.00605	0.007524	0.005544
EW	3.62126	13.51472	–0.48859	–3.10	1	0.00498	0.004582	0.002206
HZ	0.09241	1.05626	–15.16297	–2.38	1	0.07600	0.044227	0.019734

Table B-3. Transmissivity values used in Equation 4-20 for fracture domains FFM01 and FFM06.

Elevation [m RHB 70]	a_T [m^2/s]	b_T [-]	c_T [m^2/s]	d_T [-]
> –200	$1.19 \cdot 10^{-06}$	1.3	1	2.0
–200 to –400	$9.76 \cdot 10^{-09}$	0.5	1	2.0
< –400	$3.98 \cdot 10^{-10}$	0.5	1	2.0

Table B-4. Parameter values used in the present report for fracture domain FFM02.

Elevation [m RHB 70]	Fracture set name	Orientation set pole: (trend, plunge), conc. κ [°,°, -]	Size model, power-law (r_0, k_r) [m, -]	Intensity ($P_{32,open}$) [m^2/m^3]	Transmissivity model constants Equation (3-4)
> –200	NS	(292, 1) 17.8	(0.038, 2.75)	0.342	$(a,b,\sigma_{logT}) = (9.0 \cdot 10^{-9}, 0.7, 1.0)$
	NE	(326, 2) 14.3	(0.038, 2.62)	0.752	
	NW	(60, 6) 12.9	(0.038, 3.20)	0.326	
	EW	(15, 2) 14.0	(0.038, 3.40)	0.156	
	HZ	(5, 86) 15.2	(0.038, 2.58)	1.582	

Table B-5. DFN parameter values used in the present report for fracture domains FFM02.

Set	λ_1 [-]	λ_2 [-]	λ_3 [-]	D [-]	L_{ref} [m]	I: > –200 [m^{-3}]
NS	–16.50136	6.66698	–0.31065	–2.75	1	0.033937
NE	–7.99159	11.84802	–0.49906	–2.62	1	0.087765
NW	11.11053	6.41467	–1.34842	–3.20	1	0.015786
EW	3.62126	13.51472	–0.48859	–3.40	1	0.005000
HZ	0.09241	1.05626	–15.16297	–2.58	1	0.192637

Table B-6. Transmissivity values used in Equation 4-20 for fracture domains FFM02.

Elevation [m RHB 70]	a_T [m^2/s]	b_T [-]	c_T [m^2/s]	d_T [-]
> –200	$1.51 \cdot 10^{-07}$	0.7	1	2.0

Table B-7. Parameter values used in the present report for fracture domains FFM03–FFM05. Transmissivity is increased by a factor 2 for fracture domain FFM04 (Appendix C in /Follin 2008/).

Elevation [m RHB 70]	Fracture set name	Orientation set pole: (trend, plunge), conc. κ [°,°, -]	Size model, power-law (r_0, k_r) [m, -]	Intensity ($P_{32,open}$) [m^2/m^3]	Transmissivity model constants Equation (3-4)
> –400	NS	(292, 1) 17.8	(0.038, 2.60)	0.091	$(a,b,\sigma_{logT}) = (1.3 \cdot 10^{-8}, 0.4, 0.8)$
	NE	(326, 2) 14.3	(0.038, 2.50)	0.253	
	NW	(60, 6) 12.9	(0.038, 2.55)	0.258	
	EW	(15, 2) 14.0	(0.038, 2.40)	0.097	
	HZ	(5, 86) 15.2	(0.038, 2.55)	0.397	
< –400	NS	As above	As above	0.102	$(a,b,\sigma_{logT}) = (1.8 \cdot 10^{-8}, 0.3, 0.5)$
	NE	As above	As above	0.247	
	NW	As above	As above	0.103	
	EW	As above	As above	0.068	
	HZ	As above	As above	0.250	

Table B-8. DFN parameter values used in the present report for fracture domains FFM03–FFM05.

Set	λ_1 [-]	λ_2 [-]	λ_3 [-]	D [-]	L_{ref} [m]	I: > –400 [m^{-3}]	I: < –400 [m^{-3}]
NS	–16.50136	6.66698	–0.31065	–2.60	1	0.010854	0.012166
NE	–7.99159	11.84802	–0.49906	–2.50	1	0.033102	0.032317
NW	11.11053	6.41467	–1.34842	–2.55	1	0.032344	0.012912
EW	3.62126	13.51472	–0.48859	–2.40	1	0.013477	0.009448
HZ	0.09241	1.05626	–15.16297	–2.55	1	0.049769	0.031341

Table B-9. Transmissivity values used in Equation 4-20 for fracture domains FFM03–FFM05. Parameter a_T for FFM04 is multiplied by two.

Elevation [m RHB 70]	a_T [m²/s]	b_T [-]	c_T [m²/s]	d_T [-]
> –400	$6.52 \cdot 10^{-08}$	0.4	1	1.6
< –400	$6.04 \cdot 10^{-08}$	0.3	1	1.0

For the region inside the six fracture domains FFM01–FFM06, approximate homogeneous CPM properties of the flow-wetted fracture surface area per unit volume of rock mass (a_r) are based on the data provided by /Joyce et al. 2010, Appendix C/, see Table B-10. A depth dependency is suggested in accordance with the depth zonations used for fracture domains FFM01 and FFM06, see Table B-1.

For the region outside the six fracture domains FFM01–FFM06, i.e. on a regional scale, there is no site-specific DFN information available in the rock mass volumes between deformation zones in SDM-Site. The approximate values of homogeneous CPM properties (hydraulic conductivity (K), kinematic porosity (f), and flow-wetted fracture surface area per unit volume of rock mass (a_r) used in SDM-Site are given in Table B-11. A depth dependency is suggested in accordance with the depth zonations used for fracture domains FFM01 and FFM06, see Table B-1.

Table B-10. Specific flow-wetted fracture surface area per unit volume of rock applied for the fracture domains inside the target area/volume, FFM01–06. (Modified after Table C-2 in /Joyce et al. 2010/.)

Elevation [m RHB 70]	FFM01, FFM06 a_r [m²/m³]	FFM02 a_r [m²/m³]	FFM03, FFM05 a_r [m²/m³]	FFM04 a_r [m²/m³]
> –200	0.30	0.66	0.18	0.18
–200 to –400	0.08	–	0.18	0.18
< –400	0.02	–	0.10	0.10

Table B-11. Homogeneous continuous porous media (CPM) properties applied in hydraulic rock domains outside FFM01–FFM06. (Source: Table 2-6 in /Selroos et al. 2010/.)

	CPM properties outside FFM01–FFM06		
Elevation [m RHB 70]	K [m/s]	ϕ [-]	a_r [m²/m³]
> –200	$1 \cdot 10^{-7}$	$1 \cdot 10^{-5}$	0.60
–200 to –400	$1 \cdot 10^{-8}$	$1 \cdot 10^{-5}$	0.30
< –400	$3 \cdot 10^{-9}$	$1 \cdot 10^{-5}$	0.30

The general approach in DarcyTools is to specify the fracture thickness b_f [L] and the fracture kinematic porosity f_f [-] of the stochastically generated fractures by fracture set and by fracture size interval. Hence, in DarcyTools there is no direct relationship between transmissivity and transport aperture similar to Equation 4-18, but the fracture transport aperture is obtained from the thickness-porosity product, i.e.

$$(e_t)_f = b_f \, \phi_f \tag{B-9}$$

In the work reported here all stochastically generated fractures have the same values of the fracture thickness and the fracture kinematic porosity. The values used are presented in Table B-12 together with some other fracture specifications.

Table B-12. Additional specifications used in DarcyTools.

Specification	Value	Minimum value
Generated fracture size interval	15–1,000 [m][4]	
Fracture thickness	0.1 [m]	
Fracture kinematic porosity	$1 \cdot 10^{-3}$ [-]	
Diffusion coefficient in free water	$1 \cdot 10^{-10}$ [m^2/s]	
Minimum grid cell hydraulic conductivity[3]		$3 \cdot 10^{-11}$ [m/s] (~ $4 \cdot 10^{-18}$ [m^2])
Grid cell hydraulic conductivity below –1,000 m Grid cell hydraulic conductivity below –1,600 m		$5 \cdot 10^{-10}$ [m/s] (~ $6.7 \cdot 10^{-17}$ [m^2]) $5 \cdot 10^{-11}$ [m/s] (~ $6.7 \cdot 10^{-18}$ [m^2])
Minimum grid cell kinematic porosity[3]		$1 \cdot 10^{-5}$ [-]

[3] Used for cells without fractures

[4] This data range refers to square-shaped fractures. The interval for disc-shaped fractures is 8.5–564 m.

Isostasy is not accounted for in the work reported here but the potential impact on groundwater flow of an uneven surface loading at the ice sheet terminus (the forebulge phenomenon) is addressed here by changing the transmissivity of all deformation zones and fractures that strike towards northwest based on the results from the rock mechanics modelling conducted for SR-Site /Hökmark et al. 2010, Lönnqvist and Hökmark 2010/, see Table B-13.

Table B-13. Multiplication factors for transmissivity of all deformation zones and fractures that strike towards northwest in the THM variant (case (c) in Table 1-1).

Elevation [m RHB 70]	Multiplication factor [-]
> –200	7
–200 to –400	3
–400 to –1,000	1.5
< –1,000	1

Appendix C

Compilation of input files

Name of file in DarcyTools	Date	Name of file at delivery
HCD		
HCDcage	2008-10-08	081006_sheet_joints_v5.zip
HCD	2009-04-24	0900423_DZ_PFM_REG_v22_SJ_r2._dt.zip
DEM		
topxyz.dat	2009-01-26	fm.50
REPOSITORY LAYOUT		
(only used for visualisation)		
scenario_1.stl	2008-12-19	senario_1.stl
scenario_2.stl	2008-12-23	senario_2.stl
scenario_3.stl	2008-12-27	senario_3.stl
OTHER GEOMETRIES		
WD.dat (Water Divide)	2009-04-20	boundary2.stl
PROPERTY FILE	2009-05-06	Forsmarkproperty20090428.xlsx
ICE SHEET PROFILE	2009-07-03	y3a_row21_at_time_14.300BP_2.xls
DEPOSITION HOLE	2009-05-06	fs_Q1_2000_pline_merged.ptb

A list of all input files above, including storage location, is for traceability documented in the SKB data base SKBdoc under id nr 1271535.

Appendix D

Groundwater salinity

D.1 Introduction

It has been suggested that an understanding of the evolution of salinity throughout geological time is a powerful tool to predict the future development of groundwater flow and its chemical composition /NEA-OECD 1993, Bath and Lalieux 1999/. In this appendix, the data support for the applied initial and boundary conditions during periods with periglacial and glacial climate conditions is discussed, in particular the data support for assuming a fixed (undisturbed) groundwater salinity on the bottom boundary of the model domain during glaciation and deglaciation.

D.2 Invoked assumptions and their data support

D.2.1 Assumptions

The initial hydrochemical conditions used in the work reported are the same as those used in SDM-Site, see Table 5-2, i.e. the increase in salinity with depth in the fracture water is assumed to be similar to that observed in the matrix porewater at the start of the flow simulations, but with a small difference in the increase rate between the target area/volume and the rest of the model domain. This to reflect the observed contrasts in fracture frequency and fracture transmissivity. Second, during the pre-LGM, LGM and post-LGM stages, the initial fracture water salinity in the grid cells on the bottom boundary is fixed as specified in Table 5-3 and Table 5-4.

The assumption of a fixed fracture water salinity on the bottom boundary of the model domain is supported by a low hydraulic conductivity at depth. In the model, the grid cell hydraulic conductivity is set to $5 \cdot 10^{-10}$ m/s in all grid cells below –1,000 m elevation and to $5 \cdot 10^{-11}$ m/s in all grid cells below –1,600 m elevation, see Table B-12. Further, the minimum value of the grid cell kinematic porosity is set to $1 \cdot 10^{-5}$, implying a total fracture aperture of 1 mm/100 m of rock, see Appendix B and Table B-12. This minimum value is assigned to grid cell not intersected by fractures. Grid cells intersected by fractures have an order of magnitude or more higher grid cell kinematic porosities.

D.2.2 Hydraulic data support

Table D-1 shows the hydraulic conductivity/permeability of intact rock cores gathered at Forsmark. These values are determined in the laboratory and range between approximately 10^{-15} to 10^{-12} m/s ($\sim 10^{-22}$ to 10^{-19} m^2).

The low hydraulic conductivity observed in the laboratory samples is supported by the field data shown in Figure D-1 and Figure D-2. Figure D-1 shows a cumulative distribution plot of 151 $\log_{10}(K_{PSS})$ data measured with the Pipe String System (PSS) and a packer spacing (test scale) of 20 m in the depth interval –400 to –700 m. Approximately 90 % of the PSS data set have values below –10.4 (or $4 \cdot 10^{-11}$ m/s) which is the robust lower measurement limit of the PSS method.

The fracture transmissivity data acquired with the Posiva Flow Log (PFL) shown in Figure 3-12 are repeated in Figure D-2. The data come from the rock mass volumes between the deterministically modelled deformation zones in the target area/volume. Above –200 m elevation, the conductive fracture frequency is much higher than below this elevation. In fact, there are hardly any conductive fractures below –400 m elevation[14]. The decrease in fracture transmissivity is not as significant as the decrease in frequency, although the highest transmissivity values are clearly observed above –200 m elevation.

[14] It is noted that the data occurring around –450 m elevation are observed in the cored borehole KFM02A at drill site 2. This segment of KFM02A intersects the rock mass volume sandwiched in between two deformation zones, ZFMA2 and ZFMF1, and is not part of the planned repository volume. In conclusion, the fractured rock mass volumes between the deterministically modelled deformation zones look very different above and below approximately –400 m elevation from a safety assessment point of view.

Table D-1. Average permeability and hydraulic conductivity values for confining pressures greater than 14 MPa. A = parallel to core axis, B = normal to core axis. Sample positions along the borehole are shown between parentheses /Vilks 2007/.

Sample	Permeability [m2]	Hydraulic conductivity [m/s]
KFM01D–3A (254.93–255.03)	$(6.8 \pm 1.6) \cdot 10^{-20}$	$(5.9 \pm 1.4) \cdot 10^{-13}$
KFM01D–3B (254.93–255.03)	$(1.3 \pm 0.9) \cdot 10^{-20}$	$(1.1 \pm 0.8) \cdot 10^{-13}$
KFM01D–8A (499.90–500.00)	$7.4 \cdot 10^{-22}$	$6.4 \cdot 10^{-15}$
KFM01D–12A (700.07–700.17)	$(2.5 \pm 0.7) \cdot 10^{-19}$	$(2.2 \pm 0.6) \cdot 10^{-12}$
KFM01D–13A (747.09–747.19)	$(9.2 \pm 1.5) \cdot 10^{-21}$	$(8.0 \pm 1.3) \cdot 10^{-14}$
KFM01D–13B (747.09–747.19)	$(2.9 \pm 1.8) \cdot 10^{-21}$	$(2.5 \pm 1.3) \cdot 10^{-14}$
KFM01D–14A* (790.38–790.48s)	$(4 \pm 5) \cdot 10^{-21}$	$(4 \pm 4) \cdot 10^{-14}$

*Average for confining pressures from 2.2 to 2.7 MPa.

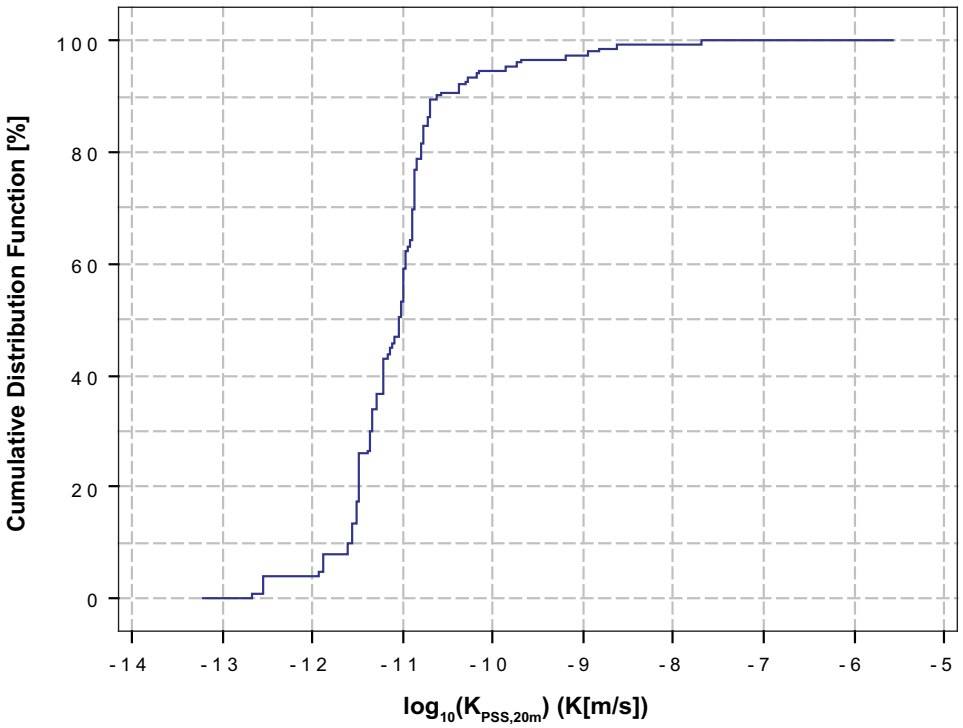

Figure D-1. *Cumulative distribution plot of 151 $\log_{10}(K_{PSS})$ data measured with a packer spacing (test scale) of 20 m between elevations –400 m to –700 m within the target area/volume at Forsmark. (Source: Figure 2-7 in /Selroos and Follin 2010/.) The robust lower measurement limit of the PSS method is $4 \cdot 10^{-11}$ m/s ($\log (K_{pss,\ 20\ m}) = -10.4$).*

Figure D-2. *PFL transmissivities in boreholes KFM01A, -01D, -02A, -04A to -08A, -08C and -08D outside deformation zones within the target area/volume.*

Figure D-3 shows Terzaghi corrected frequencies of open fractures and of flowing fractures (detected with the PFL method) in the target area/volume. Figure D-5 shows also the specific capacities of the flowing fractures. At repository depth, the mean value of the Terzaghi corrected frequency of flowing fractures detected with the PFL method is very low, approximately 0.005 fractures per metre (5/km). The geometric mean of the specific capacity is also low, approximately $6.5 \cdot 10^{-9}$ m^3/s per metre of head change. The product of these two values suggest an equivalent hydraulic conductivity of approximately $3.3 \cdot 10^{-11}$ m/s (~$3.3 \cdot 10^{-18}$ m^2) for 200-m blocks of rock located below –400 m elevation. The validity of this simple calculation is confirmed by the measurements conducted with the PSS method shown in Figure D-3.

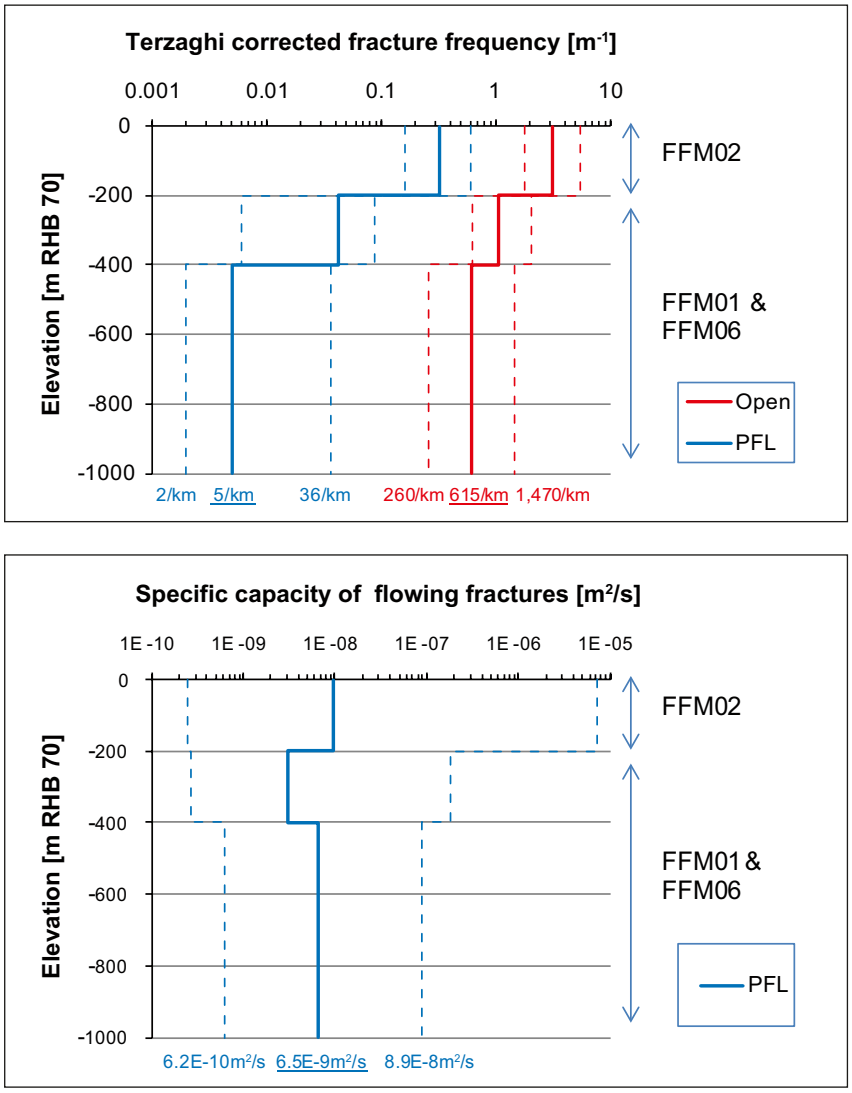

Figure D-3. *Top: Terzaghi corrected frequencies of open fractures and of the flowing fractures detected with the PFL method. Bottom: Specific capacities of the flowing fractures detected with PFL method. The thicker lines represent the geometric means over all boreholes and the thinner lines represent the spread between individual boreholes, i.e. the minimum and maximum values observed in any borehole. (Source: Figure 2-9 in /Selroos and Follin 2010/.)*

D.2.3 Hydrochemical data support

The bedrock is investigated to approximately –1,000 m elevation at Forsmark, see Figure D-4. The measured fracture water salinity at this elevation is approximately 1.4%. At repository depth, the fracture water salinity is approximately 0.9 %.

The deepest borehole investigated by SKB is borehole KLX02 at Laxemar. The vertical depth of KLX02 is 1,660 m and the salinity at the bottom of KLX02 is approximately 8 %, see Figure D-5. The increase in the fracture water salinity shown in Figure D-4 is inserted in Figure D-5 for the sake of comparison.

The left plot in Figure D-6 shows fracture water and matrix porewater salinity data from two boreholes (KFM01D and KFM06A) drilled through the target area/volume at Forsmark, i.e. through fracture domains FFM02 and FFM01, see Chapter 3. The salinity data shown in Figure D-6 suggest that the salinities of the fracture water and of the matrix porewater are more or less identical in the uppermost 200 m of the bedrock, i.e. where the conductive fracture intensity is high, see Figure D-3. In the interval –300 m to –600 m elevation, the conductive fracture water frequency drops significantly and the

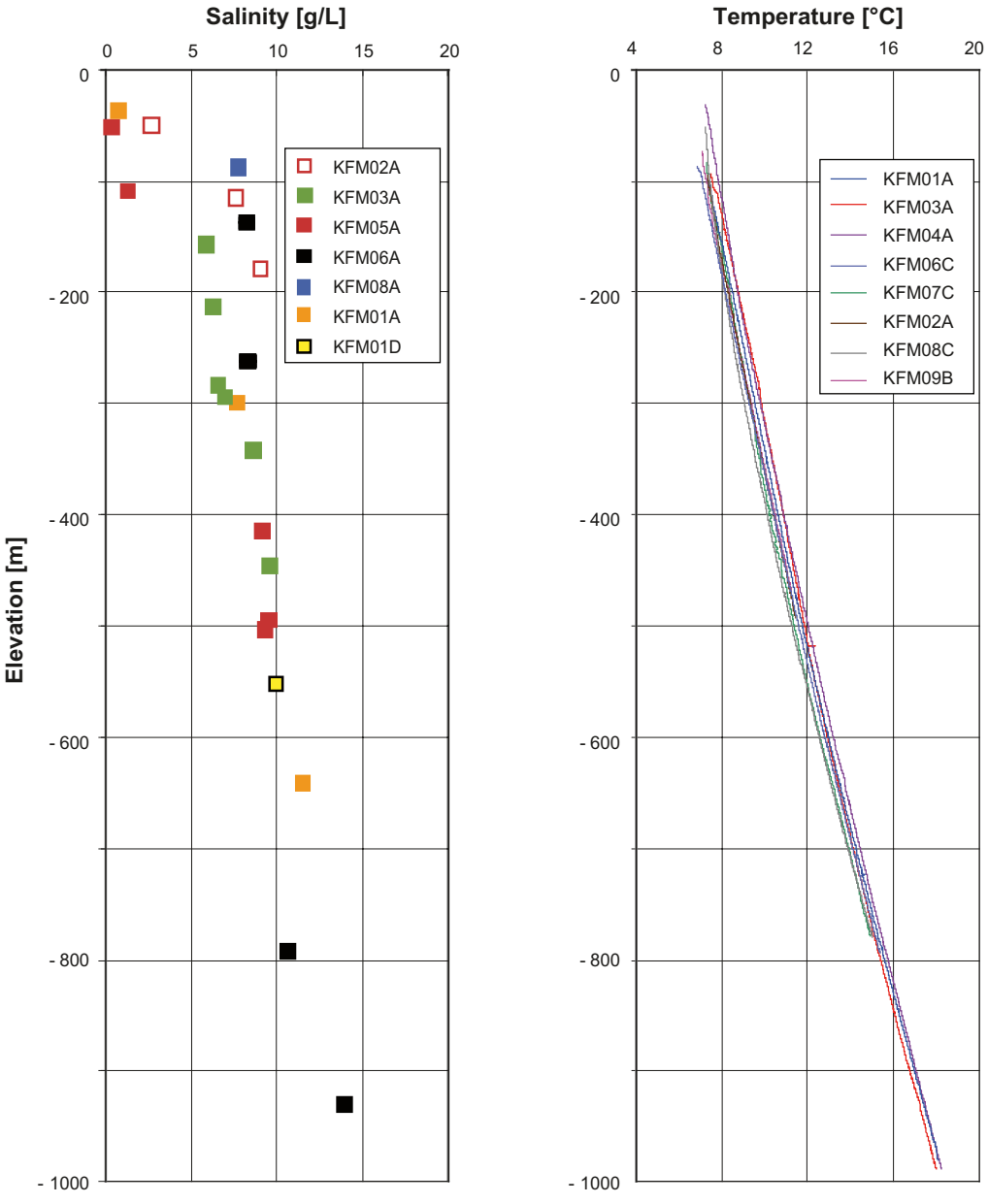

Figure D-4. *Compilation of high-quality fracture water salinity data (left) and temperature data (right) gathered at Forsmark. (Modified after Figure 5-15 in /Follin et al. 2008a/ and Figure 6-5 in /SKB 2008b/.)*

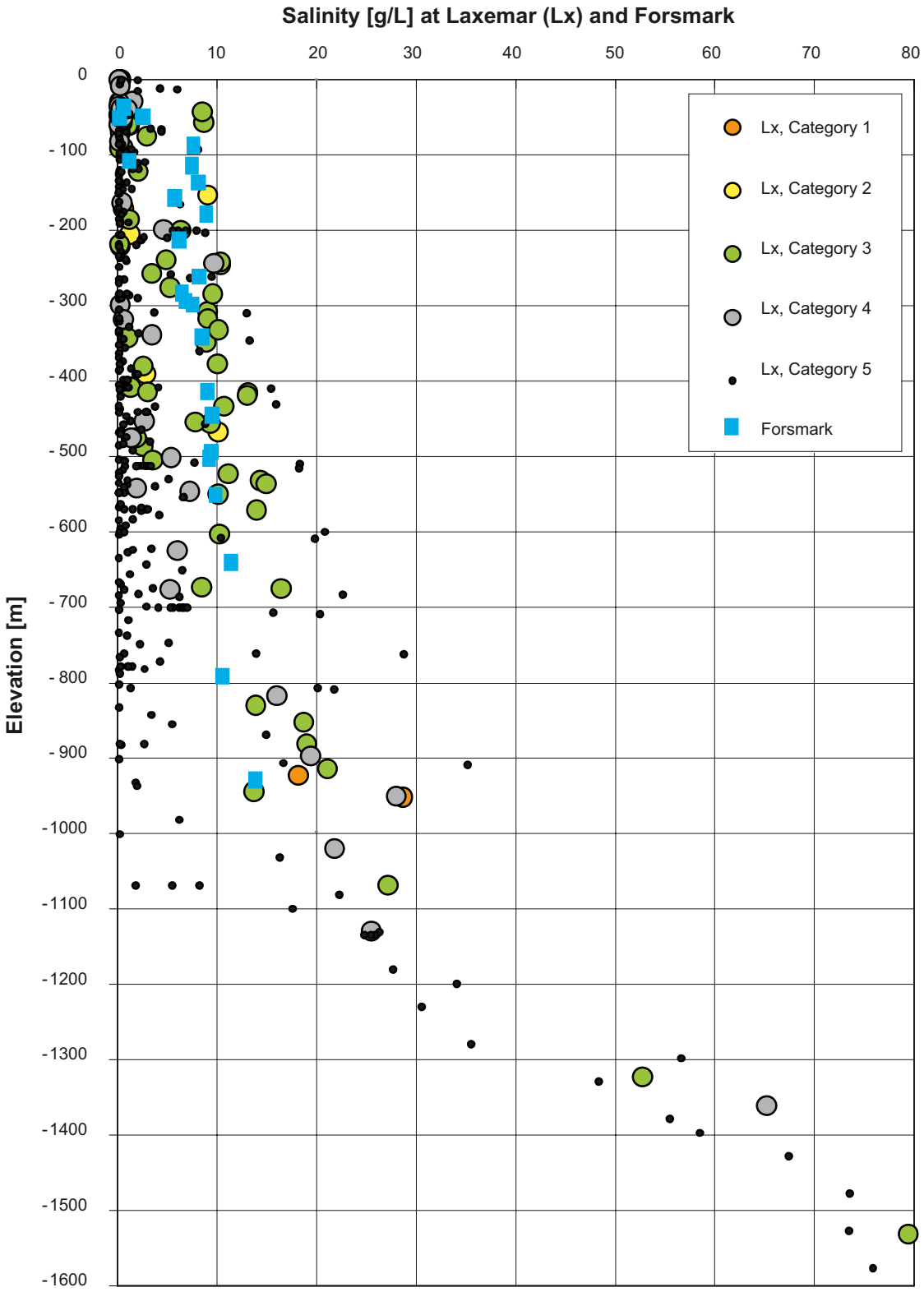

Figure D-5. *Compilation of all fracture water salinity data gathered in borehole KLX02 at Laxemar and in seven boreholes at Forsmark, cf. Figure D-4. The data in KLX02 are classified into five categories with regard to the quality of the sampling and/or analysis method, where category 1 represent the best quality and category 5 is the poorest. The Forsmark data are all of good quality in this regard (category 3 or better). (Modified after Figure 5-15 in /Follin et al. 2008a/ and Figure 5-18 in /Rhén et al. 2009/.)*

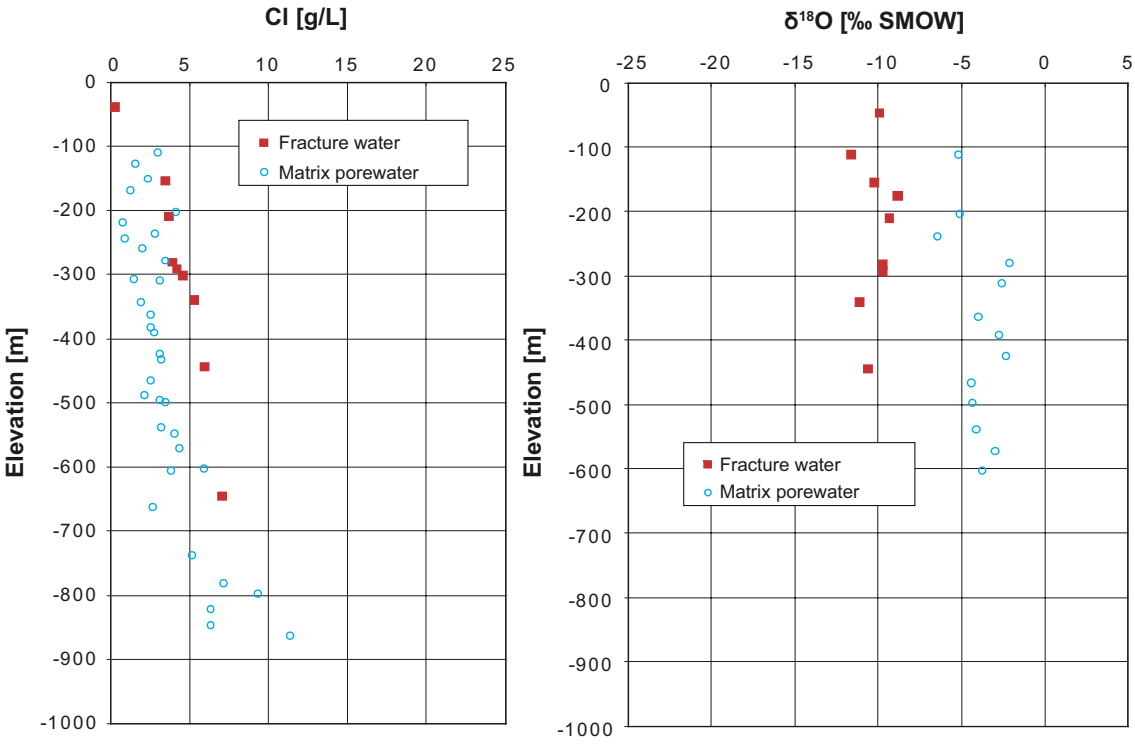

Figure D-6. *Measured concentrations of chloride (left) and oxygen-18 (right) in boreholes KFM01D and KFM06A at different elevations in the target area/volume at Forsmark. (Modified after Figure 7-6 and Figure 7-8 in /Follin et al. 2008/.)*

salinity appears to be slightly greater in the fracture water than in the matrix porewater. Below –600 m elevation, there are almost no flowing fractures detected in the target area/volume, see Figure D-2 and Figure D-3, and hence data on fracture water salinity are scarce.

The Littorina Sea is a potential source for the salinity seen in the fracture water samples above repository depth in Figure D-6. In comparison, little or no remnants of Littorina Sea water are observed in the samples that represent fracture water at, or below, repository depth. Further, the matrix porewater samples are probably neither affected by the Littorina Sea nor by glacial meltwater as the low contents of salt seen in matrix porewater is accompanied by high values of oxygen-18, approximately –5 to –4 ‰ of $\delta^{18}O$ SMOW, see the right plot in Figure D-6. Glacial meltwater is considered to be depleted of oxygen-18, approximately –20 to –16 ‰ of $\delta^{18}O$.

D.3 Penetration of fracture water into the matrix porewater

Regarding the simulated exchange of dissolved solids between the fracture water and the matrix porewater, the simulation results shown in Figure 6-11 imply that it is the matrix close to the fracture surface that is included in the model rather than the matrix further away.

The physical interpretation of the multi-rate diffusion model of /Haggerty and Gorelick 1995/ used in this work is briefly discussed in /Svensson et al. 2010/. In principle, the penetration depth, L_i [L], of each exchange rate coefficient, α_i [T^{-1}], may be evaluated as:

$$L_i = 2\sqrt{\left(\frac{D_e}{\phi_m \alpha_i}\right)} \qquad \text{(D-1)}$$

where D_e [L^2T^{-1}] is the effective diffusion coefficient and ϕ_m is the matrix porosity. These parameters are not used in the model of /Haggerty and Gorelick 1995/, however, and hence not specified in /Svensson et al. 2010/.

The penetration depth of the remotest diffusive exchange rate is estimated by assuming that D_e in Equation D-1 is similar to the effective diffusion coefficients used in the temperate flow modelling

for SR-Site /Joyce et al. 2010/. Second, the value of the matrix porosity is estimated from the following relationship:

$$\phi_m = \beta \phi \qquad \text{(D-2)}$$

where β [-] is the ratio between the diffusive and advective pore spaces and ϕ is the grid cell kinematic porosity. Inserting $D_e = 4 \cdot 10^{-15} - 4 \cdot 10^{-14}$ m^2/s /Joyce et al. 2010, Appendices C and F/, $\beta = 10$ and $\alpha_{min} = 4 \cdot 10^{-12}$ s^{-1} (section 4.2.4) and $\phi = 1 \cdot 10^{-4}$ (from the ECPM model realisation), into Equation D-1, render penetration depths of the remotest diffusive exchange rate that vary in the range of a few metres (2–6 m). These penetration depths are reached after approximately 8,000 years (=1/α_{min}), which matches roughly the time scale of the studied problem (19,000). A value of α_{min} that matches the time span of a full glacial cycle, e.g. 100,000 years, renders penetration depths of 10–20 m. As these penetration depths are much smaller than the spacing between the flowing fractures at repository depth, see Figure D-5, it may be concluded that the matrix porewater chemistry far away from the flowing fractures at and below reporitory depth is probably unaffected by the hydrodynamics during a glacial cycle. It is only the matrix porewater adjacent to the flowing fractures that is affected by matrix diffusion. The inserted numbers are provisional, of course, but the calculation does provide an explanation for the appearance of the simulated results shown in Figure 6-11. That is, the penetration depth simulated here is limited.

Figure D-6 indicates that the salinities in both the fracture water and matrix porewater increase with depth. From Figure D-5 it is concluded that the fracture water salinity at Laxemar at –1,000 m elevation is probably somewhat higher than the salinity at Forsmark at this elevation, but the increase in salinity is fairly similar. A salinity of 6–7 % by weight in both the fracture water and the matrix porewater at –2,000 m elevation at Forsmark appears as a reasonable assumption.

D.4 On the role of the shoreline displacement

Concerning the applied top boundary conditions, the present-day shoreline (2000 AD) is used in all glacial cases without permafrost during the pre-LGM stage. This model simplification is considered appropriate from a hydraulic point of view for two reasons. First, the hydraulic gradients that occur when the ice sheet margin passes the repository area exceed by far the regional gradients caused by a distant shoreline of a low elevation. Second, the groundwater table in Sweden is close to the ground surface regardless of the shoreline elevation due to abundant precipitation and the relatively low permeability of glacial till and fractured crystalline rock. The shoreline elevation during the post-LGM stage is assumed to be at approximately +100 m, i.e. submerged conditions will prevail in front of the retreating ice sheet margin, see Figure 1-2 and Figure D-7 at 8000 BC. Figure D-7 shows the shoreline displacement between 8000 BC and 12,000 AD. Between 8000 BC and 2000 AD, the total shoreline displacement is approximately 100 m, and the top boundary condition at Forsmark changes from submerged to terrestrial. During the next 10,000 years[15], the terrestrial conditions are reinforced as the expected additional total shoreline displacement is estimated to approximately 40 m /Påsse 1997, SKB 2010/.

Discontinuities in the permafrost layer are accounted for in the groundwater flow simulations that take periglacial conditions into account. As mentioned in Section 1.3, potential locations of taliks are estimated from the forecasted landscape development following the ongoing shoreline displacement /Brydsten and Strömgren 2010/. However, this forecast does not allow for taliks in the proximity of a repository at Forsmark unless the present-day shoreline is changed. Thus, the groundwater flow simulations that take permafrost into account use a different shoreline elevation. The used elevation of –28 m is representative for a time period of approximately 50,000–60,000 years from today /SKB 2010/.

Figure D-8 shows the evolution of the sea water salinity in the Forsmark area between 8000 BC and 12,000 AD. At 8000 BC, the Forsmark area was submerged by Lake Ancylus, which was a freshwater lake that received huge amounts of glacial meltwater from the retreating ice sheet margin. At about 6500 BC, the salinity started to increase as the Littorina Sea began to form. The Littorina Sea reached its maximum salinity between 4000 BC and 3000 BC. During the next 10,000 years, the present-day salinity is expected to decrease by approximately a factor of two /Lindborg 2010/. In conclusion changes in the seawater salinity are not important for the work reported here as the simulation of the post-LGM stage ends soon after the ice sheet margin has retreated from the Forsmark site.

[15] /SKB 2010/ considers temperate conditions for at least another 8,000 years.

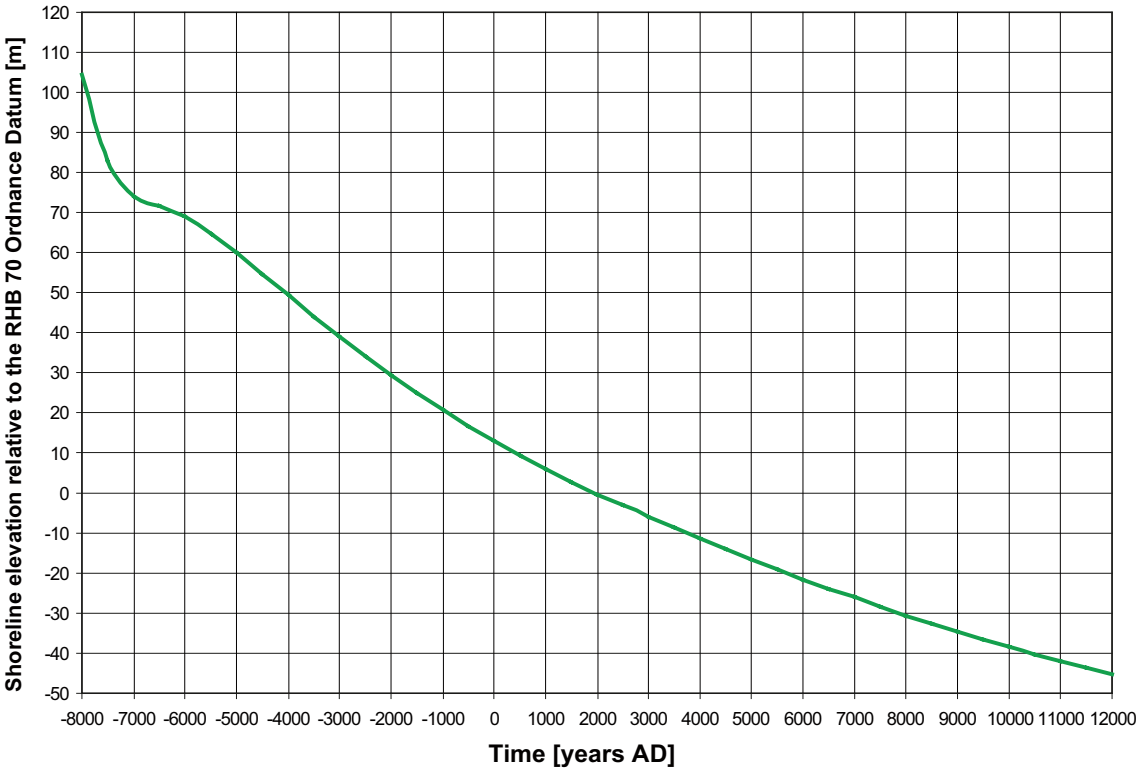

Figure D-7. *Evolution of the shoreline displacement at Forsmark during Holocene time (8000 BC to 12,000 AD). (Modified after Figure 4-5 in /Joyce et al. 2010/.)*

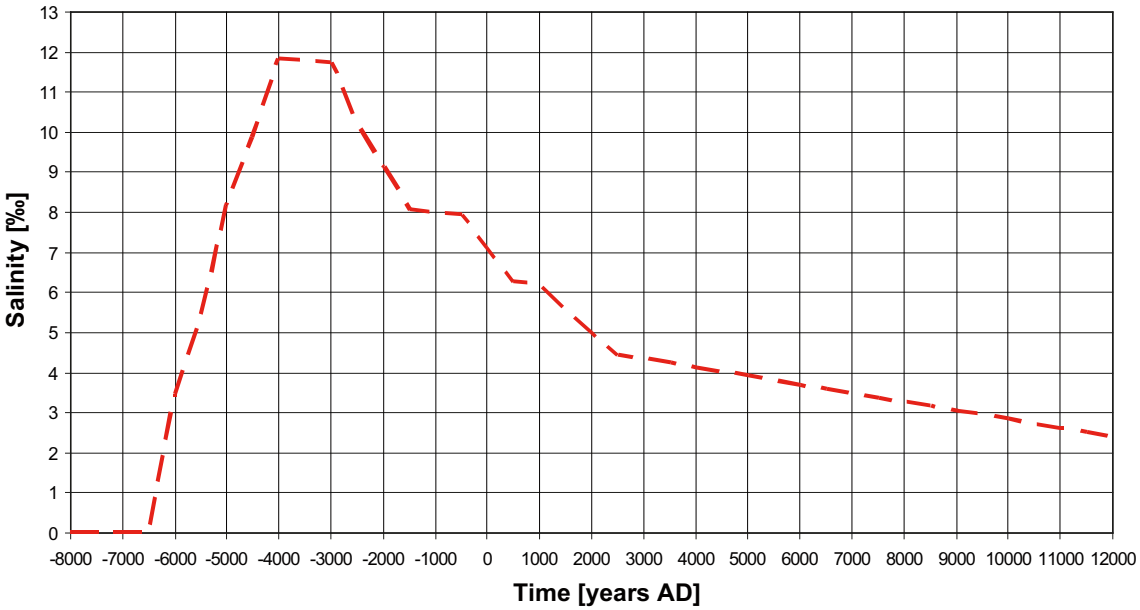

Figure D-8. *Evolution of the seawater salinity at Forsmark during Holocene time (8000 BC to 12,000 AD). (Modified after Figure 4-6 in /Joyce et al. 2010/.)*

Appendix E

Temperate climate conditions

E.1 Salinity

Figure E-1 shows the salinity field in terms of three cross-sections. Figure E-2 shows the fracture water and the matrix porewater salinities along the NW-SE cross-section. The salinity at repository depth within the target volume is approximately 0.5–1.0%.

The undulations in the salinity field reflect the simulated variations in the pressure field, which are affected by the spatial variability of different factors such as initial conditions and topography, resolution of the computational grid, hydraulic heterogeneity and structures, e.g. outcropping deformation zones.

E.2 Darcy flux

Figure E-3 shows the Darcy flux field along the same cross-section as shown in Figure E-2. At the repository depth within the target volume, the Darcy fluxes are fairly low and uniform with values around 10^{-13}–10^{-12} m/s.

E.3 Recharge and discharge locations

Figure E-4 shows the simulated recharge and discharge locations for particle traces that pass through the 6,916 deposition hole positions. All recharge locations coincide with topographic highs inside the regional model domain of SDM-Site. The majority of the discharge locations are found close to the present-day coastline. Approximately 2.5% of the discharge locations are found in the area above the repository, all in conjunction with outcropping deformation zones.

Figure E-5 shows the simulated recharge and discharge locations for particle traces that pass through the five measurement localities (ML 1–5). The recharge locations for all five measurement localities are found upstream along the regional gradient. Typically the recharge flow path length is between 2–4 km. Recharge locations of ML 1 and ML 2 are found at the envisaged boundary of the SDM-Site Forsmark model. The discharge of all but ML 1 are found close to the present-day coastline. The discharge flow path length for ML 1 is only some 600 m discharging almost on top of the ML 1 location along the deformation zone NW0003 (see /Stephens et al. 2007/).

E.4 Recharge characteristics

Particles are released at the 6,916 deposition hole positions and at the five measurement localities, ML 1–5, and tracked in a backward direction for 1,000 years to investigate their recharge characteristics. Not all of the released particles reached the ground surface within this period of time.

Table E-1 presents recharge flow path lengths, travel times, and flow-related transport resistances for the particles released at the measurement localities ML 1–5.

Figure E-6 to Figure E-8 show cumulative distribution (probability) plots of the recharge flow path lengths, travel times, and flow-related transport resistances for all released particles.

Figure E-6 shows the cumulative distribution of the recharge flow path lengths (L_R). The recharge flow path lengths can be divided into two main groups. The first group represents particles traveling a relatively short distance, approximately 1 km. The second group represents particles traveling a longer distance, at least 4–5 km. The values representing ML 1 and ML 3–5 are found in the transition zone between these two groups. The value representing ML 2 value is found in the upper range of the second group.

Figure E-7 shows the cumulative distribution of the recharge travel times ($t_{w,R}$). Approximately 94% of the tracked particles reach repository depth in less than 1,000 years. Some 10% of the deposition hole positions have a recharge travel time shorter than 40 years and 20% have an travel time shorter than 100 years. The median recharge travel time is approximately some 250 y. Except for ML 2, the measurement localities fall in the region of travel times between 10–100 years.

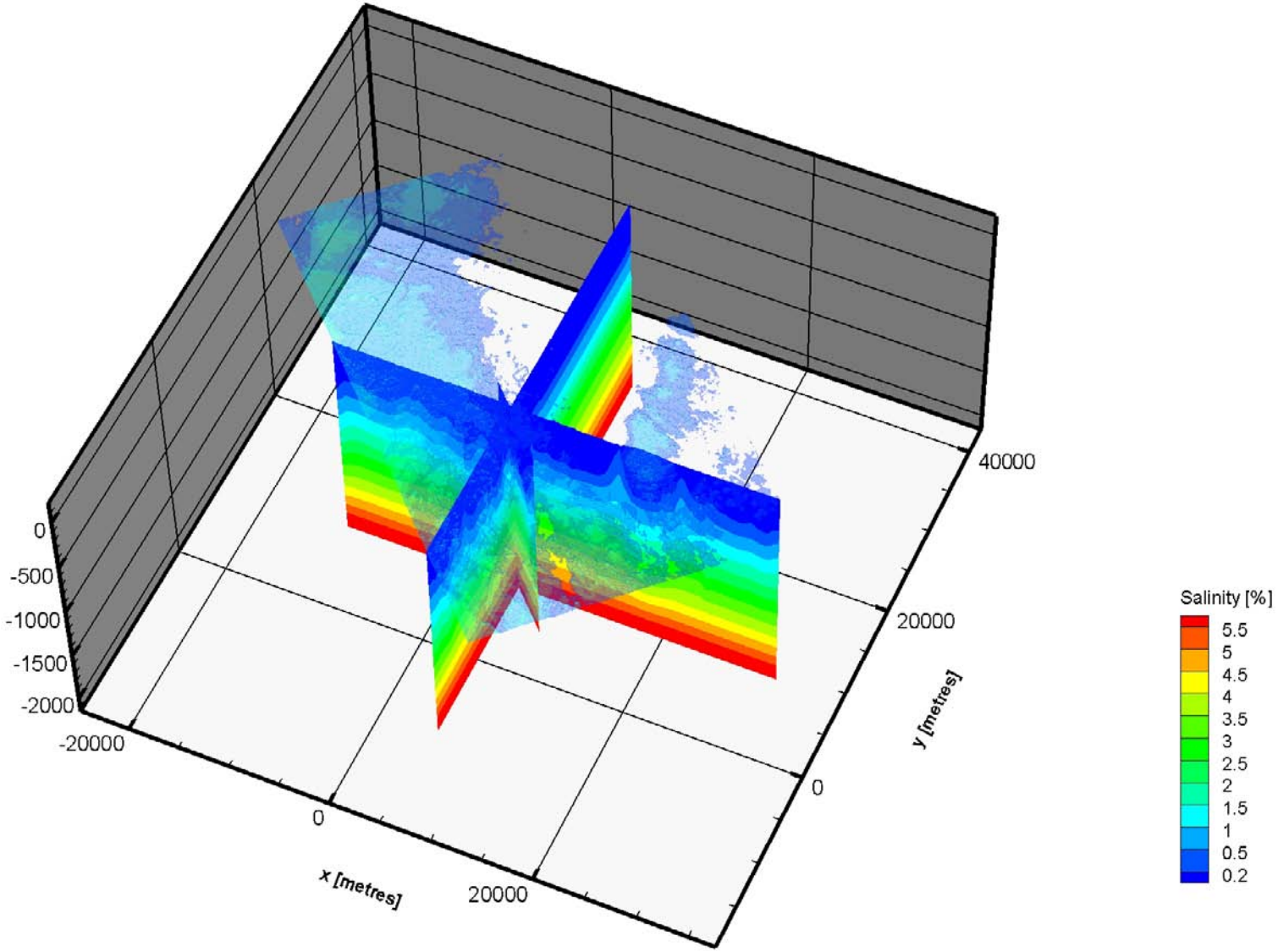

Figure E-1. *Salinity for the temperate case along three vertical cross-sections together with the present-day shoreline. The y-axis points towards north.*

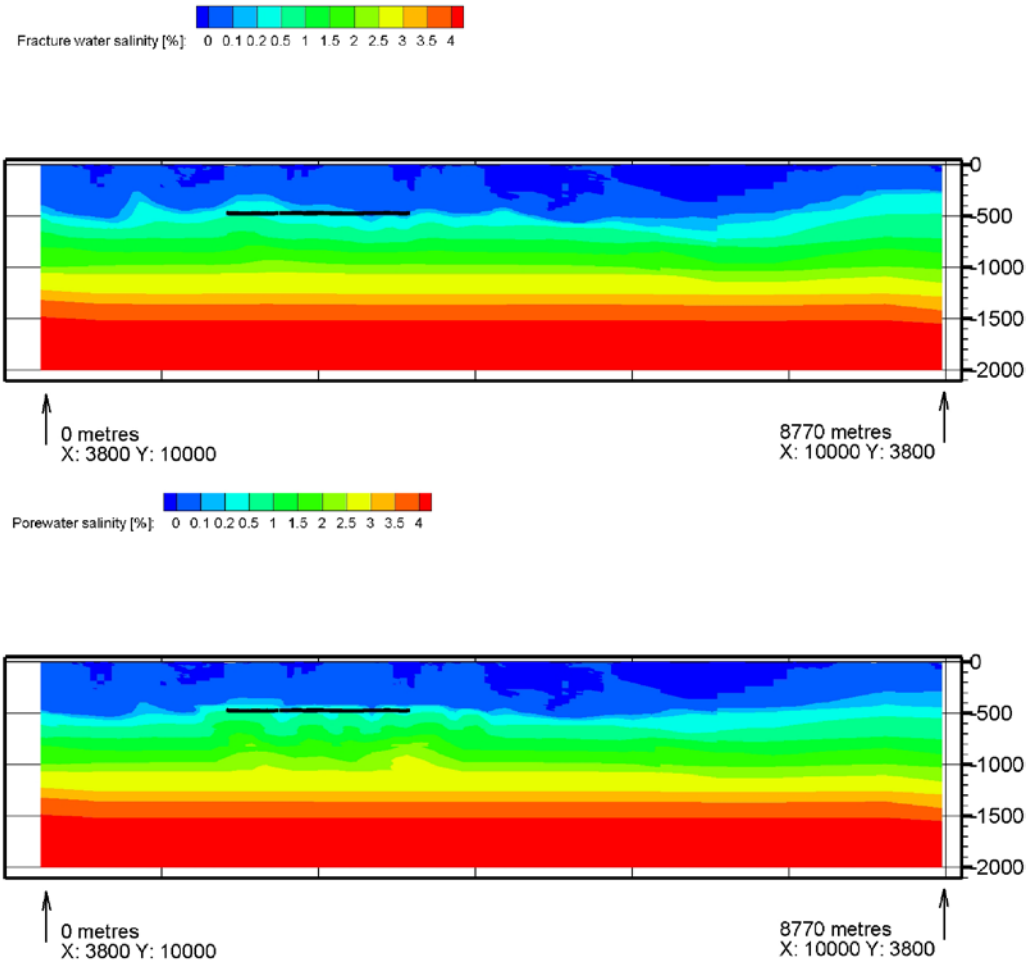

Figure E-2. *Fracture and matrix porewater salinities along the NW-SE cross-section shown in Figure E-1. The black line at –465 m elevation indicates the location of the repository.*

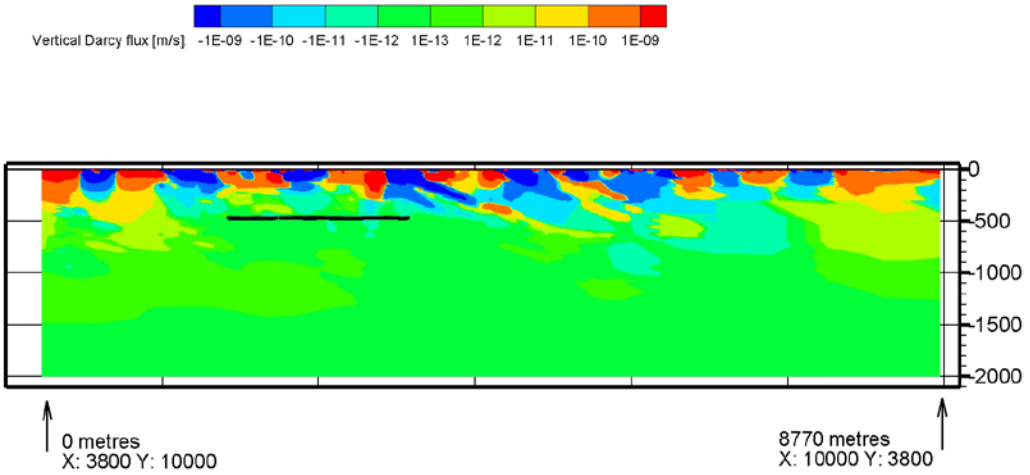

Figure E-3. *Darcy flux field along a NW-SE cross-section shown in Figure E-1. Positive values represent upward directed fluxes and negative values represent downward directed fluxes. The black line at –465 m elevation shows the location of the repository.*

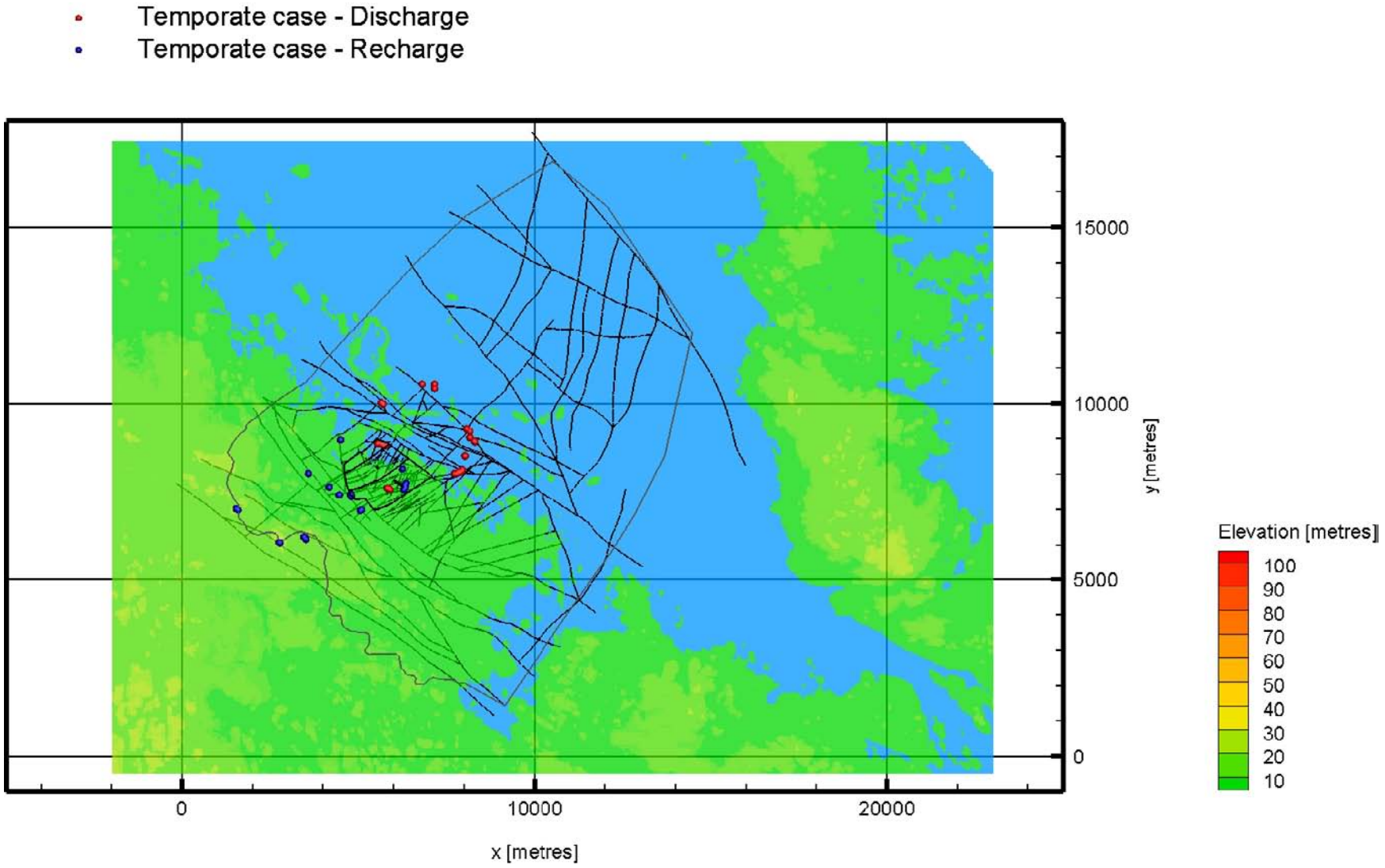

Figure E-4. *Recharge (blue) and discharge (red) locations for particle traces passing through the 6,916 deposition hole positions. The trace lines represent outcropping deformation zones. The repository is located close to the shoreline (the thicker black lines).*

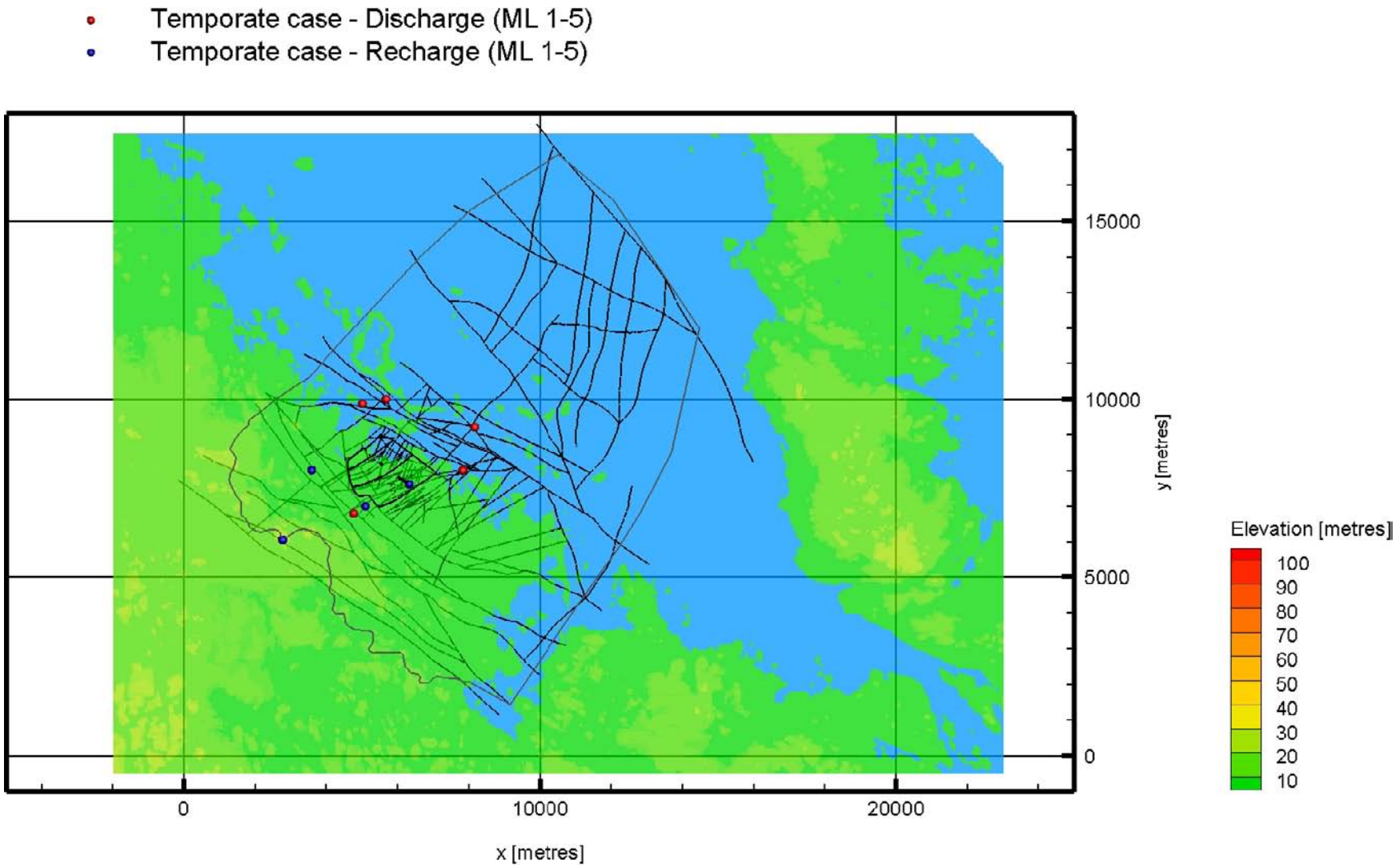

Figure E-5. *Recharge (blue) and discharge (red) locations for particle traces passing through ML 1–5. The trace lines represent outcropping deformation zones. The repository is located close to the shoreline (the thicker black lines).*

Table E-1. Temperate case recharge performance measures for ML 1–5.

Measurement locality	Flow path length [m]	Travel time [y]	Flow-related transport resistance [y/m]
1	3,104	60	$1.8 \cdot 10^6$
2	4,570	330	$3.9 \cdot 10^6$
3	2,221	63	$1.0 \cdot 10^6$
4	2,338	38	$9.2 \cdot 10^5$
5	2,467	50	$1.4 \cdot 10^6$

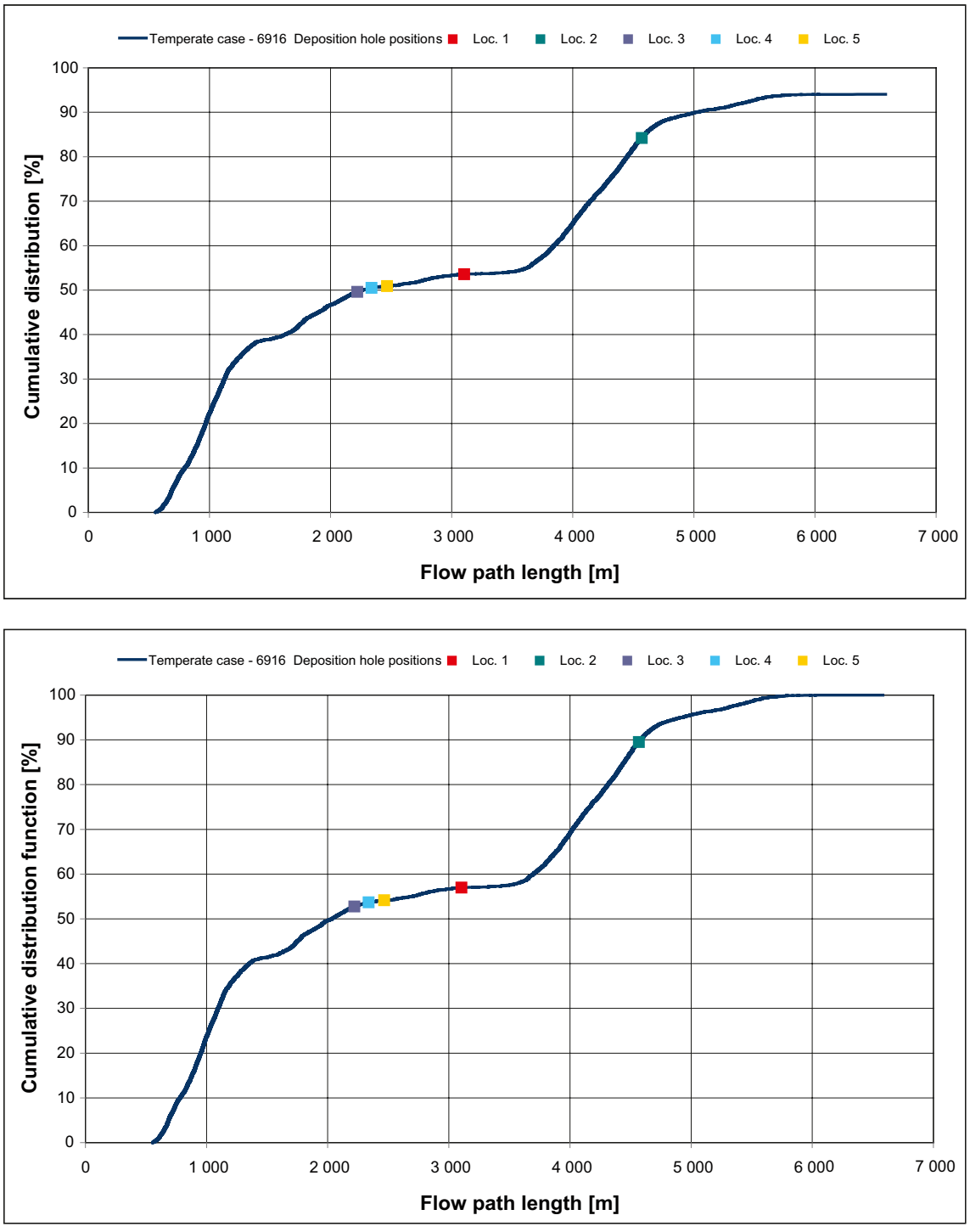

Figure E-6. *Cumulative distribution (probability) plots of the simulated recharge flow path lengths, L_R, for the temperate case. The maximum value in the upper plot is set to 100% in the lower plot.*

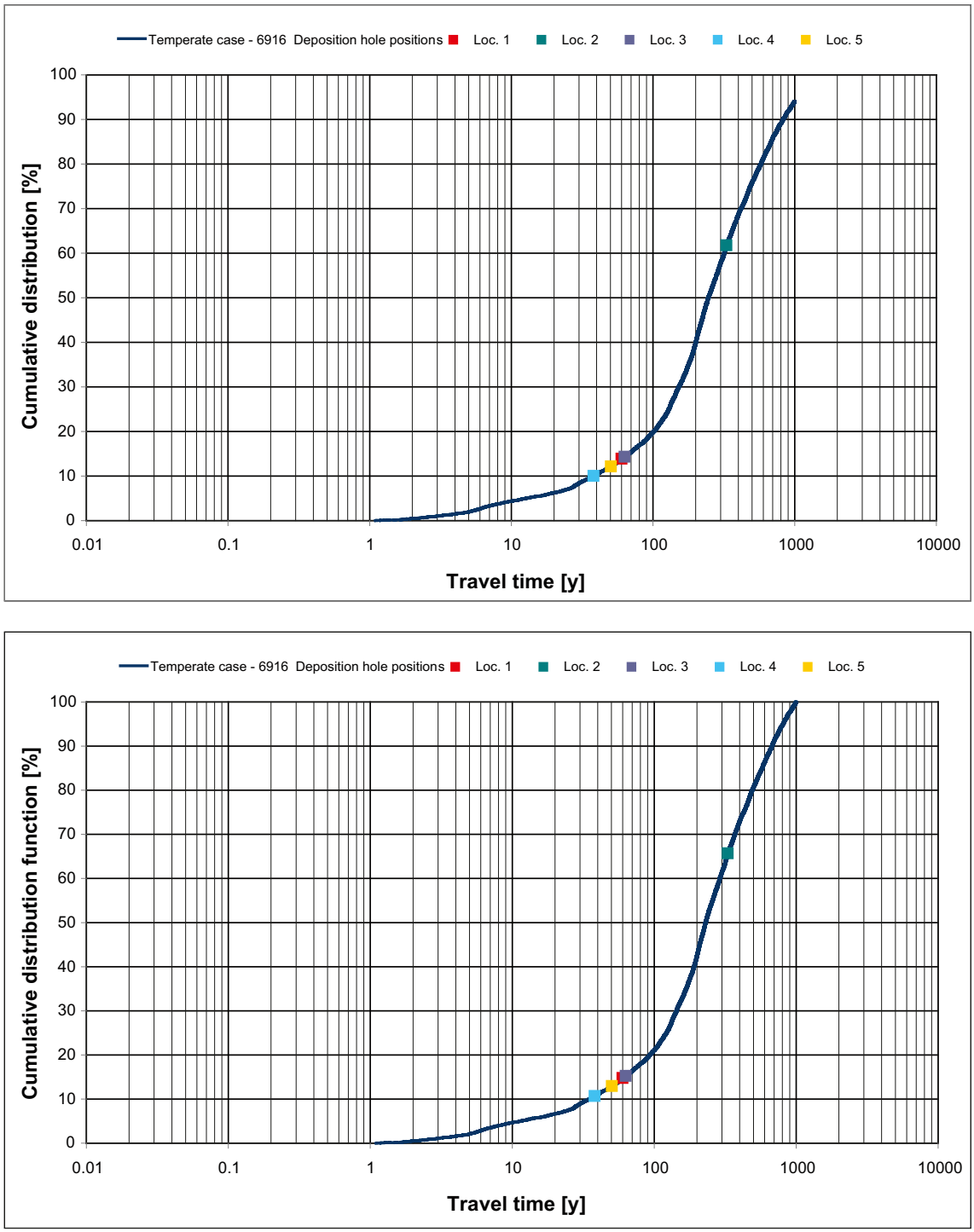

Figure E-7. *Cumulative distribution (probability) plots of the simulated recharge travel times, $t_{w,R}$, for the temperate case. The maximum value in the upper plot is set to 100% in the lower plot.*

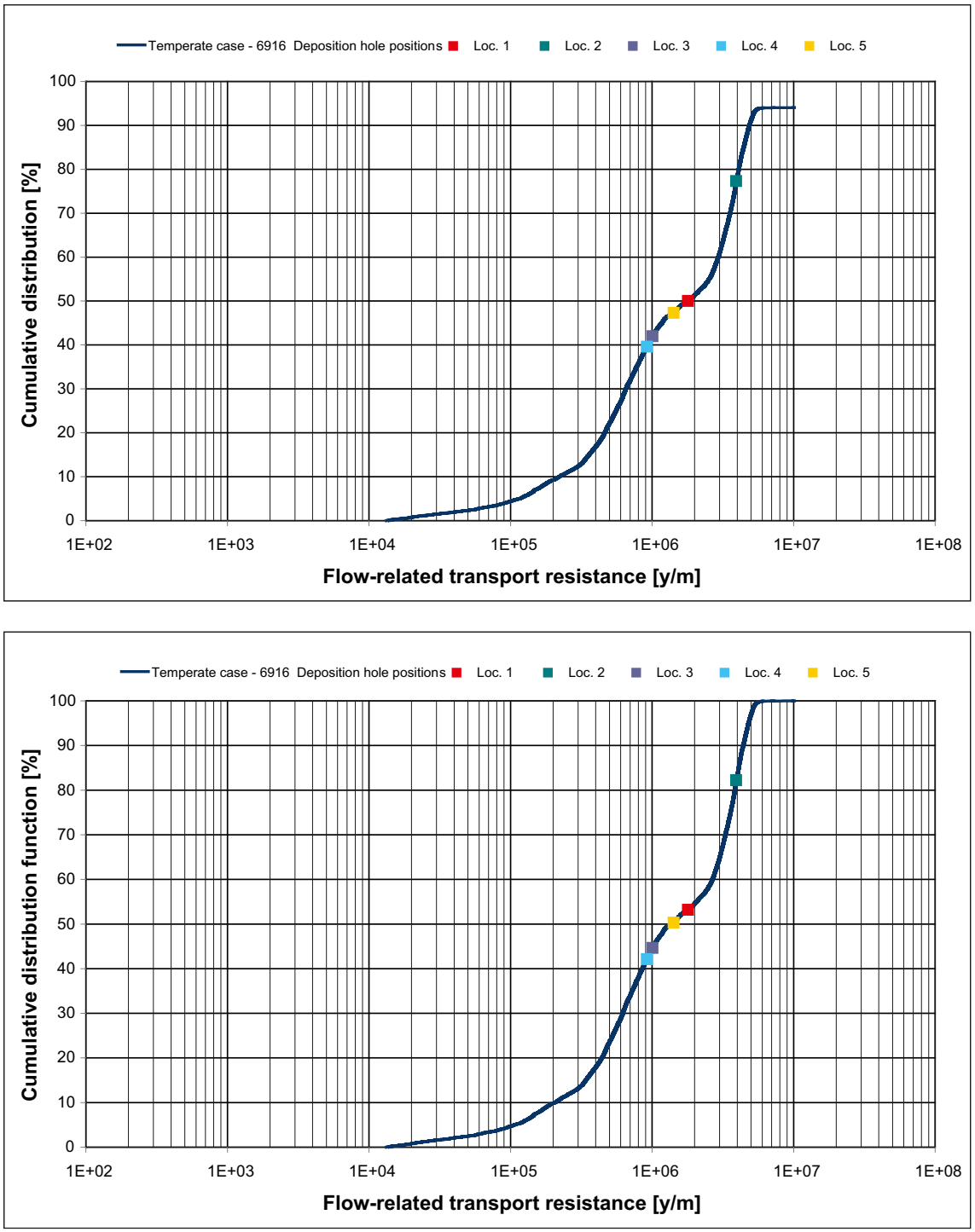

Figure E-8. *Cumulative distribution (probability) plots of the simulated recharge flow-related resistances, F_R, for the temperate case. The maximum value in the upper plot is set to 100% in the lower plot.*

Figure E-8 shows the cumulative distribution of the recharge flow-related transport resistances (F_R). The values are all greater than $1 \cdot 10^4$ y/m with a median of approximately $2 \cdot 10^6$ y/m. The measurement localities ML 1–5 are found around the median value or, in the case of ML 2, toward the right end of the range.

E.5 Discharge characteristics

Particles are released at the 6,916 deposition hole positions and at the five measurement localities, ML 1–5, and tracked in a forward direction for 1,000 years to investigate their discharge characteristics. Not all of the released particles reached the ground surface within this period of time.

Table E-2 presents discharge flow path lengths, travel times, and flow-related transport resistances for the particles released at the measurement localities ML 1–5.

Figure E-9 to Figure E-11 show cumulative distribution (probability) plots of the discharge flow path lengths, travel times, and flow-related transport resistances for all released particles.

Figure E-9 shows the cumulative distribution of the discharge flow path lengths (L_R). The discharge flow path lengths are broadly distributed between approximately 1–5 km reached in the tracked time span. Some 15% of the particles discharge with a shorter flow path length than 1 km.

Figure E-10 shows the cumulative distribution of the discharge travel times ($t_{w,D}$). Approximately 41% of the tracked particles reach the surface from a deposition hole position in 1,000 years or shorter. The fastest particle reaches the surface after about 10 years. The median travel time indicated is roughly 1,200 years. Measurement locality ML 4 has a shorter travel time than any of the 6,916 deposition hole positions . ML 1 has also a short travel time. ML 4 are located within a deformation zone and ML 1 is fringing another deformation zone. The particle that is released at ML 2 discharges after approximately 875 years.

Figure E-11 shows the cumulative distribution of the discharge flow-related transport resistances (F_R). All values are greater than $7 \cdot 10^4$ y/m with a median of approximately $5 \cdot 10^8$ y/m. The measurement localities ML 1–5 are found within the range of the flow-related transport resistances recorded for the 6,916 deposition hole positions.

Table E-2. Discharge performance measures for ML 1–5.

Measurement locality	Flow path length [m]	Travel time [y]	Flow-related transport resistance [y/]m
1	602	11	$3.4 \cdot 10^5$
2	3,403	875	$8.4 \cdot 10^6$
3	1,918	380	$8.9 \cdot 10^6$
4	1,635	4	$4.4 \cdot 10^4$
5	1,198	361	$7.6 \cdot 10^5$

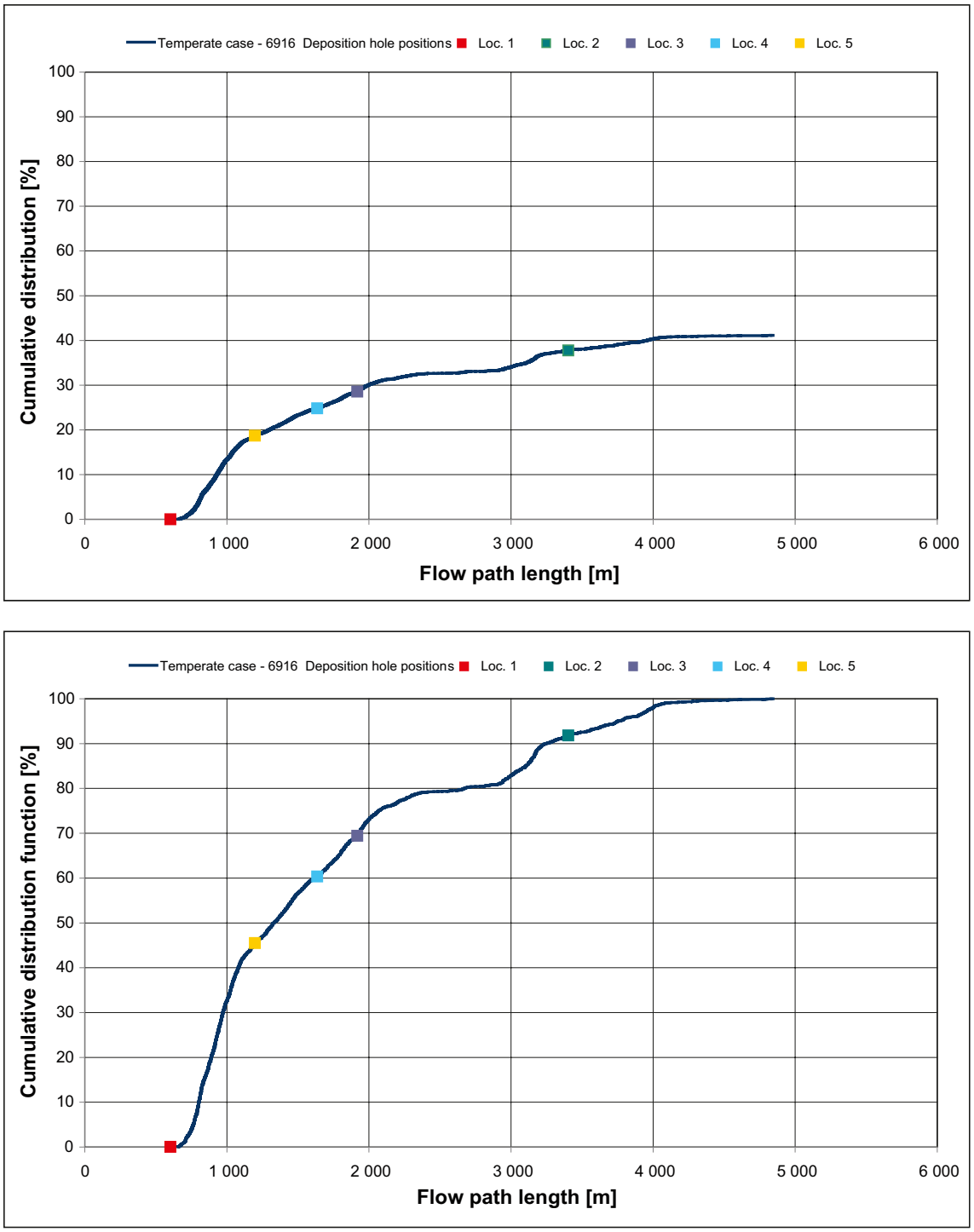

Figure E-9. *Cumulative distribution (probability) plots of the simulated discharge flow path lengths, L_R, for the temperate case. The maximum value in the upper plot is set to 100% in the lower plot.*

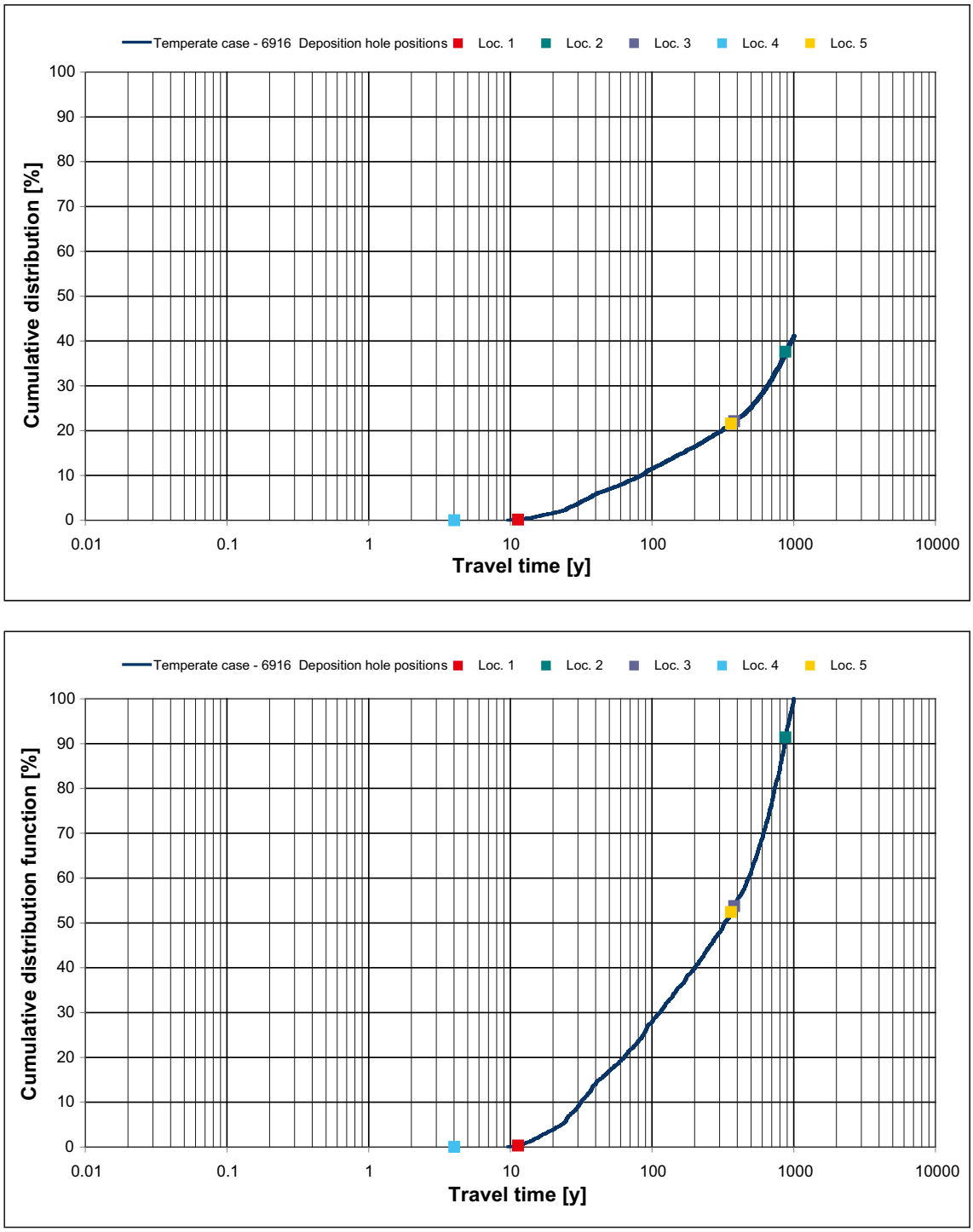

Figure E-10. *Cumulative distribution (probability) plots of the simulated discharge travel times, $t_{w,R}$, for the temperate case. The maximum value in the upper plot is set to 100% in the lower plot.*

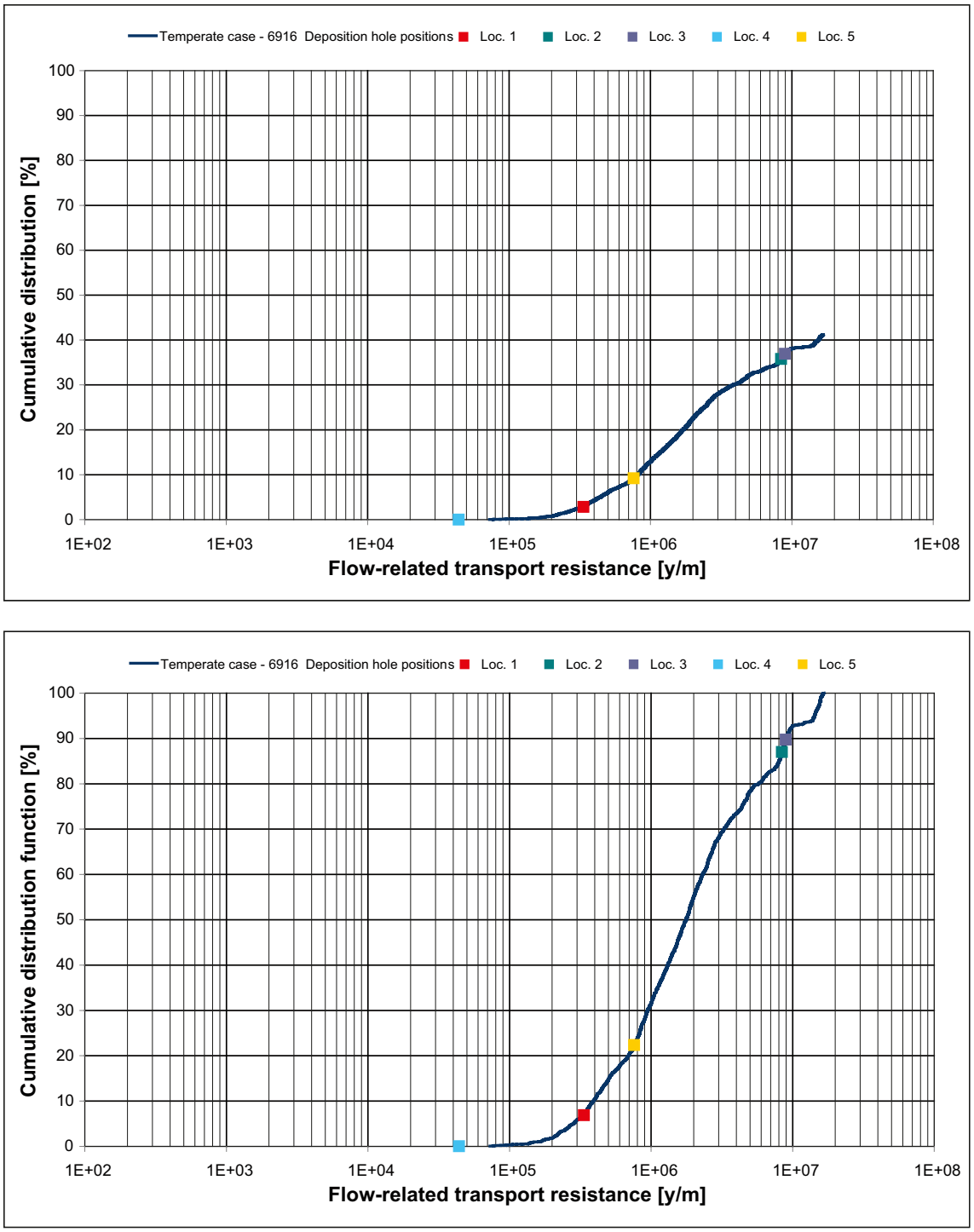

Figure E-11. *Cumulative distribution (probability) plots of the simulated discharge flow-related transport resistances, F_R, for the temperate case. The maximum value in the upper plot is set to 100% in the lower plot.*

Appendix F

Scenario A: Glacial climate conditions without permafrost

F.1 Introduction

All plots shown is this appendix refer to case (a), see Table 5-1 and Figure 5-1, except for one plot that compares case (a) with case (b) and another plot that compares case (a) with case (c). These exceptions are explicitly stated.

F.2 Top boundary conditions

Figure F-1 shows the situation during glaciation when the ice sheet margin is at ice-front location II (IFL II). The grayish area indicates the ice sheet thickness. The speed of the ice sheet margin is 50 m/y, thus IFL II is reached about 600 years after the it enters the model domain. A residual pressure equal to 92% of the weight of the ice sheet thickness is specified on the top boundary below the ice. Elsewhere, the residual pressure is set to zero in all terrestrial parts and to the hydrostatic pressure below the ice-free sea and lakes.

In front of the ice sheet margin, the pressure was set to zero at the ground surface and to the hydrostatic pressure below the sea.

F.3 Pressure

Figure F-2 shows the pressure (P) in two vertical cross-sections during glaciation when the advancing ice sheet margin is at ice-front location II (IFL II).

Figure F-3 shows the simulated development of the pressure during glaciation at the five measurement localities (ML 1–5). The pressures develop similarly at these localities. The effect of the approaching ice sheet margin is not visible until the ice sheet margin is fairly close to ML 1–5.

Figure F-4 shows a comparison of the pressure developments during glaciation and deglaciation. Apart from the offset of 1 MPa during the retreat, the pressure envelopes are close to identical. The 1 MPa offset during deglaciation is due to the elevated sea level, which is set to 100 m above the Swedish Ordnance Datum during glaciation.

F.4 Darcy flux

Figure F-5 to Figure F-8 show the spatial distribution of the vertical Darcy flux (q) in a horizontal slice at –465 m elevation. The slice passes through the target volume where the repository is located.

Figure F-5 shows the vertical Darcy flux for the temperate case.

Figure F-6 shows the vertical Darcy flux during glaciation when the ice sheet margin is at ice-front location II, i.e. immediately above the repository.

Figure F-7 shows the vertical Darcy flux during glaciation when the ice sheet margin is at ice-front location III.

Figure F-8 shows the vertical Darcy flux during glaciation when the ice sheet margin is at ice-front location IV, i.e. when the entire target volume is covered by a thick ice sheet.

Figure F-9 shows the vertical Darcy flux during glaciation mapped on a NW-SE cross-section parallel to the ice flow direction during glaciation.

Figure F-10 shows a comparison between the simulated Darcy flux at the five measurement locations during glaciation and deglaciation. The peaks and the envelopes of the Darcy fluxes are very similar.

Figure F-11 shows the normalised Darcy flux (q/q_{temp}) at ML 1–5 during the glaciation (pre-LGM), the complete ice coverage (LGM) and the deglaciation (post-LGM). During the two ice front passages, the fluxes are up to 100 times greater than those prevailing during the temperate conditions.

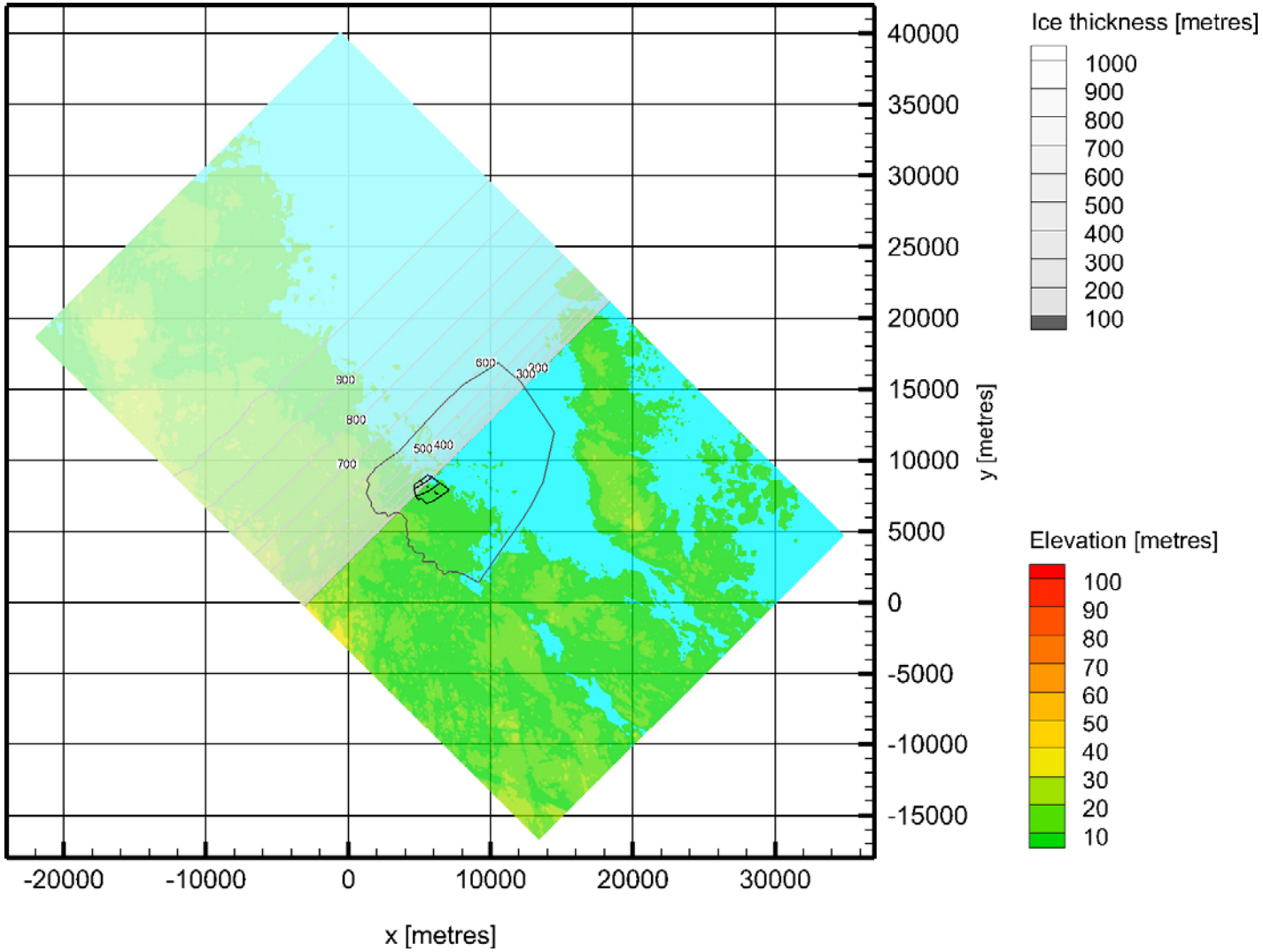

Figure F-1. *Visualisation of ice sheet thickness during glaciation when the ice sheet margin is at IFL II. The short black lines in the centre indicate the location of the repository. The y-axis points towards north.*

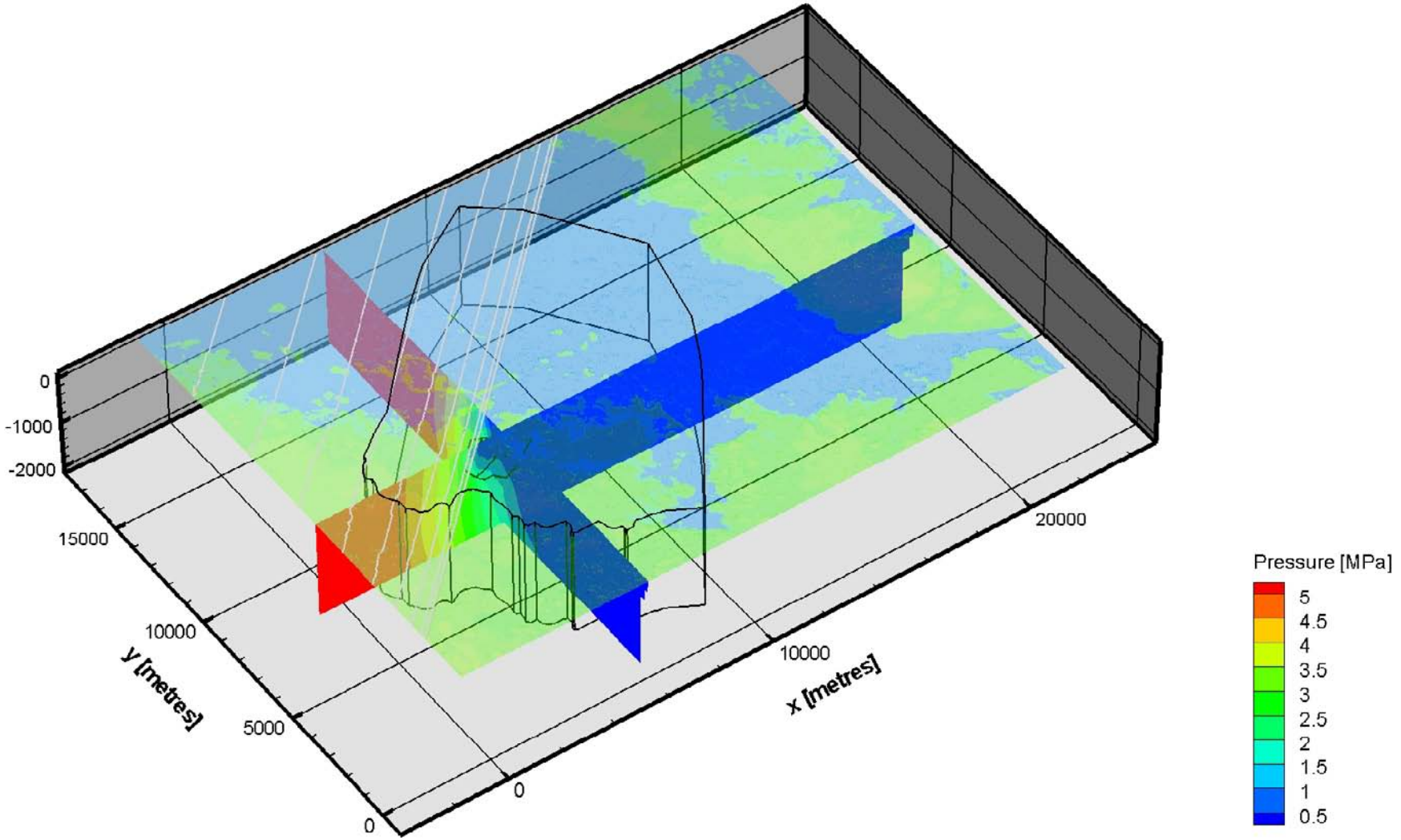

Figure F-2. *Visualisation of the residual pressure during glaciation when the ice sheet margin is at IFL II. The short black lines in the centre indicate the location of the repository. The y-axis points towards north.*

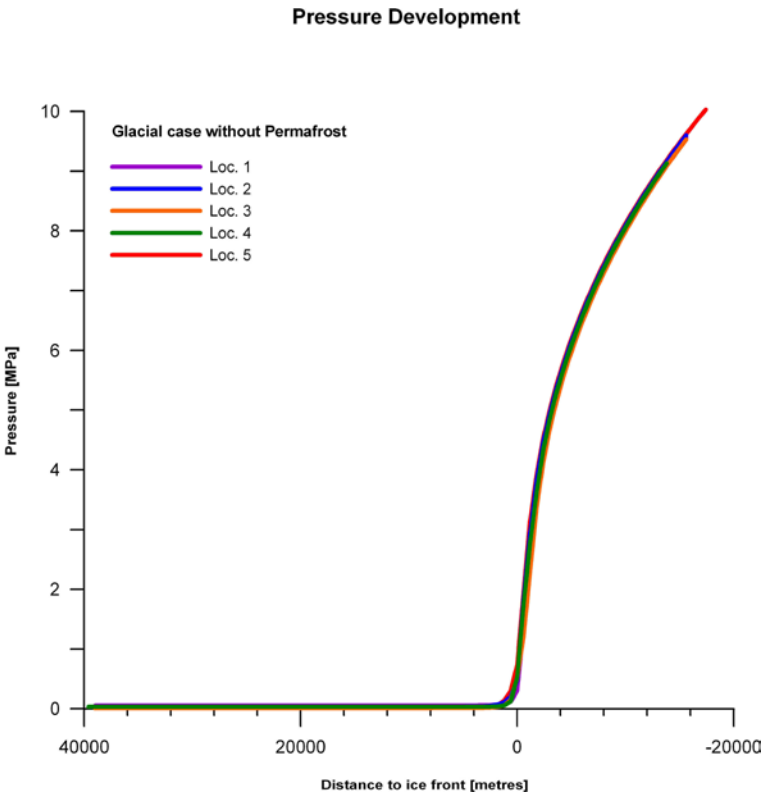

Figure F-3. *Pressure during glaciation at ML 1–5 during glaciation. Positive distance values mean that the ice sheet margin has not yet arrived to the measurement locations.*

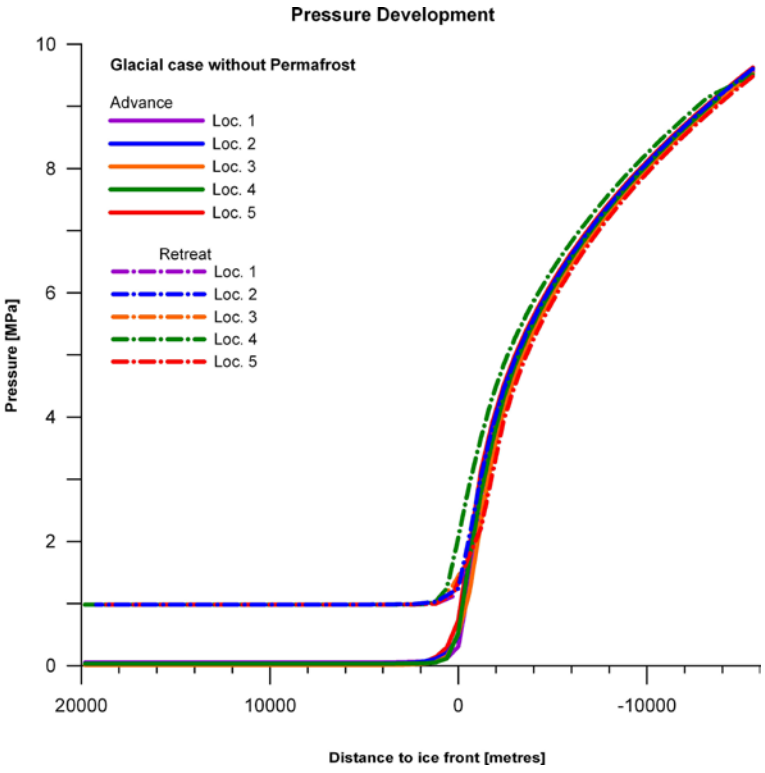

Figure F-4. *Pressure at ML 1–5 during glaciation and deglaciation. Positive distance values mean that the ice sheet margin has not yet arrived to the measurement locations.*

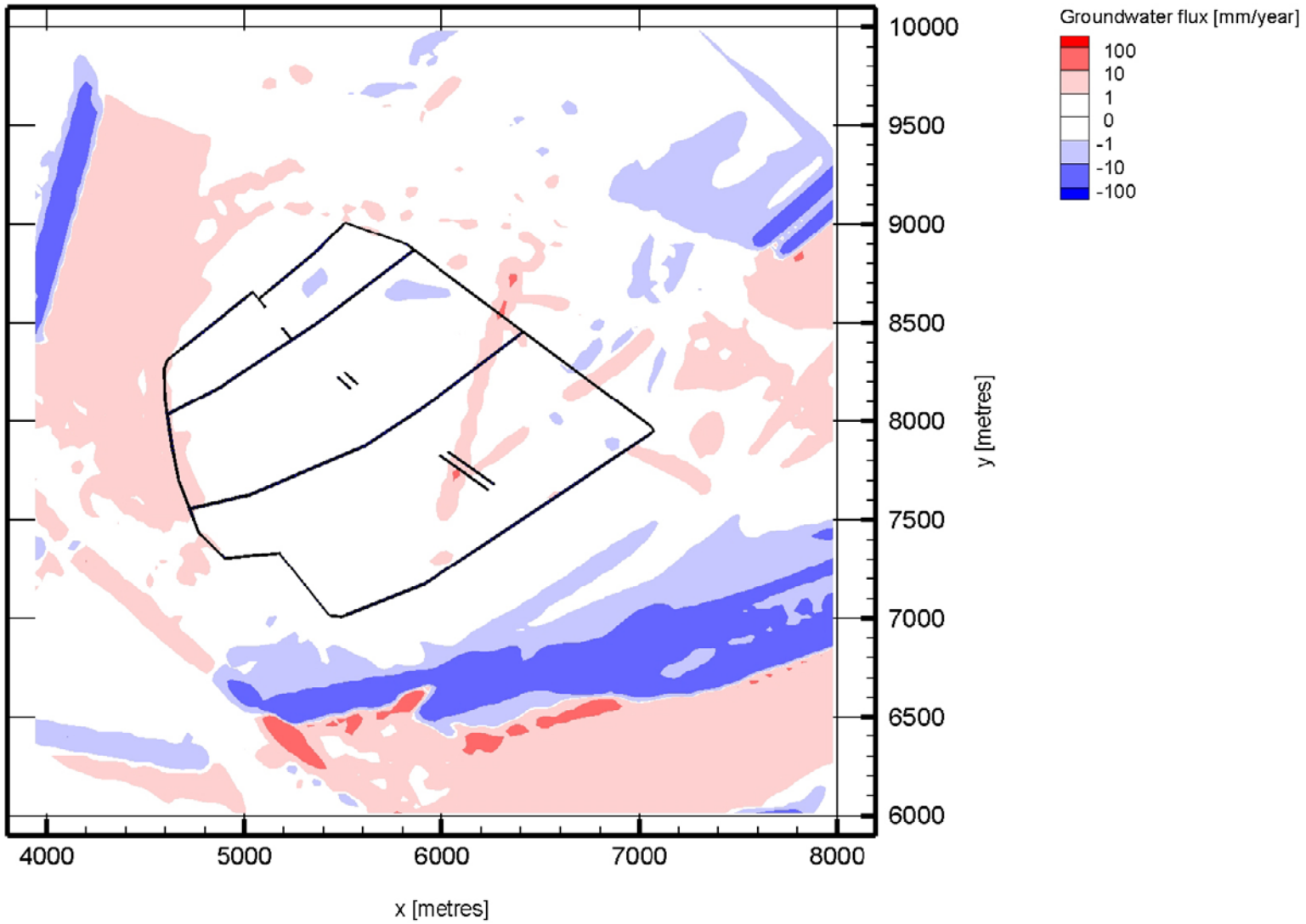

Figure F-5. *Horizontal view of the vertical Darcy flux in mm/y at –465 m elevation for the temperate case. Red colours show positive values (upward directed fluxes), whereas blue colours show negative values (downward directed fluxes). The short black lines indicate major tunnels. The y-axis points towards north.*

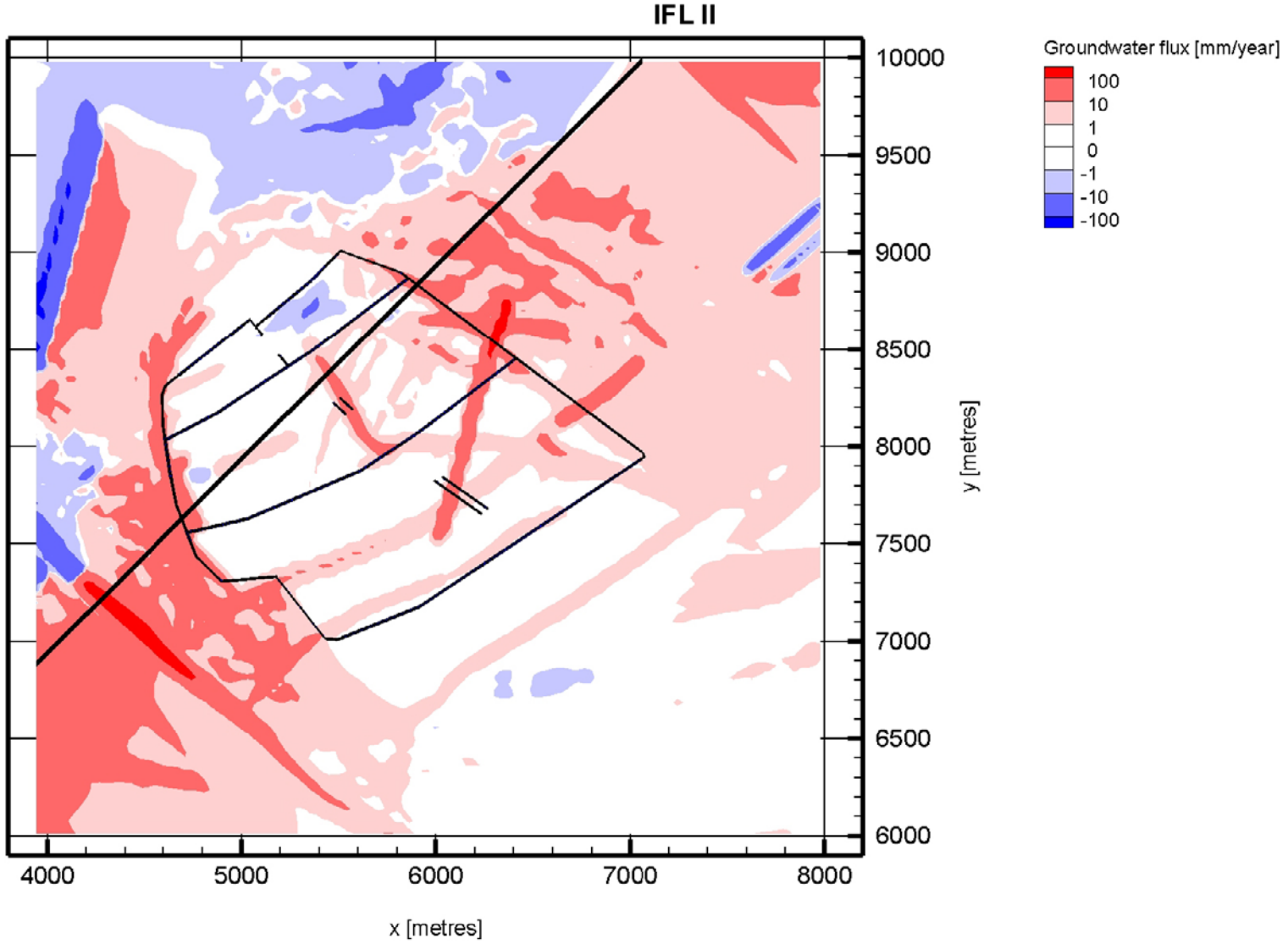

Figure F-6. *Horizontal view of the vertical Darcy flux in mm/y at –465 m elevation during glaciation when the ice sheet margin is at IFL II (black line). Red colours show positive values (upward directed fluxes), whereas blue colours show negative values (downward directed fluxes). The short black lines indicate major tunnels. The y-axis points towards north.*

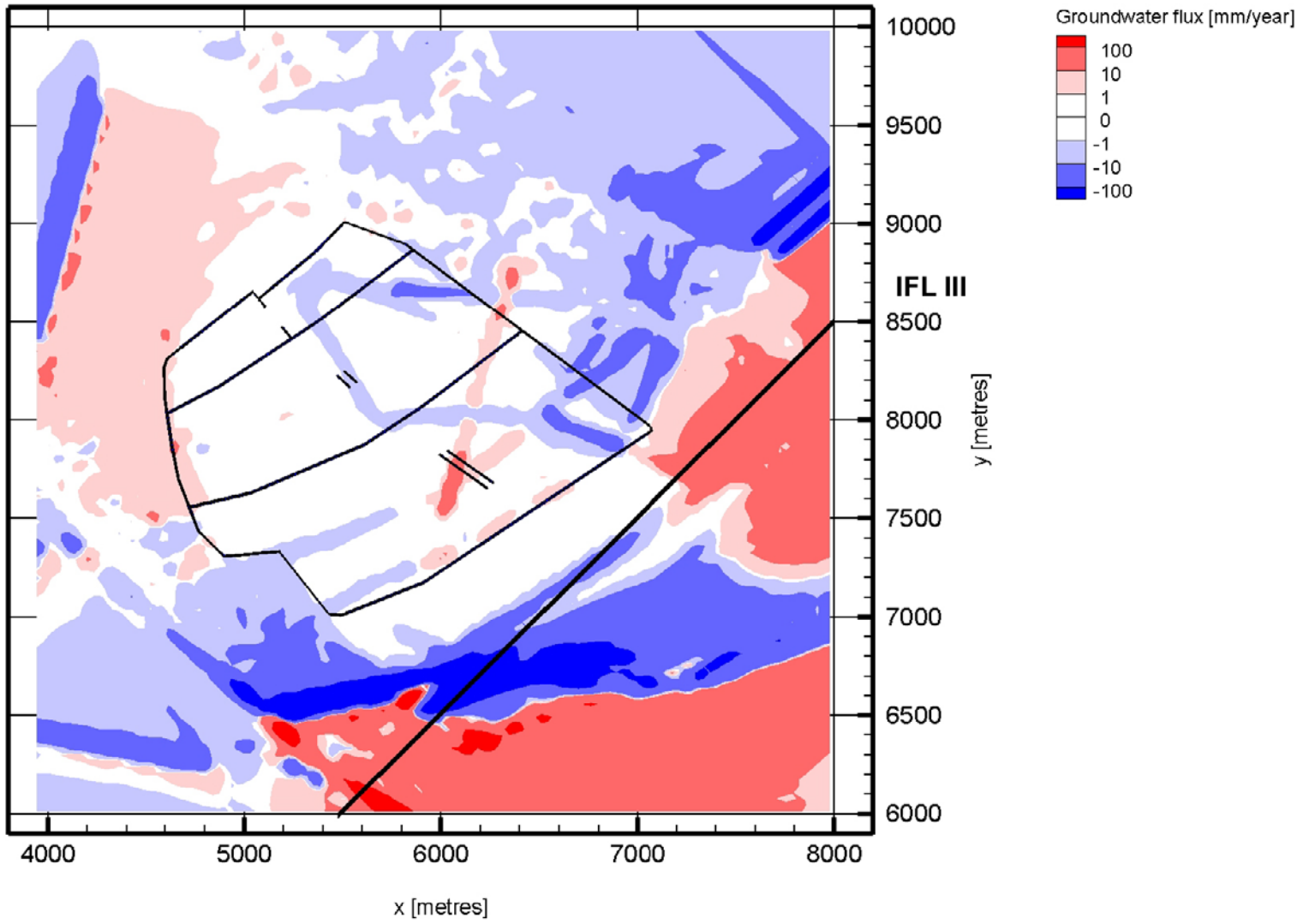

Figure F-7. *Horizontal view of the vertical Darcy flux in mm/y at –465 m elevation during glaciation when the ice sheet margin is at IFL III (black line). Red colours show positive values (upward directed fluxes), whereas blue colours show negative values (downward directed fluxes). The short black lines indicate major tunnels. The y-axis points towards north.*

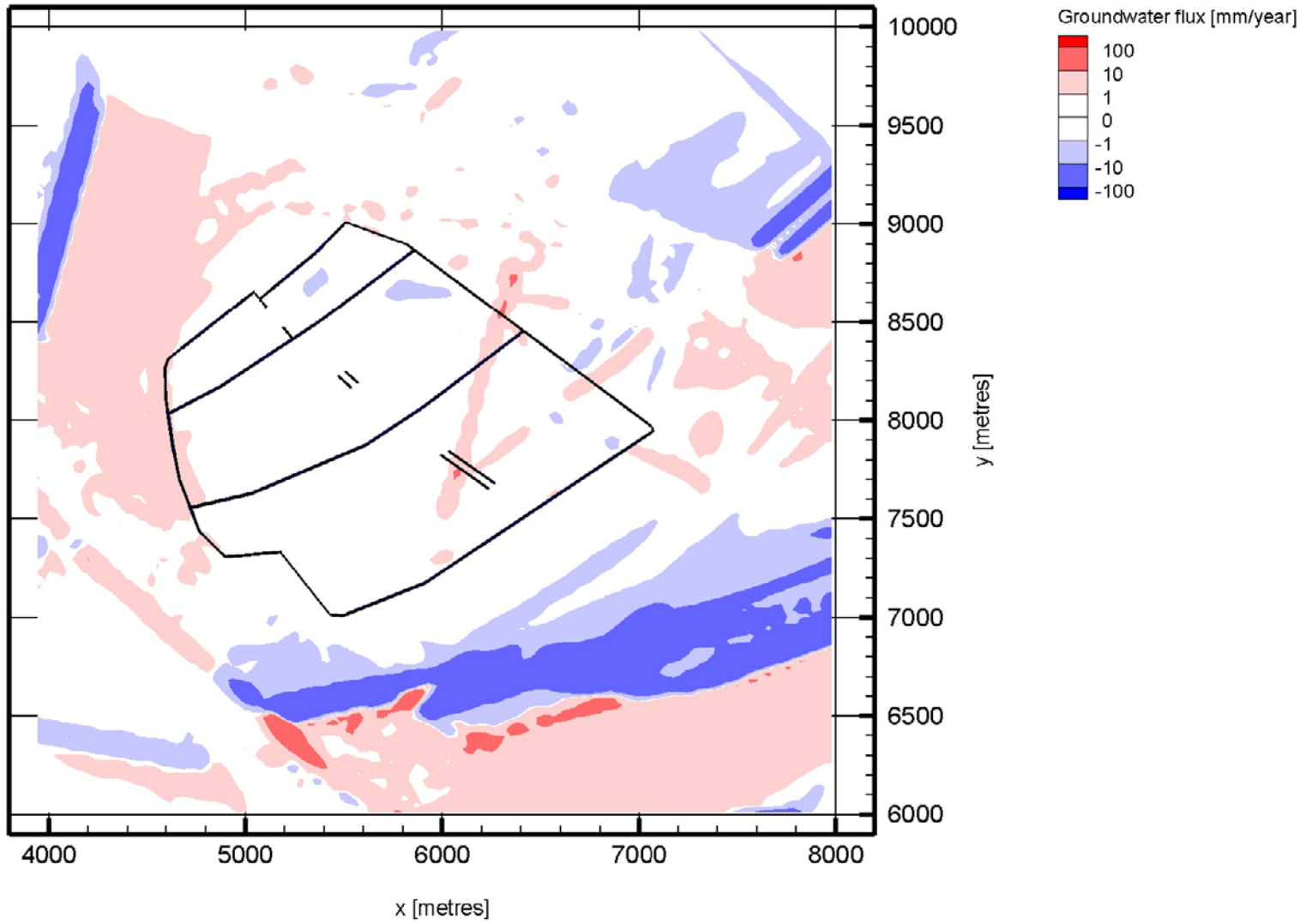

Figure F-8. *Horizontal view of the vertical Darcy flux in mm/y at –465 m elevation during glaciation when the ice sheet margin is at IFL IV (not visible in this plot). Red colours show positive values (upward directed fluxes), whereas blue colours show negative values (downward directed fluxes). The short black lines indicate major tunnels. The y-axis points towards north.*

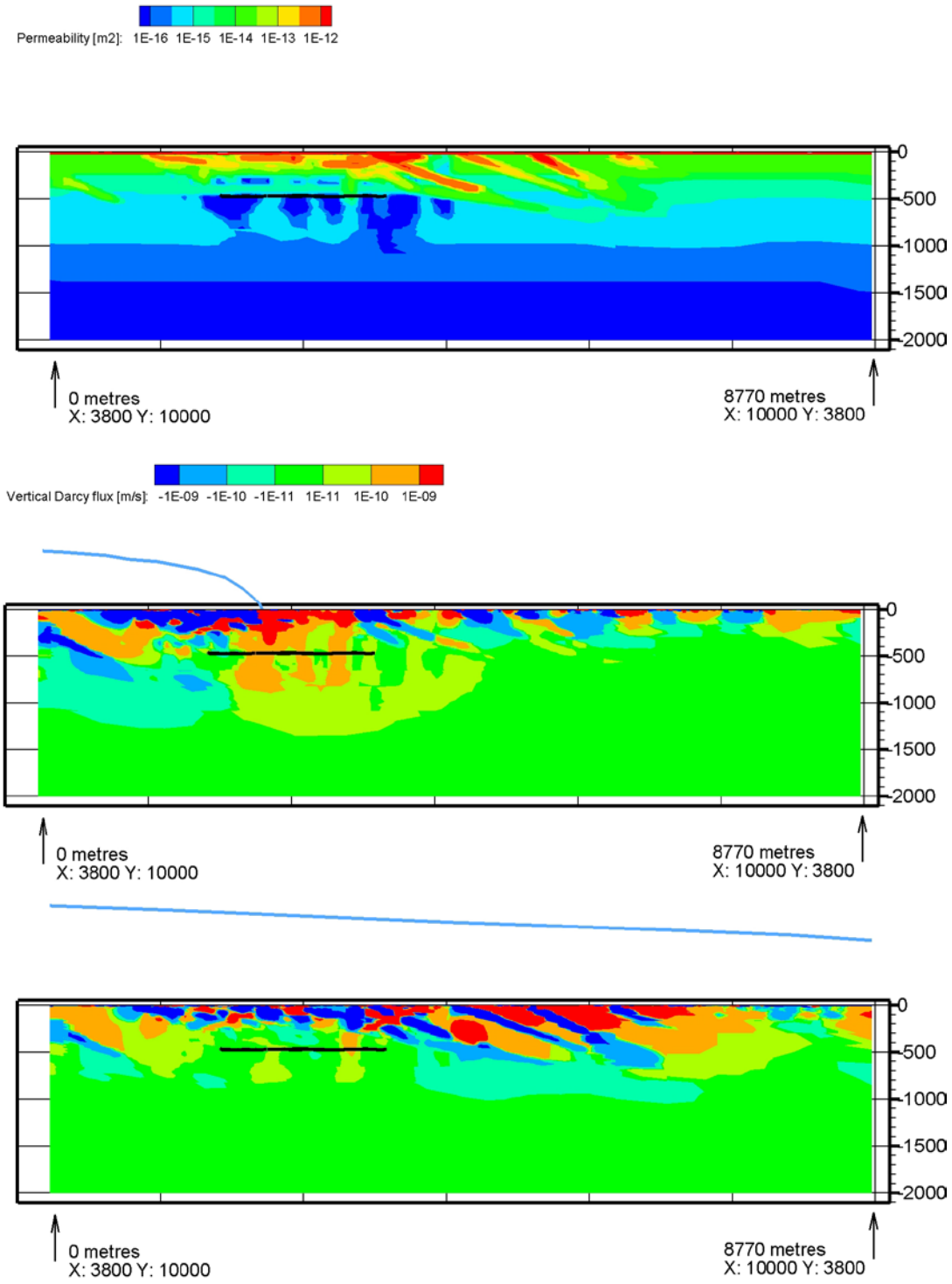

Figure F-9. *Top: Permeability field mapped on a NW-SE cross-section parallel to the ice flow direction. Middle: Vertical Darcy flux during glaciation when the ice sheet margin is at IFL II. Bottom: Vertical Darcy flux during glaciation when the ice sheet margin is at IFL IV. Positive values represent upward directed fluxes and negative values represent downward directed fluxes. The ice sheet thickness is illustrated with a blue curve. The black line at –465 m elevation shows the location of the repository.*

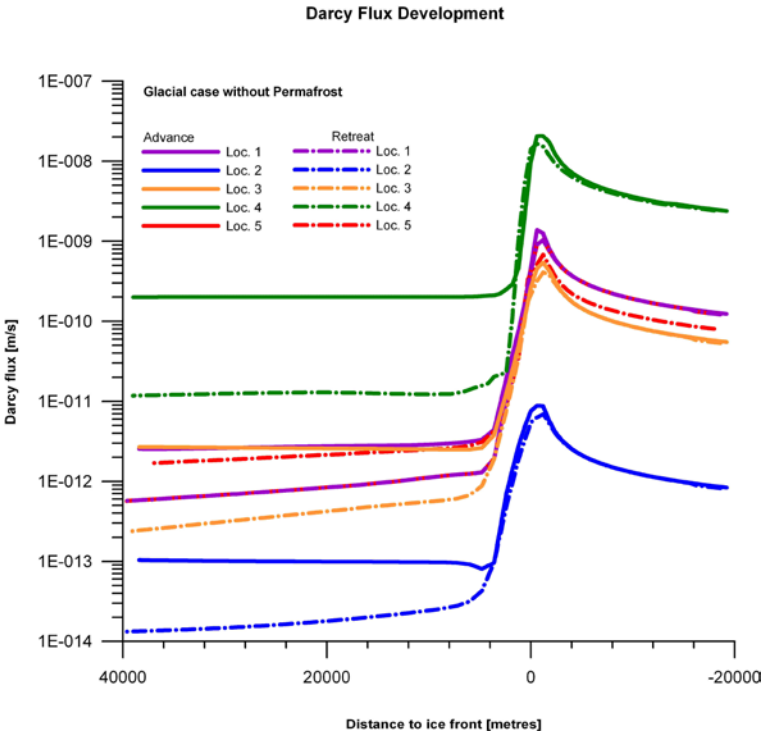

Figure F-10. *Darcy flux at ML 1–5 during glaciation and deglaciation. Positive values of "Distance to ice front" during glaciation mean that the ice sheet margin has not yet arrived to the measurement location. During the retreat, positive values indicate ice free conditions and an elevated sea level.*

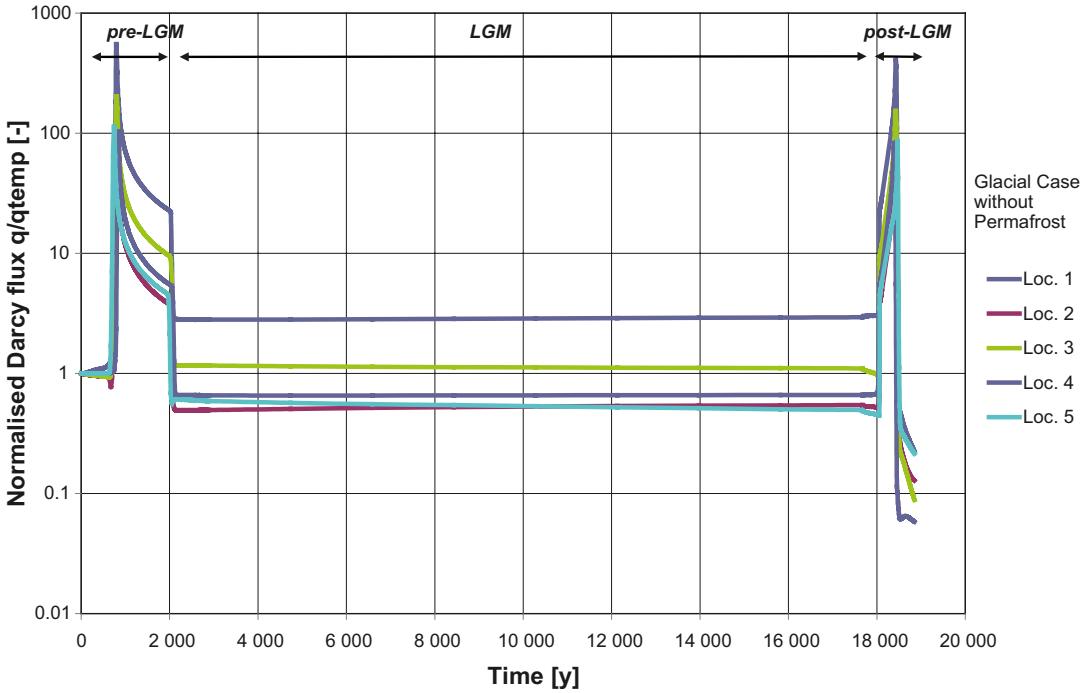

Figure F-11. *Normalised Darcy flux, q/q_{temp}, at ML 1–5 during glaciation (pre-LGM), complete ice coverage (LGM) and deglaciation (post-LGM).*

Between the two ice front passages, the model domain is completely covered by ice for a long period of time. When model domain is completely covered by ice for a long period of time, the simulated Darcy fluxes at ML 2, ML 4 and ML 5are approximately 30% lower than the fluxes during the temperate conditions, whereas they are approximately 30% higher at ML 1.

Figure F-12 shows the simulated Darcy flux at measurement localities 2 and 4 during the glaciations considered in cases (a) and (b). The direction of the advancing ice sheet margin does not appear to be significant for the Darcy flux.

Figure F-13 shows the simulated Darcy flux at the five measurement locations during the glaciations considered in cases (a) and (c). The increased transmissivity of structures that strike NW does not appear to be significant for the Darcy flux.

F.5 Salinity

The recharge of fresh meltwater during glaciation and deglaciation distorts the interface between fresh and saline groundwater. The saline groundwater is pushed forward and upward and some saline groundwater is flushed out of the model domain at the top boundary in the periglacial region in front of the ice sheet margin during the two ice sheet passages, see Figure F-14 and Figure F-15, respectively.

Figure F-16 shows the salinity field plotted on two cross-sections during glaciation when the ice sheet margin is at IFL II.

Figure F-17 shows that the distorted salinity field is influenced by the transmissive gently dipping deformation zones.

Figure F-18 shows the simulated fracture water salinity development at ML 1–5 during glaciation. All measurement localities experience an increase in salinity due to the upconing along the ice sheet margin. The peak salinity values at repository depth approach 1.5% at a time when the ice sheet margin is approximately 4 km from the site. At ML 4, which is located within deformation zone A2, the flushing occur somewhat earlier and the increase in salinity is less.

Figure F-19 shows a comparison between the simulated fracture water salinity at the five measurement locations during glaciation and deglaciation. The final values are approximately the same as those used as initial conditions prior to the glaciation.

Figure F-20 shows the simulated salinity development in the fracture water and in the matrix porewater at ML 2 during glaciation. During the passage of the ice sheet margin, the fracture water salinity at repository depth is flushed out and replaced by fresh glacial meltwater for a short period of time. The slowly decreasing salinity in the matrix porewater seen in Figure F-20 is due to (out) diffusion of salt from the matrix to the fractures.

Figure F-21 shows the normalised fracture water salinity (C/C_{temp}) at ML 1–5 during the glaciation (pre-LGM), the complete ice coverage (LGM) and the deglaciation (post-LGM). During the two ice front passages, the salinities undulate considerably. Between the two ice front passages, the model domain is completely covered by ice for a long period of time. The observed recovery of the fracture water salinity during the period of complete ice coverage is due buoyancy forces from the more saline fracture water below.

Figure F-22 shows the simulated fracture water salinity development at measurement locations ML 2 and ML 4 during the glaciations considered in cases (a) and (b). The direction of the advancing ice sheet margin does not appear to be significant for the fracture water salinity.

Figure F-23 shows the simulated fracture water salinity development at the five measurement locations during the glaciations considered in cases (a) and (c). The increased transmissivity of structures that strike NW does not appear to be significant for either the timing or magnitude of the peak fracture water salinity.

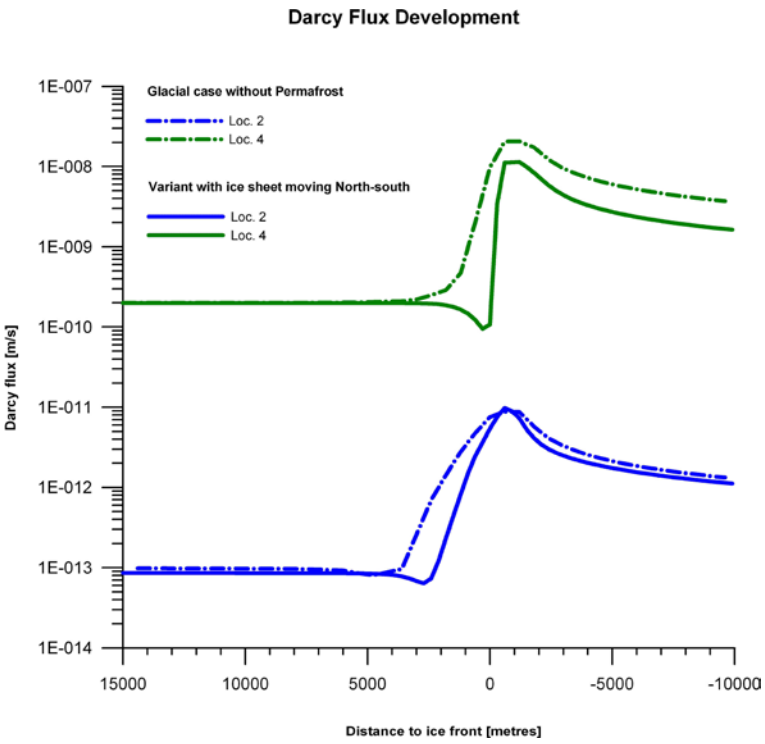

Figure F-12. *Comparison between the Darcy flux at ML 2 and ML 4 during glaciation for the conditions considered in cases (a) and (b). Positive distance values mean that the ice sheet margin has not yet arrived to the measurement locations.*

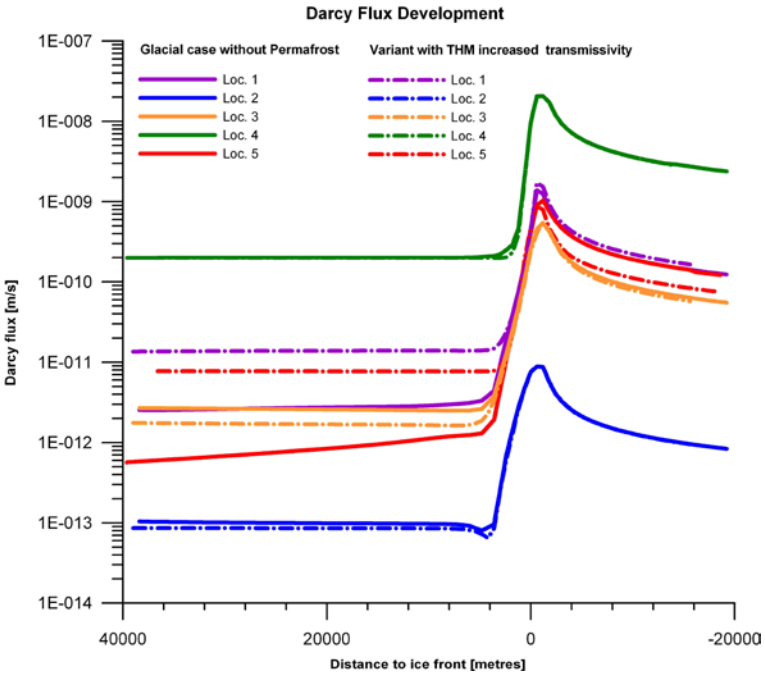

Figure F-13. *Comparison between the Darcy flux at ML 2 and ML 4 during glaciation for the conditions considered in cases (a) and (c). Positive distance values mean that the ice sheet margin has not yet arrived to the measurement locations.*

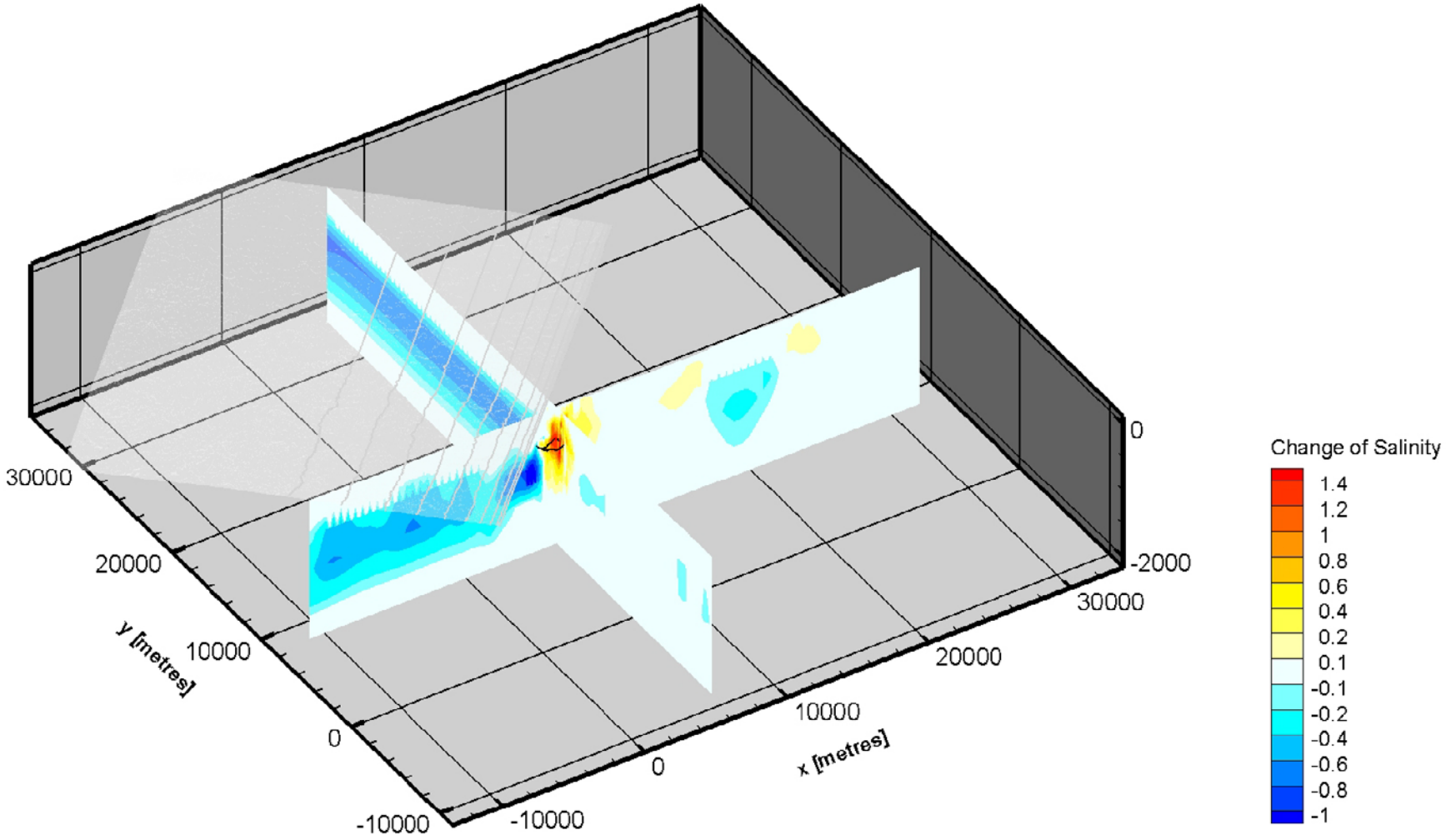

Figure F-14. *Visualisation of the change in fracture water salinity, $C–C_{temp}$, during glaciation when the ice sheet margin is at IFL II. The short black lines in the centre indicate the location of the repository. The y-axis points towards north.*

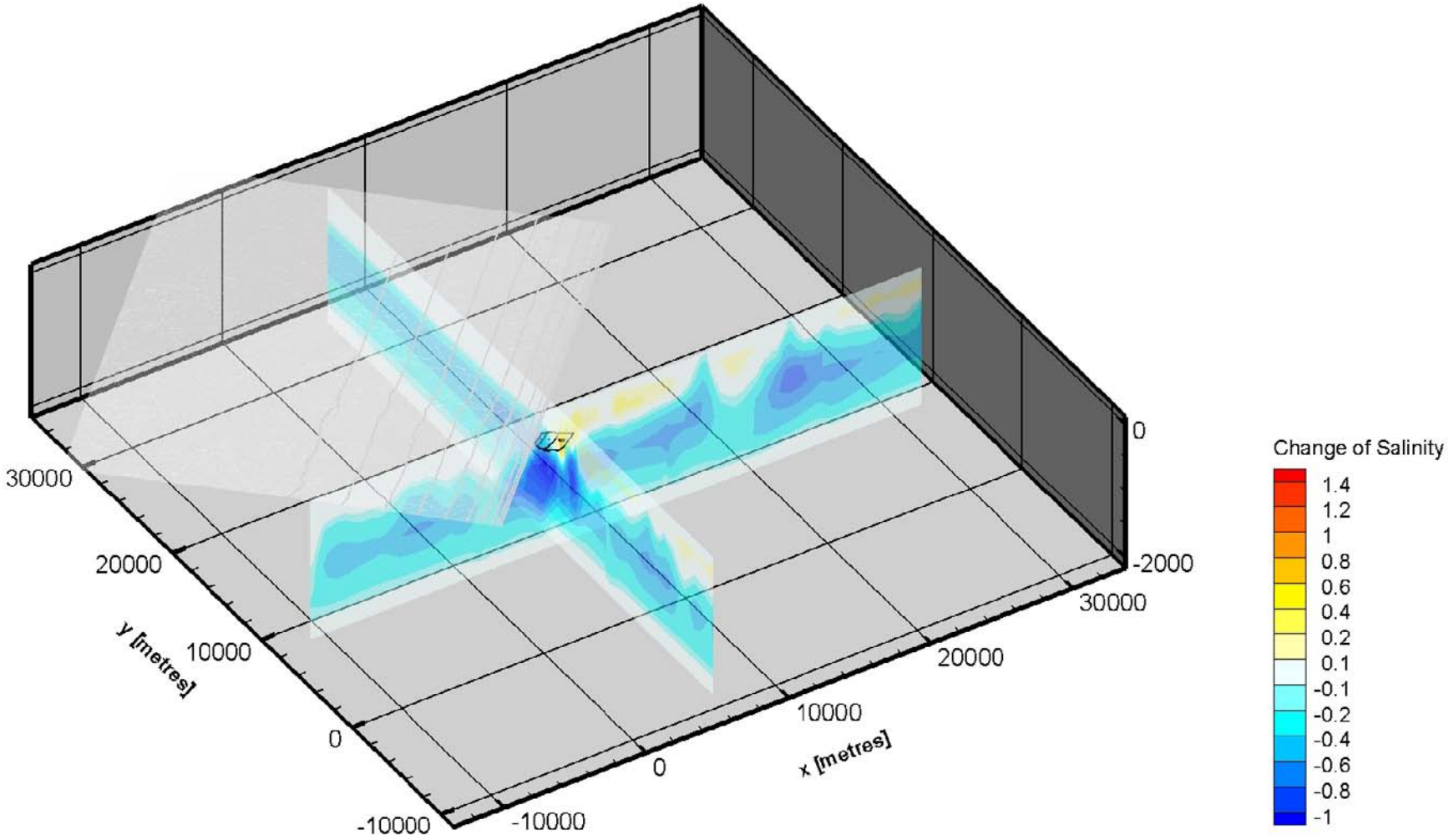

Figure F-15. *Visualisation of the change in fracture water salinity, $C–C_{temp}$, during deglaciation when the ice sheet margin is at IFL II. The short black lines in the centre indicate the location of the repository. The y-axis points towards north.*

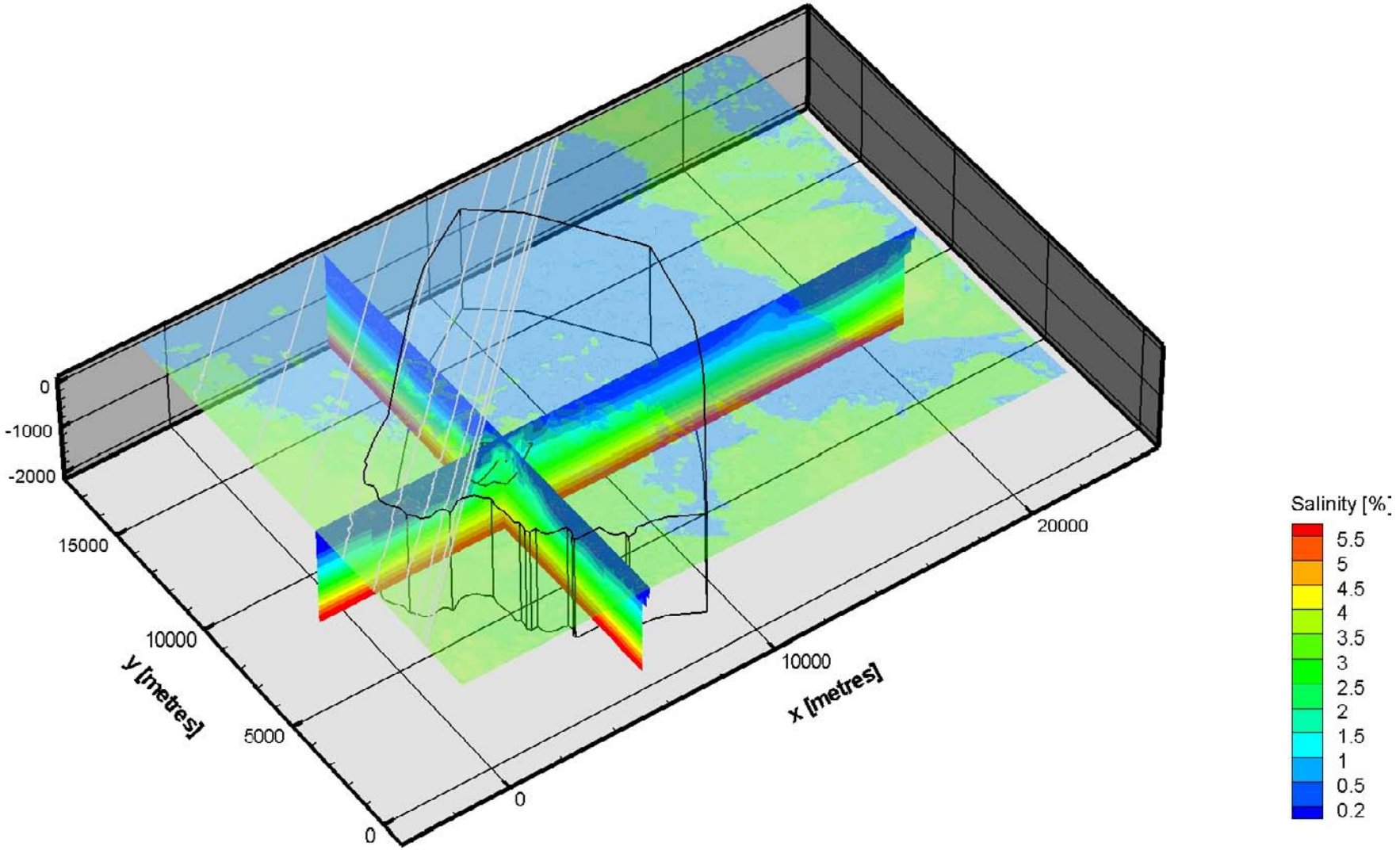

Figure F-16. *Visualisation of the salinity during glaciation when the ice sheet margin is at IFL II. The short black lines in the centre indicate the location of the repository. The y-axis points towards north.*

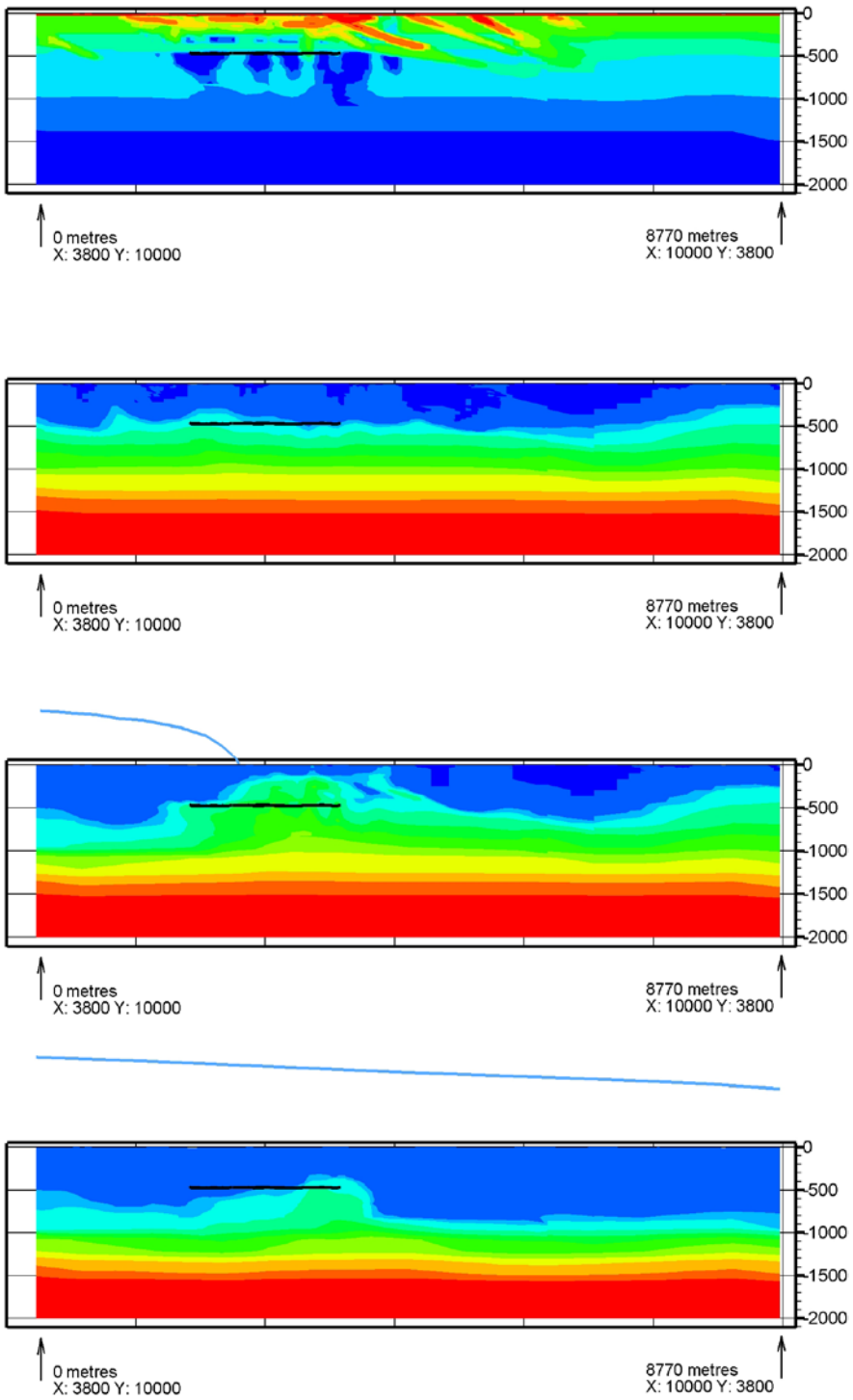

Figure F-17. *Top: Permeability field mapped on a NW-SE cross-section parallel to the ice flow direction. Upper Middle: Salinity field in the temperate case. Lower Middle: Salinity field when the ice sheet margin in case (a) is at IFL II. Bottom: Salinity field when the ice sheet margin in case (a) is at IFL IV. The ice sheet thickness is illustrated with a blue curve. The black line at –465 m elevation shows the location of the repository.*

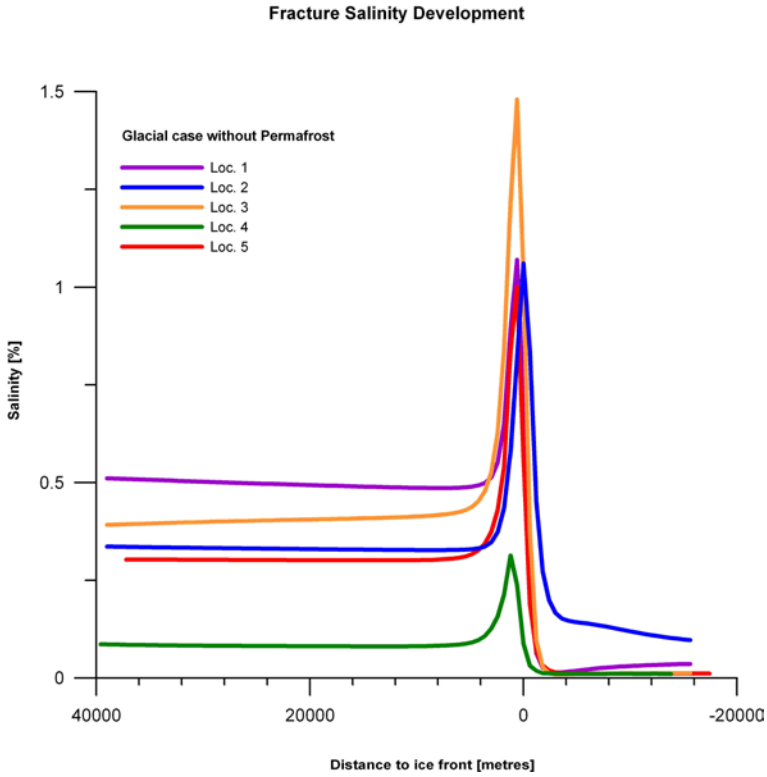

Figure F-18. *Fracture water salinity during glaciation at ML 1–5 during glaciation. Positive distance values mean that the ice sheet margin has not yet arrived to the measurement locations.*

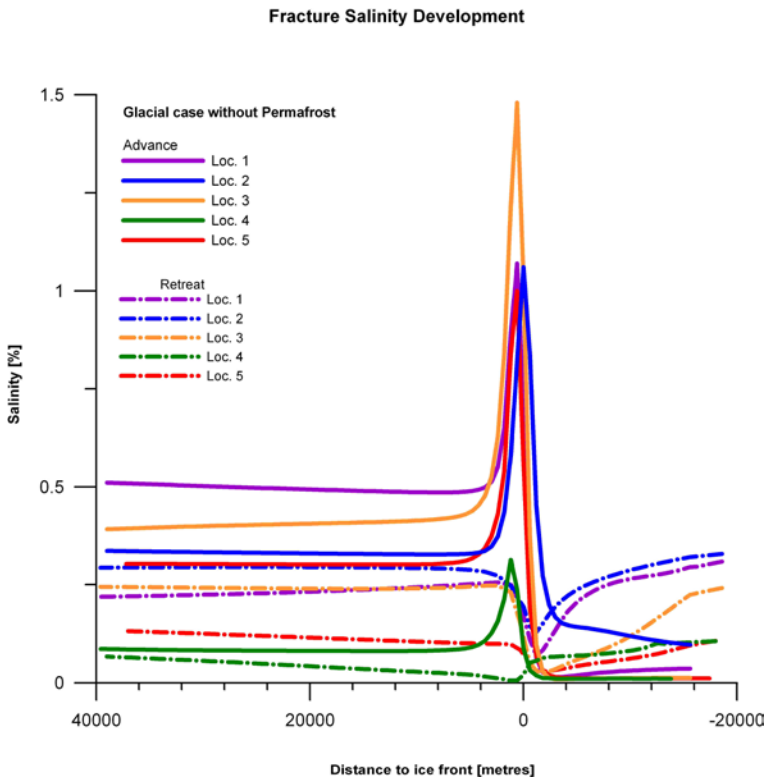

Figure F-19. *Fracture water salinity at ML 1–5 during glaciation and deglaciation in case (a). Positive values of "Distance to ice front" during glaciation mean that the ice sheet margin has not yet arrived to the measurement location. During the retreat, positive values indicate ice free conditions and an elevated sea level.*

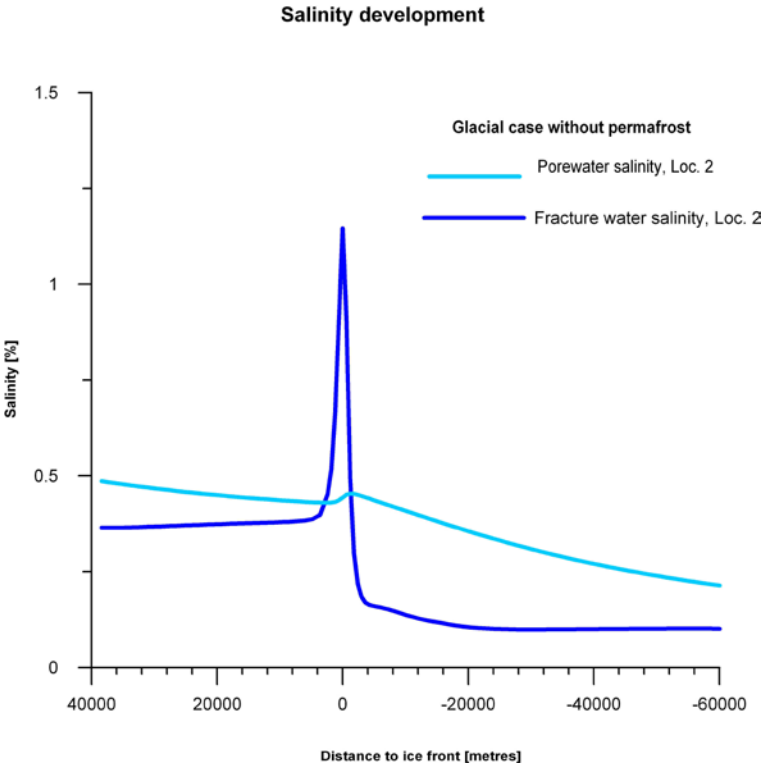

Figure F-20. *Salinity in the fracture water and in the matrix porewater at ML 2 during glaciation. Positive distance values mean that the ice sheet margin has not yet arrived to the measurement locations.*

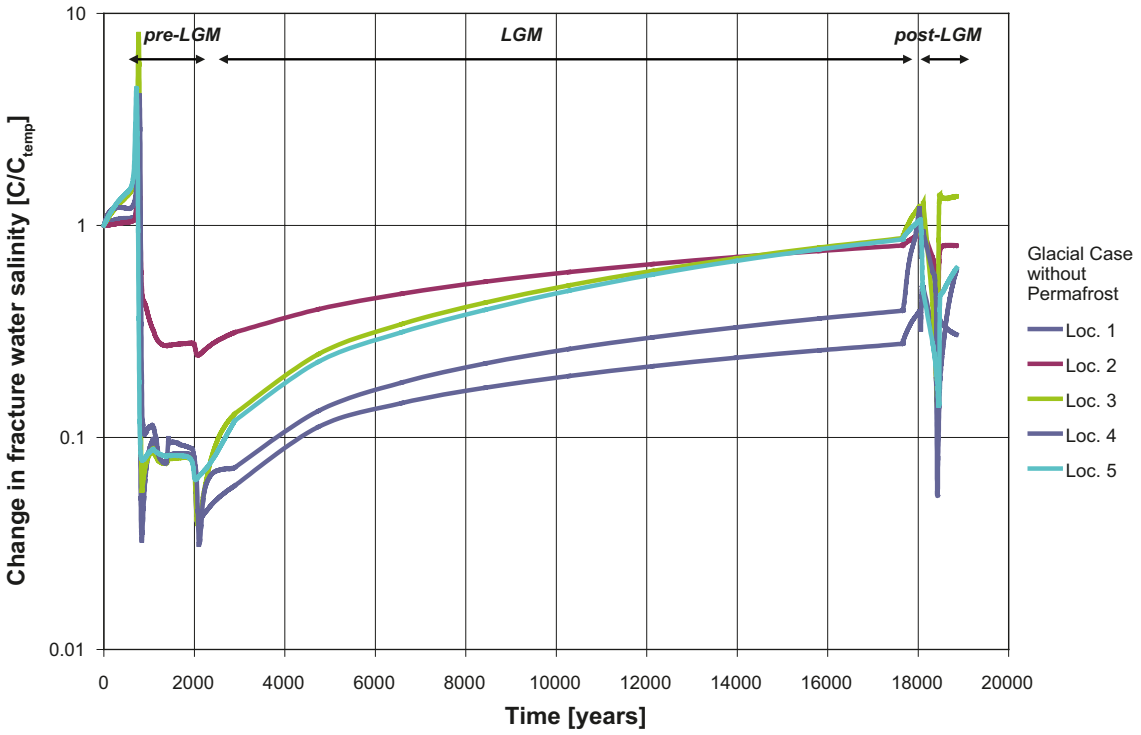

Figure F-21. *Normalised salinity, C/C_{temp}, at ML 1–5 during glaciation (pre-LGM), complete ice coverage (LGM) and deglaciation (post-LGM).*

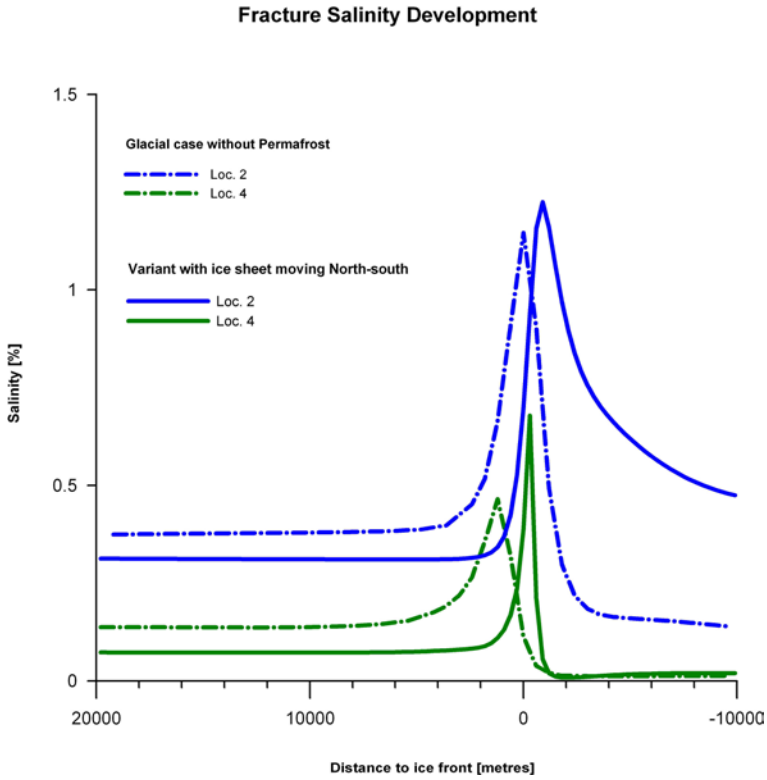

Figure F-22. *Comparison between the fracture water salinity at ML 2 and ML 4 during glaciation for the conditions considered in cases (a) and (b). Positive distance values mean that the ice sheet margin has not yet arrived to the measurement locations.*

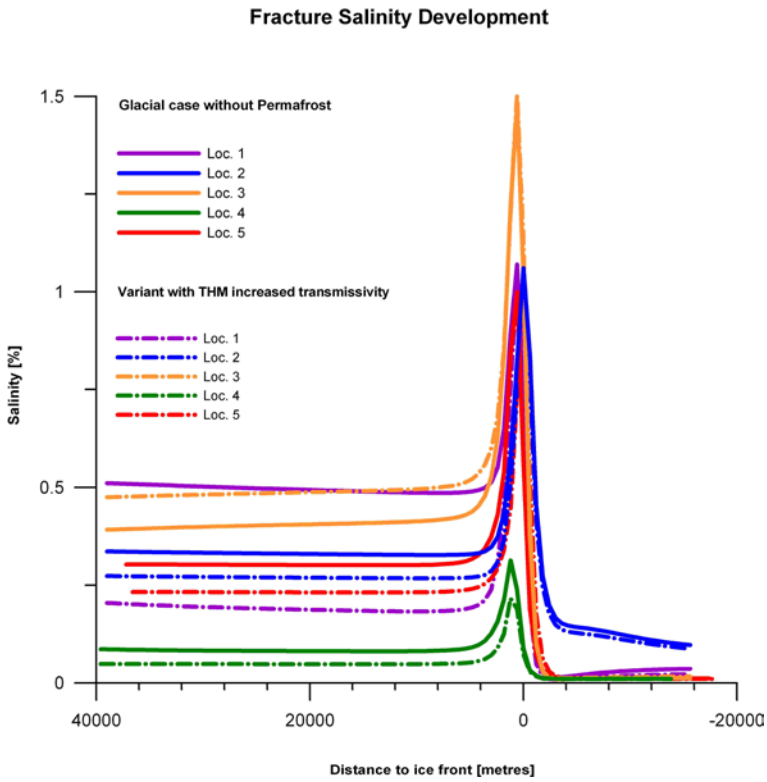

Figure F-23. *Comparison between the fracture water salinity at ML 2 and ML 4 during glaciation for the conditions considered in cases (a) and (c). Positive distance values mean that the ice sheet margin has not yet arrived to the measurement locations.*

F.6 Recharge and discharge locations

The repository contains 6,916 deposition hole positions. One particle is released at each deposition hole position and all particles are tracked backwards and forwards as a means to identify their recharge and discharge locations, respectively. It is noted that the ice sheet margin is fixed during the particle tracking, which is a simplification since the boundary conditions at ground surface change continuously during glaciation and deglaciation with the movement of the advancing/retreating ice sheet.

Figure F-24 shows the results from the particle tracking when the ice sheet margin during glaciation reached ice-front location II, III and IV. Figure F-24 reveals that a number particles recharge at the upstream boundary of the model domain, which suggests that the model domain is too small to give an undistorted view of all recharge locations for a fixed Darcy flux field. Nevertheless, it may be concluded that the present-day topographic water divides, which play an important role in recharge and discharge during temperate conditions, are of significantly diminished importance during glacial conditions.

In contrast, the majority of the discharge locations are well within the physical boundaries of the model domain and, as a matter of fact, often very close to the ice sheet margin. The differences seen in the discharge pattern between the two ice-front locations, IFL II and IFL IV, are largely caused by the varying resolution of geological structures in the hydrogeological model. At IFL II, the discharge pattern is strongly affected by the structural-hydraulic properties of the deformation zone model that exist within the regional model domain of SDM-Site. At IFL IV, the ice sheet margin is outside the regional model domain of SDM-Site and the discharge pattern in front of the ice sheet margin is to a greater extent affected by the topography because the bedrock is here modelled as a homogenous continuous porous medium (CPM).

F.7 Recharge performance measures

Particles are released at the 6,916 deposition hole positions and at the five measurement localities, ML 1–5, and tracked for 100 years. Not all of the released particles reach the ground surface within this period of time. Figure F-25, Figure F-26 and Figure F-27 show cumulative distribution (probability) plots of the recharge flow path lengths, travel times, and flow-related transport resistances for the particles released at the 6,916 deposition hole positions during glaciation when the ice sheet margin is at IFL II and IFL IV, respectively. For the sake of comparison, the corresponding cumulative distribution plots of these performance measures derived for the temperate case are also shown in these figures as well as the corresponding data for the particles released at the ML 1–5 when the ice sheet margin is at IFL II.

Figure F-25 shows the cumulative distribution (probability) plots of the recharge flow path lengths (L_R). Typically, the presence of an ice sheet increases the recorded recharge flow path lengths compared to the temperate case. The shortest pathways are approximately 4 km, which is approximately of the same order of magnitude as the longest recharge pathway lengths during temperate conditions. During glaciation, a significant amount of particle recharge occurs at the upstream boundary. The permeability conditions affect the recharge location. For instance, ML 2 is located in the centre of the suggested target area in a region where the permeability is low. In contrast, ML 1,3–5 are located closer to the perimeter of the target area where the permeability is higher than at ML 2. As a consequence, the flow path passing through ML 2 have a fairly local recharge, whereas the flow paths passing through ML 1, 3–5 recharge at the upstream model boundary.

Figure F-26 shows the cumulative distribution (probability) plots of the recharge travel times ($t_{w,R}$). Typically, the presence of an ice sheet decreases the recorded recharge travel times compared to the temperate case. However, the greatest effect of glaciation on the recharge travel time is on the slowest particles, whereas the faster particles are less affected. The recharge travel times of ML 1–5 is are all within the range of recharge travel times recorded for the 6,916 deposition hole positions. It is worth noting that during 100 y, the ice sheet margin would have moved forward approximately 5 km if allowed to advance. The time needed for the ice sheet margin to move from IFL II to IFL IV is approximately 200 years.

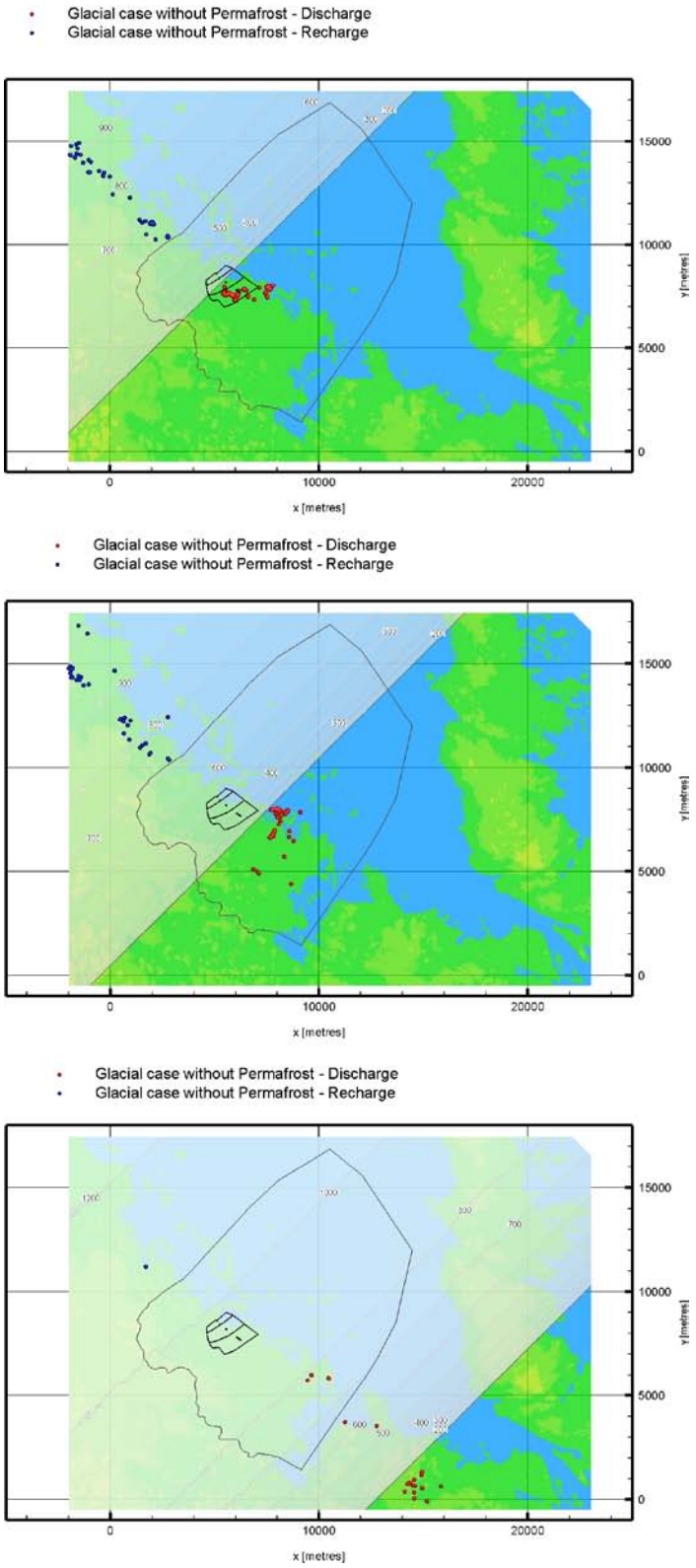

Figure F-24. *Recharge (blue) and discharge (red) locations during glaciation for 6,916 particles released at repository depth when the ice sheet margin is at IFL II (top), IFL III (middle) and IFL IV (bottom). The short black lines in the centre of each image indicate the location of major tunnels. The y-axis points towards north.*

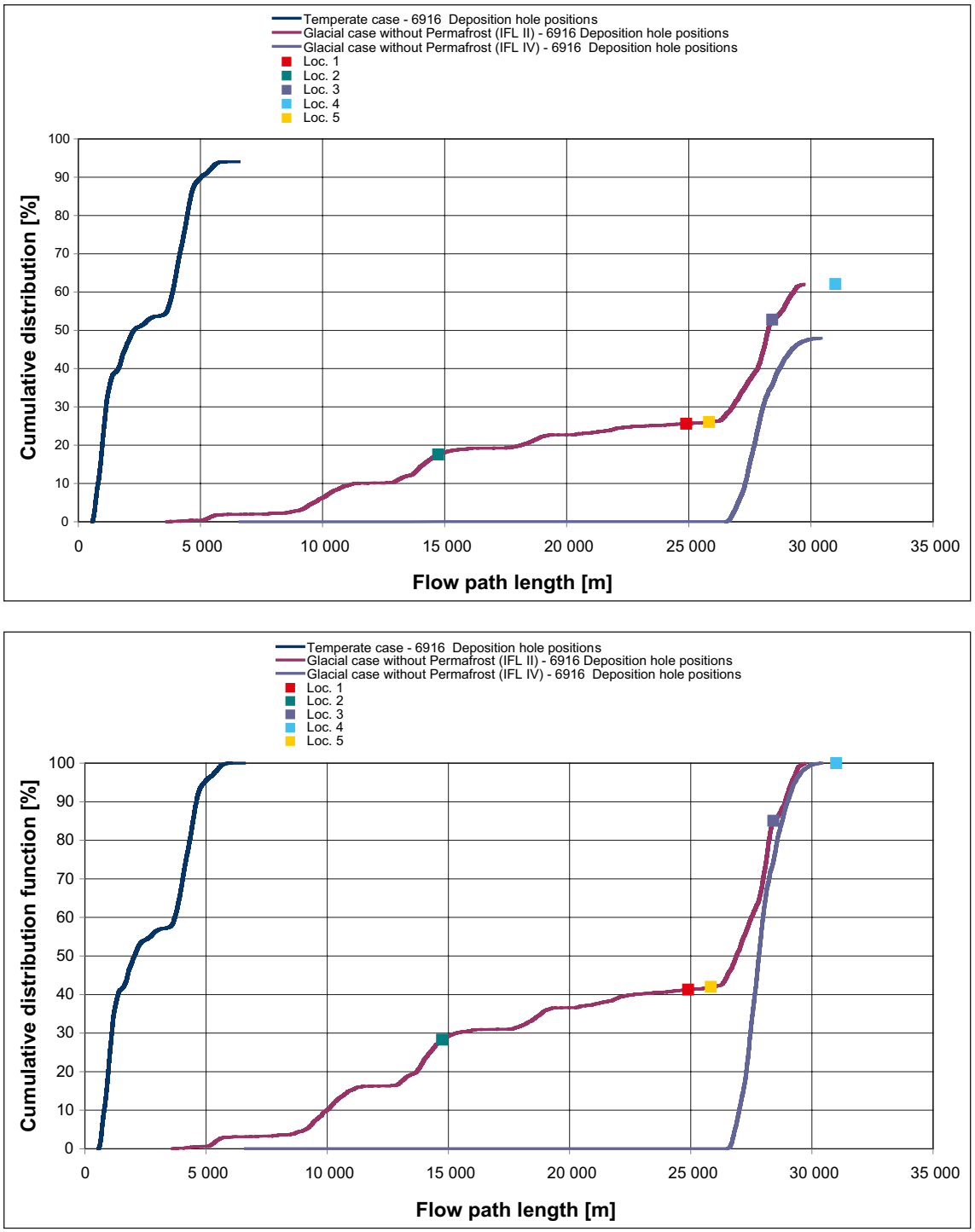

Figure F-25. *Cumulative distribution (probability) plots of the simulated recharge flow path lengths, L_R, when the ice sheet margin is at IFL II and IV, respectively. The distribution for the temperate case is also shown as well as the data for ML 1–5 at IFL II. The maximum value in the upper plot is set to 100% in the lower plot.*

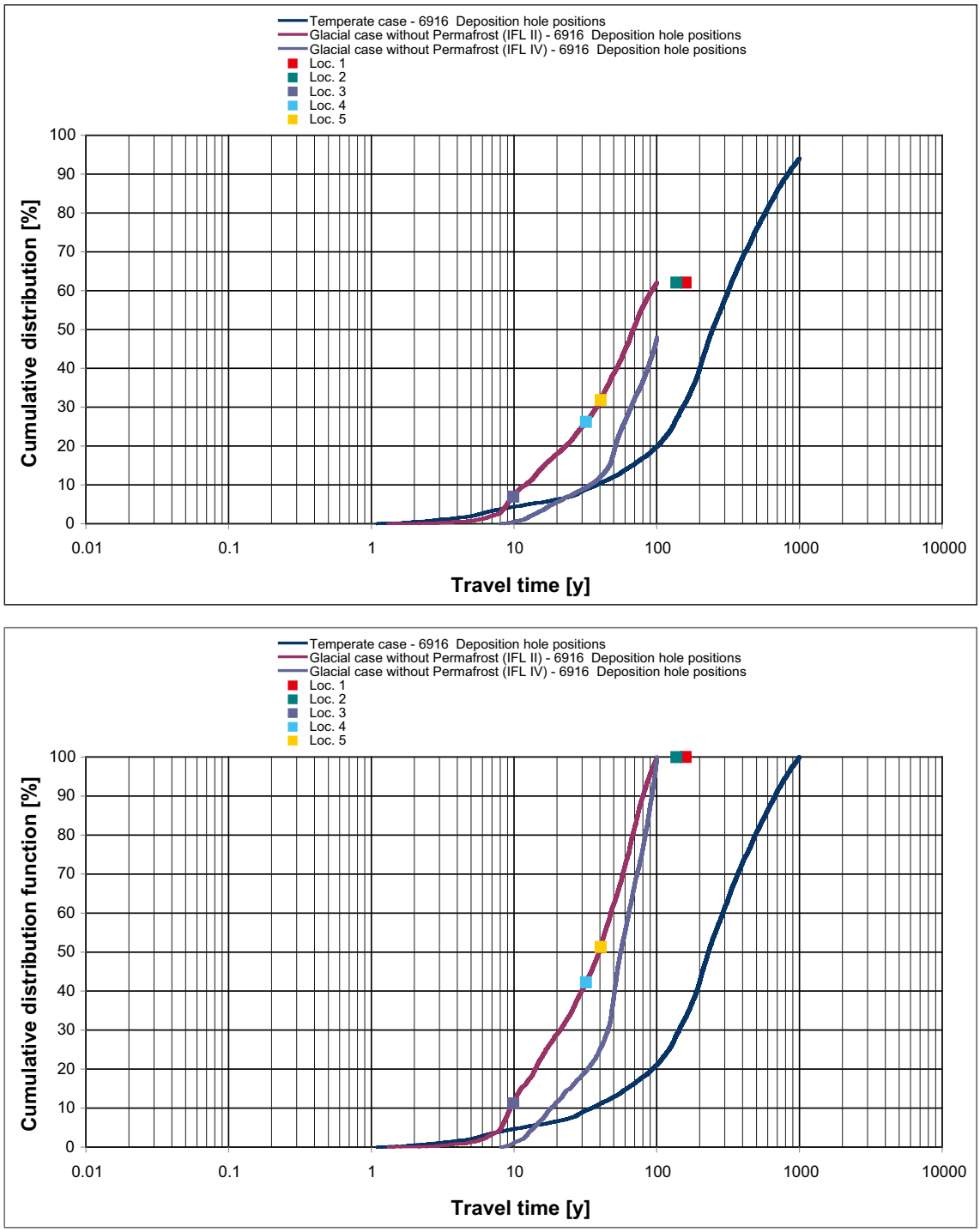

Figure F-26. *Cumulative distribution (probability) plots of the simulated recharge travel times, $t_{w,R}$, when the ice sheet margin is at IFL II and IV, respectively. The distribution for the temperate case is also shown as well as the data for ML 1–5 at IFL II. The maximum value in the upper plot is set to 100% in the lower plot.*

Figure F-27 show the cumulative distribution (probability) plots of the recharge flow-related transport resistances (F_R). Typically, the presence of an ice sheet decreases the recorded flow-related transport resistances compared to the temperate case. However, the smallest values recorded in the particle tracking are only slightly smaller than the smallest values recorder for the temperate case. Further, as the glaciation proceeds, as illustrated by IFL IV, the recorded recharge flow-related transport resistances increase and are somewhat greater as compared with the temperate case. The measurement localities all have transport resistances clustered around the median value of the 6,916 deposition hole positions.

For the sake of clarity, it is noted that the period of the ice front passage is relatively limited and that the methodology used here for the particle tracking probably creates unduly low values of the recharge flow path lengths, advective travel times, and flow-related transport resistances.

F.8 Discharge performance measures

Particles are released at the 6,916 deposition hole positions and at the five measurement localities, ML 1–5, and tracked for 100 years. Not all of the released particles reach the ground surface within this period of time. Figure F-28, Figure F-29 and Figure F-30 show cumulative distribution (probability) plots of the discharge flow path lengths, travel times, and flow-related transport resistances for the particles released at the 6,916 deposition hole positions when the ice sheet profile addressed in case (c) is at ice-front locations II and IV, respectively. For the sake of comparison, the corresponding cumulative distribution plots of these performance measures derived for the temperate case are also shown in these figures as well as the corresponding data for the particles released at the ML 1–5 when the ice sheet margin is at IFL II.

Figure F-28 shows the cumulative distribution (probability) plots of the discharge flow path lengths (L_D). Figure F-28 shows that the passage of the ice front at IFL II does not seem to affect the minimum value of the discharge flow path length as compared with the case. However, the distribution is much affected, as 90% of the flowpaths rather than 40% have lengths of less than 4 km. As the ice moves on, the flow path lengths becomes successively larger as the majority of particles travel all the way to the ice margin before discharging. Figure F-28 shows that ML 1–5 have flow path lengths that fall within the range of the 6,916 deposition hole positions.

Figure F-29 shows the cumulative distribution (probability) plots of the discharge travel times ($t_{w,D}$). As expected, the travel times are shorter when the ice front is at IFL II than at IFL IV. In comparison with Temperate case, the discharge travel times are lowered by 2 to 3 orders of magnitude and 90% of particles discharge within 100 y; the fastest particles discharge after some weeks. The particle passing through ML 1 discharges after approximately 50 days. ML 1 is located fringing a NW-SE trending major deformation zone (NW0003) and hence is affected by its ability to transport significant amount of water along the main pressure gradient. As the ice sheet margin proceeds, the sub-glacial travel times approach the values recorded for the temperate case. It is worth noting that during 100 y, the ice sheet margin would have moved forward approximately 5 km if allowed to advance. The time needed for the ice sheet margin to move from IFL II to IFL IV is approximately 200 years.

Figure F-30 shows the cumulative distribution (probability) plots of the discharge flow-related transport resistances (F_D). The flow-related transport resistance is in general decreased by 2–3 orders of magnitude. As the ice sheet margin proceeds, the recorded values of the flow-related transport resistances approach the values recorded for the temperate case. The measurement localities all have values that fall quite close to the median value for the 6,916 deposition hole positions, with the possible exception of ML 1 that has a lower flow-related transport resistance as compared with the other four measurement localities.

For the sake of clarity, it is noted that the period of the ice front passage is relatively limited and that the methodology used here for the particle tracking probably creates unduly low values of the recharge flow path lengths, advective travel times, and flow-related transport resistances.

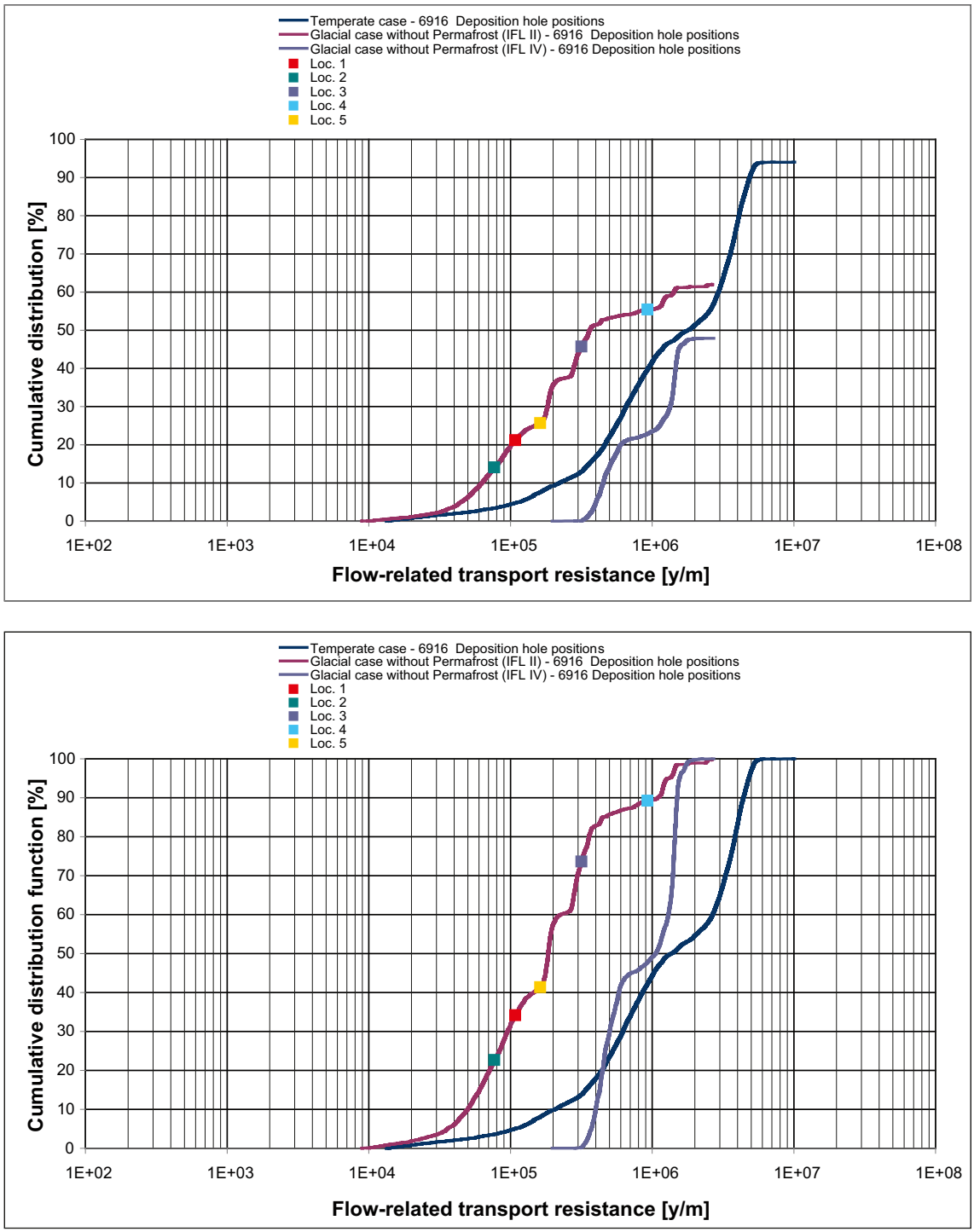

Figure F-27. *Cumulative distribution (probability) plots of the simulated recharge flow-related The distribution for the temperate case is also shown as well as the data for ML 1–5 at IFL II. The maximum value in the upper plot is set to 100% in the lower plot.*

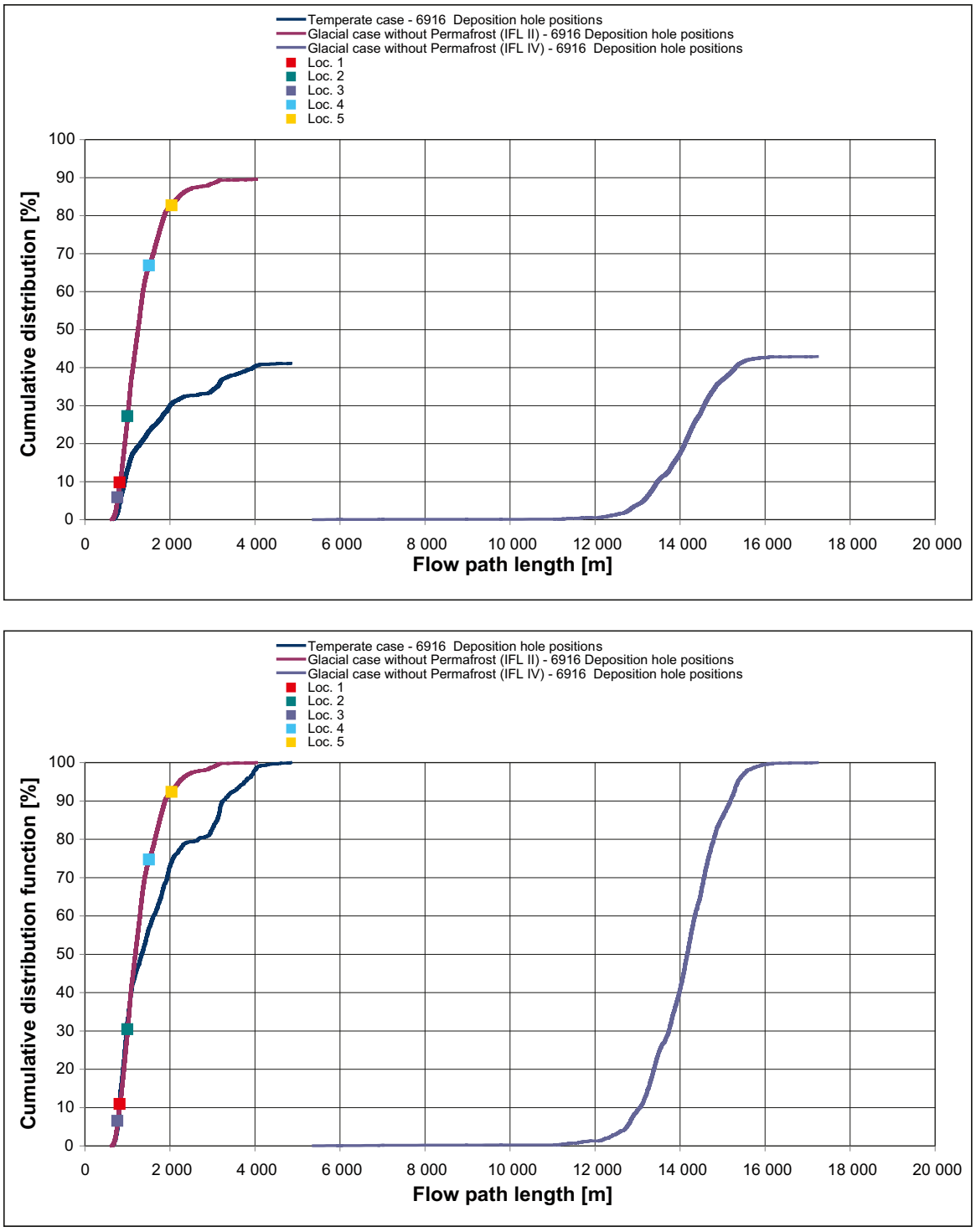

Figure F-28. *Cumulative distribution (probability) plots of the simulated discharge flow path lengths, L_D, when the ice sheet margin is at IFL II and IV, respectively. The distribution for the temperate case is also shown as well as the data for ML 1–5 at IFL II. The maximum value in the upper plot is set to 100% in the lower plot.*

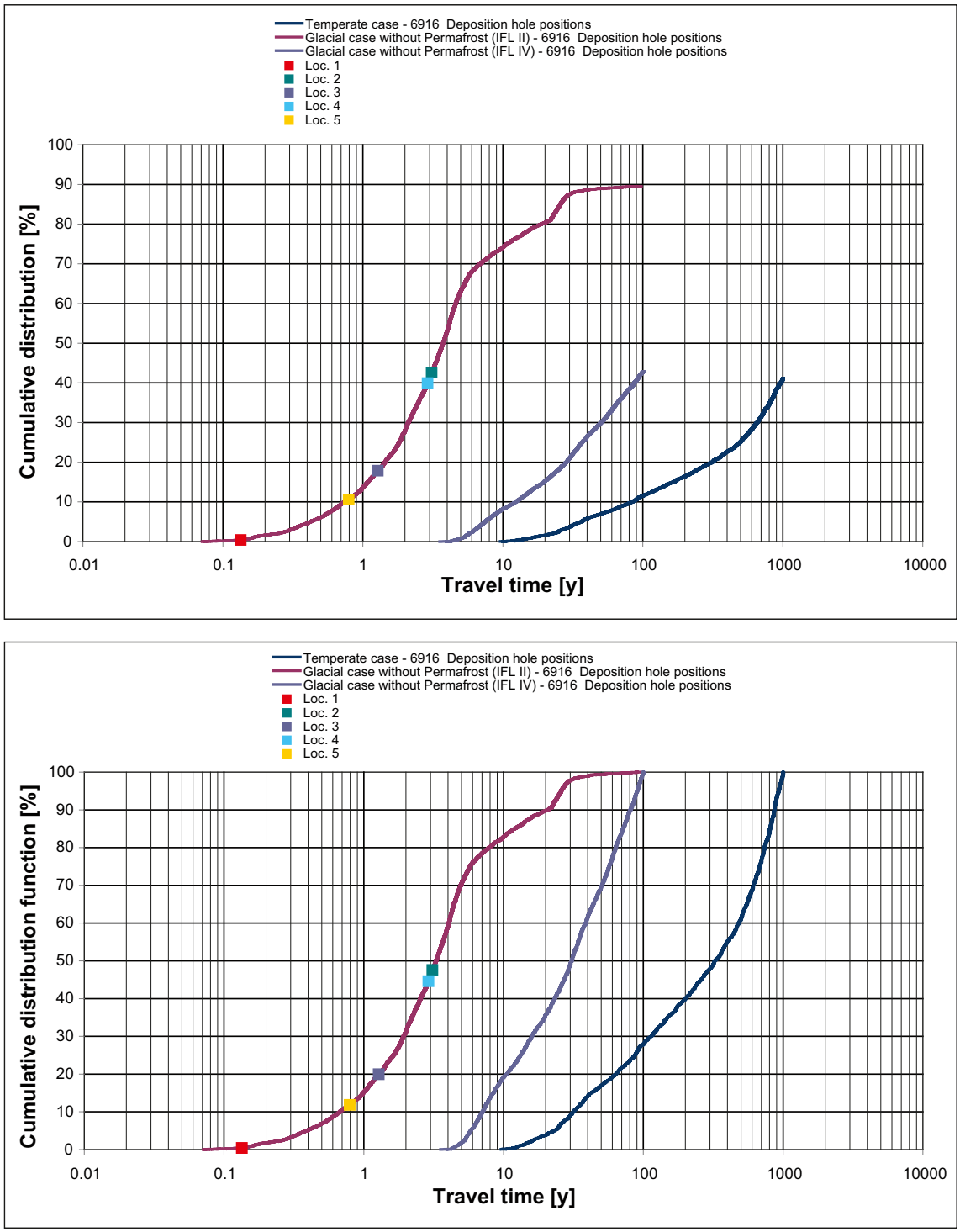

Figure F-29. *Cumulative distribution (probability) plots of the simulated discharge travel times, $t_{w;D}$, when the ice sheet margin is at IFL II and IV, respectively. The distribution for the temperate case is also shown as well as the data for ML 1–5 at IFL II. The maximum value in the upper plot is set to 100% in the lower plot.*

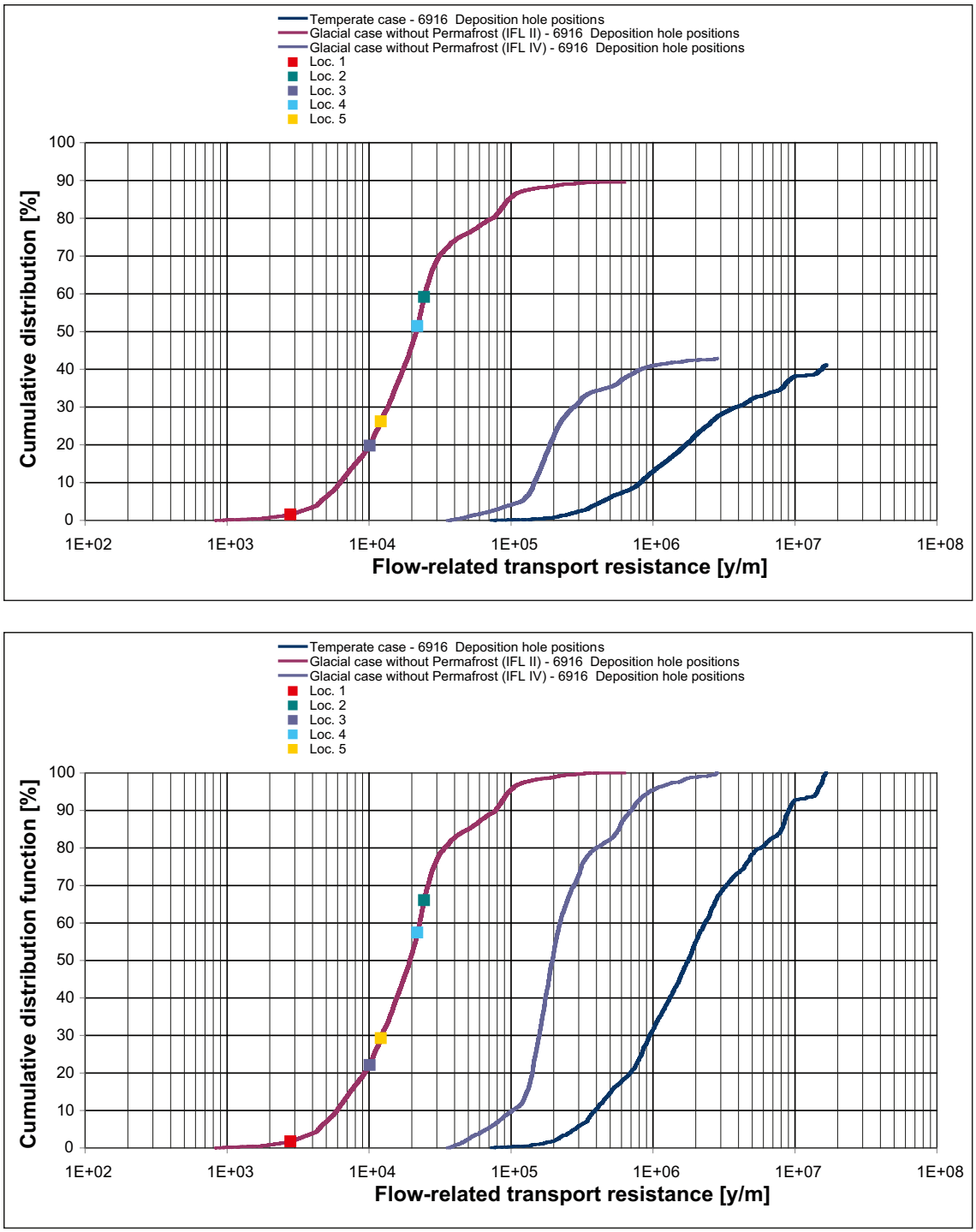

Figure F-30. *Cumulative distribution (probability) plots of the simulated discharge flow-related transport resistances, F_D, when the ice sheet margin is at IFL II and IV, respectively. The distribution for the temperate case is also shown as well as the data for ML 1–5 at IFL II. The maximum value in the upper plot is set to 100% in the lower plot.*

Appendix G

Scenario B: Glacial climate conditions with permafrost

G.1 Introduction

All plots shown is this appendix refer to case (d), see Table 5-1 and Figure 5-3, except for one plot that compares case (d) with case (e). This exceptions are explicitly stated.

G.2 Top boundary conditions

The grayish area in Figure G-1 indicates the ice sheet thickness when the ice sheet margin during glaciation is at ice-front location II (IFL II). The speed of the ice sheet margin is 50 m/y and it reaches IFL II after approximately 600 years in relation to the north-west boundary of the model domain.

Ice-free elevations above –28 m are subjected to permafrost; the temperature is fixed at –4.5°C. Ice-free elevations below –28 m are modeled as taliks; the temperature is fixed at +4°C. Beneath the ice sheet, the temperature is set to +0.01°C except for a 2 km long tongue behind the ice sheet margin where the temperature increases linearly from –4.5°C to +0.01°C. In case (e), there is no such linear increase, but the temperature is set to +0.01°C already at the margin.

A pressure equal to 92% of the weight of the ice sheet thickness is specified on the top boundary where the temperature is +0.01°C. Elsewhere, the pressure is set to zero in all terrestrial parts and to the hydrostatic pressure below the ice-free sea, lakes and taliks.

G.3 Pressure

Figure G-2 shows the pressure (P) mapped on two cross-sections when the ice sheet margin is at ice-front location II. The pressure gradient between the ice sheet and the taliks is very different from the pressure gradient shown in Figure F-2 for the glacial case without permafrost.

Figure G-3 shows the simulated development of the pressure during glaciation at the five measurement localities (ML 1–5). The pressures develop similarly at these localities. The effect of the approaching ice sheet margin is not visible until the ice sheet margin is fairly close to ML 1–5. The undulations between x = 0 and x = –5,000 m are caused by the changes in the permeability that occur when the ice sheet margin passes over the permafrost.

It is expected that a permafrost zone beneath an advancing ice sheet margin will exist, see /SKB 2010/. However, great uncertainties in the size of this zone prevail hence a sensitivity case is used in order to see the effect of not including such a zone. Figure G-4 shows the effect of no permafrost behind the ice sheet margin (case (e)). It is seen that a “permafrost tongue” increases the complexity of the flow solution due to the aforementioned changes in the permeability that occur when the ice sheet margin passes over the permafrost.

G.4 Darcy flux

Figure G-5 to Figure G-9 show the simulated spatial distribution of the vertical Darcy flux across a plane at –465 m elevation. The plane passes through the target volume and the location of the repository adopted for modelling for SR-Site Forsmark.

Figure G-5 shows the vertical Darcy flux for the temperate conditions addressed in case (a).

Figure G-6 shows the vertical Darcy flux for the frozen ground conditions addressed in case (d) before the introduction of an ice sheet. In this figure, a different colour scale is used in order to illustrate the extremely low Darcy flux at such times.

Figure G-7 shows the vertical Darcy flux when the front of the advancing ice sheet margin addressed in case (d) is at ice-front location II, i.e. immediately above the repository. Little effect of the ice sheet margin is observed due to the frozen ground “barrier” beneath.

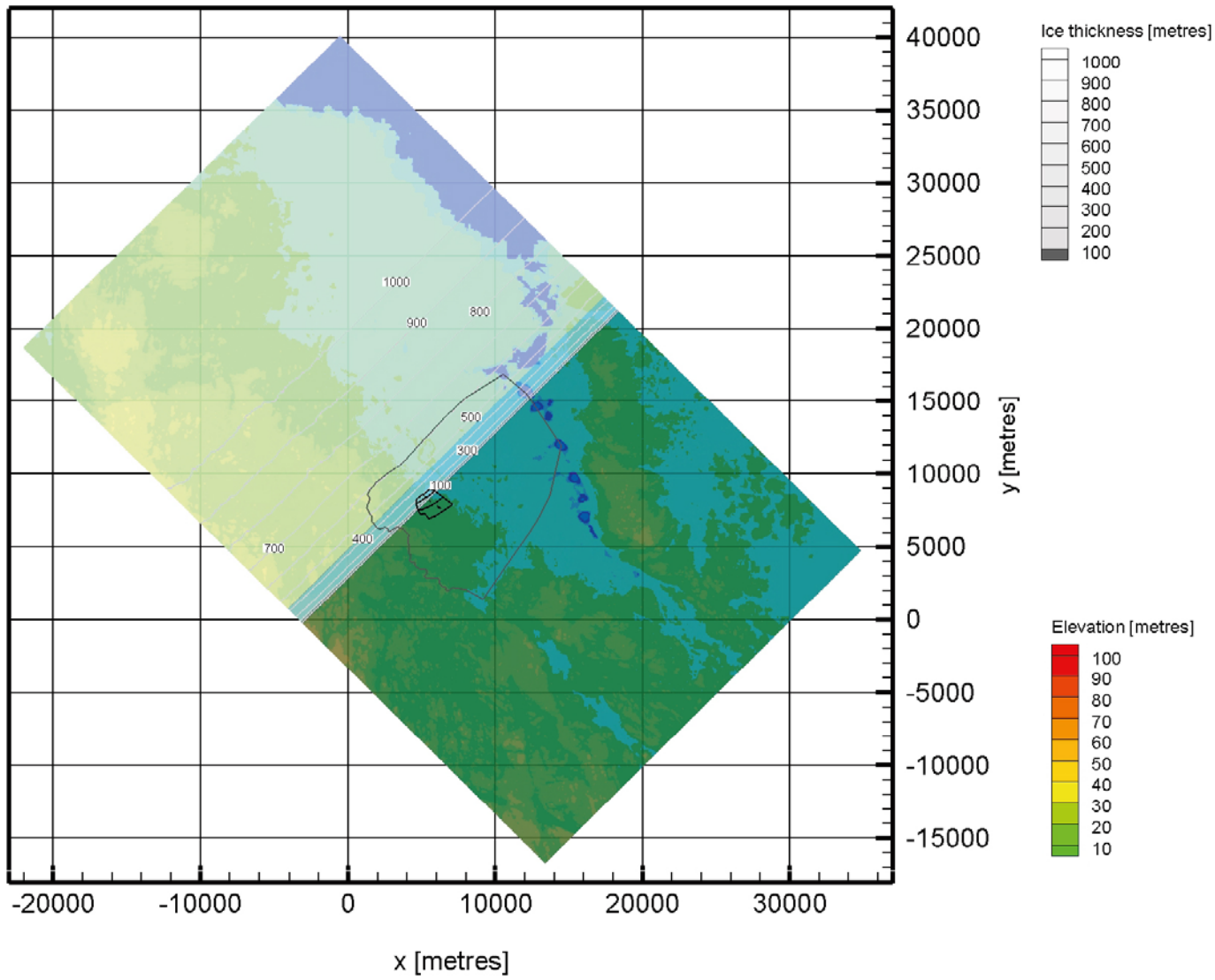

Figure G-1. *Visualisation of the ice thickness when the ice sheet margin in case (d) is at IFL II. Ice-free elevations above –28 m are subjected to permafrost and are shown in dull green (> 0 m) or dull turquoise (0 to –28 m). Ice-free elevations below –28 m are shown in blue. When the ice sheet margin is at IFL II there are few taliks in the periglacial area. The y-axis points towards north*

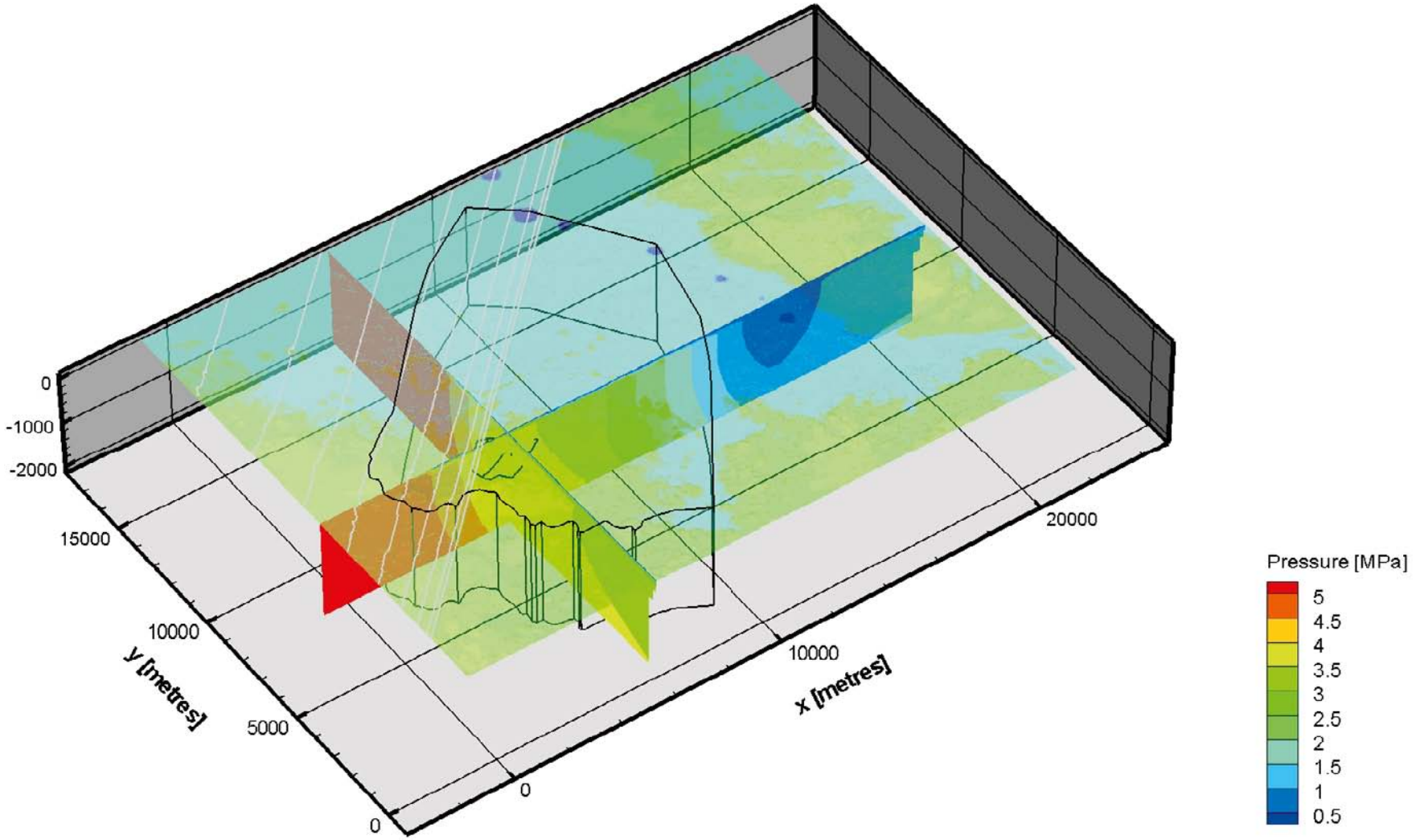

Figure G-2. *Visualisation of the residual pressure during glaciation when the ice sheet margin is at IFL II. The short black lines in the centre indicate the location of the repository. The y-axis points towards north.*

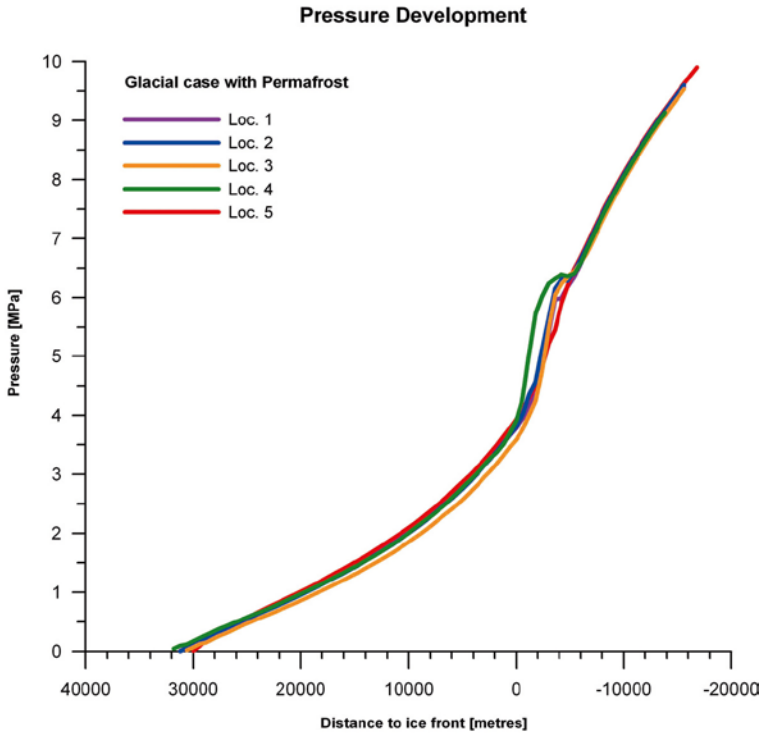

Figure G-3. *Pressure at ML 1–5 during glaciation. Positive distance values mean that the ice sheet margin has not yet arrived to the measurement locations.*

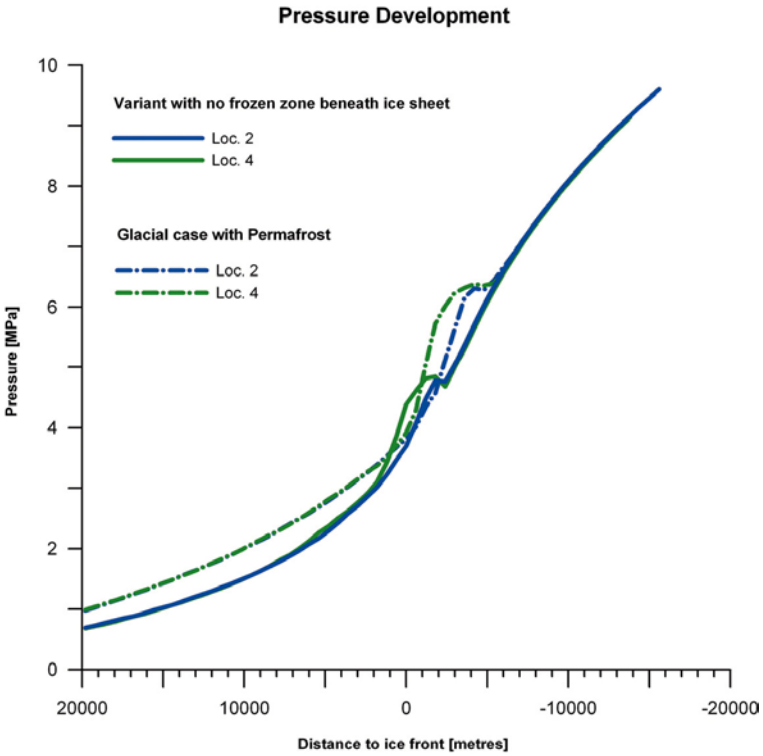

Figure G-4. *Comparison between the pressure at ML 2 and ML 4 during glaciation for the conditions considered in cases (d) and (e).*

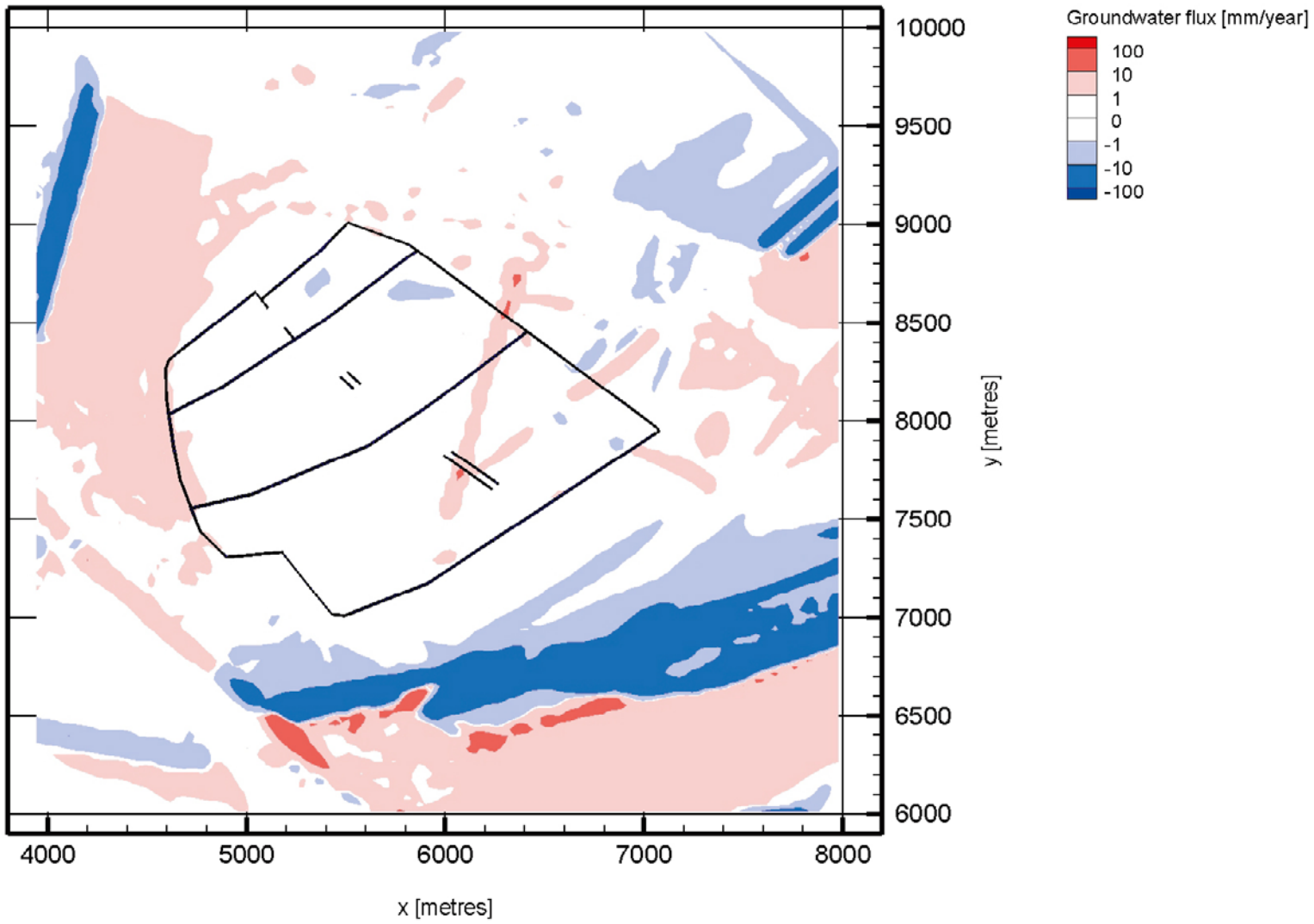

Figure G-5. *Horizontal view of the vertical Darcy flux in mm/y at –465 m elevation for the temperate case. Red colours show positive values (upward directed fluxes), whereas blue colours show negative values (downward directed fluxes). The short black lines indicate major tunnels. The y-axis points towards north.*

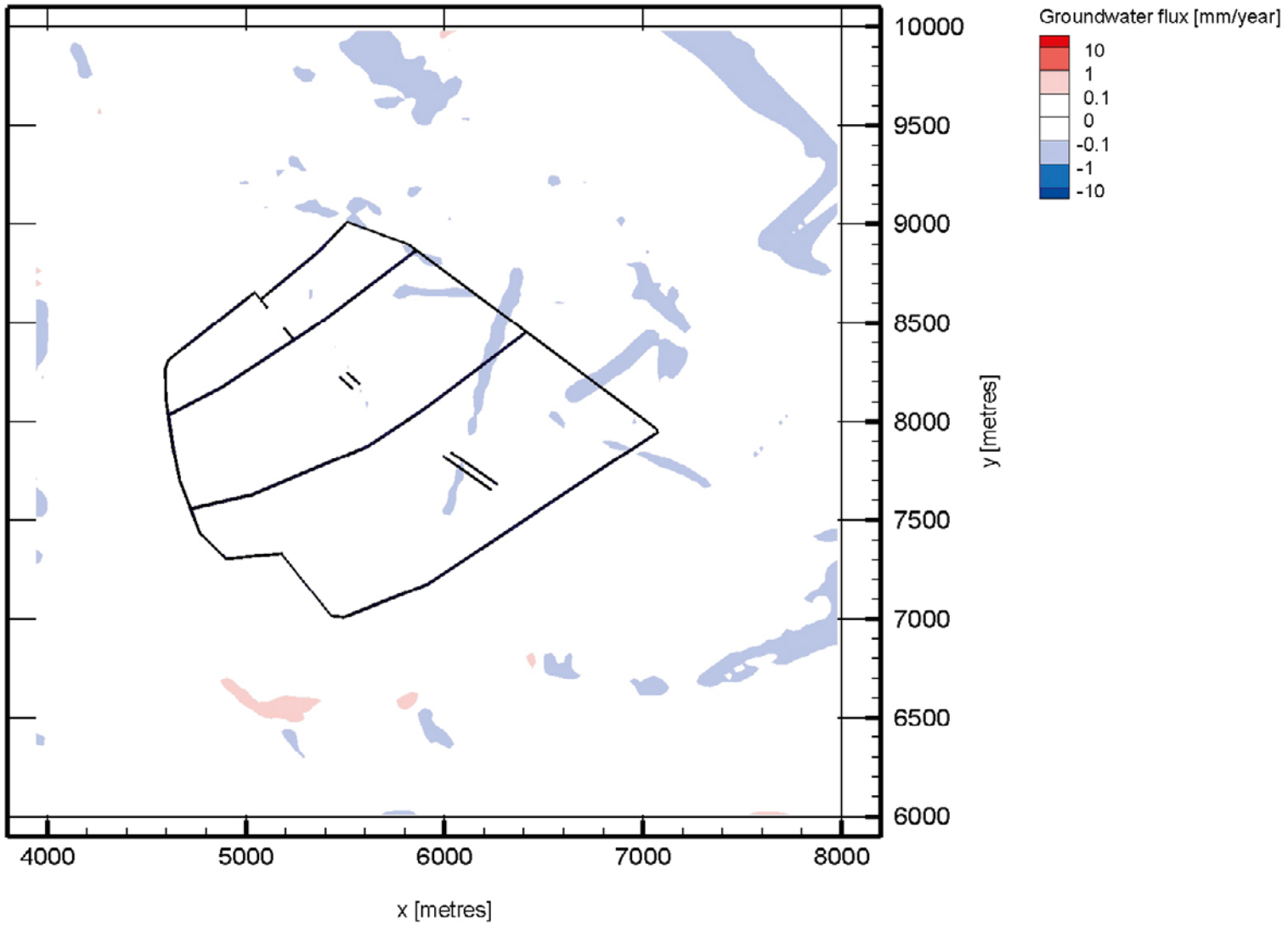

Figure G-6. *Horizontal view of the vertical Darcy flux in mm/y at –465 m elevation during glaciation before the ice sheet margin enters the model domain. Red colours show positive values (upward directed fluxes), whereas blue colours show negative values (downward directed fluxes). The short black lines indicate major tunnels. The y-axis points towards north.*

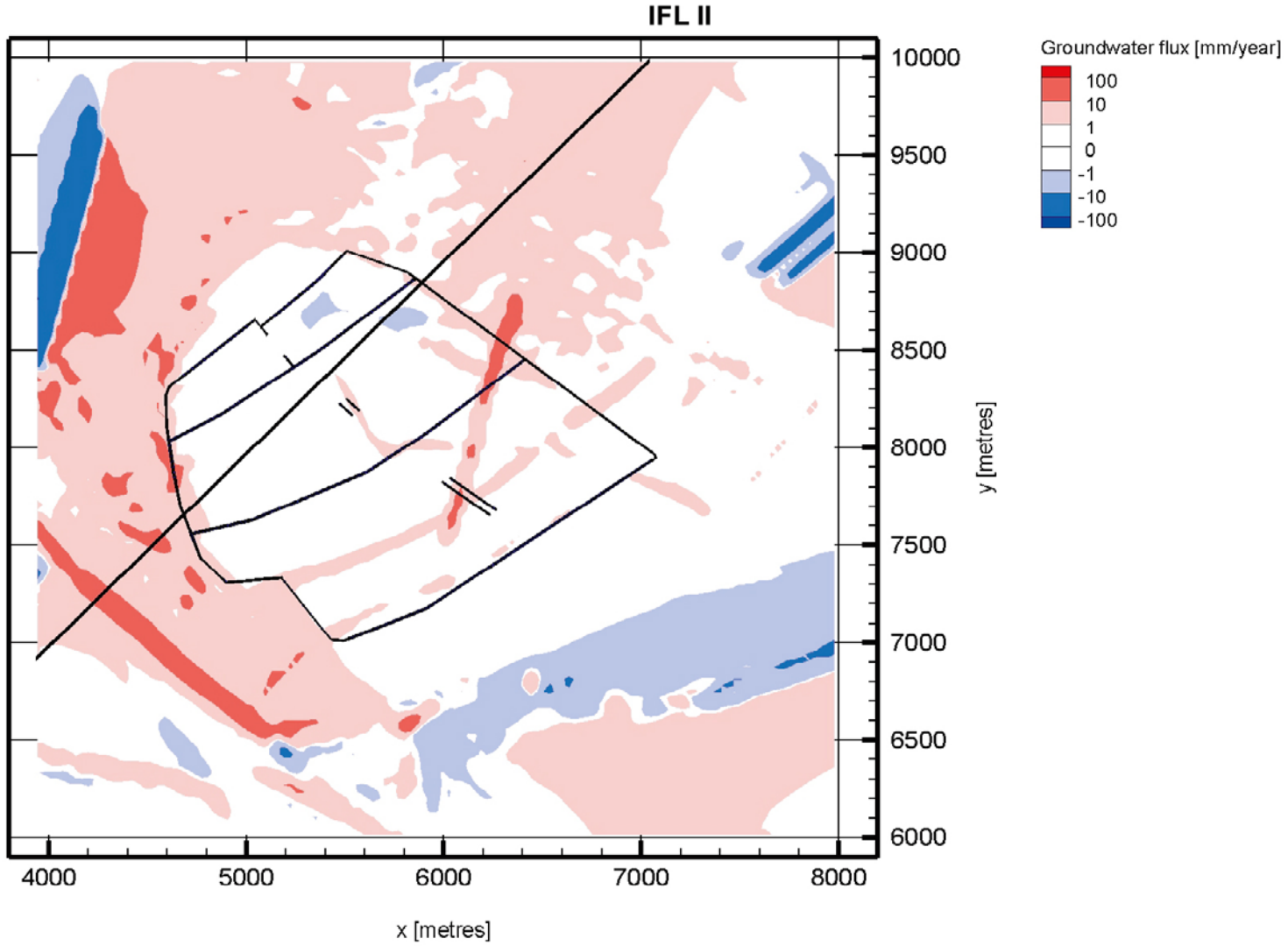

Figure G-7. *Horizontal view of the vertical Darcy flux in mm/y at –465 m elevation during glaciation when the ice sheet margin is at IFL II (black line). Red colours show positive values (upward directed fluxes), whereas blue colours show negative values (downward directed fluxes). The short black lines indicate major tunnels. The y-axis points towards north.*

Figure G-8 shows the vertical Darcy flux when the front of the advancing ice sheet margin addressed in case (d) is approximately at ice-front location III. Little effect of the ice sheet margin is observed due to the frozen ground "barrier" beneath.

Figure G-9 shows the vertical Darcy flux when the front of the advancing ice sheet margin addressed in case (d) is at ice-front location IV, i.e. when the entire repository area is covered by the advancing ice sheet margin. At this location the permafrost effect is gone and the case (d) is identical with case (c).

Figure G-10 shows the vertical Darcy flux mapped on a NW-SE cross-section parallel to the ice flow direction addressed in case (d). Observe the "transient" permeability field due to the frozen ground conditions.

Figure G-11 shows the Darcy flux at two measurement localities (ML 2,4) for cases (g)–(h) as a function of the distance to the ice sheet margin.

Figure G-12 shows the simulated changes in the Darcy flux, (q/q_{temp}), at the five measurement localities during an ice sheet cycle that simulates the ice sheet profile addressed in case (d). (After the passage of the ice front, the Darcy fluxes merge with that for case (c), which is copied into Figure G-12 from IFL IV and onward.) During the two ice front passages, the fluxes are up to 100 times greater than those prevailing during the temperate conditions. Between the two ice front passages, the model domain is completely covered by ice for a long period of time. At ML 2, ML 4 and ML 5, the simulated Darcy fluxes are c. 30% lower than the fluxes during the temperate conditions, whereas at ML 1 they are c. 30% higher. Thus, on the average, the Darcy simulated fluxes at repository depth at ML 1–5 are more or less the same when model domain is completely covered by ice for a long period of time.

G.5 Salinity

The occurrence of permafrost and a lowered sea level in themselves affect the salinity as seen in Figure G-15.

The interface between freshwater and saltwater is pushed downward and forward and some saltwater is flushed out in the periglacial region in front of the ice sheet margin along with the up-coning that occurs. That is, the salinity beneath an advancing, or retreating, ice sheet margin is altered by the recharge of fresh melt water, see Figure G-16 and Figure G-17, respectively.

Figure G-13 shows the salinity field in terms of two cross-sections when the advancing ice sheet margin is at ice-front location II. The shape of the up-coning in the target volume is influenced by the occurrence of transmissive and gently dipping deformation zones, see Figure G-14, but here is mainly influenced by the presence of frozen ground inhibiting discharge at the surface along the ice margin. The permafrost layer enhances the pushing forward of the saltwater that eventually discharges in taliks occurring along the eastern boundary of the domain.

Figure G-18 and Figure G-19 show the salinity at the five measurement localities (ML 1–5) for cases (g)–(h) as a function of the distance to the front of the ice sheet margin. Figure G-20 shows the simulated changes in the salinity at the five measurement locations during the advance of the ice sheet addressed in case (d).

Figure G-18 shows the simulated fracture water salinity development at the five measurement localities during the advance of the ice sheet addressed in case (d). All measurement localities experience an increase in salinity due to up-coning caused by the approaching ice sheet margin. The salinity peak values at repository depth approach 1.25% when the ice front is some 20 km away; these values are maintained until the ice sheet margin has passed over the measurement localities. The effects of the passage are more complex with salinity values both increasing and decreasing along with changes in pressure and flow path when the permeability field is changed by the melting of the permafrost.

Figure G-19 shows the simulated fracture water salinity development at two measurement localities (ML 2,4) during the advance of the ice sheets addressed in cases (g) and (h).

Figure G-20 shows the simulated changes in the fracture water salinity, (C/C_{temp}), at the five measurement localities during the advance of the ice sheet addressed in case (d).

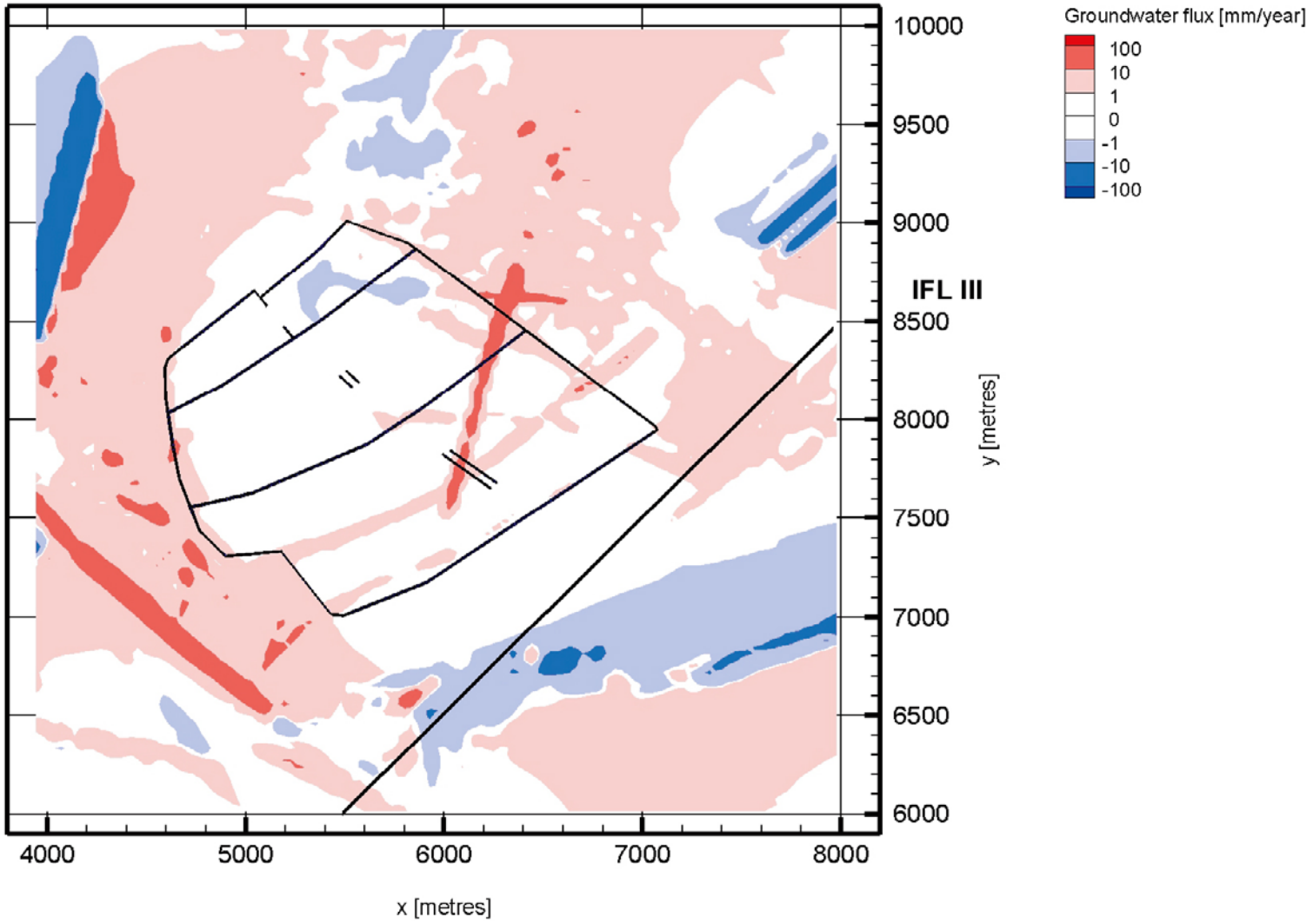

Figure G-8. *Horizontal view of the vertical Darcy flux in mm/y at –465 m elevation during glaciation when the ice sheet margin is at IFL III (black line). Red colours show positive values (upward directed fluxes), whereas blue colours show negative values (downward directed fluxes). The short black lines indicate major tunnels. The y-axis points towards north.*

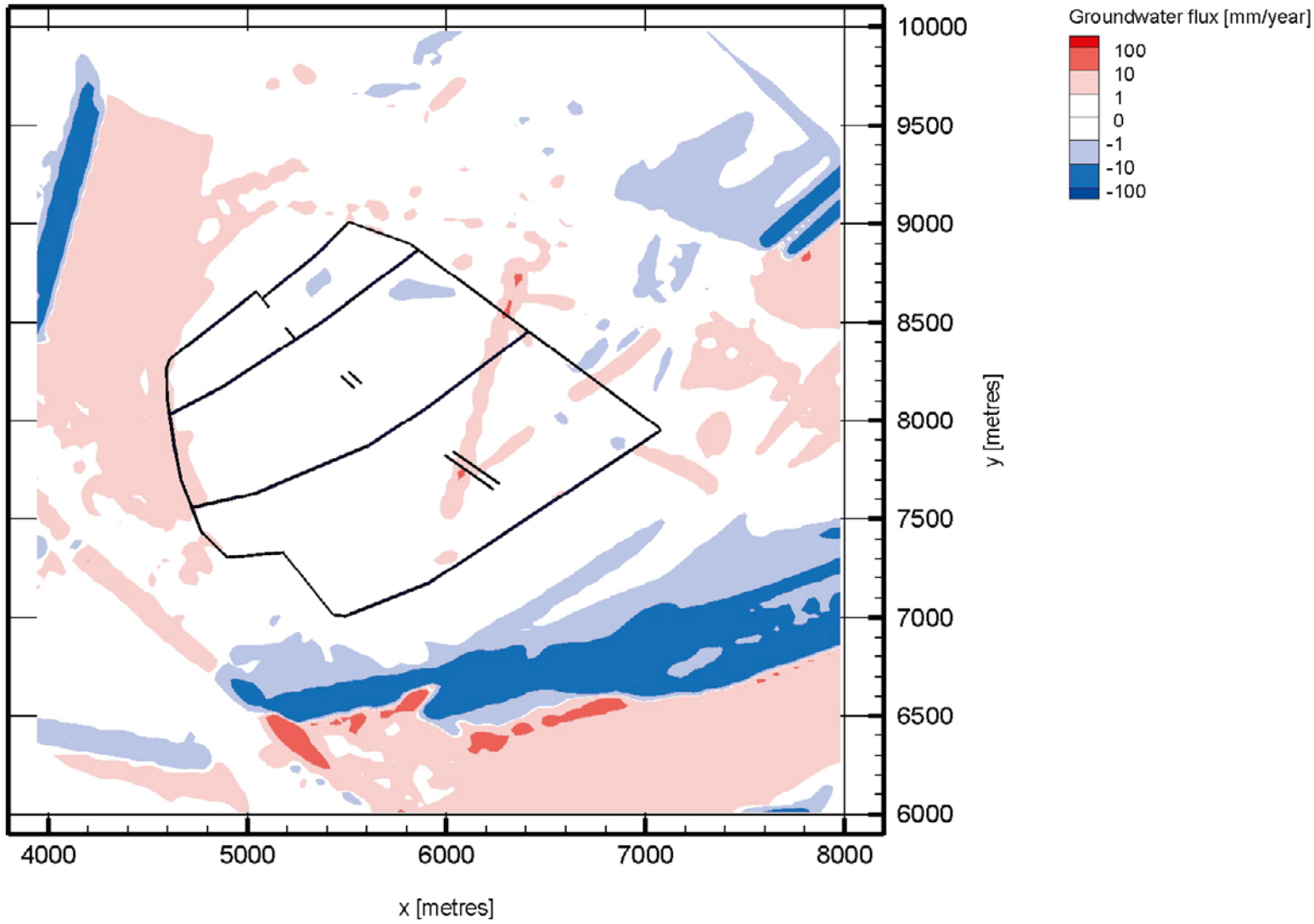

Figure G-9. *Horizontal view of the vertical Darcy flux in mm/y at –465 m elevation during glaciation when the ice sheet margin is at IFL IV (not visible in this image). Red colours show positive values (upward directed fluxes), whereas blue colours show negative values (downward directed fluxes). The short black lines indicate major tunnels. The y-axis points towards north.*

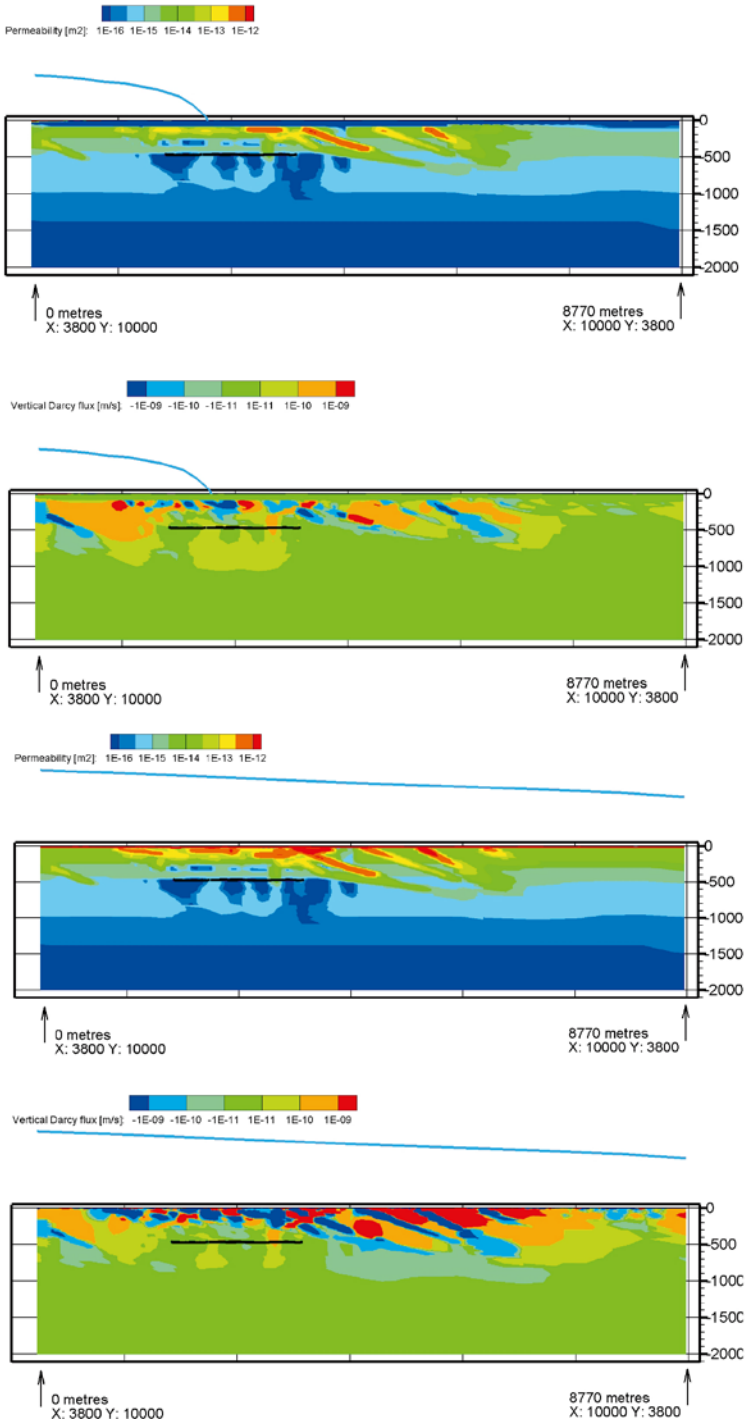

Figure G-10. *Top: Permeability field during glaciation mapped on a NW-SE cross-section parallel to the ice flow direction when the ice sheet margin is at IFL II. Upper Middle: Vertical Darcy flux when the ice sheet margin is at IFL II. Lower Middle: Permeability field during glaciation mapped on a NW-SE cross-section parallel to the ice flow direction when the ice sheet margin is at IFL IV. Bottom: Vertical Darcy flux when the ice sheet margin is at IFL IV. The ice sheet thickness is illustrated with a blue curve. The black line at –465 m elevation shows the location of the repository.*

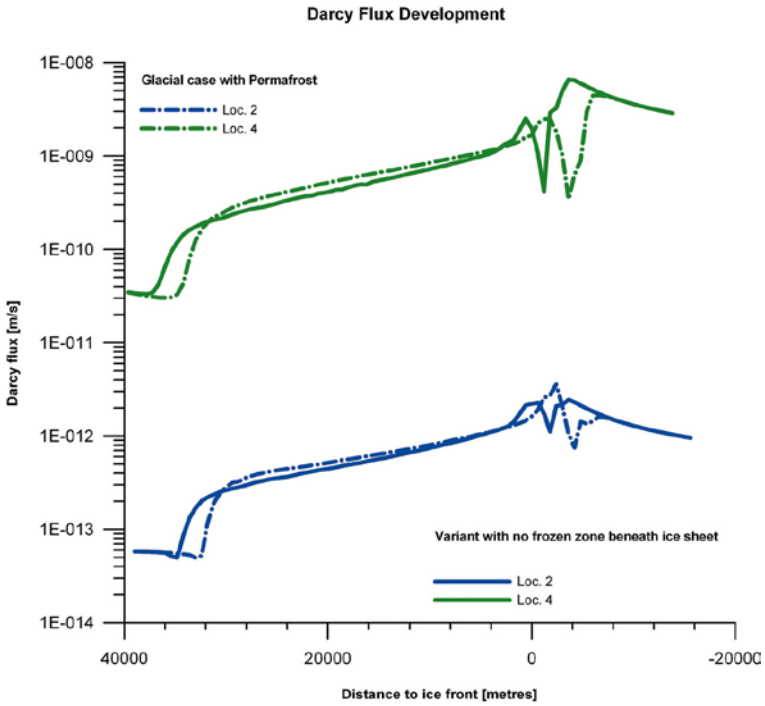

Figure G-11. *Comparison between the Darcy flux at ML 2 and ML 4 during glaciation for the conditions considered in cases (d) and (e). Positive distance values mean that the ice sheet margin has not yet arrived to the measurement locations.*

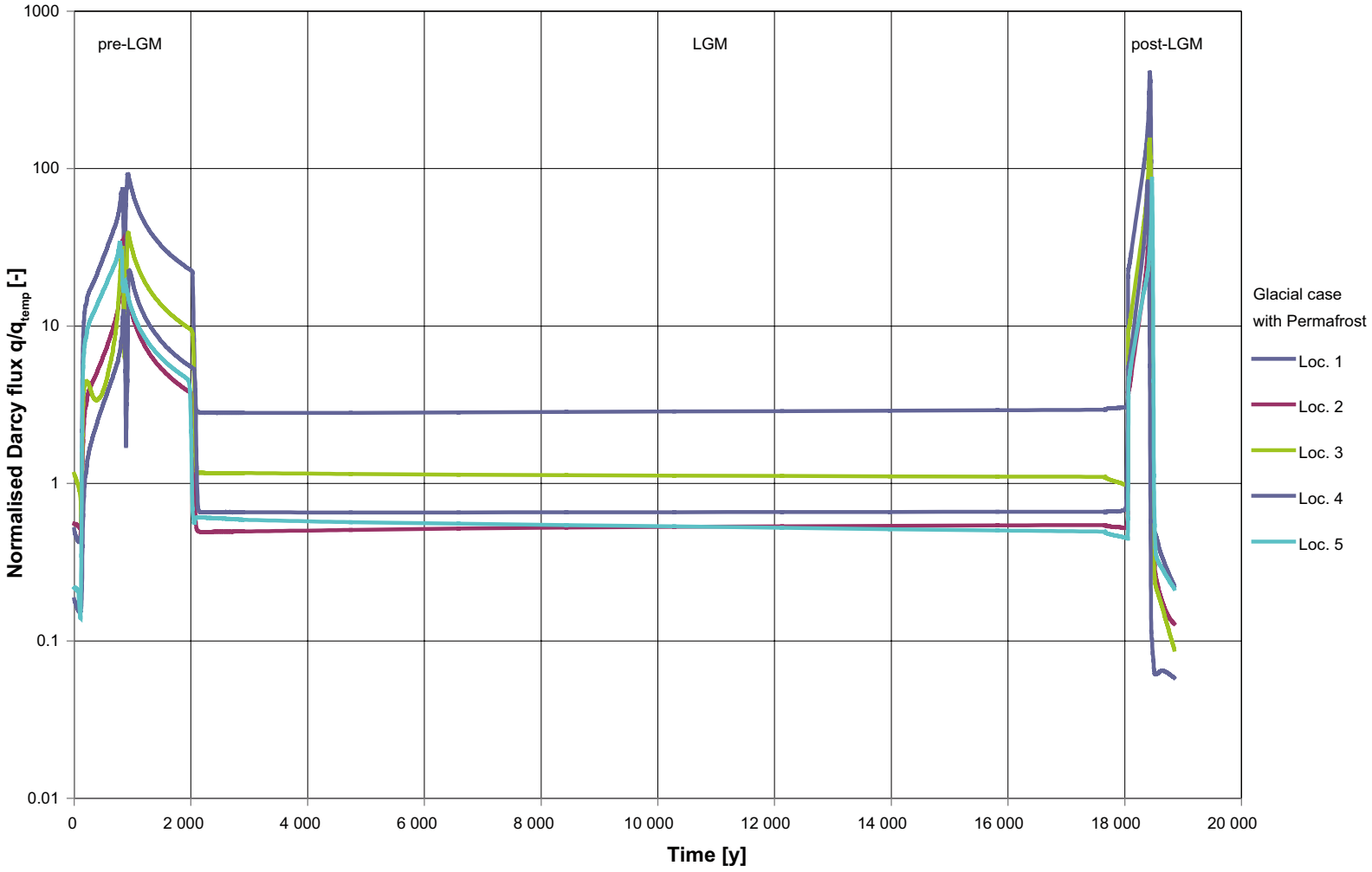

Figure G-12. *Normalised Darcy flux, q/q_{temp}, at ML 1–5 during glaciation (pre-LGM), complete ice coverage (LGM) and deglaciation (post-LGM).*

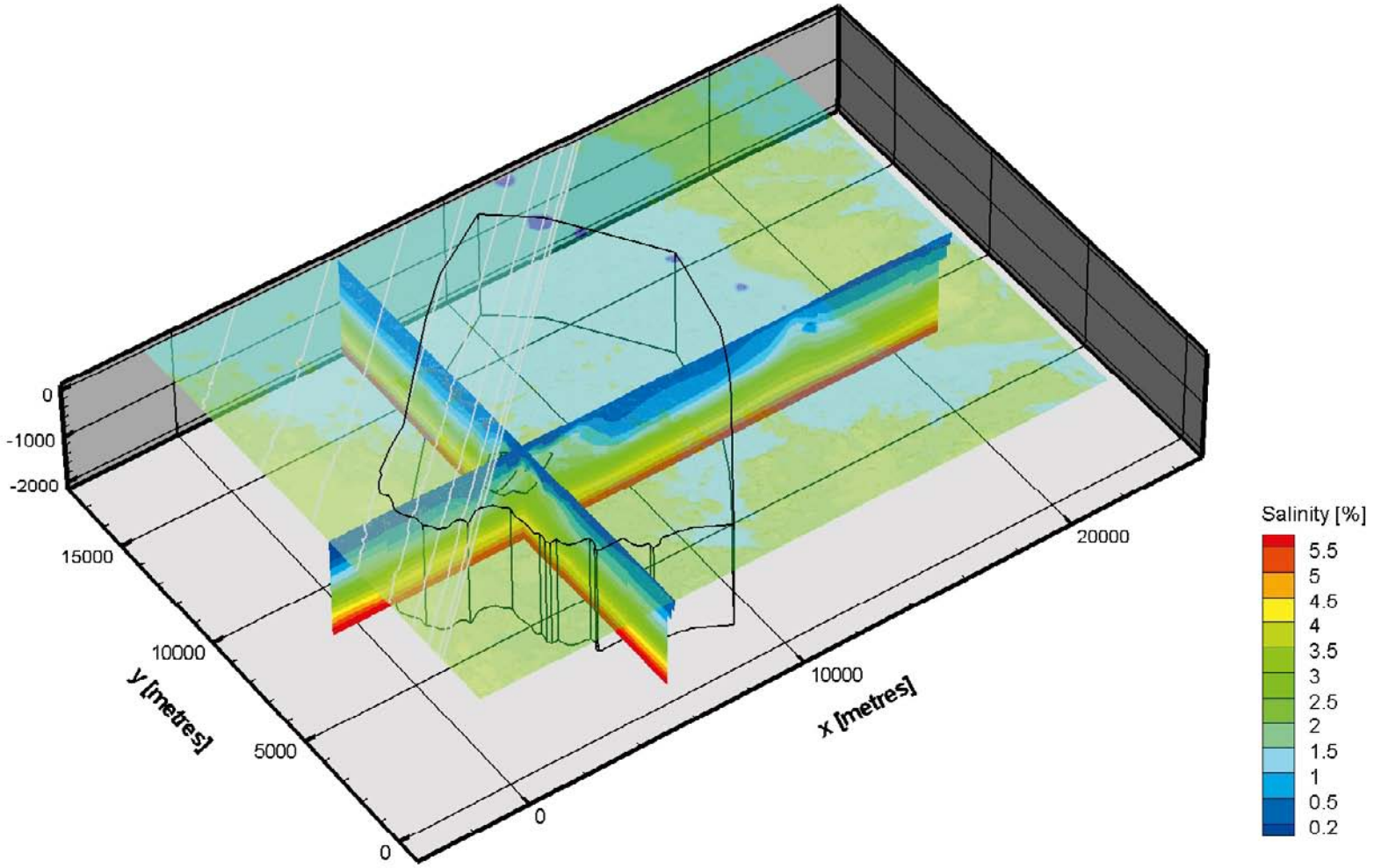

Figure G-13. *Visualisation of the salinity during glaciation when the ice sheet margin is at IFL II. The short black lines in the centre indicate the location of the repository. The y-axis points towards north.*

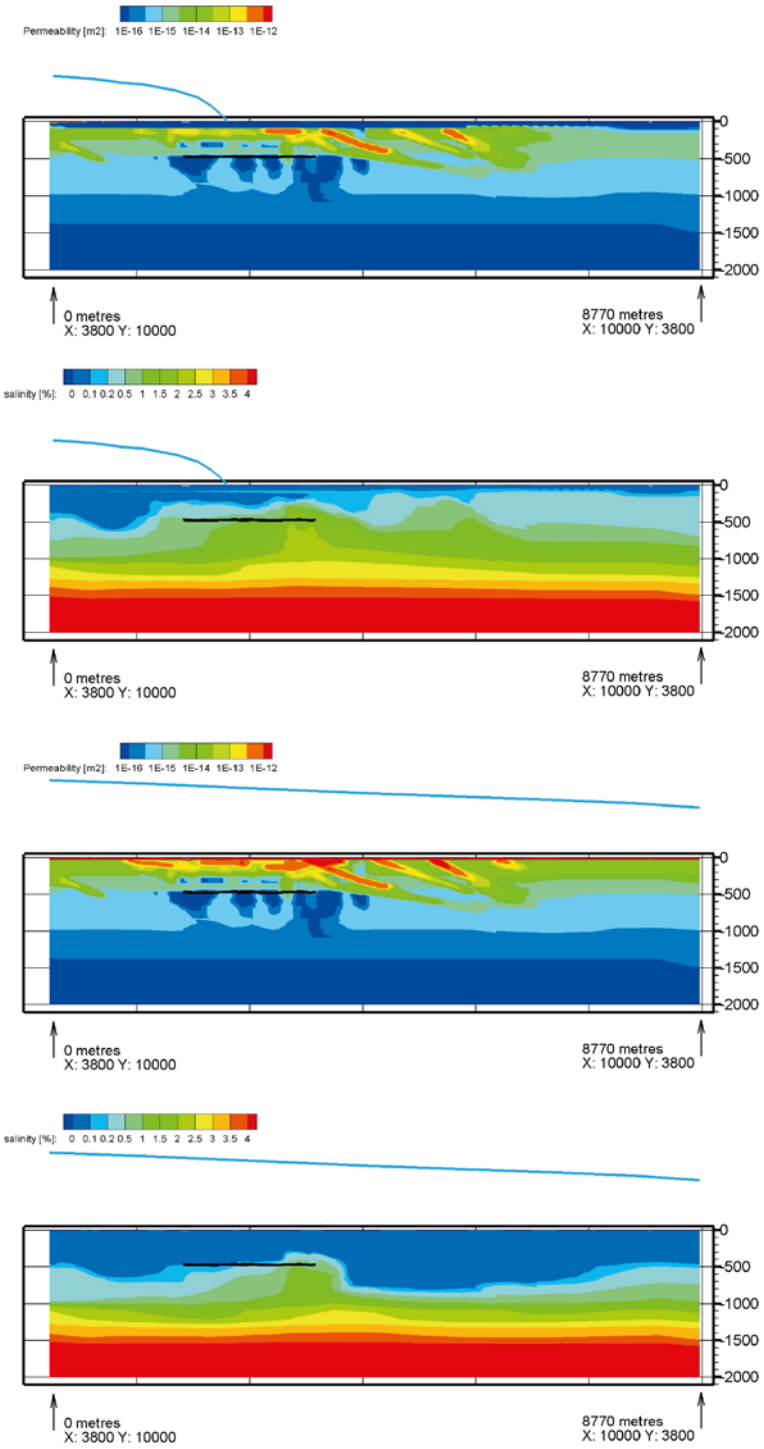

Figure G-14. *Top: Permeability field during glaciation mapped on a NW-SE cross-section parallel to the ice flow direction when the ice sheet margin is at IFL II. Upper Middle: Salinity when the ice sheet margin is at IFL II. Lower Middle: Permeability field during glaciation mapped on a NW-SE cross-section parallel to the ice flow direction when the ice sheet margin is at IFL IV. Bottom: Salinity when the ice sheet margin is at IFL IV. The ice sheet thickness is illustrated with a blue curve. The black line at –465 m elevation shows the location of the repository.*

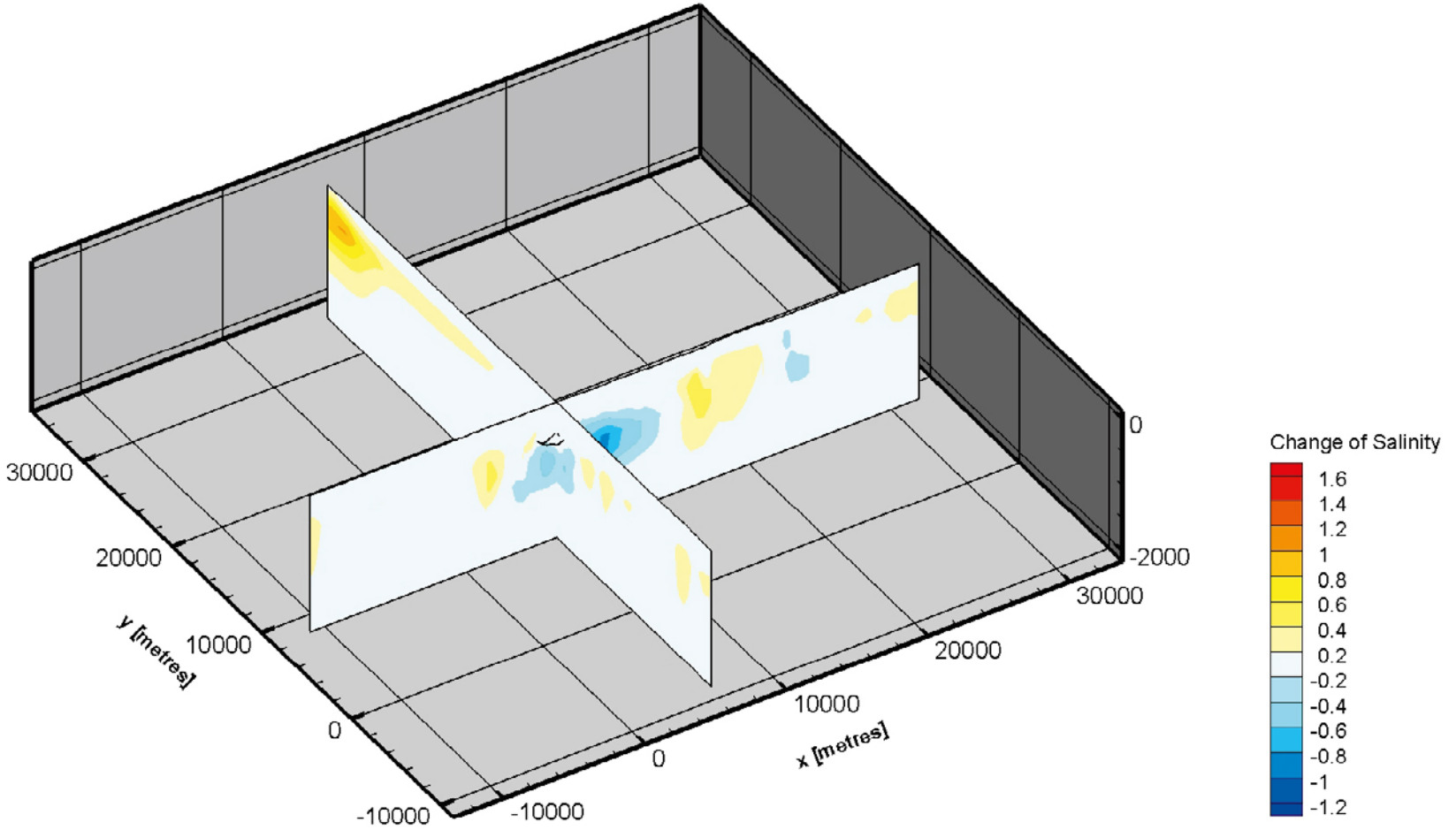

Figure G-15. *Change in the salinity field due to shoreline displacement and permafrost, $C_{glac,IFL0} - C_{temp}$, before the front of the ice sheet margin enters the model domain. The short black lines in the centre indicate the location of the repository. The y-axis points towards north.*

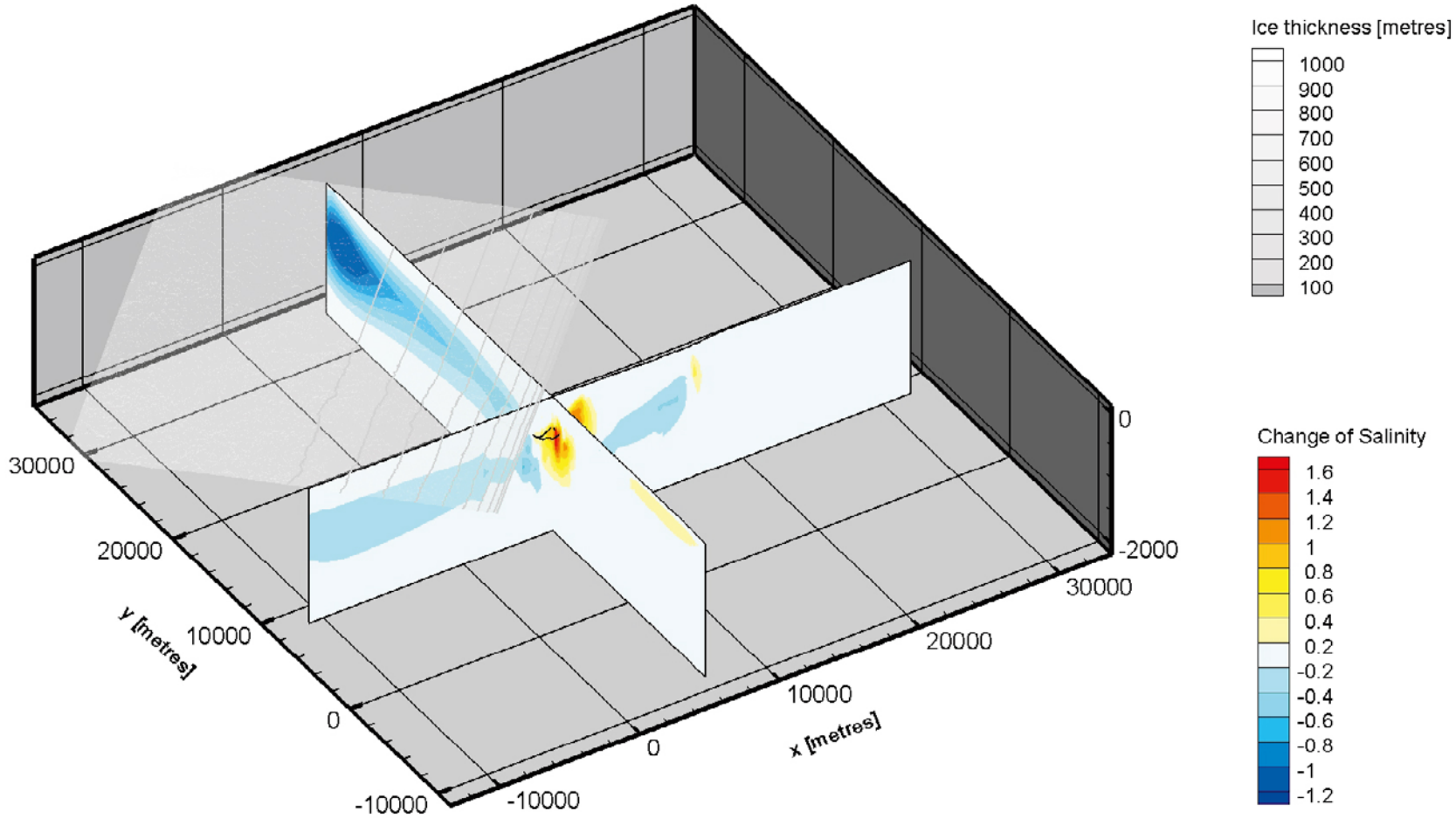

Figure G-16. *Change in the salinity field, $C_{glac,IFL\ II} - C_{glac,IFL\ 0}$, during glaciation when the ice sheet margin is at IFL II. The short black lines in the centre indicate the location of the repository. The y-axis points towards north.*

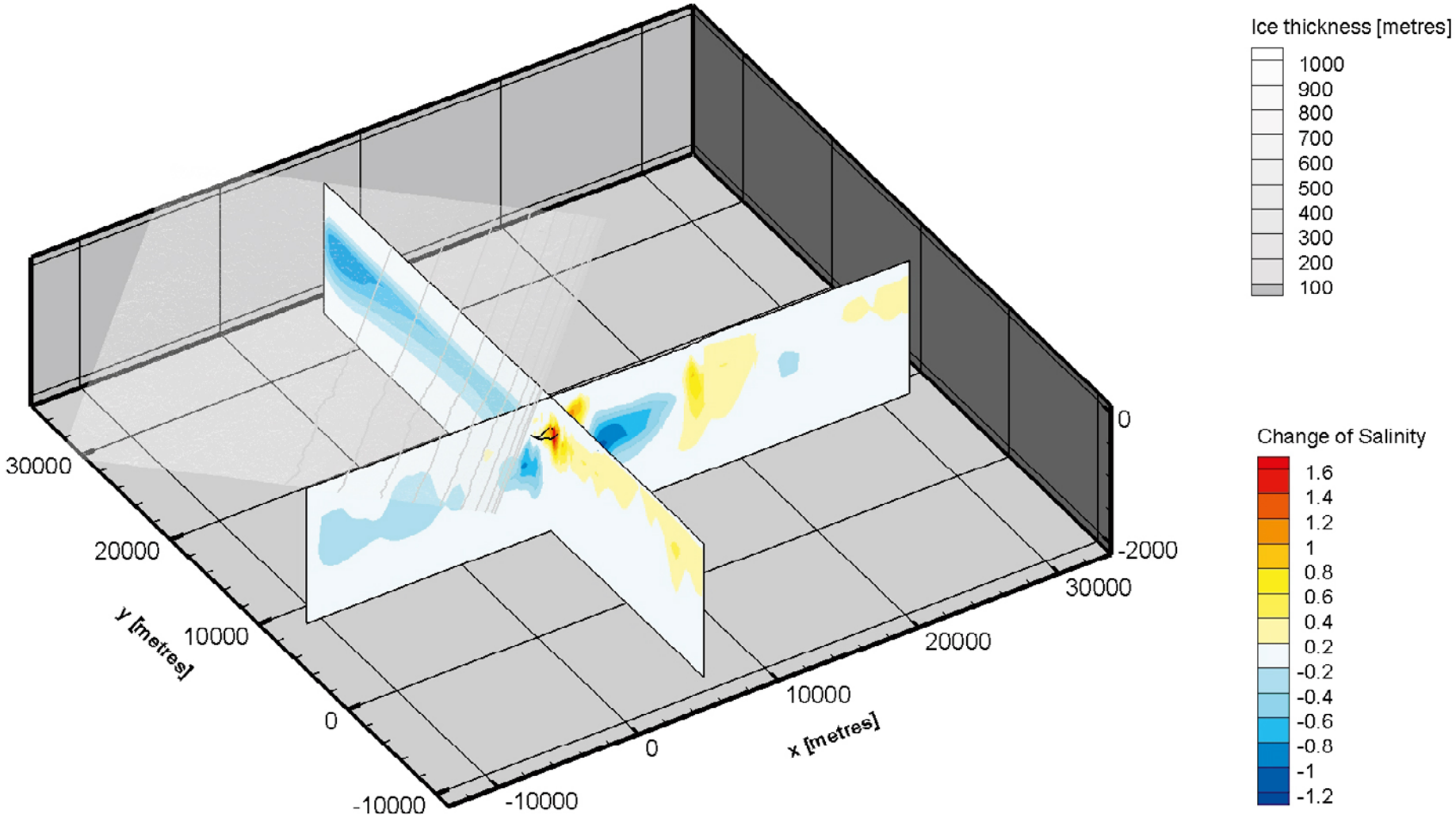

Figure G-17. *Change in the salinity field, $C_{glac,IFL\ II} - C_{glac,IFL\ 0}$, during deglaciation when the ice sheet margin is at IFL II. The short black lines in the centre indicate the location of the repository. The y-axis points towards north.*

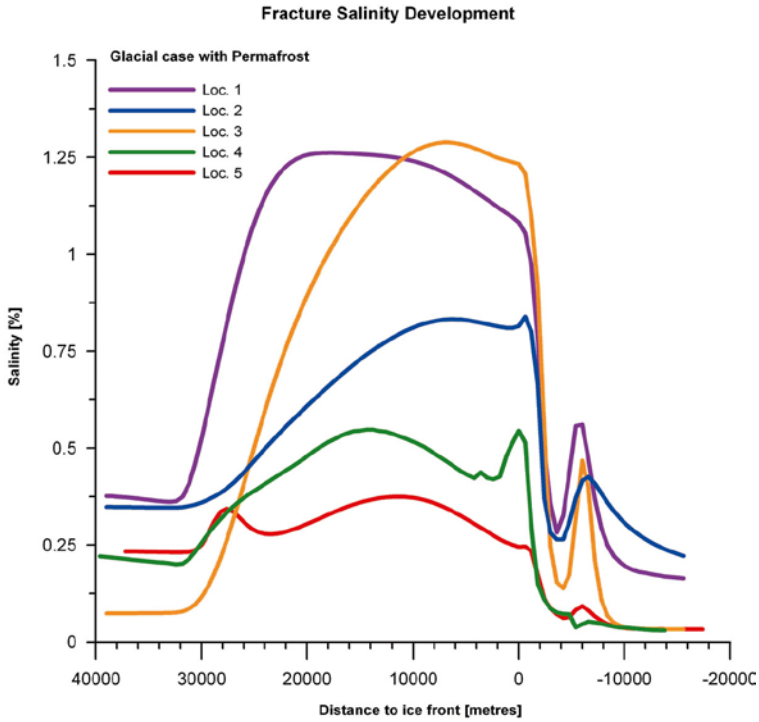

Figure G-18. *Fracture water salinity at measurement localities ML 1–5 during glacial conditions. Positive distance values mean that the ice sheet margin has not yet arrived to the measurement locations.*

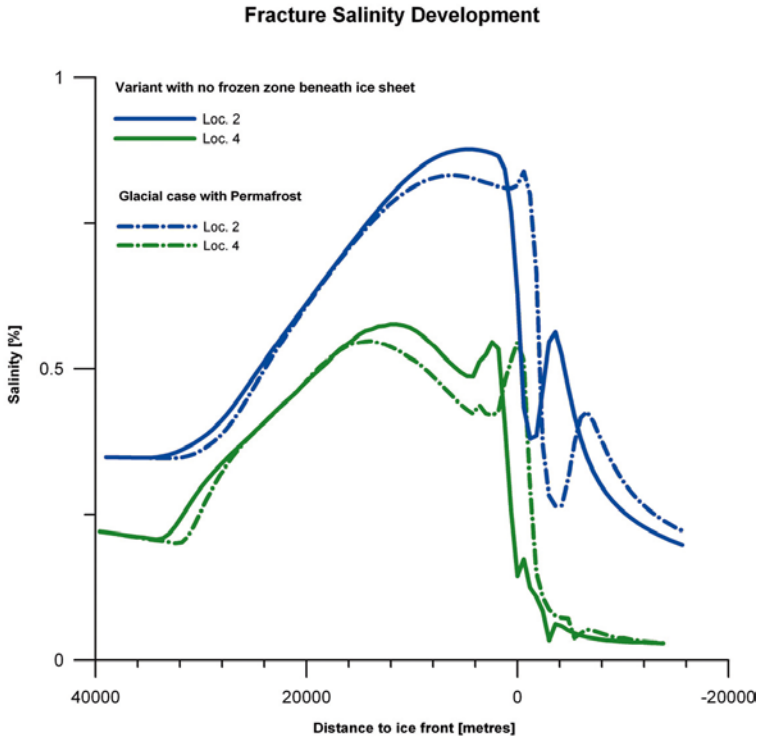

Figure G-19. *Comparison between the fracture water salinity at ML 2 and ML 4 during glaciation for the conditions considered in cases (d) and (e). Positive distance values mean that the ice sheet margin has not yet arrived to the measurement locations.*

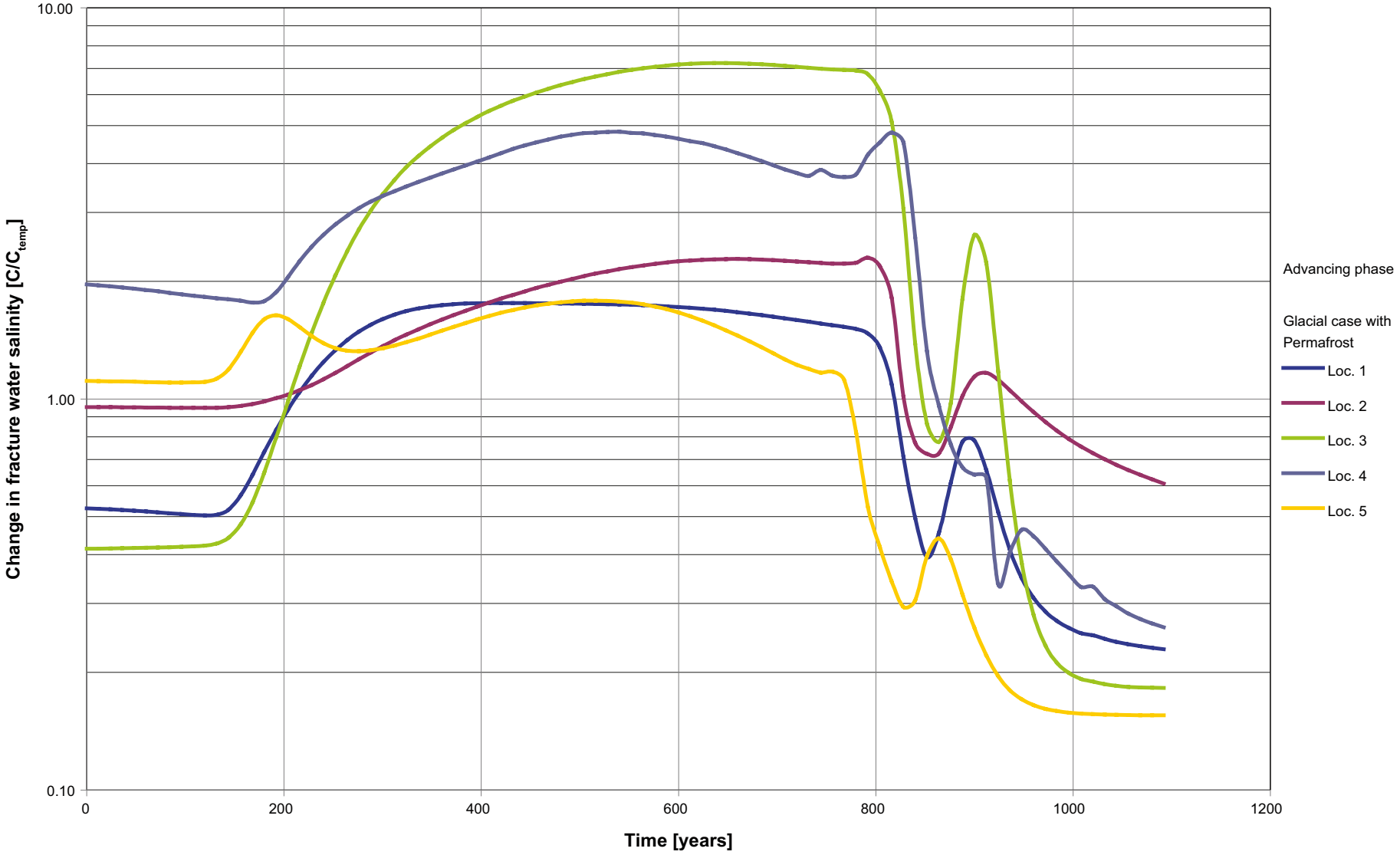

Figure G-20. *Normalised fracture water salinity, C/C_{temp}, at ML 1–5 during a period of approximately 1,000 years of glaciation.*

G.6 Recharge and discharge locations

The repository considered for modelling contains 6,916 deposition hole positions. One particle is released at each deposition hole position and all particles are tracked backwards and forwards as a means of identifying their recharge and discharge locations, respectively. It is noted that the Darcy fluxes are fixed in space and time during the particle tracking, which is a simplification since the boundary conditions at ground surface change with the positions of the advancing ice sheet margin. Figure G-21 shows the results from the particle tracking when the ice sheet profile addressed in case (d) reached ice-front location II. Figure G-21 reveals that all particles recharge at the upstream boundary of the model domain, which strongly indicates that the model domain is too short to give a undisturbed view of the recharge locations for a fixed Darcy flux field. Nevertheless, it may be concluded that the present-day topographic water divides, which play an important role in recharge and discharge during temperate conditions, are significantly diminished in importance during glacial conditions and especially during glacial conditions together with extensive permafrost development.

In contrast, the discharge locations are predominantly found well within the physical boundaries of the model domain and, as a matter of fact, mostly within some of the taliks in the domain. At ice-front location II (Figure G-21), the discharge pattern is strongly affected by the deformation zone model that exists within the regional model domain treated in SDM-Site. In Figure G-21, 6,355 particles discharge in the taliks, whereas the 147 particles discharge through the permafrost layer. That is, the permafrost has a low permeability (less than $1 \cdot 10^{-22}$ m^2), but it is not impervious with regard to the strong hydraulic gradient close to the ice sheet margin.

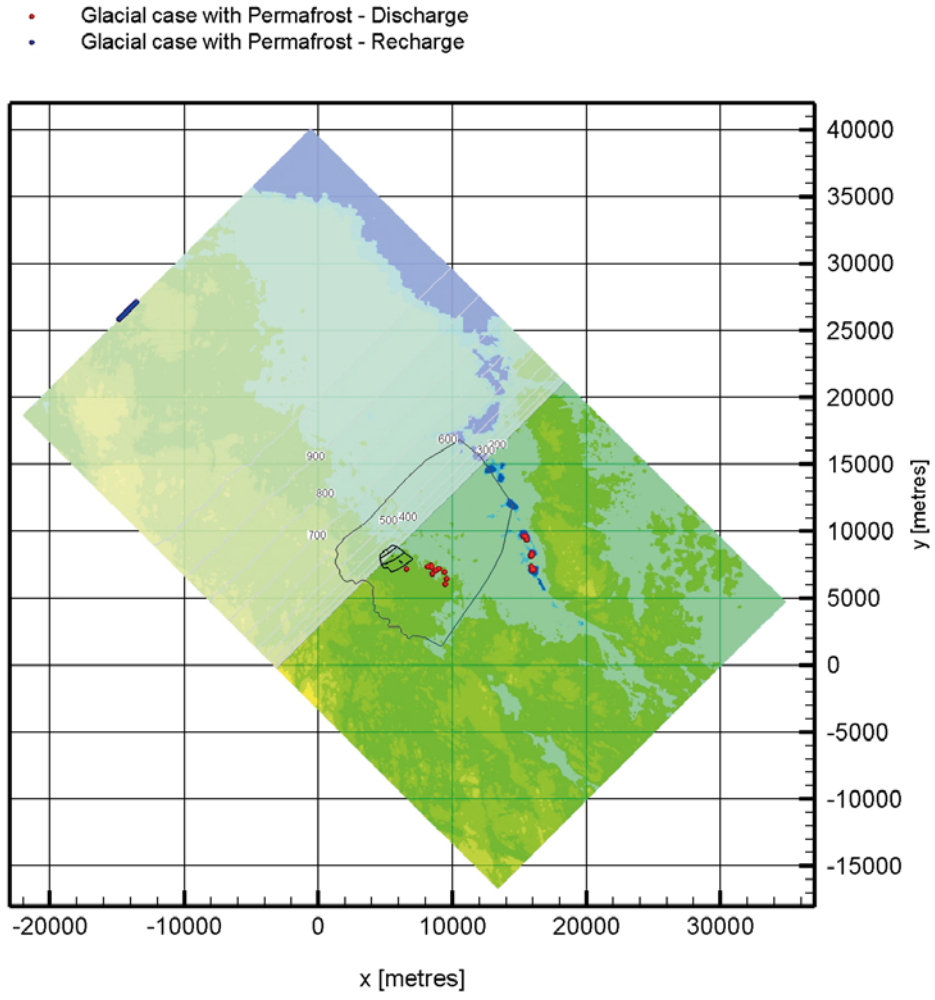

Figure G-21. *Recharge (blue) and discharge (red) locations during glaciation for 6,916 particles released at repository depth when the ice sheet margin is at IFL II. The short black lines in the centre of each image indicate the location of major tunnels. The y-axis points towards north.*

G.7 Recharge performance measures

The results from the backward particle tracking are shown in Figure G-22 to Figure G-24. It is noted that careful consideration needs to be given as to whether any quantitative conclusions can be drawn in the SR-Site project based on this information as the recharge locations are all on the model boundary. However, the information provided here can be used for qualitative conclusions.

Particles are released at the 6,916 deposition hole positions and at the five measurement localities, ML 1–5, and tracked for 100 years. Not all of the released particles reach the ground surface within this period of time. Figure G-22, Figure G-23 and Figure G-24 show the cumulative distribution (probability) plots of the recharge flow path lengths, travel times, and flow-related transport resistances for the particles released at the 6,916 deposition hole positions when the ice sheet profile addressed in case (d) is at ice-front location II. The corresponding cumulative distributions of these performance measures for the temperate situation addressed in case (a) are also shown in these figures as well as the data for ML 1–5 when the ice sheet profile addressed in case (d) is at ice-front location II.

Figure G-22 shows cumulative distribution plots of the recharge flow path lengths (L_R). Typically the influence of an ice sheet with permafrost give greater flow path lengths. All measurement localities as well as deposition hole positions recharge at the upstream model boundary. Thus the assessed model domain is too small to capture the complete recharge behavior.

Figure G-23 shows cumulative distribution plots of the recharge travel times ($t_{w,R}$). The influence of an ice sheet slows up the fastest particles by a factor 10. However, in general the increase in recharge travel time is about a factor 2. The results for the measurement localities are scattered around there-sults for the tracked deposition hole positions. It is worth noting that during the tracked 100 y the ice sheet if allowed continued advance would have moved forward some 5 km and that the time needed for an ice sheet to move from ice-front location II to ice-front location IV is only about 200 years.

Figure G-24 shows cumulative distribution plots of the recharge flow-related transport resistances (F_R). The flow-related transport resistance is in general increased approximately by a factor 2 to 3. The results for the measurement localities are scattered around the results for the tracked deposition hole positions.

G.8 Discharge performance measures

Particles are released at the 6,916 deposition hole positions and at the five measurement localities, ML 1–5, and tracked for 100 years. Not all of the released particles reach the ground surface within this period of time. Figure G-25, Figure G-26 and Figure G-27 show the cumulative distribution (probability) plots of the discharge flow path lengths, travel times, and flow-related transport resistances for the particles released at the 6,916 deposition hole positions when the ice sheet profile addressed in case (d) is at ice-front location II. The corresponding cumulative distributions of these performance measures for the temperate situation addressed in case (a) are also shown in these figures as well as the data for ML 1–5 when the ice sheet profile addressed in case (d) is at ice-front location II.

Figure G-25 shows cumulative distribution plots of the discharge flow path lengths (L_D). A majority of the particles (98%) discharge in the taliks. A limited number of particles discharges through the less frozen deformation zones; these include the particle from ML 5 which is located upstream of the low-permeable bedrock volume given a detailed description in the model.

Figure G-26 shows cumulative distribution plots of the discharge travel times ($t_{w,D}$). The discharge travel times are significantly shorter in case (d) as compared with the temperate conditions, even though the particles have around 10 km longer flow path lengths. This, of course, is a result of the in general higher Darcy fluxes in case (d). The measurement localities give results within the expected range based on the deposition hole positions.

Figure G-27 shows cumulative distribution plots of the discharge flow-related transport resistances (F_D). The flow-related transport resistance is in general lowered by one order of magnitude for the 20% of particles that result in the earliest discharge. Thereafter the flow-related transport resistance of the remaining particles in case (d) is approximately constant at $5 \cdot 10^5$ y/m, whereas for the temperate situation the flow-related transport resistance continues to increase as more particles arrive at its discharge locations.

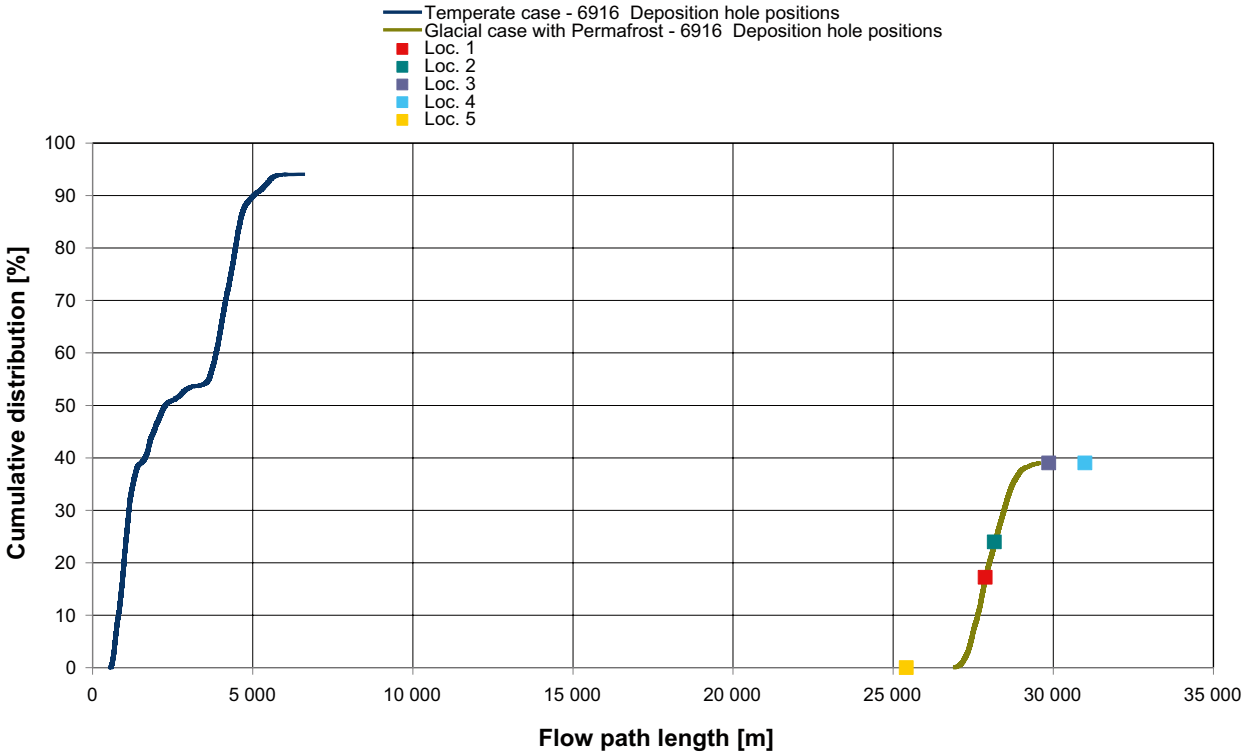

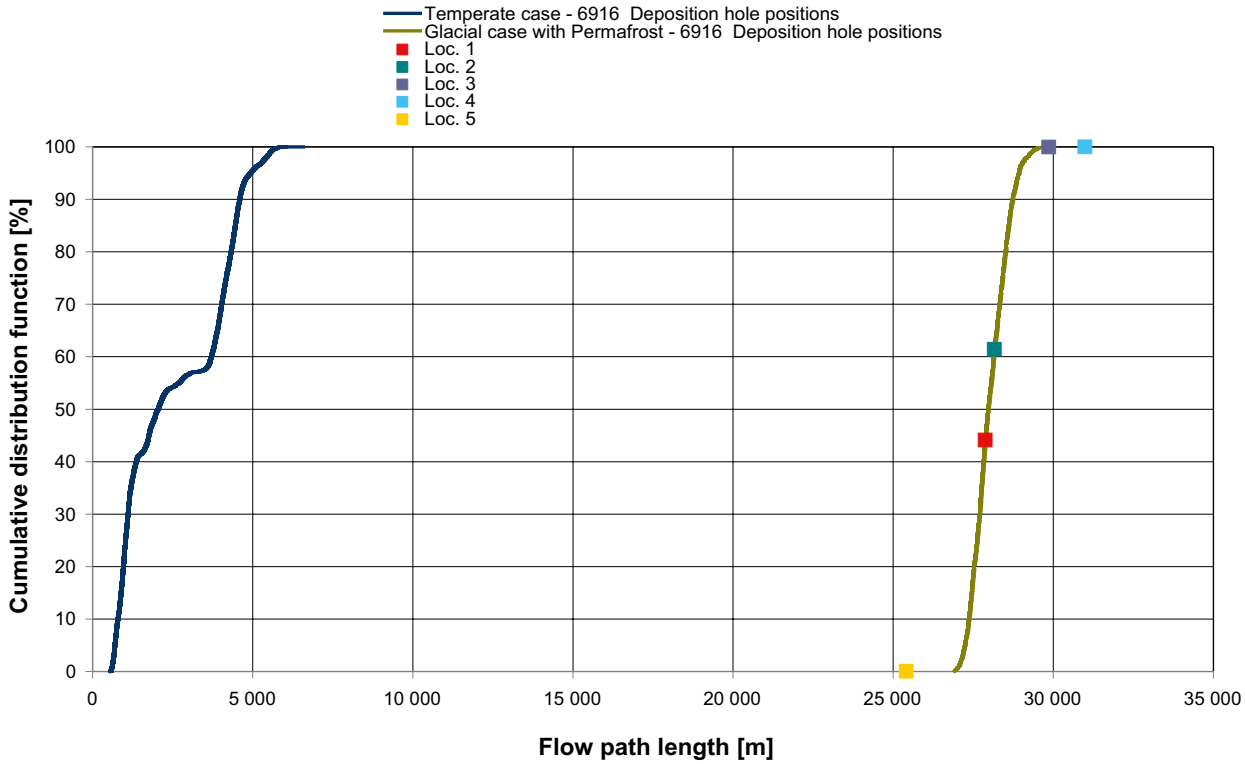

Figure G-22. *Cumulative distribution (probability) plots of the simulated recharge flow path lengths, L_R, when the ice sheet margin is at IFL II. The distribution for the temperate case is also shown as well as the data for ML 1–5 at IFL II. The maximum value in the upper plot is set to 100% in the lower plot.*

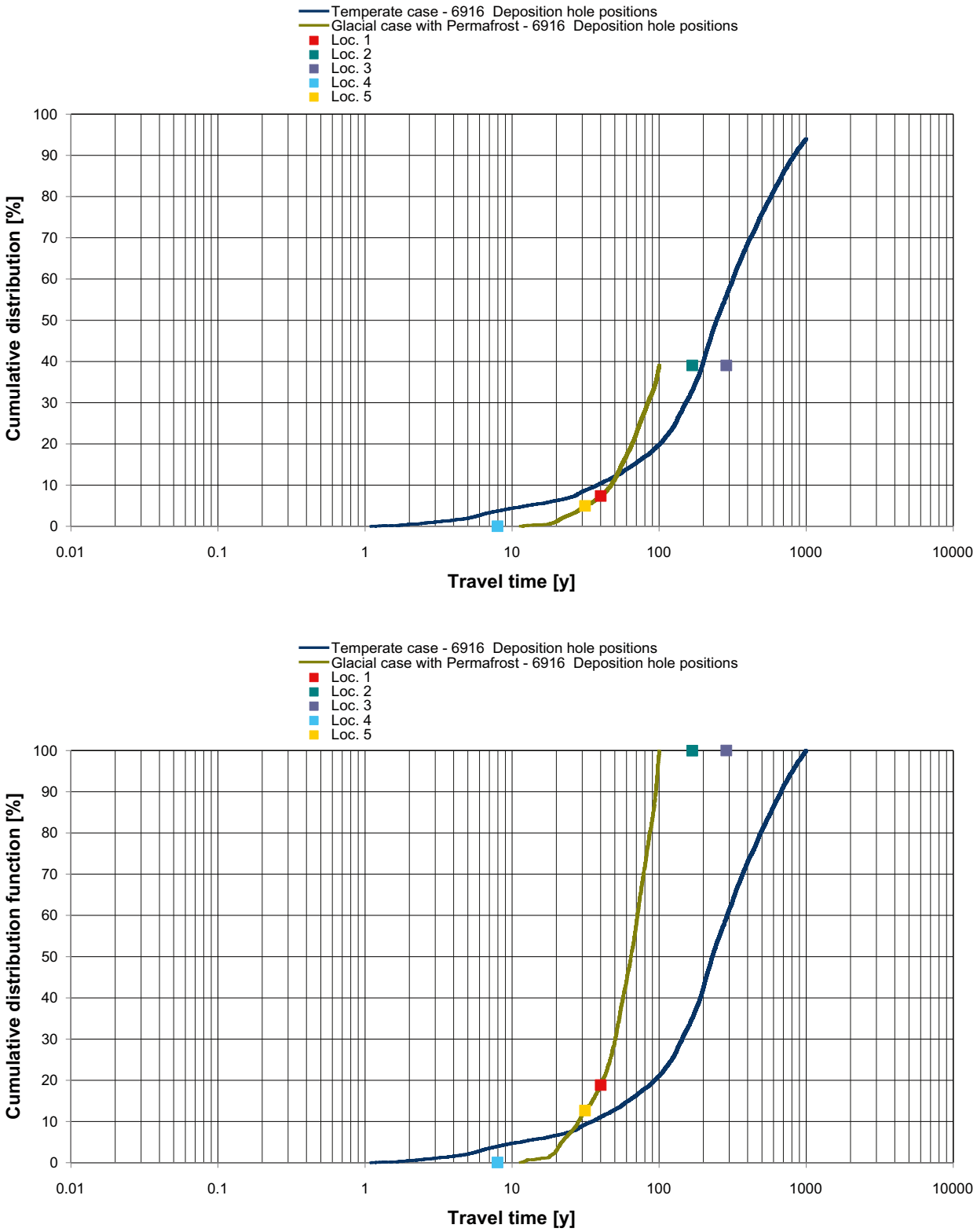

Figure G-23. *Cumulative distribution (probability) plots of the simulated recharge travel times, $t_{w,R}$, when the ice sheet margin is at IFL II. The distribution for the temperate case is also shown as well as the data for ML 1–5 at IFL II. The maximum value in the upper plot is set to 100% in the lower plot.*

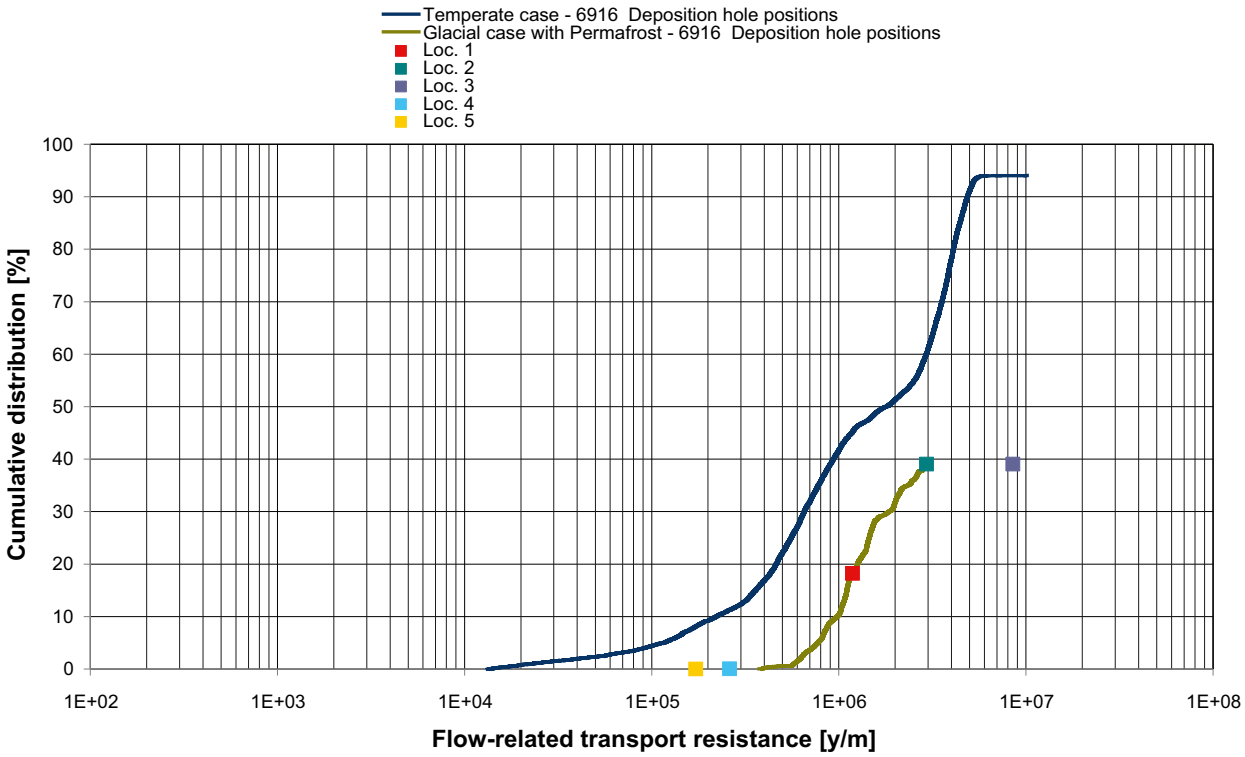

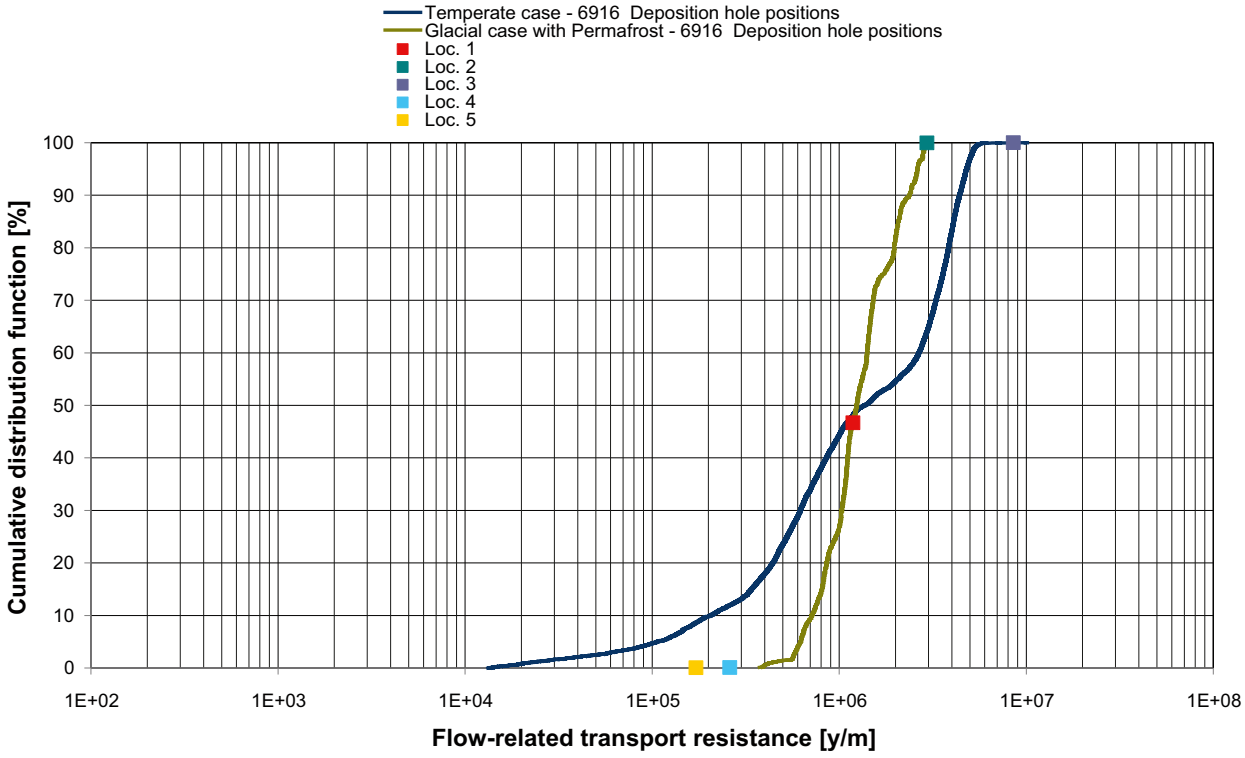

Figure G-24. *Cumulative distribution (probability) plots of the simulated recharge flow-related transport resistances, F_R, when the ice sheet margin is at IFL II. The distribution for the temperate case is also shown as well as the data for ML 1–5 at IFL II. The maximum value in the upper plot is set to 100% in the lower plot.*

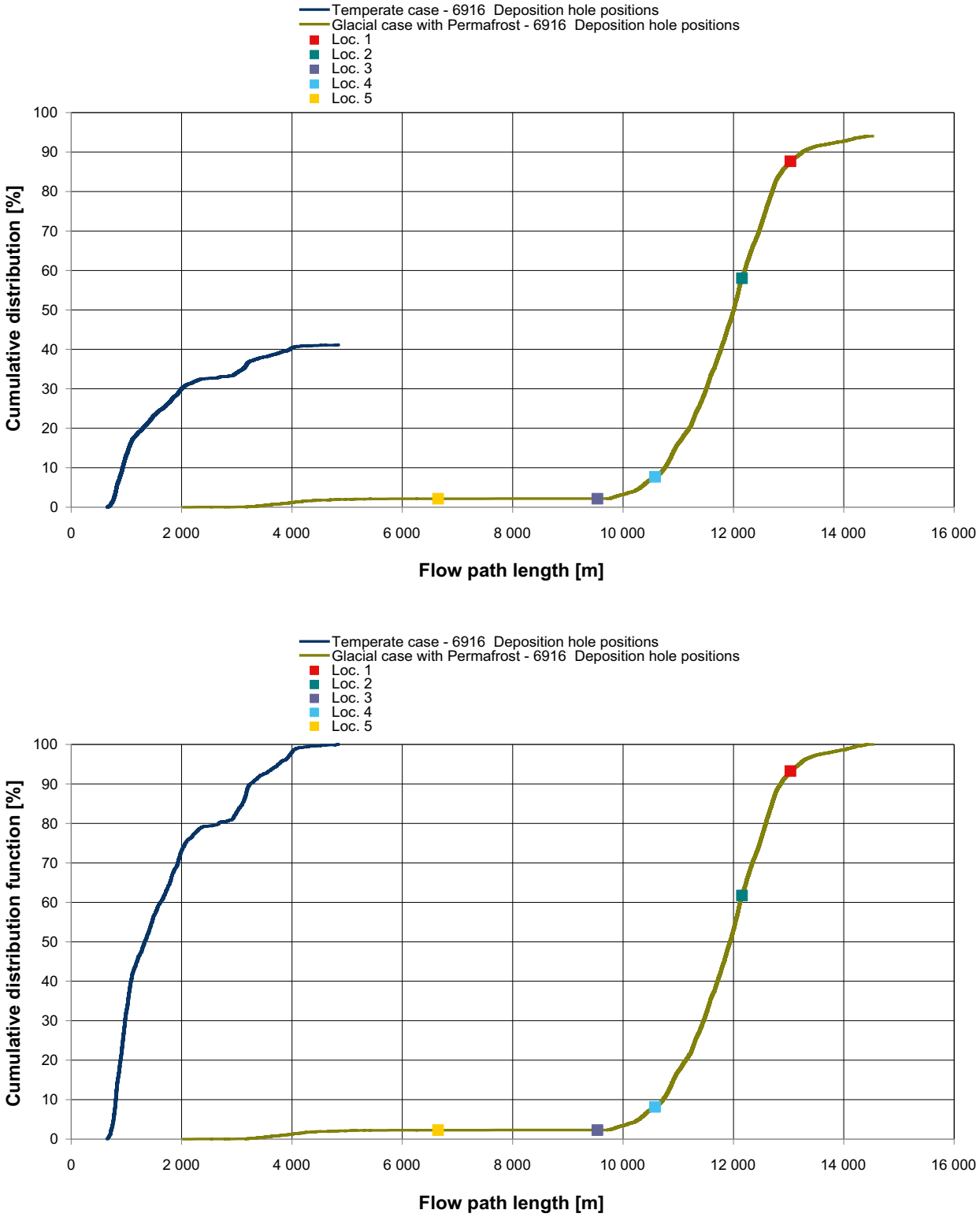

Figure G-25. *Cumulative distribution (probability) plots for the simulated discharge flow path lengths, L_D, when the ice sheet margin is at IFL II. The distribution for the temperate case is also shown as well as the data for ML 1–5 at IFL II. The maximum value in the upper plot is set to 100% in the lower plot.*

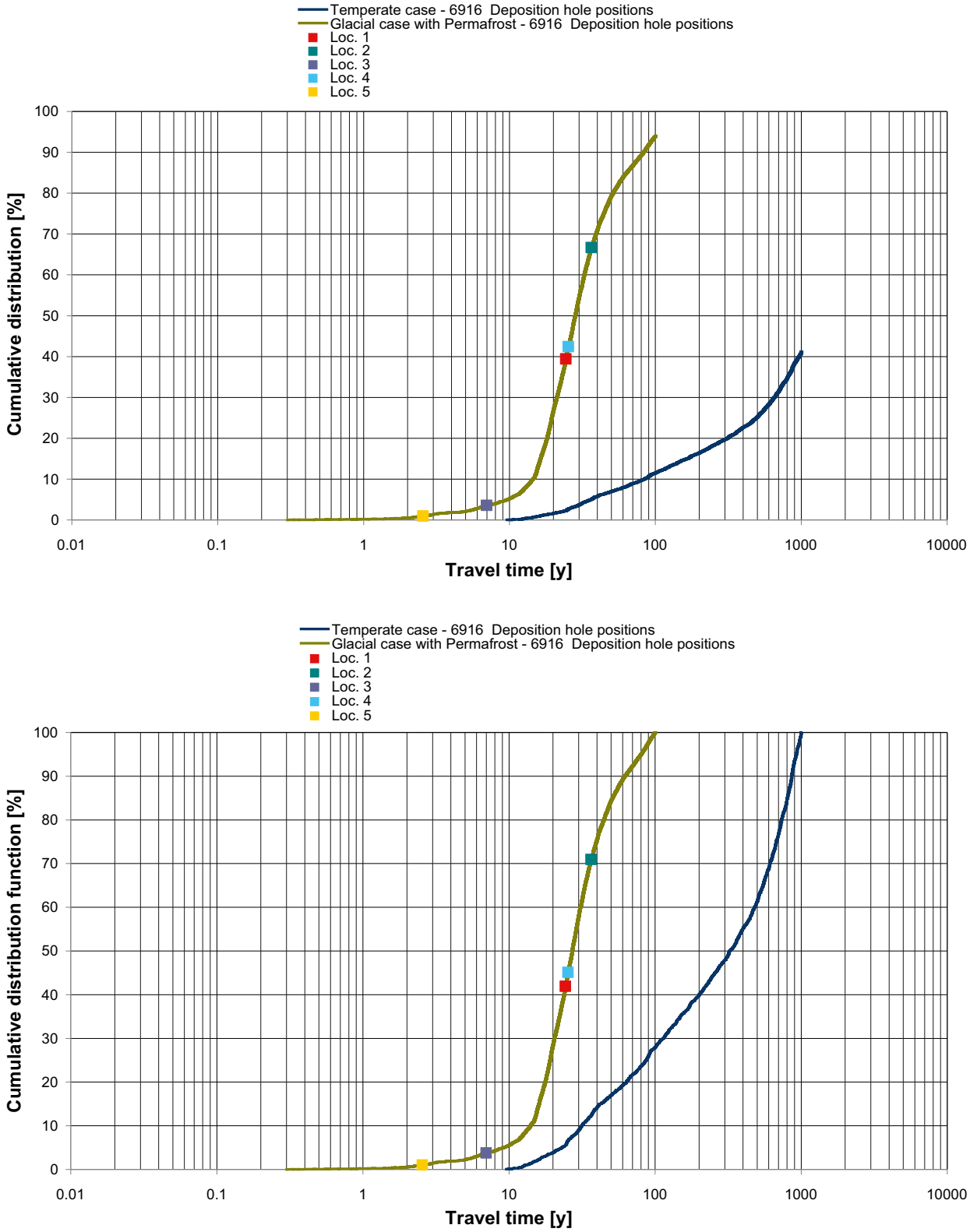

Figure G-26. *Cumulative distribution (probability) plots for the simulated discharge travel times, $t_{w,D}$, when the ice sheet margin is at IFL II. The distribution for the temperate case is also shown as well as the data for ML 1–5 at IFL II. The maximum value in the upper plot is set to 100% in the lower plot.*

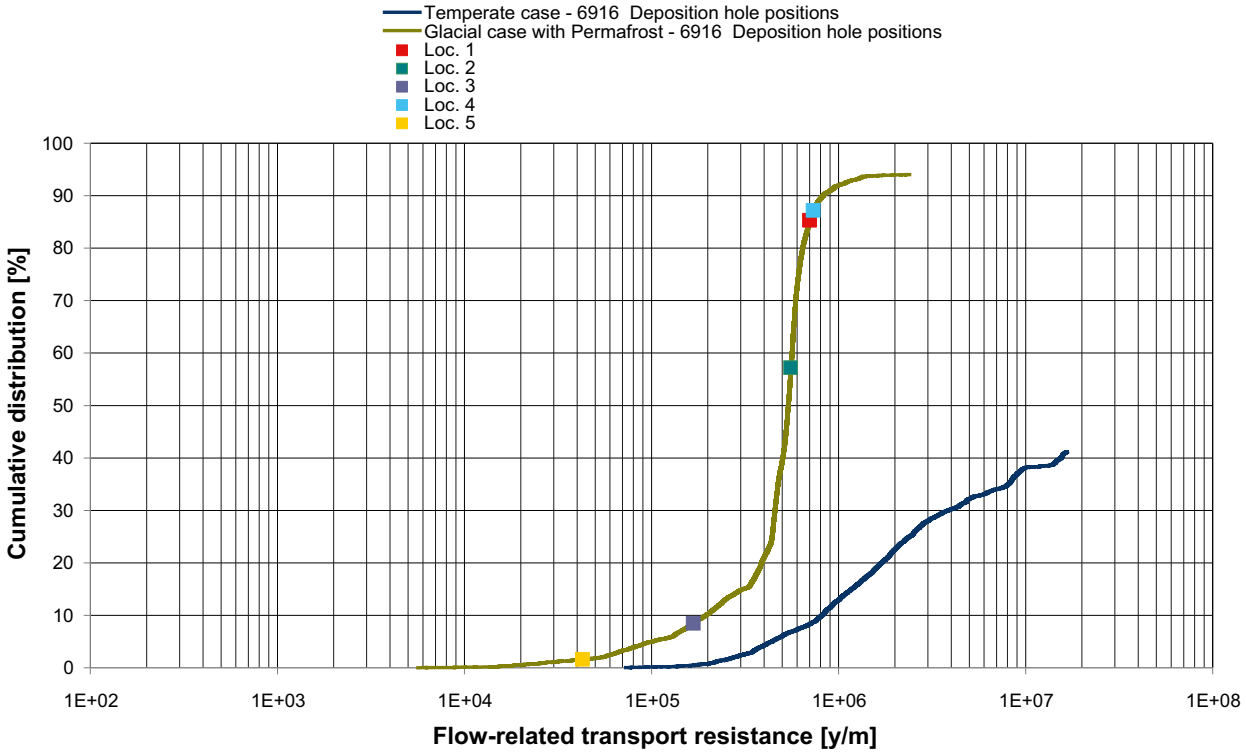

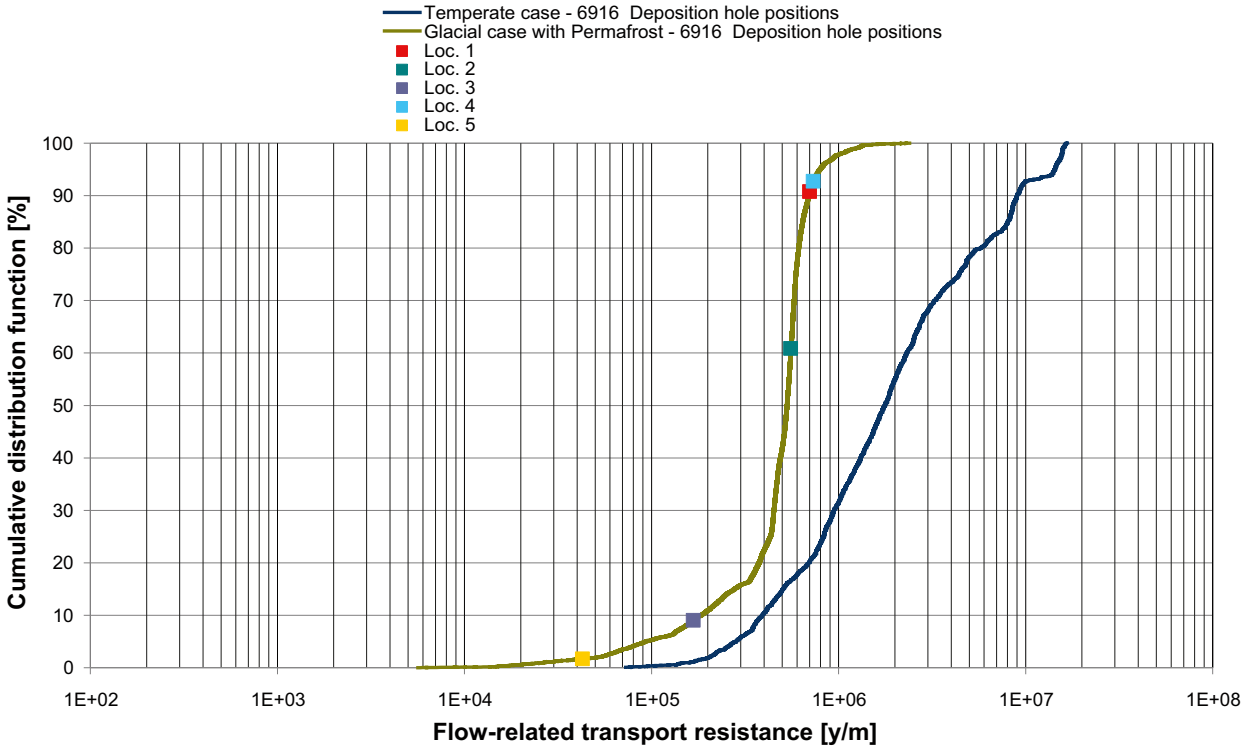

Figure G-27. *Cumulative distribution (probability) plots for the simulated discharge flow-related transport resistances, F_D, when the ice sheet margin is at IFL II. The distribution for the temperate case is also shown as well as the data for ML 1–5 at IFL II. The maximum value in the upper plot is set to 100% in the lower plot.*

Appendix H

DFN parameters for FFM02

Posterior to the completion of the work reported here it was discovered that the orientation data used to model the discrete fracture network (DFN) of FFM02, see Table B-4, deviate from derived data of SDM-Site Forsmark shown in Table C-2 in /Follin 2008/. This appendix explains the deviations and comments the implications for the groundwater flow modelling of periods with periglacial and glacial climate conditions. The DFN data for FFM02 shown in Table C-2 in /Follin 2008/ are repeated below in Table H-1. Table H-2 shows the DarcyTools parameter values associated with Table H-1.

Table H-1 reveals that the primary fracture set, HZ, is more concentrated around the mean pole and trend than modelled in the work reported here, see Table B-4. Table H-1 also reveals that the other fracture sets are both less steeply dipping and less concentrated than modelled in the work reported here. Hence, the employed DFN model exaggerates the vertical flow capacity of fracture domain FFM02 compared to the findings of SDM-Site Forsmark. In effect, the modelling results reported here are probably overestimating the penetration depth of the flushing of the bedrock by glacial melt water. Thus, in this regard, the modelling results of this study are judged to be overly pessimistic from a safety assessment point of view.

Table H-1. Parameter values used in SDM-Site for fracture domain FFM02 (Appendix C in /Follin 2008/).

Elevation (m RHB 70)	Fracture set name	Orientation set pole: (trend, plunge), conc. κ (°,°, –)	Size model, power-law (r_0, k_r) (m, –)	Intensity ($P_{32,open}$) valid size interval: (r_0, 564 m) (m^2/m^3)	Transmissivity model constants Equation (3-4)
> –200	NS	(83, 10) 16.9	(0.038, 2.75)	0.342	$(a,b,\sigma_{logT}) = (9.0 \cdot 10^{-9}, 0.7, 1.0)$
	NE	(143, 9) 11.7	(0.038, 2.62)	0.752	
	NW	(51, 15) 12.1	(0.038, 3.20)	0.326	
	EW	(12, 0) 13.3	(0.038, 3.40)	0.156	
	HZ	(71, 87) 20.4	(0.038, 2.58)	1.582	

Table H-2. DFN parameter values for FFM02 corresponding to Table H-1.

Set	λ_1 (–)	λ_2 (–)	λ_3 (–)	D (–)	L_{ref} (m)	I: > –200 (m^{-3})
NS	16.51919	2.02830	–2.93465	–2.75	1	0.033937
NE	6.95455	–9.22899	–1.83028	–2.62	1	0.087765
NW	9.08305	7.35531	–3.13171	–3.20	1	0.015786
EW	2.76523	13.00936	0.00000	–3.40	1	0.005000
HZ	1.00949	0.34759	–20.37204	–2.58	1	0.192637